Fe^{III} Complexes of Biuret-Amide Based Macrocyclic Ligands as Peroxidase Enzyme Mimic: Applications in Analyte Detection

A DISSERTATION SUBMITTED TO THE

SAVITRIBAI PHULE PUNE UNIVERSITY

FOR THE DEGREE OF

DOCTOR OF PHILOSOPHY

IN

CHEMISTRY

BY

CHAKADOLA PANDA

RESEARCH SUPERVISOR

DR. SAYAM SEN GUPTA

CHEMICAL ENGINEERING AND PROCESS DEVELPOMENT DIVISION

CSIR-NATIONAL CHEMICAL LABORATORY

PUNE-411008

INDIA

DECEMBER 2014

राष्ट्रीय रासायनिक प्रयोगशाला
(वैज्ञानिक तथा औद्योगिक अनुसंधान परिषद)
डॉ. होमी भाभा रोड, पुणे - 411 008. भारत
NATIONAL CHEMICAL LABORATORY
(Council of Scientific & Industrial Research)
Dr. Homi Bhabha Road, Pune - 411008. India

CERTIFICATE

This is to certify that the work incorporated in the thesis entitled **"Fe^{III} Complexes of Biuret-Amide Based Macrocyclic Ligands as Peroxidase Enzyme Mimic: Applications in Analyte Detection"**, submitted by Chakadola Panda for the degree of ***Doctor of Philosophy*** to the Savitribai Phule Pune University, has been carried out by him under my supervision at Chemical Engineering and Process Development Division, CSIR-National Chemical laboratory, Pune-411008, India. All the materials from the other sources have been duly acknowledged in the thesis.

Research Supervisor
(Dr. Sayam Sen Gupta)

Communications Channels ☎ +91 20 25902000 +91 20 25893300 +91 20 25893400 Fax +91 20 25902601 (Director) +91 20 25902660 (Admin.) +91 20 25902639 (Business Development) URL : www.ncl-india.org

DECLARATION

I hereby declare that the thesis entitled **"Fe^{III} Complexes of Biuret-Amide Based Macrocyclic Ligands as Peroxidase Enzyme Mimic: Applications in Analyte Detection"**, submitted for the degree of ***Doctor of Philosophy*** to the Savitribai Phule Pune University, has been carried out by me at Chemical Engineering and Process Development Division, CSIR-National Chemical laboratory, Pune-411008, India, under the supervision of Dr. Sayam Sen Gupta. The work is original and has not been submitted in part or full by me for any other degree or diploma to this or any other University.

Chakadola Panda

Dedicated to My Parents

Acknowledgement

I take this opportunity to express my deep sense of gratitude to one and all; the persons who have contributed directly or indirectly to this thesis.

Foremostly, I would like to thank my teacher and mentor, Dr. Sayam Sen Gupta, for his continuous guidance and encouragement that helped me to execute most of the projects successfully. I salute his passion toward chemistry and fundamental science. I sincerely acknowledge the freedom provided by him to think and work independently. It has been a wonderful experience working with such a vibrant and dynamic person in my life. He has been the source of inspiration and the role model in many aspects of my life; whether scientific or non-scientific. I'll remain indebted to him for shaping me to be a good researcher and a good human being as well.

I would like to thank the Council of Scientific and Industrial Research, New Delhi, for award of research fellowship. I am thankful to Dr. S. Sivaram, Ex-Director, Dr. B. D. Kulkarni, Ex-Deputy Director, Dr. S. Pal, Director and Dr. V. V. Ranade, Deputy Director, National Chemical Laboratory for extending all possible infrastructural facilities to complete my research work. I would also like to express my heartfelt thanks to all the scientific members of our CEPD Division, especially, Dr. A. Kulkarni, Dr. V. Panchagnula and Mrs. S. Shingote for their helping nature and fruitful discussions. I need to express my thanks to the support group (Patane kaka, Kamble kaka, Subbi, Ravi & Radha) and all the staff members of our division, especially Mr. Raheja for his valuable cooperation and help to process all the official work.

Several people from NCL have indirectly contributed to the thesis; I must thank each one of them. My Special thanks to, Dr. B. L. V. Prasad, Dr. Satish B. Ogale, Dr. H. V. Thulasiram Ram, Dr. Sreekumar Kurungot, Dr. C. V. Avadhani, Dr. P. P. Wadgaonkar, Dr. D. Srinivas, Dr. Satyanarayana, Dr. C. S. Gopinath, Dr. Kumar Vanka, Dr. Mahesh J. Kulkarni and Dr. B. Santhakumari for allowing me to use their laboratory facility and/or scientific discussions during my whole research study at NCL. I would like to acknowledge, Dr. R. Banerjee and his research group (special thanks to Tamas and Arijit) for help with X-ray crystallography. I thank Dr. S. K. Asha and Dr. Nandini Devi and her research group (Leena and Anupam) for the help they provided in UV-vis and GC instrumentation. I am thankful to Joyasish and Sreekuttan for their help in cyclic

voltammetry experiments. I acknowledge Dr. P. R. Rajamohanan, from central NMR facility and Mrs. D. Dhoble, Mrs. P. Purohit and Mr. S. Jha for help regarding NMR, FT-IR and UV-vis spectroscopy. I would like to thank each research group (Dr. Amitabha Das, Dr. Shubhangi B. Umbarkar, Dr. E. Balaraman, Dr. B. Punji, Dr. S. Chikkali, Dr. S. Sen, and Dr. K. Vanka) of our organometallic seminar forum for the healthy scientific discussions over last one year.

I have been very lucky to get an opportunity to work with several great people from different institutions other than NCL, without their help, this thesis would not have completed. I sincerely thank Prof. Shyamalava Mazumdar and his group for allowing me to work at TIFR, Mumbai for the protein detection project. I would also like to thank Prof. Ranjan Das and his group and prof. Jyotishman Dasgupta for help with EPR analysis at TIFR. I acknowledge Dr. S. Hotha (IISER, Pune) and his group (Asif, Maidul and Shivaji) for help with mass spectrometric studies. I thank, Prof. Pradyut Ghosh, Prof. Tapan K. Paine and their research group from IACS, Kolkata for help and discussion on EPR studies.

I would like to accolade the key persons, who made my NCL life easy and enjoyable; my labmates and friends (past and present); with whom I spent the most time. I thank my seniors, Malvi, Mrityunjoy, Debasis and Anal for their help and invigorative suggestions. I must thank my current labmates, Basab da, Sushma, Munmun, Soumen, Vinita, Kundan, Santanu, Praveen, Bhawana, Nimisha, Sandipan, Bittu, Nikhil and Maria for their presence in all aspects of my Ph.D. career. Special thanks to Basab da, who taught me kinetics, how to look at reaction mechanism and has enormously contributed to the thesis. I would like to thank Yudhajit, Abhishek, Shanti, Preetam, Anindita, Hridesh, Suyana, Bijoy, Rajeesh, Lakha, Umesh, Neha, Asif, Deepika, Ajeet, Nivedita, Amrish and Sandeep for their help and support at NCL. It has been a great working environment in the D-wing of PAML building, NCL. I have really enjoyed my research time with all the members of D-wing. I am thankful to all and wish them great success ahead.

I take this opportunity to express my special thanks to my odiya group friends (past and present), Debasish bhai, Gokarneswar bhai, Rosy apa, Ramakanta bhai, Pitambar bhai, Manaswini apa, Subash bhai, Karubaki, Mandakini, Siba, Jitu, Raju, Kshirodra, Puspanjali, Bishnu, Lakshmi, and Manoj for making my life joyful during weekends, trips and get-togethers.

I would like to convey my heartfelt gratitude to my teachers (Prof. S. Bhattamishra, Dr. Prafulla Ratha, Pradeep sir, Rabi sir and Sarath sir) who ignited my imaginations during my earlier study career and encouraged me to reach this extent.

I owe all my achievements to my father (late Shri. Prakash Ch. Panda) and family (Bou, Santosh bhai, Bhauja, Sridhar, Rajani, Aditya and Rajashri). I express my sense of gratitude to my maternal family (Aie, Binayak mamu, Narayan mamu, Runi mnai, Archana mnai, Soham and Subham) for their constant support and encouragements. I also thank my paternal family (kaka, khudi and younger ones) for their constant help and support.

Chakadola

Table of Contents

List of Figures

List of Schemes

List of Tables

List of Abbreviations

OEC	Oxygen evolving complex
WO	Water oxidation
His	Histidin
MMO	Methane monooxygenase
EXAFS	X-ray absorption fine structure
Cpd I	Compound I
TMB	3,3',5,5' Tetramethyl benzedine
HRP	Horseradish peroxidase
ELISA	Enzyme linked immunosorbent assays
TON	Turnover number
TOF	Turnover frequency
UV-vis	Ultraviolet-visible
EPR	Electron paramagnetic resonance
FTIR	Fourier transform infrared spectroscopy
NMR	Nuclear magnetic resonance
ESI-MS	Electron spray ionization mass spectrometry
GC	Gas chromatography
GC-MS	Gas chromatography mass spectrometry
HR-MS	High resolution mass spectrometry
TMP	meso-Tetramesityl porphyrin
TPPS	meso-tetrakis(4-sulfonatophenyl) porphyrin
TCP	2,4,6-Trichloro phenol
PCP	2,3,4,5,6-Pentachloro phenol
DCQ	2,6-dichloro-1,4- benzoquinone
m-CPBA	*meta*-Chloroperoxybenzoic acid
PcS	Sulfonated pthalocyanins
RhB	Rhodamine B
TPA	Tris(2-pyridylmethyl)amine
TACN	1,4,7-Triazacyclononane
PyTACN	1-(2′-pyridylmethyl)-4,7-dimethyl-1,4,7-triazacyclononane
N_4Py	1,1-di(pyridin-2-yl)-N,N-bis(pyridin-2-ylmethyl)methanamine
TMC	1,4,8,11-tetramethyl-1,4,8,11-tetraazacyclotetradecane
TAPH	1,4,8,12-tetraazacyclopentadecane
BPMCN	N,N'-bis(2-pyridylmethyl)-N,N'-dimethyl-trans-1,2-diaminocyclohexane
TPEN	N,N,N',N'-tetrakis(2-pyridylmethyl)ethylenediamine
TAML	Tetraamido macrocyclic ligand

MHz	Megahertz
ppm	Parts per million
CV	Cyclic voltammetry
WE	Working electrode
RE	Reference electrode
CE	Counter electrode
Fc/Fc^+	Ferrocene/Ferrocenium
THF	Tetrahydrofuran
Et_3N	Triethyl amine
EtOAc	Ethyl acetate
CD_3OD	Methanol-d4
DMSO	Diethyl sulfoxide
n-BuLi	n-Butyl lithium
MeOH	Methanol
DCM	Dichloromethane
ORTEP	Oak Ridge Thermal Ellipsoid Plot
LMCT	Ligand to metal charge transfer
CH_3CN	Acetonitrile
PCET	Proton coupled electron transfer
OE	Oxygen evolution
OEC-PSII	Oxygen-evolving complex of photosystem II
NPs	Nanoparticles
WOC	Water oxidation catalyst
POM	Polyoxometalates
DLS	Dynamic light scattering
TEM	Transmission electron microscopy
AFM	Atomic force microscopy
SPR	Surface plasmon resonance
SERS	Surface enhanced Raman spectroscopy
SEM	Scanning electron microscopy
LED	Light-emitting diode
NaOCl	Sodium hypochlorite
CAN	Ceric ammonium nitrate
$[Ru(bipy)_3]^{2+}$	Tris (2,2′-bipyridyl) dichlororuthenium(II)hexahydrate
$Na_2S_2O_8$	Sodium persulfate
SHE	Standard hydrogen electrode
$t_{1/2}$	Half life
OD	Optical density
SDS PAGE	Sodium dodecyl sulfate poly acrylamide gel electrophoresis

Fe-MSN	Fe-TAML immobilized inside mesoporous silica nanoparticle
PVDF	Polyvinylidene difluoride
ABPP	Activity-based protein profiling
APS	Ammonium persulphate
Tris	Tris(hydroxymethyl)aminomethane
TEMED	N,N,N',N' Tetramethylethylenediamine
HSA	Human serum albumin
THPTA	Tris(3-hydroxypropyltriazolylmethyl) amine
TLC	Thin-layer chromatography
HCl	Hydrochloric acid
NHS	N-hydroxysuccinamide
HSA-N_3	Azide grafted human serum albumin
CuAAC	Copper(I) catalysed cycloaddition reaction of azide and alkyne
HSA-Fe-TAML	Fe-TAML conjugated HSA
KDa	Kilodalton
CN^-	Cyanide ion
ICP-OES	Inductively coupled plasma-optical emission spectroscopy
ppb	Parts-per-billion
DI	De-ionized water
PB	Phosphate buffer
LOD	Limit of detection
WRC	Water reduction catalyst

Abstract of the Thesis

Designing metal complexes that activate H_2O_2 or O_2 but are themselves inert to oxidation is the key to the synthesis of efficient transition metal oxidation catalysts. An approach pursued by many chemists to achieve this goal has been to mimic enzymes that function as oxidation catalysts. Nature has evolved enzymes that are very efficient as oxidation catalysts. These include cytochrome P450 and peroxidases; enzymes that use an iron(IV) oxoporphyrin radical cation intermediate to catalyze the oxidation of various organic substrates selectively and efficiently. Major research efforts have been directed towards the synthesis of biologically inspired metal complexes that mimic the structure and function of these oxidases. In recent years, several metal complexes that activate H_2O_2 or O_2 have been synthesized from biologically relevant transition metals and a myriad of electron donating ligands. Among these, Fe(III) complexes based on a class of tetraamide macrocyclic ligands (Fe-TAML's) developed by Collins *et al.* have several attributes that render them to be excellent functional mimics of peroxidases. These include; a) stability of the complex in water at a variety of pH and ionic strength, and b) fast rates and very high turnover numbers that are similar to peroxidases. These are truly "green catalysts" as these perform various oxidations in water using H_2O_2 and have been used for the degradation of various environmental pollutants. However, there are certain limitations (low hydrolytic and oxidative stability) of Fe-TAMLs that need to be addressed while moving towards new generation oxidation catalysts.

The thesis describes the design and synthesis of Fe(III) complex of a biuret-amide based macrocyclic ligand synthesized from common elements of biochemistry that exhibit both excellent reactivity for the activation of H_2O_2 and high stability, especially at low pH and high ionic strength. They not only mimic the peroxidase enzymes but also outperform the same there by overcoming the limitations of the enzymes especially in various analyte detection protocols. Also the ability of these catalysts towards homogeneous photochemical and chemical water oxidation was accomplished and the mechanism of the process was studied.

Chapter I includes a comprehensive survey of literatures showing importance of oxidation in sustaining life where the natural enzymes play the crucial role of myriad of

oxidation reactions by activating small molecules like O_2 and H_2O_2. The design principles of metal-ligand complexes necessary for the synthesis of more powerful oxidation catalysts especially from large scale synthetic point view are also covered in this chapter.

Chapter II discusses the synthesis of the Fe(III) complexes of biuret-modified tetra-amido macrocyclic ligands (biuret-modified Fe-TAML) as peroxidase enzyme mimic and their detailed characterization by conventional spectroscopic techniques (UV-vis, FT-IR, EPR, NMR, HR-MS), cyclic voltammetry and X-ray crystal structures. H_2O_2 activation by these complexes to completely decolorize organic dyes with detailed kinetic study and a comparison of stability and reactivity with respect to previously reported complexes is also provided in the later part of this chapter.

Chapter III discloses the first ever example of photochemical water oxidation by the molecular iron complex biuret-modified Fe-TAML. Based on the spectroscopic techniques (UV-vis, EPR and HR-MS) we were able to identify a high valent $Fe^{V}(O)$ species for the first time during photochemical water oxidation in a mixed solvent system of CH_3CN and H_2O mixtures. In an attempt to elucidate the exact role of the *in situ* generated $Fe^{V}(O)$ species, we proved that $Fe^{V}(O)$ alone cannot oxidise water but it needs to be further oxidised in order to be a water oxidation catalyst. A plausible mechanism is discussed based on theoretical calculations reported in literature and our experimental findings where a second water molecule neucleophilically attacks the $Fe^{V}(O)$ intermediate to form the corresponding hydroperoxo species (Fe^{III}-OOH) which is further oxidised to release a molecule of dioxygen.

Chapter IV discusses the use of biuret-modified Fe-TAML as a potential replacement of the HRP in various analyte detection methodologies. The concept relies on use of signal amplification as HRP does in most of the biological assays for detection of ultra-low concentrations biomarkers.

First part of this chapter provides the synthesis of a clickable alkyne tailed biuret-modified Fe-TAML which was used to develop detection protocols for protein biomarker

sensing by applying the peroxidase like activity of biuret-modified Fe-TAML to generate a visual signal in presence of H_2O_2 and a colorless substrate. The second part of this chapter discusses colorimetric detection of CN^- in aqueous media by using the enzyme catalase in tandem with mesoporous silica nanoparticle based synthetic HRP enzyme mimic Fe-MSNs. Signal amplification up to a maximum of eight fold was observed for the reporter ‘‘oxidized TMB’’ with respect to the added CN^- ion.

Chapter V presents an overall summary of the work done and describes the major findings of the studies. Future directions based on the work reported in the thesis are also discussed.

Chapter I

Introduction to Bio-inspired Oxidations and Literature Survey

1.1 Introduction

The selective oxidation of various substrates is of fundamental importance in the sustenance of life processes. Oxidation also has tremendous industrial application, since the majority of chemicals, fuels, and materials used daily come from the oxidation of petroleum feedstocks. The oxidation of natural hydrocarbons is the first key step for bulk chemical synthesis, but many challenges remain, such as the oxidation of methane to methanol on an industrial scale.[1] The fundamental challenge lies in the activation of inert C-H bonds and their subsequent functionalization.[1-3] An important technology in this area is catalytic oxidation using molecular oxygen, but its success in organic synthesis has been very modest, as O_2 undergoes free radical reactions that leads to undesired products with organic molecules in the absence and presence of metal catalysts. Although the oxidation of organic molecules with O_2 is thermodynamically favorable, due to their exothermic nature, these reactions are kinetically very slow, because of the spin mismatch between ground-state oxygen (triplet) and most organic substrates (singlet). This explains how all forms of life (mostly organic materials) are protected from burning up in air into carbon dioxide and water.

However, nature has evolved metalloenzymes to activate molecular oxygen ($^3O_2$), by overcoming the kinetic barrier and performing selective and controlled oxidation of specific substrates. These metalloenzymes are of great significance, because these use cheap and earth-abundant transition metals, such as iron, copper, and manganese for these processes;[4] often exhibit exquisite substrate specificity as well as regioselectivity and/or stereo selectivity; and operate under mild conditions through inherently 'green' processes. Classic examples of metalloenzyme-mediated transformations are key metabolic functions such as hydroxylation of methane in methanotrophs, desaturation of fatty acids in plants, DNA and RNA repairs, biosynthesis of β-lactam antibiotics, and sensing of hypoxia in mammalian cells to signal the formation of blood vessels.[5-8] The metal-active centers in native enzymes are well protected by protein scaffolds from potential deactivation routes, and therefore can adopt unique structures and exhibit unusual properties to perform substrate-specific oxidations. The use of transition metal complexes to activate the naturally abundant green oxidant O_2 efficiently to facilitate industrial oxidative transformations is also important.[9,10] Hence, much effort has been

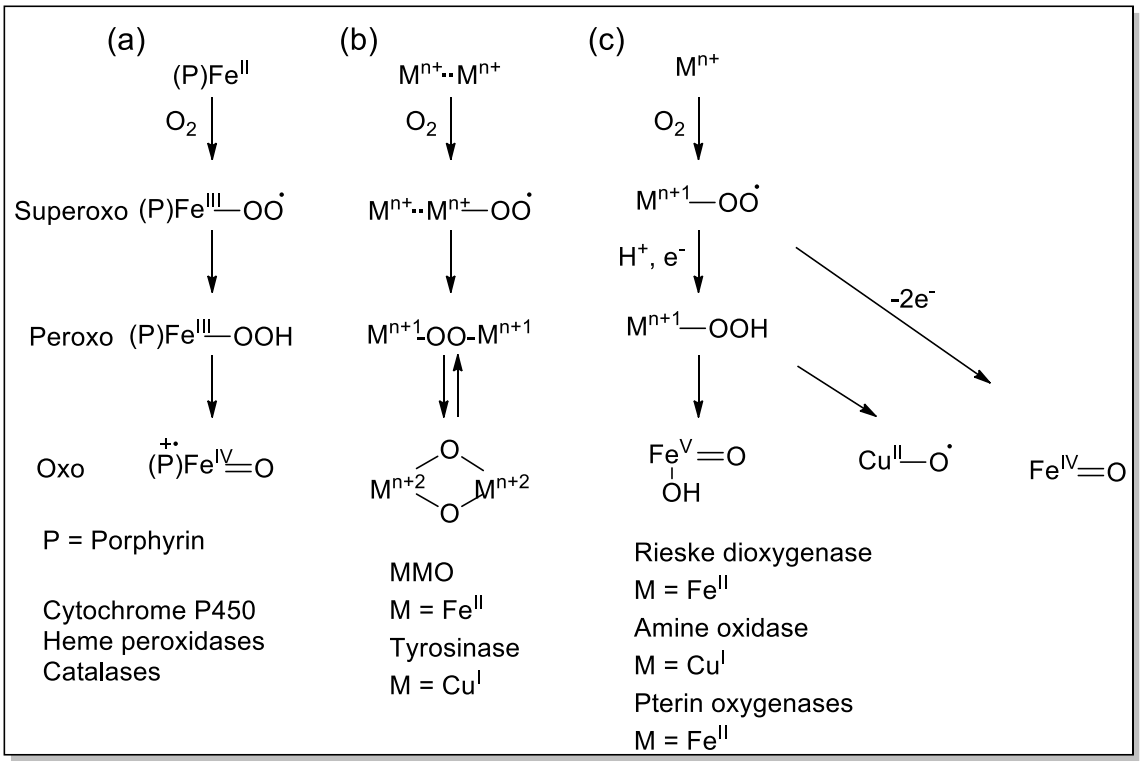

Figure 1.1: Generally accepted mechanisms of metallo-oxygenases[4] (adapted with permission).

made to understand the mechanisms of dioxygen activation in a number of heme and non-heme monooxygenase enzymes.[4,5,11-21] Figure 1.1 describes a general mechanistic approach applicable to a broad range of metalloenzyme mediated oxidations, which have been studied using X-ray crystallography and spectroscopic characterization of enzyme-resting states/reactive intermediates, intertwined kinetics, synthetic modelling, and theoretical investigations.

Another application of oxidation that has a major impact on sustainability is in environmental remediation, such as wastewater treatment. In this process, toxic compounds like polychlorophenols and effluent from the textiles and paper and pulp industries are oxidized into small, non-toxic compounds that meet emissions standards.[22-27]

Oxidation is also fundamentally important from the energy perspective. One reaction that distinguishes Earth from other planets is photosynthesis, in which plants and green algae convert solar energy into chemical energy. Photosynthesis comprises the very

initial sunlight-driven oxidation of water by the oxygen evolving complex (OEC)—composed of earth-abundant manganese and calcium clusters—to produce dioxygen, four protons, and four electrons, followed by a reduction of atmospheric CO_2, following a cascade of reactions, to prepare carbohydrate as chemical energy.[28,29] In consequence, great research effort is being given worldwide to study the exact mechanism of water oxidation catalyzed by natural OEC and to prepare functional synthetic mimics that can function as catalysts for efficient water oxidation (WO) that can be further developed into a proton-reduction process to produce H_2, which is a cleaner energy source.

1.2 Iron-containing enzymes and the reactions they catalyze

Most metalloenzymes have evolved with an iron-containing active center that can be correlated to their abundance, inherent electronic properties, and accessible redox potentials. Based on the type of biological reaction these perform, these are classified as oxygenases, oxidases, reductases, hydrogenases, or dehydrogenases. Most importantly, these enzymes use molecular oxygen to perform many oxidation reactions that are important in executing many biological processes, including the biosynthesis of hormones, the metabolism of drugs, DNA and RNA base repair, and the biosynthesis of antibiotics.[5-8] Based on their structural feature, iron-containing enzymes that activate O_2 have been categorized into 'heme', with iron-porphyrin cofactors, and 'non-heme', with iron active centers bound to amino acid residues.

1.2.1 *Heme iron enzymes*

These enzymes have an iron active site coordinated to a porphyrin cofactor in a square pyramidal fashion, with one axial cysteine/histidine ligand from the protein backbone, and the other axial position available for O_2/H_2O_2 binding and activation. Depending on the activation of O_2 and H_2O_2, these are classified as oxidases or peroxidases. Peroxidases are the class of heme enzymes where a histidine residue occupies one of the two axial coordination sites and the other axial site is used for H_2O_2 activation. The detailed structural and mechanistic properties of peroxidases are described in Section 1.2.3. Oxidases are heme enzymes that activate O_2 at one of the two axial sites and have the cysteine axial ligand in the other axial site. The cytochrome

P450s are the most extensively studied oxygen-activating enzymes known to carry out hydroxylation of aliphatic C–H bonds and olefin epoxidation with high regioselectivity and stereoselectivity. The generally accepted oxygen activation mechanism associated with cytochrome P450 is referred to as the heme paradigm (Figure 1.1a).[4] At first, O_2 coordinates to the reduced iron center and is progressively reduced to superoxo and peroxo forms, followed by O–O bond cleavage, to generate a formally $Fe^{V}(O)$ oxidant that, in turn, carries out the two-electron oxidation of the substrate. Of these two oxidizing equivalents, one is localized at the iron center and the other is delocalized over the porphyrin ligand and is generally accepted as an $Fe^{IV}(O)$-(porphyrin radical cation) species.

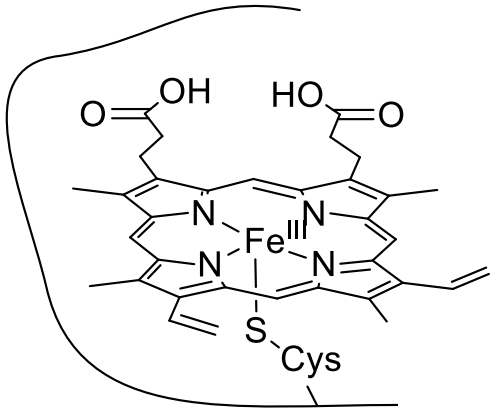

Figure 1.2: Molecular structure of the catalytically active centers of cytochrome P450.

1.2.2 *Non-heme metalloenzymes (the 2-His-1-carboxylate facial triad)*

Based on whether the active metal center is mononuclear or dinuclear, these non-heme enzymes are broadly classified into two types. Crystal structures of several mononuclear non-heme iron enzymes have been determined, and that has helped chemists understand the relationship between their structure and functional ability to catalyze diverse oxidative transformations.[5,12,30,31] Amino acid residues form the coordinating environment in the case of non-heme enzymes, which is in contrast to the heme enzymes (porphyrin cofactor). As per the available structural data, a common structural motif—comprising a mononuclear iron(II) metal center coordinated by two histidine residues and one carboxylato in a facial mode—has been obtained for the activation of dioxygen.[31] The carboxylate ligand can be either a glutamate or aspartate

residue, and the structural motif has been coined as the '2-His-1-carboxylate facial triad': Nature's recurring motif, like the heme cofactor and iron–sulfur clusters (Figure 1.3).[32,33]

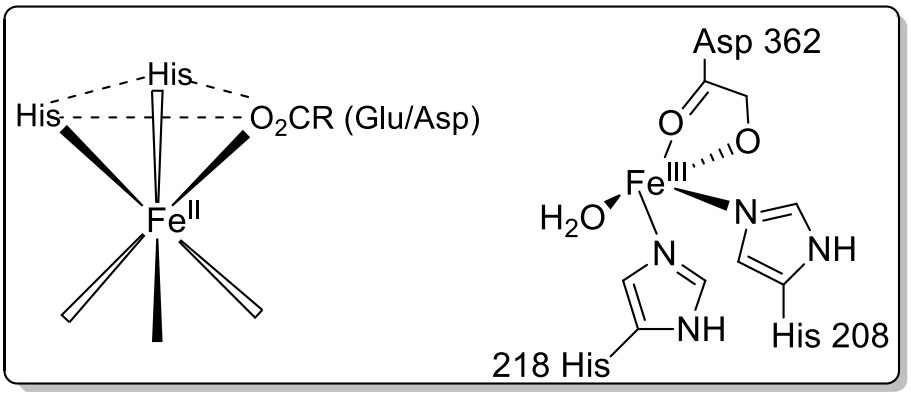

Figure 1.3: The common structural motif '2-His-1-carboxylate facial triad' for non-heme mononuclear iron enzymes (left); molecular structure of catalytically active centers of Rieske dioxygenase (right)

The octahedral coordination sphere of the ferrous metal center is occupied by three endogenous ligands from amino acid residues, i.e. two histidines and one aspartate or glutamate in one face; the other face is occupied by three weakly bound and easily displaceable solvent molecules or vacant sites (Figure 1.3). These three weak/vacant sites are readily available for the binding and activation of dioxygen, substrates, and cofactors. The unique structural occupancy in the triad motif is therefore the prime reason for specific oxidative transformations by specific enzymes.[5] Typical examples of mononuclear-type non-heme enzymes are Rieske dioxygenases, α-Ketoglutarate-dependent enzymes, and pterin-dependent hydroxylases. Rieske dioxygenases activate O_2 and catalyze the *cis*-dihydroxylation of arene double bonds to initiate the biodegradation of aromatics in the soil.[5] Unlike the porphyrin (redox non-innocence) cofactor in heme enzymes, the redox innocence nature of amino acid residues allows these enzymes to store two oxidizing equivalents in the iron atom, thereby facilitating the formation of an $Fe^{V}(O)$ oxidant. Until now, no direct spectroscopic evidence for a non-heme $Fe^{V}(O)$ species had been obtained in the enzyme cycle. However, the iron(III)–peroxo precursor (Figure 1.1c) has been characterized by X-ray crystallography,[34] and it is proposed that

the side-on peroxo moiety either attacks the arene double bond directly or isomerizes first to an $Fe^{V}(O)(OH)$ (iron oxo hydroxo) species. Several examples of $Fe^{IV}(O)$ intermediates have been trapped and characterized[35] in studies of non-heme iron enzymes that use organic cofactors such as α-ketoglutarate or tetrahydrobiopterin. Figure 1.1 presents the general mechanistic scheme. Non-heme iron enzymes catalyze a wide range of reactions by the activation of dioxygen, including monooxygenation, dioxygenation, desaturation, and the 4-electron reduction of dioxygen to water. The proposed mechanisms for non-heme iron enzymes of both type in general follow the same heme paradigm, and evidence for Fe(III)–peroxo and high-valent iron–oxo intermediates has been obtained for some of these enzymes.

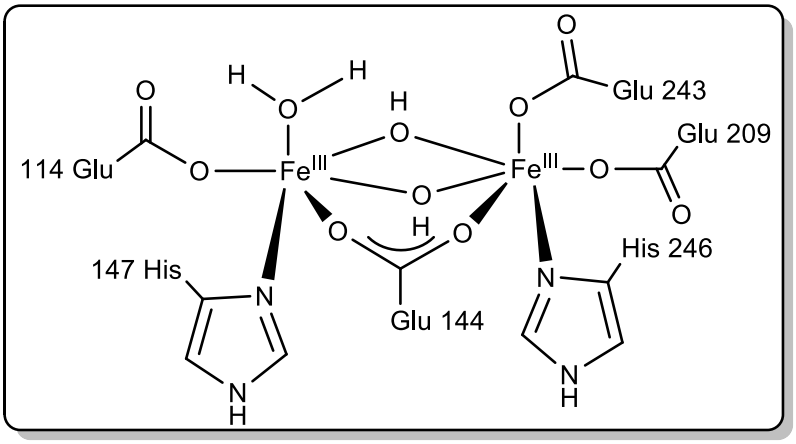

Figure 1.4: Molecular structures of catalytically active centers of the dinuclear non-heme iron enzyme methane monooxygenase (MMO).

The dinuclear non-heme enzymes are methane monooxygenases, toluene monooxygenase, tyrosynases, etc. For example, the di-iron enzyme methane monooxygenase (MMO)[36] that catalyzes the conversion of methane to methanol activates O_2 via di-iron(III)–peroxo and di-iron(IV) intermediates (Figure 1.1b). Although the peroxo-intermediate has been implicated as the oxidant in the epoxidation of electron-rich alkenes such as ethyl vinyl ether[37], the terminal oxo species has been demonstrated to be kinetically competent for methane hydroxylation.[38] A di(μ-Oxo) di-iron(IV) core[39] (popularly known as diamond core) has been confirmed by extended X-ray absorption fine structure (EXAFS) analysis for the di-iron(IV) species (Figure 1.4).

1.2.3 *Enzymes that activate H_2O_2: Peroxidases and catalases*

In contrast to the cytochrome P450, the iron-porphyrin active center in peroxidases and catalases is linked to the protein backbone through a histidine or tyrosine axial site, respectively. These are the class of the heme enzymes that short-circuit the dioxygen activation process of cytochrome P450 by two oxidation steps, thereby activating H_2O_2 directly to form the corresponding metal oxo intermediates (Cpd I). In the case of peroxidases,[40-42] the two oxidation equivalents in the iron oxo species are generally utilized for substrate oxidation. However, in the case of catalases,[43,44] the iron oxo species acts on another molecule of H_2O_2 to disproportionate into H_2O and O_2 (Figure 1.5). Although catalases are of biological importance—they protect cells from oxidative damage caused by reactive oxygen species like peroxide and superoxide—their application in industrial processes is rare, especially from the synthetic point of view. However, peroxidases that activate H_2O_2 for myriad substrate oxidations and produce new compounds are of great importance from the biological and industrial synthetic points of view.

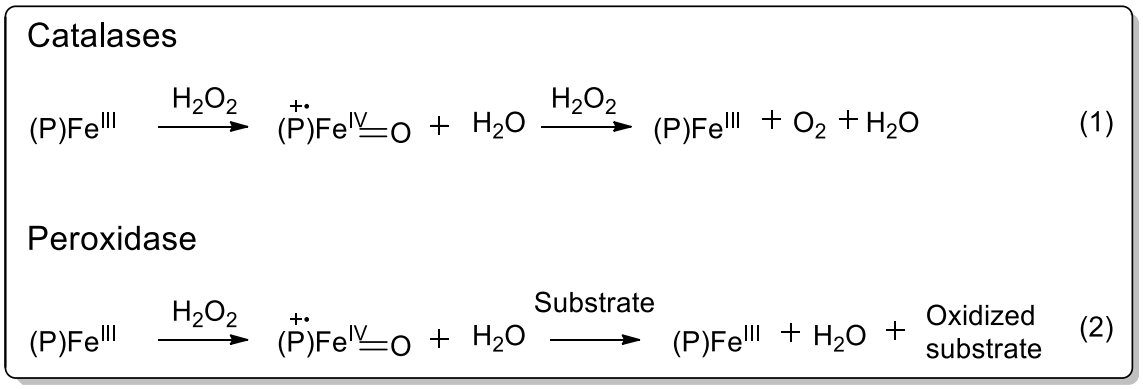

Figure 1.5: Peroxide activation mechanism by catalases and peroxidases

Peroxidases have been implicated in diverse biological processes that include both cell wall synthesis and degradation, stress response, signalling during oxidative stress, and removal of xenobiotics.[45-49] Among the many known peroxidase enzymes, horseradish peroxidase (HRP) has found enormous applications in oxidation catalysis and degradation of environmental pollutants like azo dyes.[23,24,27] More importantly, HRP is routinely used in the field of analytical diagnostics like enzyme immobilized

immunosorbent assays (ELISA; Figure 1.6),[50-52] western blots,[53-55] etc. to detect ultra-low quantities of biomolecules responsible for diseases. In these assays, HRP oxidizes a colorless peroxidase substrate to generate a colored product in the presence of H_2O_2, and so is used as a signalling tool. Peroxidase-based biosensors are widely used in analytical systems for determinations of hydrogen peroxide, and also in practical analytical applications in diagnostic kits, such as quantitation of uric acid,[56,57] glucose,[58,59] lactose,[60] cholesterol,[61a] etc. Lignin peroxidases[61b] are widely used in wastewater treatment to remove pheonlic, cresol, and chlorinated phenols.

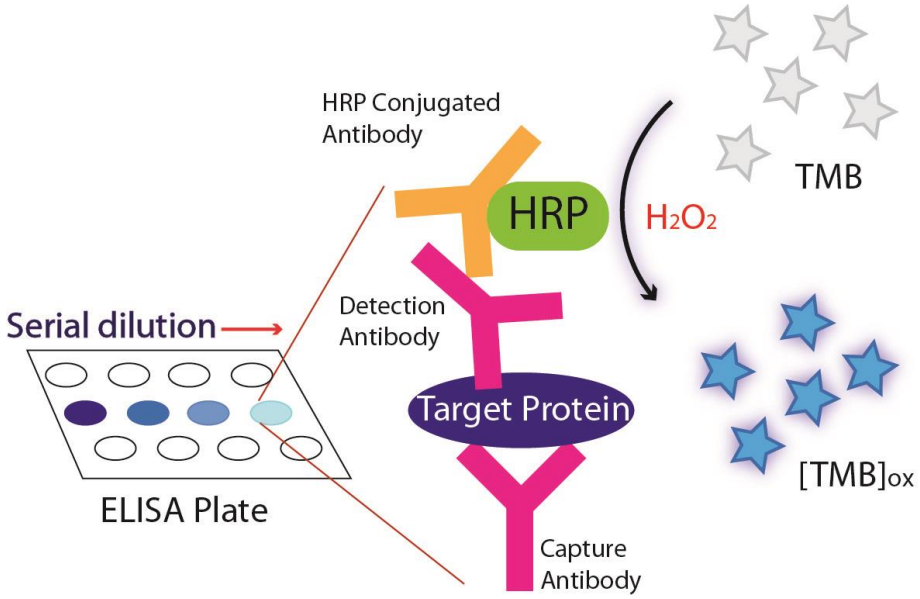

Figure 1.6: Peroxide being activated by HRP for signal generation (oxidation of TMB) in ELISA.

1.2.3.1 *Detailed mechanism of peroxidase enzyme*

Scheme 1.1 shows the important steps in peroxide activation, followed by substrate oxidation. In the peroxidase cycle, the initial step involves axial attack of H_2O_2 to the iron-porphyrin active center, followed by proton abstraction by the distal histidin (His-52). The subsequent release of a water molecule, following a heterolytic cleavage of O-O bond with the concomitant two-electron oxidation of the heme, forms the popularly known intermediate compound I (Cpd I), which comprises a ferryl species $Fe^{IV}(O)$ and a porphyrin radical cation.[41] Cpd I is then converted back to the resting enzyme via two successive single-electron transfers from reducing substrate molecules. The first

reduction, of the porphyrin radical cation, yields a second enzyme intermediate, compound II, which retains the heme $Fe^{IV}(O)$ state.[41]

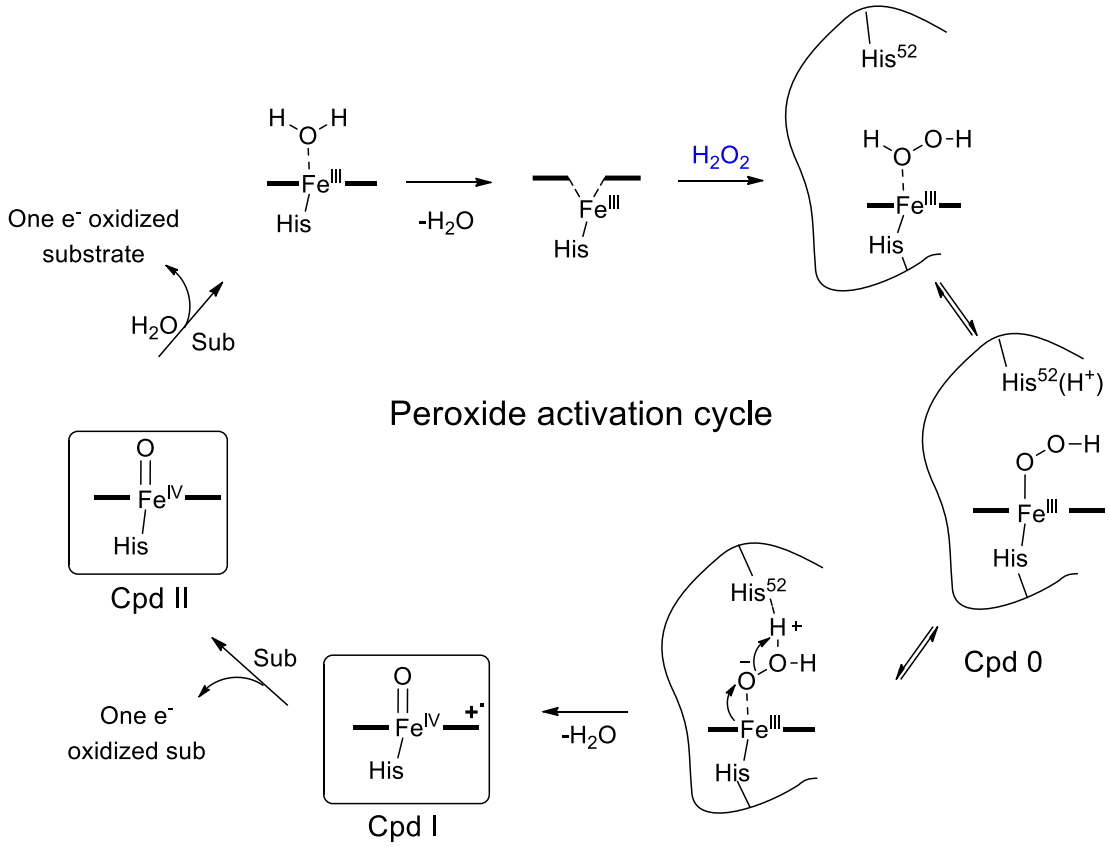

Scheme 1.1: Detailed mechanism of peroxide activation by peroxidase enzymes.[42]

1.3 Toward large-scale peroxide activation schemes

Traditionally, Cl_2/NaOCl/ClO_2 are used as common household chemicals for water treatment and degradation of stain bleaching schemes. These produce toxic, environmentally harmful chlorinated by-products. Other potential oxidizing agents—such as O_3, hydroxyl radicals (Fenton reaction), stoichiometric metal salts like permanganate, dichromate, etc.—have serious limitations from the point of cost, selectivity, or hazards associated with use and disposal. H_2O_2 is an environmentally benign and cheap oxidant—its by-product is water—and is therefore more attractive than traditional oxidants for bleaching wood pulp and textile effluents. Therefore, approximately 2.2 million metric tons of H_2O_2 is produced worldwide each year, and 60 per cent of it is used in the pulp/paper and textile bleaching processes. However, most of these bleaching procedures

are inefficient for many reasons. These include the use of very high temperatures (100 °C) due to slow reaction rates and the use of stoichiometric Fenton reagents to produce hydroxyl radicals (lack selectivity), etc. Therefore, industry depends on traditional chlorine-based oxidation protocols for bleaching pulp/paper and textiles. Hence, it is extremely important to devise efficient H_2O_2 activation schemes to eliminate the use of chlorine-based oxidants for large-scale applications. This can be achieved by designing robust oxidation catalysts based on transition metals (especially first-row) not only for bleaching purposes but also for large-scale industrial synthesis of bulk chemicals. Researchers have to follow certain design principles of metal-ligand complexes to achieve efficiency in terms of reaction rates and turnover similar to the use of native enzymes.

1.4 Challenges in designing powerful oxidizing catalysts

Unlike enzymatic oxidations, small-molecule synthetic homogeneous catalysts run oxidations with poor turnover numbers (TON) as they are susceptible to self-destruction in ambient operating conditions. The prime requirement for designing an enzyme mimetic catalyst is that it should comprise all biocompatible elements such that its toxicity—associated with their decomposition followed by disposal—to the environment is minimal. In the case of metalloenzymes and synthetic small molecules, the catalytically active center consists of multidentate ligands (mostly nitrogen donors) bound to a metal site by coordinate bonds or covalent sigma bonds. It is solely the nature of structure and bonding relations between the ligand and metal that decides the oxidation catalysts' activity and stability in ambient operating conditions. Hence, the electronics and steric around the metal active center can be rationally designed so that the overall activity of an oxidation catalyst does not affect their stability or vice versa.

1.4.1 *Activation parameters*

It is well studied that the metal active center undergoes at least two equivalent of oxidation in the presence of oxidants to form a high-valent metal oxo intermediate species which in turn oxidizes the substrate. The rates for these two processes are denoted k_I and k_{II} respectively (Scheme 1.2). For native enzymes, both the formation of the metal

oxo intermediate (k_I) and its subsequent substrate oxidation (k_{II}) are normally much higher than those of synthetic small molecular mimics.[62] The challenge lies in designing metal complexes that display reactivity (k_I and k_{II}) comparable to native enzymes.

1.4.2 *Inactivation parameters*[63-65]

In a typical oxidation reaction, various inactivating paths are always in competition with the activation pathways, as discussed above, where either the precursor metal complex or the metal oxo intermediate species undergoes complete deactivation, thereby shutting down the reaction.

1.4.2.1 *Medium induced hydrolytic decomposition*

The starting metal complex can undergo medium induced hydrolytic decay (k_d) to end up with free ligand and metal ion, as outlined in Scheme 1.2. Complexes with weak metal-nitrogen bond dissociate in water in the presence of Bronstead acids or Bronstead acid buffers to generate free metal ions. In the presence of bases, an intial formation of metal hydroxides, followed by a complete dissociation of the metal-nitrogen bond, is observed.

1.4.2.2 *Oxidative self-decay*

Metal oxo intermediate species generated upon oxidation of the precursor complex can undergo self-oxidative decay where these oxidize their own ligand framework without oxidizing the substrate. This decay is either intramolecular (k_i) or intermolecular (k_{2i}) self-oxidation (Scheme 1.2). In inter-molecular self-oxidation, the metal oxo intermediate oxidizes the ligand framework of a nearby catalyst. In intra-molecular self-oxidation, metal oxo intermediate oxidizes the ligand in the same catalyst. The inter-molecular self-oxidative decay can be minimized by working at lower catalyst concentrations. However, the intra-molecular catalyst can be minimized only by designing ligand frameworks that are robust enough to be oxidized preferentially over the substrate.

1.4.3 *Ideal catalyst (design principles of transition metal-ligand complexes)*

Based on these challenges of designing powerful oxidation catalysts, an ideal catalyst should have very high activation parameters (k_I and k_{II}) and low inactivation

parameters (k_{-I}, k_d, k_i and k_{2i}). In principle, the bonded nitrogens should be very strong sigma-donating in nature, so that a high-valent metal oxo species could be stabilized in oxidizing conditions. Therefore, anionic ligands (N^-) would be much preferred over neutral ligands (N). Also, greater the sigma donation from the ligand to the metal, greater the strong interaction (stronger bond) between them; hence, the catalyst would be stable enough (low k_d) to resist acids, base, and high ionic strengths. Also, ligand systems without any oxidation-prone sites can be designed so that the oxidation catalyst has the least ability to oxidize its own ligand framework; hence, oxidative decay (k_i and k_{2i}) can be minimized. The central challenge in developing small-molecule Fe-based catalysts that mimic the functions of peroxidases lies in designing an oxidatively robust ligand around the metal center that can also stabilize a high-valent metal intermediate that oxidizes the substrate.

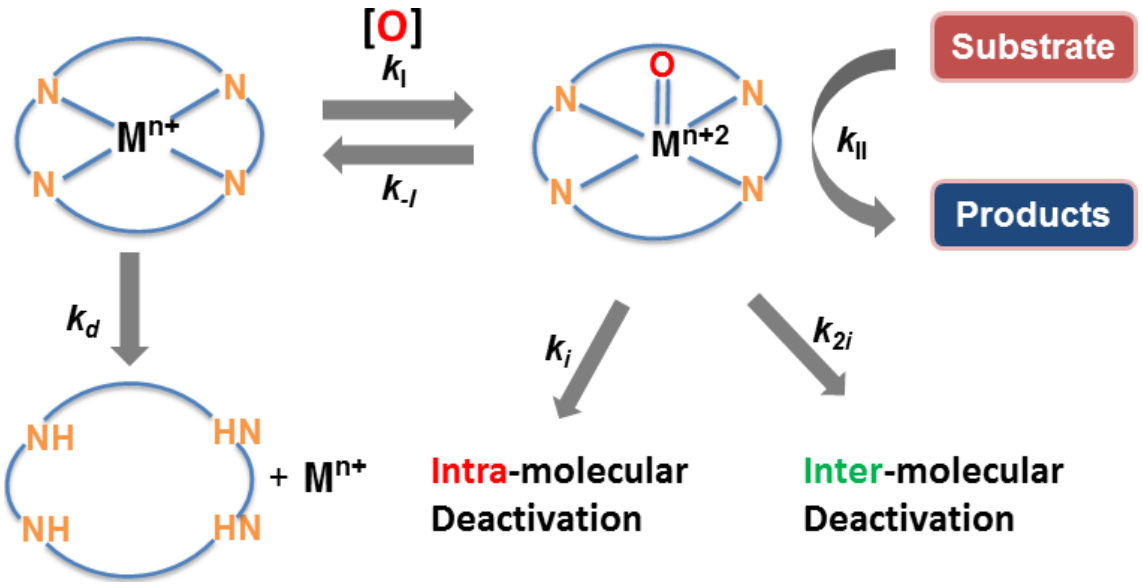

Scheme 1.2: Various activation and deactivations pathways of oxidation catalysts.[63]

1.5 Molecular metal complexes as functional analogs of peroxidases

The design of well-described model compounds can provide vital insight into the mechanism of enzymatic reactions. This would lead to the development of efficient, industrial peroxide-based technologies, especially for the synthesis of bulk and fine chemicals and for environmental remediation. Consequently, synthetic chemists have

made considerable effort to prepare viable structural and functional models of natural enzymes for putative H_2O_2 activation reactions and to isolate intermediates found in the catalytic cycles of O_2 and H_2O_2 activating enzymes. These include various heme transition metal complexes (both structural and functional mimics) and non-heme transition metal complexes (functional mimics), as those oxidation catalysts have been synthesized and shown to mimic these enzymes. To identify reactive intermediates in the presence of oxidants like H_2O_2, organic peroxides, NaOCl, PhIO, etc., conventional spectroscopic techniques like ultraviolet-visible (UV-vis), electron paramagnetic resonance (EPR), Mossbauer, electron spray ionization mass spectrometry (ESI-MS), and magnetic measurement techniques have been used. Most of these have been shown to form the corresponding two equivalent oxidized iron oxo species and used in various oxidations like C-H bond hydroxylations, olefin epoxidations, sulfoxidations and dehydrogenations, and degradation of environmental pollutants.

1.5.1 *Heme analogs and sulfonated pthalocyanines*

Synthetic, small-molecular iron porphyrines that are structurally very similar to the catalytically active center of native heme enzymes fall in this category, prepared to study in detail the mechanism of oxidation reactions mediated by these enzymes. Groves *et al.* in 1981 reported the first high-valent $Fe^{IV}(O)$ porphyrin π-radical cation $[(TMP^{+\bullet})Fe^{IV}(O)(CH_3OH)]^+$ from the oxidation of $[(TMP)Fe^{III}(Cl)]$ (TMP = meso-tetramesityl porphinate anion) with meta-chloroperbenzoic acid at -78 °C in a mixed dichloromethane-methanol solvent mixture.[66,67] $[(TMP^{+\bullet})Fe^{IV}(O)(CH_3OH)]^+$ was found to have spectroscopic features very similar to that of Cpd I in heme enzymes, and was used successfully for olefin epoxidation and alkane hydroxylations.[66,68] In an attempt to tune the electronic effects of porphyrins and, consequently, the chemical properties of the oxoiron(IV) intermediates, many electron-rich and electron-deficient porphyrins have been prepared; and it has been shown that electron-deficient iron porphyrins oxidize organic substrates better than electron-rich ones.[15,66,68] The reactivity of $[(TMP^{+\bullet})Fe^{IV}(O)(CH_3OH)]^+$ was also markedly influenced by different axial ligands bound *trans* to the iron–oxo moiety (Figure 1.7).[69] Other important oxidations involve sulfoxidation, asymmetric epoxidation, and hydroxylations, where the well-known

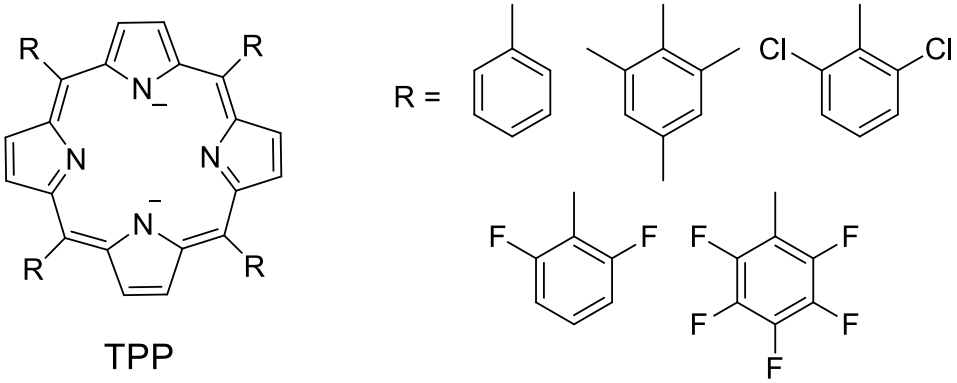

Figure 1.7: Porphyrin macrocycle with electron-rich and electron-deficient substituents.

reactive intermediate $Fe^{IV}(O)$ porphyrin radical cation was trapped by spectroscopic techniques and characterized.

Munier *et al.* developed water-soluble iron- and manganese-sulfonated porphyrins (M^{III}TPPS, TPPS = dianion of *meso*-tetrakis(4-sulfonatophenyl) porphyrin) as chemical models of ligninase to remove completely undesired lignin from wood pulp (mixture of cellulose and lignin) to have good quality white paper.[70,71] This alternative approach of using synthetic metalloporphyrins to activate H_2O_2 to remove lignin quickly is more eco-friendly than the classical chlorine-based method of oxidative degradation of lignin because there are no chlorinated phenol residues.[71]

Biodegradation of most man-made organic chemicals involves reductive or oxidative steps or successive combinations of both modes of activation by microorganisms in the body. However, some molecules like organic halides (e.g. DDT and lindane, common names for l,l,l-trichloro-2,2-bis *p*-chlorophenyl) ethane and lα,2α,3β,4α,5α,6β-hexachlorocyclohexane and poly chlorophenols like TCP, PCP etc.) are recalcitrant to biotransformation and are subject to biomagnification and accumulation in plant or animal tissues.[71,72] Among these compounds, organic halide pollutants resist microbial destruction. Thus, there is an urgent need for new catalytic processes that can remove recalcitrant molecules from wastewater or industrial effluents so that they do not accumulate in the environment. The biomimetic complexes discussed above were able to catalyze efficiently the oxidation of 2,4,6-trichlorophenol (TCP) to the corresponding 2,6-dichloro-1,4- benzoquinone (DCQ), which can be easily excreted from

the body. Catalytic activities as high as 20 cycles s^{-1} have been observed.[70,71] The same catalytic systems are also able to oxidize DDT and lindane.

Synthetic metalloporphyrin models of cytochrome P-450 have also been used to catalyze the metabolization of various drugs. The first models used were simple, non–water-soluble iron porphyrins, such as Fe(TPP)Cl. For example, the PhIO/Fe(TPP)Cl system oxidized (1) antergan[71] to N-demethylated products; (2) benzo(α)pyrene or 2-aminofluorene to mutagens in the Ames assay;[71] and (3) phencyclidine to a piperidine-3-oxo compound,[71] and performed the aromatization of tetralone derivatives.[71] Robust iron porphyrins associated with m-CPBA have been used to oxidize polycyclic aromatic hydrocarbons yielding mixtures of phenols and quinones[71,73] or steroid aldehydes to the corresponding acid derivatives.[71,74]

In an attempt to overcome the limitations of catalytic reactions owing to the cost of metalloporphyrins, Sorokin and coworkers developed water-soluble iron-sulfonated pthalocyanins (PcS) as an alternative chemical model of peroxidase enzymes. They are structurally very close to porphyrins but slightly different (extra nitrogens in the macrocycle) and are readily accessible from the synthesis point of view (Figure 1.8). In contrast to the chemistry of metalloporphyrins, which involved extensive mechanistic studies, including isolation and characterization of proposed intermediates by spectroscopic methods, the PcS have been poorly exercised, although they have intensively been studied as catalysts, mostly in the oxidation field. Recently, much effort has been focused on mechanistic studies and characterization of active species involved in catalysis. In particular, it was shown that iron tetrasulfophthalocyanine (FePcS) can perform oxidative degradation of recalcitrant chlorinated phenols by activating H_2O_2 in aqueous solutions under mild conditions with partial mineralization.[75-78] This system has been used by several researchers for the degradation of different pollutants, such as the photodegradation of Rhodamine B (RhB), salicylic acid, and Orange II.[79] FePcS can be prepared in high yield (65–70 per cent) in a one-step reaction by improving the Weber-Busch method.[80,81] The iron and manganese phthalocyanine catalysts were found to be less active in oxidation reactions than metalloporphyrins.[82] This is consistent with the formation of a catalytically inactive μ-Oxo Fe^{III} dimer structure with an intense visible band at 632 nm.[77,80]

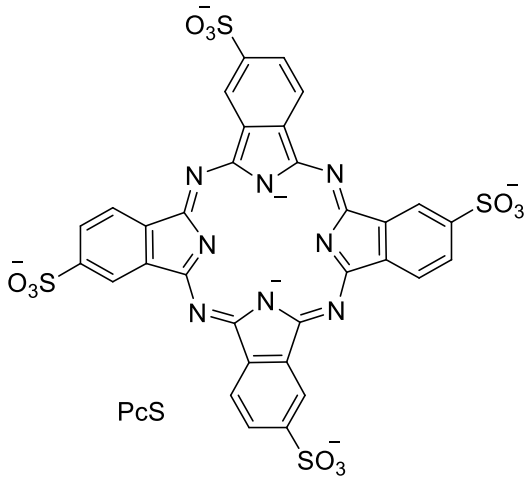

Figure 1.8: Molecular structure of sulfonated pthalocyanine macrocyclic ligand

1.5.2 *Non-heme functional analogs*

Transition metal complexes with multidentate neutral or anionic nitrogen-donating ligands that are structurally different from those of porphyrins have been synthesized to mimic the non-heme class of metallo enzymes.[4,13,83-86] Unlike heme analogs that stabilize a $Fe^{IV}(O)$ porphyrin radical cation, non-heme ligand systems are believed to stabilize a $Fe^{V}(O)$ intermediate (metal-centered oxidation-equivalent). A group of ligand systems, depicted in Figure 1.9, was used to synthesize the corresponding iron and manganese complexes as native enzyme mimics. The neutral donating ligands generally form Fe^{II} precursor complexes, and anionic ligands form Fe^{III} precursor complexes. On oxidation in the presence of peroxides, these form $Fe^{IV}(O)$[87-92] and $Fe^{V}(O)$[93,94] intermediates respectively. In turn, these oxidize a wide variety of organic substrates, e.g. olefin epoxidation, sulfoxidation, and alkane hydroxylation in organic media. The non-heme TPA ligand system has also been shown to mimic the structure of the dinuclear non-heme enzyme MMO and study the C-H bond activation of dihydroanthracene and triphenyl posphene oxidation.[95-97] Very few of these have been explored for aqueous applications like waste water treatment or degradation of toxic chemicals. For example, iron complexes of TPA, TACN, N_4Py, salen etc. have been evaluated for H_2O_2-mediated bleaching processes and delignifications.[98] However, owing to the metal-ligand weak interactions, all these complexes were prone to hydrolysis when taken in water and/or subjected to slight pH change. For example, it is well-known that most iron complexes of

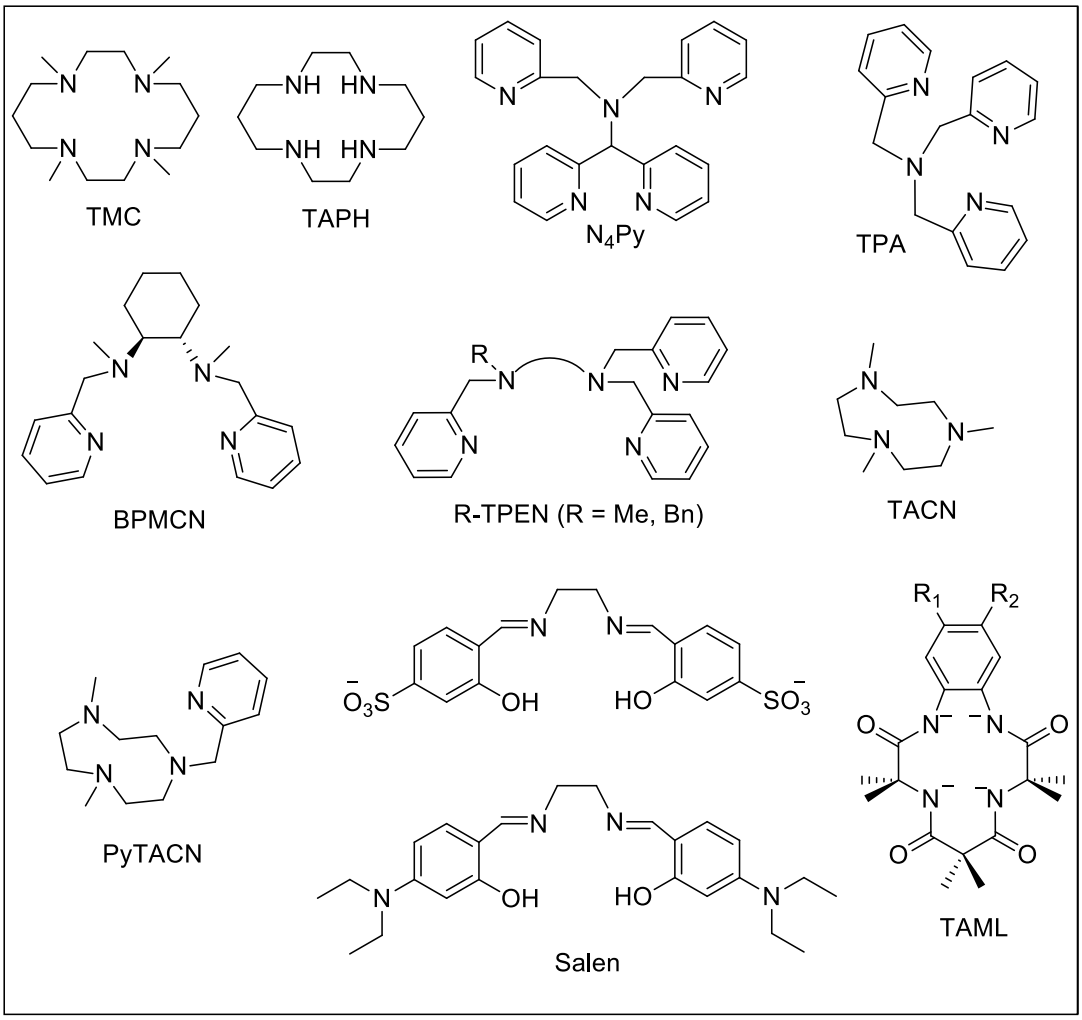

Figure 1.9: Various ligands systems have been designed whose metal complexes (mostly iron) are shown to functionally mimic peroxide-activating enzymes.[4]

neutral nitrogen-donating ligands form iron oxide/hydroxide nanoparticles in basic pH (>8).[99,100] Hence, none of these has been explored for application in the field of analytical diagnostics as a signal transducer like HRP. In attempts to use some non-heme iron complexes for water oxidation, these complexes have been shown to produce CO_2 as a by-product because of ligand oxidations.[100] Until recently, Fe^{III} complexes of tetra-amido macrocyclic ligands (Fe-TAML) have been shown to have the best peroxidase activity, especially in water, and have been used successfully in the decolorization of azo dyes[101,102], degradation of polychlorophenols,[103] and organic pesticides.[104] Some (not all) of these Fe-complexes have also been used for chemical water oxidation in the presence

of a sacrificial oxidant (Ce^{IV}) simply because most other precursor complexes undergo medium-induced decomposition in water.[100,105,106]

1.6 Fe-TAMLs

The Fe^{III} complexes of tetra-amido macrocyclic ligands (Fe-TAMLs) developed by T. J. Collins that belong to the class of tetra-anionic nitrogen-donating ligands (Figure 1.10) are stable over a broad range of pH and ionic strengths. These have been extensively used for wastewater treatment processes like degradation of environmental pollutants such as polychlorophenols and textile effluent dyes.[62,101-104,107-116] They are known to activate H_2O_2 at low catalyst concentrations and high turnover numbers (~10000) and have been the most successful peroxidase mimic until recently. They also constitute the first example of chemical water oxidation catalyst using molecular iron complexes.[105] In contrast to synthetic porphyrines (dianionic and dineutral 'N' donating ligands) and other non-heme ligands (neutral 'N' donating ligands), TAMLs having tetra

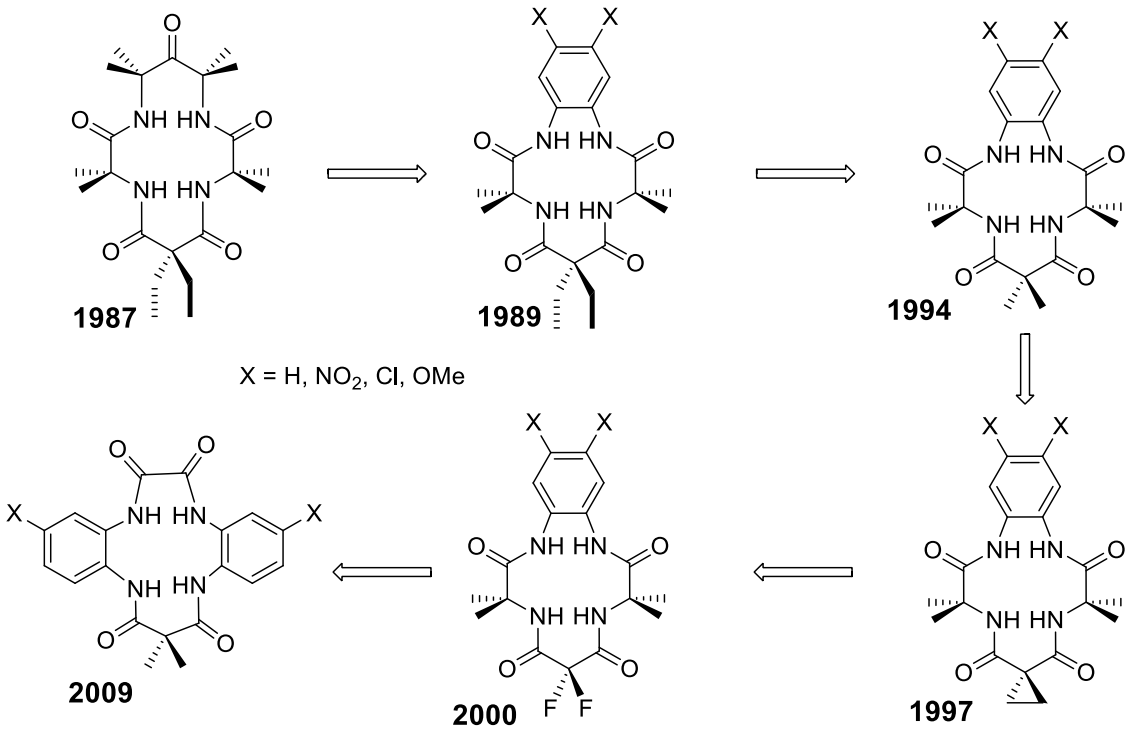

Figure 1.10: Ligand evolution toward achieving Fe-complexes of more efficient peroxidase mimic.[116]

anionic 'N' donors strongly interact with the metal active center and provide a longer lifetime to Fe-TAMLs in ambient operating conditions (aqueous).

However, Fe-TAMLs are subject to very fast demetallation in acidic media (pH<5), following a proton attack to one of the four amido nitrogens linked to the iron,[65,117] and oxidative decay, following an intra-molecular hydrogen abstraction from own ligand moiety (tail -CMe_2).[63,65,117,118] In an attempt to overcome the problem of media-induced demetallation, the tail –CMe_2 group of Fe-TAML was replaced by the corresponding electron withdrawing –CF_2 fragment, and has been shown to have very positive effects on acid stability.[64,65] This phenomenon is expected because lower the electron density on amido nitrogens, lower the chance of a proton attack leading to demetallation. An order of 11-fold improved stabilization to acid was achieved in this move toward fluorinated Fe-TAML. This exceptional acid stabilization allowed them to successfully carry out chemical water oxidation using Ce^{IV} as sacrificial oxidant at pH 1, which constitutes the first ever example of water oxidation by a molecular iron complex.[105] However, the fluorine effect was adverse in the oxidative suicide inactivation perspective, because of higher electronegativity of the 'F' that polarizes the iron to have higher reactivity not only toward substrate but also to the oxidation of its own ligand framework.[63,65] Also, the fluorinated –CF_2 unit in the catalyst framework renders its usage unsuitable for water treatment. All the discussion above for the Fe-TAMLs as peroxidase mimics comes under the first generation design.

However, it was always a challenge to have the most reactive Fe-TAML without a –CF_2 group at the tail but with elements compatible with the biosphere. In this endeavour, a second generation Fe-TAML (**Fe-D***)[108] was designed in 2009 where the fluorine effect was mimicked by installing two sp^2 hybridized carbon atoms adjacent to the amide nitrogens, keeping in mind that the increased '*s*' character would induce more electronegativity (Figure 1.11). The greatest reactivity for Fe-NO_2D with a nitro group at the aromatic rings was achieved at pH 9, whereas the maximum reactivity for **Fe-B*** and **Fe-BF_2** occurs at pH 11 and 10, respectively. The values of k_I and k_{II} define **Fe-NO_2D** as an exceptional peroxidase mimic, where these values are almost near to that of peroxide-activating enzymes. At pH 7, **Fe-NO_2D** is the most reactive Fe-TAML activator to date, bleaching Orange II, 5 times faster than **Fe-B*** and two times faster than **Fe-BF_2.**

However, only moderate aqueous stability with respective half-lives of 52 and 3500 s in 0.1 M phosphate at pH 5 and 25 °C was observed for **Fe-D*** and **Fe-NO_2D** respectively. This was most probably because the six-membered malonoyl ring was very nonplanar, that is susceptible to facile proton attack, leading to the dissociation of the Fe-N bonds.

The prototypical Fe-TAML (**Fe-B***) with $–CMe_2$ at the tail and no substituent at the head aromatic ring was successfully commercialized for wastewater treatment in the USA. However, further alteration of electronic and steric properties of the Fe-TAML to overcome their limitation associated with their hydrolytic stability and reactivity would make them much more attractive for industrial applications.

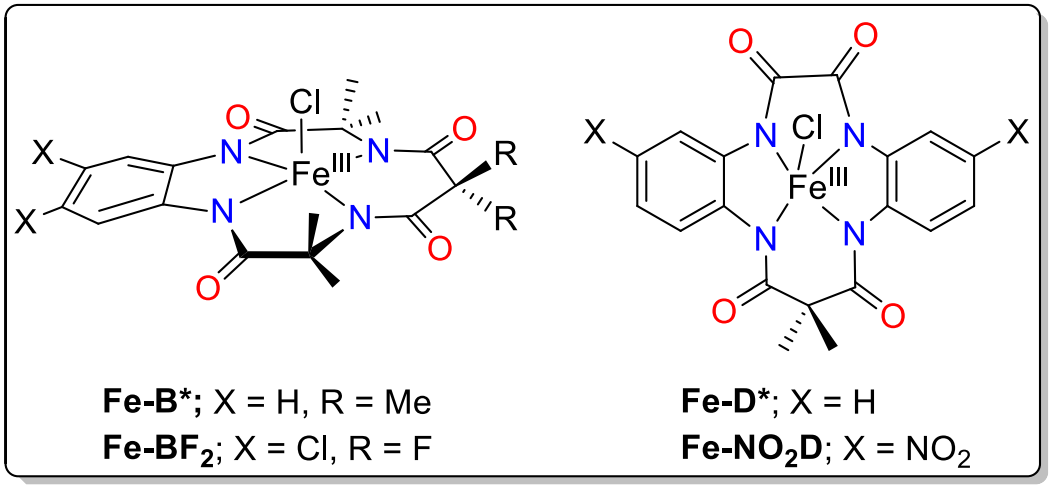

Figure 1.11: Molecular structures of 1st and 2nd generation Fe-TAMLs.

Table 1.1: Reactivity comparison of 1st and 2nd generation Fe-TAMLs toward Bleaching of orange II by [H_2O_2] at 25 °C in 0.01 M Phosphate at pH 11

Catalyst	k_I ($M^{-1}s^{-1}$)	k_{II} ($M^{-1}s^{-1}$)
Fe-B*	3.5×10^3	1.5×10^4
Fe-BF_2	$(8.4 \pm 0.6) \times 10^3$	$(1.1 \pm 0.1) \times 10^5$
Fe-NO_2D	$(10 \pm 1) \times 10^3$	$(1.2 \pm 0.1) \times 10^5$
HRP	10^7	-

1.7 Motivation and objective of the present work

Based on the above literature survey on bio-inspired oxidation, with special reference to peroxidase enzymes and the design principles of making more powerful oxidation catalysts, it is obvious that designing metal complexes that activate H_2O_2 or O_2 but are themselves inert to oxidation is the key to the synthesis of efficient transition metal oxidation catalysts.[119] As peroxidase enzyme mimics in particular, Fe-TAMLs are of great importance owing to their stability and reactivity in water in comparison to other non-heme analogs. However, the electronics and steric around the iron active center in Fe-TAMLs can be further tuned to achieve control over hydrolytic and oxidative decay, especially at lower pH. Although Fe-TAMLs are very stable at neutral to basic pH, they are weakly resistant to acids and acid salts. It has been well established by T. J. Collins that the tail malonoyl six-membered ring, being very non-planar, is susceptible to acid attack and, hence, has a striking effect on acid-induced demetallation. We envisioned that if the malonyl fragment can be replaced by a substituted biuret (NH-C(O)-N(Me)-C(O)-NH) fragment, we could probe the effect of the -NMe group on the aqueous stability and reactivity of the resulting Fe(III) complex.

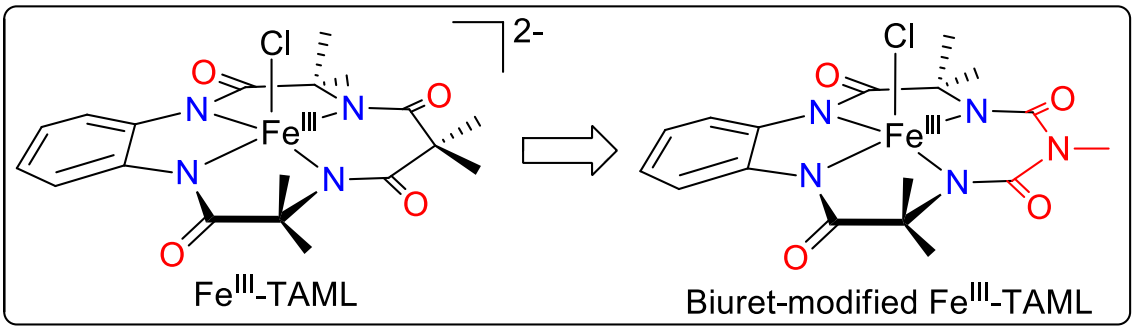

Figure 1.12: Molecular structures of proto typical Fe-TAML and biuret-modified Fe-TAML.

This would be interesting, since the lone pair on the –NMe group of the planar biuret moiety can be effectively delocalized along the six-membered ring containing the Fe(III) ion, thus altering the electron density on the Fe(III) atom (Figure 1.12). The aqueous stability and catalytic activity of the resulting complex can therefore be significantly altered. The planarity in the biuret six-membered ring would bring about the

most striking effect in the context of intra-molecular self-oxidative decay. Figure 1.13 depicts the typical presentation of a facile hydrogen abstraction by the high-valent $Fe^{V}(O)$ intramolecularly, because of the lack of planarity in the malonoyl six-membered ring of the prototypical Fe-TAMLs, in contrast to the biuret-modified Fe-TAMLs. This hypothesis suggests that because of the planar biuret six-membered ring, the N-Me hydrogens would be far apart from the $Fe^{V}(O)$ species to undergo self-oxidation (Figure 1.13).

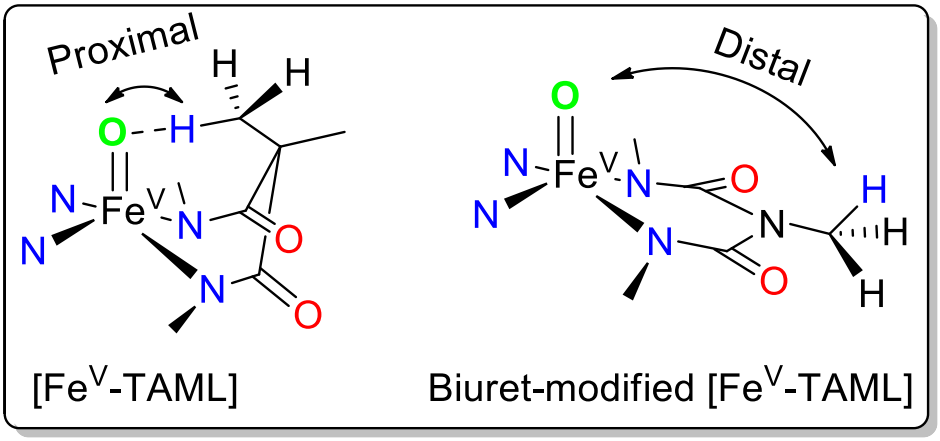

Figure 1.13: Presentation of potential intra-molecular hydrogen abstraction by the high-valent $Fe^{V}(O)$ intermediate species leading to demetallation (oxidative decay) in case of Fe-TAMLs and biuret-modified Fe-TAML.

Therefore, it could be possible to synthesize a new-generation Fe-TAML as a more efficient oxidation catalyst and with improved stability and activity. Also, the steric can be tuned further at the tail by differently substituted biuret moieties and at the head aromatic ring as well. With these motivations, the present thesis describes the development of biuret-modified Fe-TAMLs as a peroxidase enzyme mimic with improved stability and reactivity compared to the Fe-TAML counterparts. They not only mimic the peroxidase enzymes but also outperform the same, thereby overcoming the limitations of the enzymes, especially in various analyte detection protocols. Also, the oxidation ability of these catalysts toward homogeneous photochemical and chemical water oxidation was accomplished with potential reactive intermediate identifications. By

keeping the above objectives in mind, the following specific work was selected for the present thesis:

1. Synthesis and characterization of Fe(III) complexes of biuret-modified TAMLs.
2. Detailed kinetic evaluation of their activity-stability parameterizations in ambient operating conditions that render them the most successful peroxidase mimic till date.
3. Photochemical generation of a high-valent $Fe^{V}(O)$ intermediate species in the presence of a photosensitizer and sacrificial oxidant and its role in water oxidation.
4. Development of colorimetric tools for various analytes (cyanide and protein biomarkers) detection by applying the peroxidase like activity toward oxidation of a colorless substrate 3,3',5,5' tetramethyl benzedine (TMB) to a green-colored species in the presence of H_2O_2.

1.8 Outline of the thesis

This thesis is divided into five chapters. The references for each chapter are listed at the end of each chapter. The working chapters include the development of Fe(III) complexes of biuret-modified tetra-amido macrocyclic ligands (biuret-modified Fe-TAML) as oxidation catalyst and its application in various analyte detection and photochemical water oxidation.

Chapter I: This chapter presents a comprehensive survey of the relevant literature. It shows the importance of oxidation in sustaining life, where natural enzymes play the crucial role of performing myriad oxidation reactions by activating small molecules like O_2 and H_2O_2. This chapter also covers certain design principles of metal-ligand complexes necessary to move toward a new-generation catalysts that are more powerful than their predecessors. The later part of the chapter describes how, inspired by nature, various structural and functional synthetic small molecular models have been designed. Toward the end of this chapter, I have tried to adapt these necessary design principles to move ahead with our new designs, which not only mimic the peroxidase enzymes but also outperform them, thereby overcoming their limitations.

Chapter II: This chapter discusses the synthesis of the Fe(III) complexes of biuret-modified tetra-amido macrocyclic ligands (biuret-modified Fe-TAML) as peroxidase enzyme mimic and their detailed characterization by conventional spectroscopic techniques (UV-vis, FTIR, EPR, NMR, HR-MS), cyclic voltammetry, and X-ray crystal structures. The latter part of this chapter also provides a detailed kinetic study of H_2O_2 activation by these complexes to completely decolorize organic dyes and a comparison of stability and reactivity with respect to the proto typical Fe-TAML (**Fe-B***).

Chapter III: It describes the first-ever example of photochemical water oxidation by the molecular iron complex biuret-modified Fe-TAML. Based on spectroscopic techniques (UV-vis, EPR, and HRMS), we could identify a high-valent $Fe^{V}(O)$ species for the first time during photochemical water oxidation in a mixed-solvent system of CH_3CN and H_2O mixtures. In our attempt to identify the exact role of the in-situ generated $Fe^{V}(O)$ species, we proved that $Fe^{V}(O)$ alone cannot oxidize water, but that it needs to be oxidized further to be a water oxidation catalyst. The $Fe^{V}(O)$ species is a two-electron oxidized species of the precursor biuret-modified Fe-TAML complex and, hence, cannot oxidize water, which is a four-electron oxidation process, unless two $Fe^{V}(O)$ come close and radically couple each other to release a molecule of O_2. A plausible mechanism is discussed—based on the literature, reported theoretical calculations, and our experimental findings—where a second water molecule neucleophilically attacks the $Fe^{V}(O)$ intermediate to form the corresponding hydroperoxo species (Fe^{III}-OOH), which is further oxidized to release a molecule of dioxygen.

Chapter IV: It describes the synthesis of a clickable alkyne-tailed biuret-modified Fe-TAML, used to develop different analyte detection protocols for protein bio-marker and cyanide sensing, by applying the peroxidase-like activity of our complex to generate a visual signal in the presence of H_2O_2 and a colorless substrate. In the first part, a colorimetric methodology has been developed for protein bio-marker sensing that urges the potential replacement of the HRP enzyme in typical western blot techniques by our biuret-modified Fe-TAML developed in-house.

The second part of this chapter discusses a cyanide-sensing methodology where the peroxidase activity of biuret-modified Fe-TAML was coupled with catalase-mediated H_2O_2 disproportionation to modulate the H_2O_2 availability depending on cyanide input, followed by color generation.

Chapter V: This chapter presents an overall summary of the work done and describes the major findings of the studies. Future directions based on the work reported in the thesis are also discussed.

1.9 References

(1) Weissermel, K.; Arpe, H.-J. *Industrial Organic Chemistry*, 3rd ed.; Wiley-VCH: Weinheim, 1997; Derouane, E. G.; Haber, J.; Lemon, F.; Ribeiro, F.; Guisnet, M. *Catalytic Activation and Functionalization of Light Alkanes – Advances and Challenges*; Kluwer Academic Publishers: 1998; Olah, G. A.; Molnar, A. *Hydrocarbon Chemistry*, 2nd ed.; John Wiley and Sons Publishing: 2003; Wittcoff, H. A.; Reuben, B. G.; Plotkin, J. S. *Industrial Organic Chemicals*, 2nd ed.; John Wiley and Sons Publishing: 2004.; Arndtsen, B. A.; Bergman, R. G.; Mobley, T. A.; Peterson, T. H. *Accounts of Chemical Research* **1995**, *28*, 154.

(2) Hashiguchi, B. G.; Bischof, S. M.; Konnick, M. M.; Periana, R. A. *Accounts of Chemical Research* **2012**, *45*, 885.

(3) Labinger, J. A.; Bercaw, J. E. *Nature* **2002**, *417*, 507.

(4) Que, L.; Tolman, W. B. *Nature* **2008**, *455*, 333.

(5) Costas, M.; Mehn, M. P.; Jensen, M. P.; Que, L. *Chemical Reviews* **2004**, *104*, 939.

(6) Hausinger, R. P. *Critical Reviews in Biochemistry and Molecular Biology* **2004**, *39*, 21.

(7) Kovaleva, E. G.; Lipscomb, J. D. *Nature Chemical Biology* **2008**, *4*, 186.

(8) Loenarz, C.; Schofield, C. J. *Nature Chemical Biology* **2008**, *4*, 152.

(9) Arakawa, H.; Aresta, M.; Armor, J. N.; Barteau, M. A.; Beckman, E. J.; Bell, A. T.; Bercaw, J. E.; Creutz, C.; Dinjus, E.; Dixon, D. A.; Domen, K.; DuBois, D. L.; Eckert, J.; Fujita, E.; Gibson, D. H.; Goddard, W. A.; Goodman, D. W.; Keller, J.; Kubas,

G. J.; Kung, H. H.; Lyons, J. E.; Manzer, L. E.; Marks, T. J.; Morokuma, K.; Nicholas, K. M.; Periana, R.; Que, L.; Rostrup-Nielson, J.; Sachtler, W. M. H.; Schmidt, L. D.; Sen, A.; Somorjai, G. A.; Stair, P. C.; Stults, B. R.; Tumas, W. *Chemical Reviews* **2001**, *101*, 953.

(10) Shilov, A. E.; Shul'pin, G. B. *Chemical Reviews* **1997**, *97*, 2879.

(11) Bollinger Jr, J. M.; Krebs, C. *Current Opinion in Chemical Biology* **2007**, *11*, 151.

(12) Bruijnincx, P. C. A.; van Koten, G.; Klein Gebbink, R. J. M. *Chemical Society Reviews* **2008**, *37*, 2716.

(13) Hohenberger, J.; Ray, K.; Meyer, K. *Nature Communications* **2012**, *3*, 720.

(14) Krebs, C.; Price, J. C.; Baldwin, J.; Saleh, L.; Green, M. T.; Bollinger, J. M. *Inorganic Chemistry* **2005**, *44*, 742.

(15) Nam, W. *Accounts of Chemical Research* **2007**, *40*, 465.

(16) Poulos, T. L. *Chemical Reviews* **2014**, *114*, 3919.

(17) Rolff, M.; Tuczek, F. *Angewandte Chemie International Edition* **2008**, *47*, 2344.

(18) Shaik, S.; Cohen, S.; Wang, Y.; Chen, H.; Kumar, D.; Thiel, W. *Chemical Reviews* **2009**, *110*, 949.

(19) Solomon, E. I.; Heppner, D. E.; Johnston, E. M.; Ginsbach, J. W.; Cirera, J.; Qayyum, M.; Kieber-Emmons, M. T.; Kjaergaard, C. H.; Hadt, R. G.; Tian, L. *Chemical Reviews* **2014**, *114*, 3659.

(20) Solomon, E. I.; Wong, S. D.; Liu, L. V.; Decker, A.; Chow, M. S. *Current Opinion in Chemical Biology* **2009**, *13*, 99.

(21) Tinberg, C. E.; Lippard, S. J. *Accounts of Chemical Research* **2011**, *44*, 280.

(22) Husain, Q. *Reviews in Environmental Science and Bio/Technology* **2010**, *9*, 117.

(23) Kim, G.-Y.; Lee, K.-B.; Cho, S.-H.; Shim, J.; Moon, S.-H. *Journal of Hazardous Materials* **2005**, *126*, 183.

(24) Mohan, S. V.; Prasad, K. K.; Rao, N. C.; Sarma, P. N. *Chemosphere* **2005**, *58*, 1097.

(25) Onder, S.; Celebi, M.; Altikatoglu, M.; Hatipoglu, A.; Kuzu, H. *Applied Biochemistry and Biotechnology* **2011**, *163*, 433.

(26) Pirillo, S.; García Einschlag, F. S. n.; Rueda, E. H.; Ferreira, M. a. L. n. *Industrial & Engineering Chemistry Research* **2010**, *49*, 6745.

(27) Ulson de Souza, S. M. A. G.; Forgiarini, E.; Ulson de Souza, A. A. *Journal of Hazardous Materials* **2007**, *147*, 1073.

(28) McEvoy, J. P.; Brudvig, G. W. *Chemical Reviews* **2006**, *106*, 4455.

(29) Yano, J.; Kern, J.; Sauer, K.; Latimer, M. J.; Pushkar, Y.; Biesiadka, J.; Loll, B.; Saenger, W.; Messinger, J.; Zouni, A.; Yachandra, V. K. *Science* **2006**, *314*, 821.

(30) Abu-Omar, M. M.; Loaiza, A.; Hontzeas, N. *Chemical Reviews* **2005**, *105*, 2227.

(31) Koehntop, K.; Emerson, J.; Que, L., Jr. *Journal of Biological Inorganic Chemistry* **2005**, *10*, 87.

(32) Hegg, E. L.; Jr, L. Q. *European Journal of Biochemistry* **1997**, *250*, 625.

(33) Que, L. *Nature Structural and Molecular Biology* **2000**, *7*, 182.

(34) Karlsson, A.; Parales, J. V.; Parales, R. E.; Gibson, D. T.; Eklund, H.; Ramaswamy, S. *Science* **2003**, *299*, 1039.

(35) Krebs, C.; Galonić Fujimori, D.; Walsh, C. T.; Bollinger, J. M. *Accounts of Chemical Research* **2007**, *40*, 484.

(36) Merkx, M.; Kopp, D. A.; Sazinsky, M. H.; Blazyk, J. L.; Müller, J.; Lippard, S. J. *Angewandte Chemie International Edition* **2001**, *40*, 2782.

(37) Beauvais, L. G.; Lippard, S. J. *Journal of the American Chemical Society* **2005**, *127*, 7370.

(38) Wallar, B. J.; Lipscomb, J. D. *Chemical Reviews* **1996**, *96*, 2625.

(39) Shu, L.; Nesheim, J. C.; Kauffmann, K.; Münck, E.; Lipscomb, J. D.; Que, L. *Science* **1997**, *275*, 515.

(40) Dawson, J. *Science* **1988**, *240*, 433.

(41) Dunford, H. B.; Stillman, J. S. *Coordination Chemistry Reviews* **1976**, *19*, 187.

(42) Poulos, T. L.; Kraut, J. *Journal of Biological Chemistry* **1980**, *255*, 8199; Roth, J. P. and Cramer, C. J. *Journal of the American Chemical Society* 2008, 130 (25), pp 7802

(43) Nicholls, P.; Fita, I.; Loewen, P. C. In *Advances in Inorganic Chemistry*; Academic Press: 2000; Vol. Volume 51, p 51.

(44) Zámocký, M.; Koller, F. *Progress in Biophysics and Molecular Biology* **1999**, *72*, 19.

(45) Floris, R.; Moguilevsky, N.; Puppels, G.; Jacquet, A.; Renirie, R.; Bollen, A.; Wever, R. *Journal of the American Chemical Society* **1995**, *117*, 3907.

(46) Picot, D.; Loll, P. J.; Garavito, R. M. *Nature* **1994**, *367*, 243.

(47) Smith, A. T.; Veitch, N. C. *Current Opinion in Chemical Biology* **1998**, *2*, 269.

(48) Veitch, N. C.; Smith, A. T. In *Advances in Inorganic Chemistry*; Academic Press: 2000; Vol. Volume 51, p 107.

(49) Welinder, K. G. *Current Opinion in Structural Biology* **1992**, *2*, 388.

(50) Engvall, E.; Perlmann, P. *Immunochemistry* **1971**, *8*, 871.

(51) Engvall, E.; Perlmann, P. *The Journal of Immunology* **1972**, *109*, 129.

(52) Keren, D. F. *Infection and Immunity* **1979**, *24*, 441.

(53) Burnette, W. N. *Analytical Biochemistry* **1981**, *112*, 195.

(54) Renart, J.; Reiser, J.; Stark, G. R. *Proceedings of the National Academy of Sciences* **1979**, *76*, 3116.

(55) Towbin, H.; Staehelin, T.; Gordon, J. *Proceedings of the National Academy of Sciences* **1979**, *76*, 4350.

(56) Akyilmaz, E.; Sezgintürk, M. K.; Dinçkaya, E. *Talanta* **2003**, *61*, 73.

(57) Gong, Z.; Zhang, Z. *Analytical Letters* **1996**, *29*, 695.

(58) Gorton, L.; Jonsson-Pettersson, G.; Csoregi, E.; Johansson, K.; Dominguez, E.; Marko-Varga, G. *Analyst* **1992**, *117*, 1235.

(59) Kenausis, G.; Chen, Q.; Heller, A. *Analytical Chemistry* **1997**, *69*, 1054.

(60) Tkac, J.; Sturdik, E.; Gemeiner, P. *Analyst* **2000**, *125*, 1285.

(61) (a) Hirany, S.; Li, D.; Jialal, I. *The American Journal of Medicine* **1997**, *102*, 48; (b) Hammel, K. E. and Tardone, P. J.; *Biochemistry* **1988, *27,*** 6563.

(62) Ghosh, A.; Mitchell, D. A.; Chanda, A.; Ryabov, A. D.; Popescu, D. L.; Upham, E. C.; Collins, G. J.; Collins, T. J. *Journal of the American Chemical Society* **2008**, *130*, 15116.

(63) Chanda, A.; Ryabov, A. D.; Mondal, S.; Alexandrova, L.; Ghosh, A.; Hangun-Balkir, Y.; Horwitz, C. P.; Collins, T. J. *Chemistry – A European Journal* **2006**, *12*, 9336.

(64) Polshin, V.; Popescu, D.-L.; Fischer, A.; Chanda, A.; Horner, D. C.; Beach, E. S.; Henry, J.; Qian, Y.-L.; Horwitz, C. P.; Lente, G.; Fabian, I.; Münck, E.; Bominaar, E. L.; Ryabov, A. D.; Collins, T. J. *Journal of the American Chemical Society* **2008**, *130*, 4497.

(65) Ghosh, A.; Ryabov, A. D.; Mayer, S. M.; Horner, D. C.; Prasuhn, D. E.; Sen Gupta, S.; Vuocolo, L.; Culver, C.; Hendrich, M. P.; Rickard, C. E. F.; Norman, R. E.; Horwitz, C. P.; Collins, T. J. *Journal of the American Chemical Society* **2003**, *125*, 12378.

(66) Groves, J. T. *Journal of Inorganic Biochemistry* **2006**, *100*, 434.

(67) Groves, J. T.; Haushalter, R. C.; Nakamura, M.; Nemo, T. E.; Evans, B. J. *Journal of the American Chemical Society* **1981**, *103*, 2884.

(68) Fujii, H. *Coordination Chemistry Reviews* **2002**, *226*, 51.

(69) Kang, Y.; Chen, H.; Jeong, Y. J.; Lai, W.; Bae, E. H.; Shaik, S.; Nam, W. *Chemistry – A European Journal* **2009**, *15*, 10039.

(70) Labat, G.; Seris, J.-L.; Meunier, B. *Angewandte Chemie International Edition in English* **1990**, *29*, 1471.

(71) Meunier, B. *Chemical Reviews* **1992**, *92*, 1411.

(72) Alexander, M. *Science* **1981**, *211*, 132.

(73) Benson, D. R.; Valentekovich, R.; Diederich, F. *Angewandte Chemie International Edition in English* **1990**, *29*, 191.

(74) Watanabe, Y.; Takehira, K.; Shimizu, M.; Hayakawa, T.; Orita, H. *Journal of the Chemical Society, Chemical Communications* **1990**, 927.

(75) Sorokin, A.; De Suzzoni-Dezard, S.; Poullain, D.; Noël, J.-P.; Meunier, B. *Journal of the American Chemical Society* **1996**, *118*, 7410.

(76) Sorokin, A.; Fraisse, L.; Rabion, A.; Meunier, B. *Journal of Molecular Catalysis A: Chemical* **1997**, *117*, 103.

(77) Sorokin, A.; Meunier, B. *Chemistry – A European Journal* **1996**, *2*, 1308.

(78) Sorokin, A.; Meunier, B.; Séris, J.-L. *Science* **1995**, *268*, 1163.

(79) Tao, X.; Ma, W.; Zhang, T.; Zhao, J. *Chemistry – A European Journal* **2002**, *8*, 1321.

(80) Hadasch, A.; Sorokin, A.; Rabion, A.; Meunier, B. *New Journal of Chemistry* **1998**, *22*, 45.

(81) Weber, J. H.; Busch, D. H. *Inorganic Chemistry* **1965**, *4*, 469.

(82) Belal, R.; Meunier, B. *Journal of Molecular Catalysis* **1988**, *44*, 187.

(83) Chen, H.; Cho, K.-B.; Lai, W.; Nam, W.; Shaik, S. *Journal of Chemical Theory and Computation* **2012**, *8*, 915.

(84) Company, A.; Feng, Y.; Güell, M.; Ribas, X.; Luis, J. M.; Que, L.; Costas, M. *Chemistry – A European Journal* **2009**, *15*, 3359.

(85) Nam, W. *Accounts of Chemical Research* **2007**, *40*, 522.

(86) Que, L. *Accounts of Chemical Research* **2007**, *40*, 493.

(87) Hong, S.; Lee, Y.-M.; Shin, W.; Fukuzumi, S.; Nam, W. *Journal of the American Chemical Society* **2009**, *131*, 13910.

(88) Kaizer, J.; Klinker, E. J.; Oh, N. Y.; Rohde, J.-U.; Song, W. J.; Stubna, A.; Kim, J.; Münck, E.; Nam, W.; Que, L. *Journal of the American Chemical Society* **2003**, *126*, 472.

(89) Jackson, T. A.; Rohde, J.-U.; Seo, M. S.; Sastri, C. V.; DeHont, R.; Stubna, A.; Ohta, T.; Kitagawa, T.; Münck, E.; Nam, W.; Que, L. *Journal of the American Chemical Society* **2008**, *130*, 12394.

(90) Krzystek, J.; England, J.; Ray, K.; Ozarowski, A.; Smirnov, D.; Que, L.; Telser, J. *Inorganic Chemistry* **2008**, *47*, 3483.

(91) Lee, Y.-M.; Hong, S.; Morimoto, Y.; Shin, W.; Fukuzumi, S.; Nam, W. *Journal of the American Chemical Society* **2010**, *132*, 10668.

(92) Li, F.; England, J.; Que, L. *Journal of the American Chemical Society* **2010**, *132*, 2134.

(93) de Oliveira, F. T.; Chanda, A.; Banerjee, D.; Shan, X.; Mondal, S.; Que, L.; Bominaar, E. L.; Münck, E.; Collins, T. J. *Science* **2007**, *315*, 835.

(94) Kundu, S.; Thompson, J. V. K.; Ryabov, A. D.; Collins, T. J. *Journal of the American Chemical Society* **2011**, *133*, 18546.

(95) Do, L. H.; Xue, G.; Que, L.; Lippard, S. J. *Inorganic Chemistry* **2012**, *51*, 2393.

(96) Xue, G.; De Hont, R.; Münck, E.; Que, L. *Nat Chem* **2010**, *2*, 400.

(97) Xue, G.; Pokutsa, A.; Que, L. *Journal of the American Chemical Society* **2011**, *133*, 16657.

(98) Hage, R.; Lienke, A. *Angewandte Chemie International Edition* **2006**, *45*, 206.

(99) Chen, G.; Chen, L.; Ng, S.-M.; Man, W.-L.; Lau, T.-C. *Angewandte Chemie International Edition* **2013**, *52*, 1789.

(100) Hong, D.; Mandal, S.; Yamada, Y.; Lee, Y.-M.; Nam, W.; Llobet, A.; Fukuzumi, S. *Inorganic Chemistry* **2013**, *52*, 9522.

(101) Beach, E. S.; Malecky, R. T.; Gil, R. R.; Horwitz, C. P.; Collins, T. J. *Catalysis Science & Technology* **2011**, *1*, 437.

(102) Chahbane, N.; Popescu, D.-L.; Mitchell, D. A.; Chanda, A.; Lenoir, D.; Ryabov, A. D.; Schramm, K.-W.; Collins, T. J. *Green Chemistry* **2007**, *9*, 49.

(103) Gupta, S. S.; Stadler, M.; Noser, C. A.; Ghosh, A.; Steinhoff, B.; Lenoir, D.; Horwitz, C. P.; Schramm, K.-W.; Collins, T. J. *Science* **2002**, *296*, 326.

(104) Chanda, A.; Khetan, S. K.; Banerjee, D.; Ghosh, A.; Collins, T. J. *Journal of the American Chemical Society* **2006**, *128*, 12058.

(105) Ellis, W. C.; McDaniel, N. D.; Bernhard, S.; Collins, T. J. *Journal of the American Chemical Society* **2010**, *132*, 10990.

(106) Fillol, J. L.; Codolà, Z.; Garcia-Bosch, I.; Gómez, L.; Pla, J. J.; Costas, M. *Nature Chemistry* **2011**, *3*, 807.

(107) Beach, E. S.; Duran, J. L.; Horwitz, C. P.; Collins, T. J. *Industrial & Engineering Chemistry Research* **2009**, *48*, 7072.

(108) Ellis, W. C.; Tran, C. T.; Denardo, M. A.; Fischer, A.; Ryabov, A. D.; Collins, T. J. *Journal of the American Chemical Society* **2009**, *131*, 18052.

(109) Ellis, W. C.; Tran, C. T.; Roy, R.; Rusten, M.; Fischer, A.; Ryabov, A. D.; Blumberg, B.; Collins, T. J. *Journal of the American Chemical Society* **2010**, *132*, 9774.

(110) Kundu, S.; Chanda, A.; Espinosa-Marvan, L.; Khetan, S. K.; Collins, T. J. *Catalysis Science & Technology* **2012**, *2*, 1165.

(111) Banerjee, D.; Markley, A. L.; Yano, T.; Ghosh, A.; Berget, P. B.; Minkley, E. G.; Khetan, S. K.; Collins, T. J. *Angewandte Chemie International Edition* **2006**, *45*, 3974.

(112) Popescu, D.-L.; Chanda, A.; Stadler, M.; de Oliveira, F. T.; Ryabov, A. D.; Münck, E.; Bominaar, E. L.; Collins, T. J. *Coordination Chemistry Reviews* **2008**, *252*, 2050.

(113) Collins, T. J.; Gordon-Wylie, S. Long-Lived Homogeneous Oxidation Catalysts. U.S. Patent 5,847,120, December 8, **1998**.

(114) Popescu, D.-L.; Chanda, A.; Stadler, M. J.; Mondal, S.; Tehranchi, J.; Ryabov, A. D.; Collins, T. J. *Journal of the American Chemical Society* **2008**, *130*, 12260.

(115) Miller, C. G.; Gordon-Wylie, S. W.; Horwitz, C. P.; Strazisar, S. A.; Peraino, D. K.; Clark, G. R.; Weintraub, S. T.; Collins, T. J. *Journal of the American Chemical Society* **1998**, *120*, 11540.

(116) Collins, T. J. *Accounts of Chemical Research* **2002**, *35*, 782.

(117) Polshin, V.; Popescu, D.-L.; Fischer, A.; Chanda, A.; Horner, D. C.; Beach, E. S.; Henry, J.; Qian, Y.-L.; Horwitz, C. P.; Lente, G.; Fabian, I.; MÃ¼nck, E.; Bominaar, E. L.; Ryabov, A. D.; Collins, T. J. *Journal of the American Chemical Society* **2008**, *130*, 4497.

(118) Horwitz, C. P.; Fooksman, D. R.; Vuocolo, L. D.; Gordon-Wylie, S. W.; Cox, N. J.; Collins, T. J. *Journal of the American Chemical Society* **1998**, *120*, 4867.

(119) Collins, T. J. *Accounts of Chemical Research* **1994**, *27*, 279.

Chapter II

Synthesis and Characterization of Fe^{III} Complexes of Biuret-modified Tetra-amide Macrocyclic Ligands as Peroxidase Enzyme Mimic

This chapter is adapted partly from the following publications

(1) Panda, C.; Ghosh, M.; Panda, T.; Banerjee, R.; Gupta, S. S.; *Chemical Communications* **2011**, *47*, 8016.

(2) Panda, C.; Debgupta, J.; Díaz, D. D.; Singh, K. K.; Gupta, S. S. and Dhar, B. B.; *Journal of the American Chemical Society* **2014**, 136, 12273.

2.1 Introduction

The central challenge in development of small molecule Fe based catalysts that functionally mimic peroxidase enzymes lies in the design of an oxidatively robust ligand around the metal centre that can stabilize a high-valent metal intermediate which in turn oxidizes the substrate. Among several synthetic Fe based models that have been reported so far, Fe(III) complexes of tetra-amido macrocyclic ligand (Fe-TAMLs) developed by T. J. Collins *et al.*, have been shown to be exceptionally good functional mimic of peroxidases.[1-13] Fe-TAMLs activate H_2O_2 in water to form a reactive high valent iron oxo intermediate species which has been shown to catalyse a wide range of oxidation reactions.[2,6,14-16] This includes remediation of environmental pollutants such as waste water dyes,[2,4,6,7] chlorophenols[11] in paper and pulp purification processes[12] and energy applications such as water oxidation.[17,18] The reactive intermediates that were isolated and characterized to be mononuclear and dinuclear iron(IV) oxo in aqueous medium.[15,16] However, one major drawback of Fe-TAMLs is that they are subject to very fast demetallation in acidic media (pH <5) following a proton attack to one of the four amido-nitrogens bonded to the iron.[19,20] It has been studied that because of the considerable non planarity in the tail malonoyl fragment, amido-nitrogens are prone to proton attack leading to the dissociation of Fe-N bond in presence of Brønsted acids. This limits their usage in applications such as in analytical diagnostics as a replacement of the enzyme HRP.

In organic medium (CH_3CN), the proto typical Fe-TAML (**Fe-B***) with a malonoyl six member ring at the tail is the first candidate among all other reported synthetic non-heme models to form a well-defined high valent $Fe^{V}(O)$ intermediate species using *m*-CPBA as oxidant at -40 °C and extensively characterized by conventional spectroscopy (UV-vis, EPR, ESI-MS, EXAFS and Mössbauer etc.).[21,22] In contrast to other non-heme Fe complexes with neutral nitrogen donors, TAML (tetra anionic amido donors) inject more electron density to the iron active centre in oxidizing conditions and hence could stabilize such a high valent $Fe^{V}(O)$ species.[21] However the reactivity of the $Fe^{V}(O)$ has been least explored for the oxidation of a broad range of organic substrates. The likely reason for this is (i) The instability of $Fe^{V}(O)$ above -40 °C owing to intra molecular self-oxidation of its own ligand framework[12,23], and (ii) Organic transformations at such low

temperatures are kinetically slow. The designing new generation oxidation catalysts that can stabilize the high valent iron oxo intermediate in aqueous to organic medium such that it can carry out selective oxidation reactions is therefore challenging. This challenge can be met by appropriate design of ligands which can control both the hydrolytic and oxidative decay of Fe-TAMLs.

It has been shown that the stability and reactivity of Fe-TAMLs are best controlled by modulating the σ-donor ability of the deprotonated amide nitrogen atoms in the 6-membered ring. Replacement of the $–CMe_2$ of **Fe-B*** by the corresponding electron withdrawing $–CF_2$ in the malonyl fragment has been shown to have very positive effects on acid stability and reaction rates.[19,20,23] We envisioned to replace the malonyl fragment by a substituted biuret fragment, so that we could probe the effect of the -NMe group on the aqueous stability and reactivity of the resulting Fe(III) complex (Figure 2.1) The lone pair on the –NMe group of the planar biuret moiety can be effectively delocalized along the 6-membered ring containing the Fe(III) ion; thus altering the electron density on the Fe(III) atom. This can in turn stabilize the high valent oxidation state of Fe thus significantly altering the catalytic activity of the newly synthesized catalyst. Although, deprotonated amide and urea ligands have been used to design H_2O_2 activating complexes,[24,25] to the best of our knowledge, there are no reports of active oxidation catalysts synthesized using chelating biuret groups as ligands. Copper, nickel and cobalt complexes have been made of acyclic biuret ligands, but their applications have been limited to the study of their structural and spectroscopic properties.[26-28] This chapter represents the first synthesis of a Fe(III) complex based on a macrocyclic biuret amide ligand (biuret-modified Fe-TAM; **1a**) that showed 10^6 fold improved acid stabilization

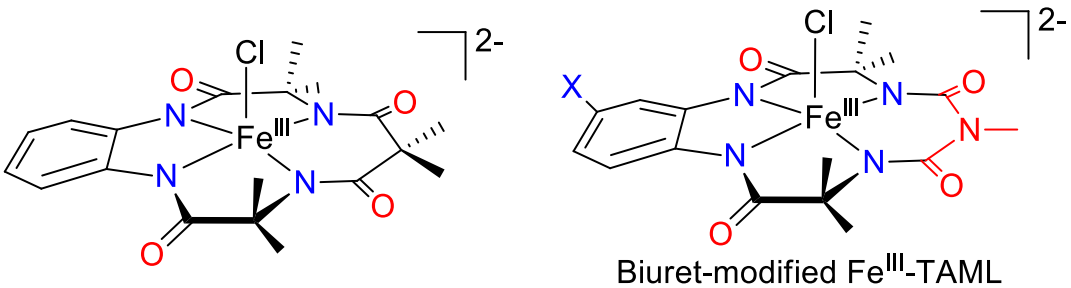

Figure 2.1: Molecular structures of Fe-TAMLs discussed in this chapter.

and 10 fold enhanced reaction rates for the activation of H_2O_2 as compared to the prototypical Fe-TAML complex **Fe-B***.[29] In addition, the acid stability of **1a** was further improved by introducing an electron withdrawing nitro group at the head aromatic ring (**1b**). This newly designed biuret-modified Fe-TAML is unique in several ways and hence the study of all the kinetic parameters for peroxide activation, substrate oxidation and inter/intra-molecular degradation is presented in this chapter.

2.2 Experimental section

2.2.1 *Physical measurements*

All the synthetic products were characterized by ^{1}H and ^{13}C NMR spectra recorded on a Bruker (200 MHz) spectrometer & these data are reported in δ (ppm) vs. $(CH_3)_4Si$ with the deuterated solvent proton residuals as internal standards. Infrared spectra were obtained by Perkin Elmer FT-IR spectrum GX instrument by making KBr pellets. Pellets were prepared by mixing 3 mg of sample with 97 mg of KBr. All the UV-vis spectra were monitored using a Perkin-Elmer – λ35 spectrophotometer housing 1.0 cm quartz cell at constant temperature of (25 ± 5) °C unless otherwise mentioned. High resolution mass spectrometry (HR-MS) was done either in the negative (for iron complexes **1a** and **1b**) or positive ion mode (neutral organic compounds) of a Thermo Scientific Q-Exactive, using electron spray ionization source, Orbitrap as analyzer and connected with a C18 column (150m × 4.6mm × 8µm). The X-band electron paramagnetic resonance (EPR) spectrum was recorded in a Bruker EMX X-band spectrometer operating at a field modulation of 100 kHz, modulation amplitude of 5 G and microwave radiation power of 10 mW at 77 K. Cyclic voltammetry (CV) was carried out using BioLogic (Model: SP300) potentiostat in a conventional three-electrode electrochemical cell with glassy carbon as the working electrode (WE), platinum wire as quasi-reference electrode (RE) and a platinum foil as a counter electrode (CE). The measurements were carried out using a solution of 1 mM of **1a** or **1b** in dry acetonitrile with 0.1 M $[n\text{-}Bu_4N]PF_6$ as the supporting electrolyte at room temperature. All peaks were independently calibrated with respect to an internal Ferrocene/Ferrocenium (Fc/Fc^+) redox couple under identical conditions.

2.2.2 *Materials*

The biuret-modified Fe-TAMLs were synthesized as described below (Scheme 2.1). N, N-dichloroformylmethylamine was procured from ChemCollect GmbH, Germany. Diethyl ether, petroleum ether (60-80 ^{o}C), ethylacetate, dichloromethane, tetrahydrofuran, acetonitrile, ethanol, methanol, benzene, hexane etc. were obtained from Merck and dried by conventional methods. KPF_6, tetrabutylammonoum hexafluorophosphate, Na_2HPO_4, $HClO_4$ and hydrogen peroxide (30% w/w) were purchased from Merk, India while orange II dye and safranin O were bought from Aldrich. Orange II was further purified by passing through a C18-silica gel column with water as eluent and safranin O was recrystallized from ethanol before experimental use. Other reagents for synthesis of the ligands used in experiments were supplied by Aldrich. Deionized water was used to make all the stock solutions for the kinetic and spectrophotometric runs.

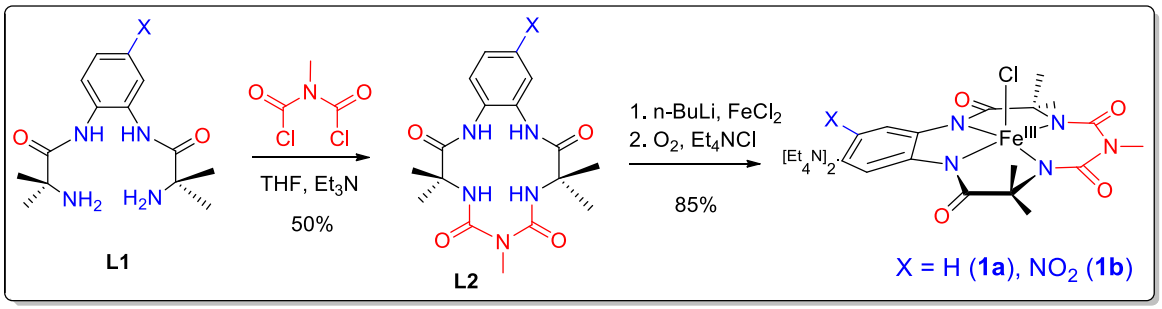

Scheme 2.1: Synthetic scheme of biuret-modified TAML (**L2**) and its Fe^{III} complexes (**1a** and **1b**)

2.2.3 *Synthesis* of L1 (X = H and NO_2)

The compounds, **L1** were prepared following earlier reported procedures.[30]

2.2.4 *Synthesis of L2* (X = H and NO_2)

2.2.4.1 *Synthesis of 3, 3, 6, 9, 9-pentamethyl-3, 4, 8, 9–tetrahydro-1H-benzo[i][1, 3, 5, 8, 11] pentaaza cyclotridecine-2, 5, 7,10 (6H, 11H)-tetraone* **(L2;** X = H**)**

Compound **L1** (X = H; 500 mg, 1.79 mmol) and dry Et_3N (0.5ml, 3.6 mmol, 2 eq) were dissolved in dry THF (50 mL) and the resultant solution was transferred into an addition funnel fitted to a 3-necked round bottom flask. N, N-dichloroformylmethylamine (0.23 ml, 1.79 mmol, 1eq) was diluted with 50 mL of dry THF and transferred into another addition funnel fitted to the same 3-necked round bottom flask. Both these solutions were added drop wise over a period of 1 hour into the round bottom flask containing 200 mL of dry THF at 0 °C under Argon. After the addition, the reaction mixture was allowed to warm to room temperature and then stirred for an additional period of 12 hours. After completion of the reaction, the reaction mixture was filtered, and purified by flash column chromatography (eluent: 100% EtOAc) to yield **L2** (326 mg, 50%). Elemental analysis: Found: C, 56.44; H, 6.31; N, 19.140. Calc. for $C_{17}H_{23}N_5O_4$: C, 56.5; H, 6.37; N, 19.39%. IR (KBr, ν_{max}/cm^{-1}): 3348(s, NH), 3245 (s, NH), 1711 (s, CO), 1652 (s, CO). ^1H NMR δ_H (200 MHZ; CD_3OD): 9.11 (s, 2 H, NH), 7.99 (s, 2 H, NH), 7.62 (dd, 2 H, J_1 = 3.5 Hz, J_2 = 6.1 Hz, Ph), 7.21 (dd, 2 H, J_1 = 3.6 Hz, J_2 = 6.0 Hz, Ph), 3.00 (s, 3 H, CH_3), 1.54 (s, 12 H, CH_3). ^{13}C NMR; δ_C (d_6 DMSO 200 MHz,): 173.6, 156.6, 130.86, 125.6, 59.0, 31.8, 25.5. ESI-MS (negative ion mode): *m/z* 360.3 ($M\text{-}H^+$, 100%).

2.2.4.2 *Synthesis of $(Et_4N)_2$[biuret-modified Fe-TAML]* (**1a ;** X = H)[29]

A solution containing compound **L2** (X = H ; 50 mg, 0.138 mmol) in 10 ml of dry THF was deoxygenated by four consecutive freeze-pump-thaw processes. Then to this solution was added n-BuLi (0.4 ml of 1.4 M solution in hexane, 0.567 mmol, 4.1 eq) at 0 °C under Argon atmosphere followed by addition of solid anhydrous $FeCl_2$ (21 mg, 0.166 mmol, 1.2 eq) under positive argon flow. The reaction was allowed to proceed under Argon at room temperature for 12 hours after which it was opened to air and stirred for one more hour to yield a dark orange-brown precipitate. The precipitate was filtered through a frit funnel and was dissolved in methanol to afford an orange solution. The solution (5 ml) containing the complex was then loaded onto a cationic ion-exchange resin (Amberlite-120; strong acid) column that had been pre-saturated with tetraethyl ammonium ion so as to exchange the lithium counter cation. The orange band was eluted with methanol and the solvent was removed under reduced pressure to yield a red-orange

solid. Further purification was achieved by column chromatography using basic alumina with CH_2Cl_2: MeOH = 99:1 as the eluent. X-ray diffracting quality crystals were obtained by slow vapor diffusion of diethyl ether into the solution of the complex in acetonitrile. Yield: 63 mg (83%). Elemental analysis: Found: C, 55.71; H, 8.14; N, 13.688%. Calc. for $C_{33}H_{59}N_7ClFeO_4$: C, 55.85; H, 8.32; N, 13.820. UV-vis: $\lambda_{max}(H_2O)$/nm; 356 (ε/dm^3 mol^{-1} cm^{-1}, 5160), IR (KBr, ν_{max}/cm^{-1}): 1601(s, CO), 1556(s, CO), 1531(s, CO). ESI-MS (negative ion mode): *m/z 413.1*(M-H$^+$, 100%).

2.2.4.3 *Synthesis of 3, 3, 6, 9, 9-pentamethyl-13-nitro-3, 4, 8, 9-tetrahydro-1H benzo[i][1, 3, 5, 8, 11] pentaazacyclotridecine-2, 5, 7, 10(6H, 11H)-tetraone* (**L2,** X = NO_2**)**

Exactly similar procedure was followed to synthesize **L2**; X = NO_2 as was carried out for **L2**; X = H with 44% yield (55 mg yielded from 100 mg of **L1**; X = NO_2). Elemental analysis: Calc. for $C_{17}H_{22}N_6O_6$ (%): C, 50.24; H, 5.46; N, 20.68; found: C, 50.30; H, 5.43; N, 20.60. FT-IR (KBr, ν_{max}/cm^{-1}): 3340 (s, NH), 1709 (s, CO), 1657 (s, CO), 1590 (s, CO). ^{1}H NMR δ_H (200 MHz; DMSO-d_6): 9.53 (s, 1 H, NH), 9.38 (s, 1 H, NH), 8.36 (d, 1 H, *J* = 2.73 Hz, Ph), 8.19 (m, 2 H, NH & Ph), 8.08 (d, 1 H, *J* =8.96, Ph), 7.97 (s, 1 H, NH), 3.01 (s, 3 H, CH_3), 1.56 (d, 12 H, *J* = 2.31 Hz, CH_3). ESI-MS: *m/z* 407.18 (M-H$^+$, 100%, +ve ion mode).

2.2.4.4 *Synthesis of (Et4N)$_2$[Fe^{III}(nitro ligated biuret-modified TAML)]* (**1b;** X = NO_2)[31]

The same procedure followed for the synthesis of **1a** was used for the synthesis of **1b**. Yield: 52 mg as dark orange crystals (83%) for 50 mg of starting **L2**, X = NO_2. Single crystals were obtained by layering hexane over a solution of the complex in acetone. Elemental analysis: Calc. For $C_{33}H_{58}N_8ClFeO_6$ (%): C, 52.56; H, 7.69; N, 14.87; found: C, 52.54; H, 7.70; N,14.89. Uv-vis: $\lambda_{max}(H_2O)$/nm; 356 (ε/dm^3 mol^{-1} cm^{-1}, 9020), IR (KBr, ν_{max}/cm^{-1}): 1623 (s, CO),1609 (s, CO),1565 (s, CO). HR-MS (negative ion mode): *m/z* 458.06 (M-35, 100%).

2.2.5 *Kinetic studies*

2.2.5.1 *Phosphate buffer based demetallation*

Stock solutions of **1a** (17.3 mM; H_2O) and phosphate buffer (0.1 M, 0.2 M, 0.3 M and 0.5 M) of pH 5 and 7 were prepared in double distilled water. For each run, a solution of **1a** (10 μL, 17.3 mM) in water was added to the appropriate phosphate buffer (990 μL) in a 1 mL cuvette and the decrease in absorbance at 356 nm (λ_{max} for **1a** in phosphate buffer) was monitored over time. The temperature of the reaction mixture was maintained at 25 ºC throughout the experiment.

2.2.5.2 *Brønsted acid induced demetallation*

The kinetics were monitored using a spectrophotometer (Perkin-Elmer –λ35) using 1.00 cm quartz cell at 356 nm (characteristic absorption peaks of complex **1a** and **1b**) in an electrically controlled thermostatted (25.0 ± 0.5 °C) cell housing. In all kinetic runs, concentration of the catalyst was kept constant at 0.173 mM and acid concentration was varied from 0.04 to 0.4 M for **1a** and 0.4 to 3.0 M for **1b** using $HClO_4$. KPF_6 was used to maintain the ionic strength of 0.1 M in the solution. For each set, solution pH was measured with the help of a pH meter (LABINDIA, $PICO^+$) with calibrated electrode. A rate equation considering all the possible proton dependent equilibria and demetallation reaction steps was followed as was reported earlier. (Details are explained in the results and discussion part). The pseudo first order rate constants (k_d) were calculated and plotted against [H^+] that fits nicely into a nonlinear curve from where the magnitude of 1st and 3rd order proton dependencies were calculated. All stock solutions were made using deionized water.

2.2.5.3. *Oxidation of biuret-modified Fe-TAML with H_2O_2 under single turnover condition*

To 990 μL of 0.092 mM **1a** was added one equivalent of H_2O_2 (10 μL of 9.2 mM) and the UV-vis spectral changes were recorded in 10 mM phosphate buffer pH 7. Concentration of H_2O_2 was calculated by dividing the UV-vis absorbance at 230 nm by the characteristic molar extinction coefficient ($\varepsilon = 72.8\ dm^3\ M^{-1}\ cm^{-1}$).[32]

2.2.5.4 *Kinetics of catalytic bleaching of orange II*

Using same Perkin-Elmer spectrophotometer orange II bleaching kinetics was carried out in 0.01 M phosphate buffer (pH 7 to 11). Gradual decrease in absorbance maxima at 485 nm (characteristic of orange II) was recorded with respect to time. Stock solutions of H_2O_2 (0.15M), orange II (4×10^{-3} M), and catalyst (2×10^{-5} M) were made in doubly distilled water. In a typical kinetic run, 10 μL each of orange II and the appropriate catalyst (**1a**, **1b** or **Fe-B***) stock solution was added to 970 μL of 0.01 M phosphate buffer (having the appropriate pH of 7, 9 or 11) in a 1 ml quartz cuvette. H_2O_2 (10 μL, 0.15 M) was added to initiate the reaction and the progress of the reaction was monitored by the disappearance of the orange II peak at 485 nm. The cell compartment was thermostatted at 25 ºC for each set of run. Initial rates were calculated from the pH dependent extinction coefficients of orange II. The initial rates were used to calculate the pseudo-first order rate constants for the bleaching of orange II by **1a**, **1b** or **Fe-B*** were measured in triplicate. Extinction coefficients of 17,800, 23,000 and 19,400 $M^{-1}cm^{-1}$ for orange II at pH 7, 9 and 11 respectively were used to calculate the initial rates of orange II oxidation.[6] Plot of concentration vs. time was taken up to 10 – 20% of conversion of the dye compared to the total reaction in the initial rate calculations.

2.2.5.5 *Kinetics of safranin O bleaching*

Safranin O oxidation bleaching kinetics was monitored at 525 nm and pH 11 in 0.01 M phosphate buffer. The strengths of stock solutions of safranin O, complexes **1a** or **1b** and hydrogen peroxide were 2×10^{-3} M, 5×10^{-5} M and 0.2 M respectively. The extinction coefficient of 3.3×10^4 $M^{-1}cm^{-1}$ at 525 nm for safranin O disappearance was used to get initial rate in terms of concentration unit (Ms^{-1}). To obtain the intramolecular inactivation rate (k_i), absorbance decrease with time was monitored until complete inactivation of the catalyst. Calculations of rate constants were performed by using Equation (4) and (5) as has been discussed below.

2.3 Results and discussions

2.3.1 *Crystal structure*

The X-ray crystal structure of **1a** revealed a square pyramidal geometry with an axial chloro ligand (Figure 2.2). The iron bound biuret six membered ring is completely planar in contrast to the Fe-TAML counterparts. This feature supported the hypothesis of extensive delocalization of the nitrogen lone pair over the sidewise carbonyls. The details of bond lengths and bond angles are described in Table A1-A6, Appendix I. The Fe-N bond length is 1.88 (2) Å and the Fe(III) lies approximately 0.448 Å above the plane formed by the four donor nitrogens (N1, N2, N3, N4). The N5 atom of the Me-biuret ring is almost 3.149 Å away from the Fe(III) indicating that this N-atom is not involved in bonding with the Fe(III) center. The Me-biuret six membered ring is very close to planarity and the torsion angle between the C1-N5 and C6-N2 planes is around -175.13º. Therefore the N5 atom in the 6-membered ring is strictly sp^2 hybridized and the nitrogen lone pair, residing in the p orbital of N5 atom, is conjugated extensively to the carbonyl C-atom on both sides.

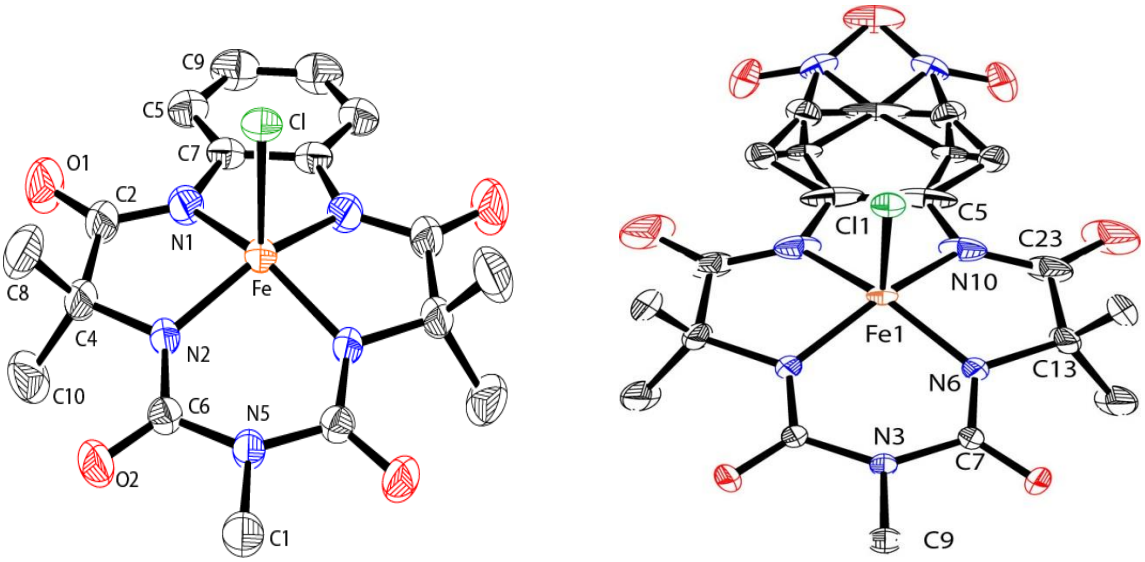

Figure 2.2: ORTEP diagrams of **1a** (left) and **1b** (right).

Very similar structural feature was also obtained in case of **1b** with distorted head aromatic ring along with the nitro functionality. We observed two fold disorder in the

crystal structure; hence the disordered atoms in the aromatic ring and nitro group were restricted up to 50% occupancy.

2.3.2 *Physical properties*

The UV-vis spectra in water displayed one absorbance maxima at 356 nm ($\varepsilon_{356\ nm}$ = 5160 and 9020 M^{-1} cm^{-1}) for **1a** and **1b** respectively corresponding to a ligand to metal charge transfer band (LMCT) followed by a less intense broad band at 450 nm characteristic of a metal based d-d transition. (Figure A8 and A9; Appendix I). The X-band EPR spectrum of **1a** and **1b** (2 mM in CH_3CN) revealed two absorption peaks at *g* values approximately 4.0 and 2.0 corresponding to an intermediate spin, *S* = 3/2 species (Figure A12; Appendix I). This is in contrast to iron porphyrins in which the weaker σ-donor ability of the porphyrin ring leads to a high spin *S* = 5/2 species. A 100% abundance peak at 413.07 and 458.07 for **1a** and **1b** respectively were observed in the high resolution mass spectrum run in the negative ion mode that corresponds to the catalysts without the axial chloride (Figure A10 and A11; Appendix I). The cyclic voltammogram in CH_3CN consisted of one reversible couple corresponding to Fe^{III}/Fe^{IV}, a quasi-reversible couple for Fe^{IV}/Fe^{V} and a ligand based irreversible peak (Figure 2.3 and Table 2.1).

Table 2.1: Physical properties: Redox potentials (mV) of **1a**, **1b** and **Fe-B*** by cyclic voltammetry in acetonitrile (0.1 M *n*-Bu_4PF_6), scan rate 100 mV/s at a glassy carbon electrode with respect to Ag/AgCl standard electrode and molar extinction coefficients.

Catalyst	$E_{1/2}(Fe^{III}/Fe^{IV})$	$E_{1/2}(Fe^{IV}/Fe^{V})$	Ligand based	$\varepsilon_{356\ nm}$/ $M^{-1}cm^{-1}$
1a	0.41	0.93	1.50	5160
1b	0.78	1.40	2.00	9020
Fe-B*[14]	0.76	-	-	

The CV of **1a** in acetonitrile containing 0.1 M [n-Bu_4N]PF_6 as the supporting electrolyte showed one reversible process with formal reduction potential $E_{1/2}$ at 0.410

(vs. Ag^{+}/Ag; ΔE_p= 70 mV) and another quasi-reversible process with $E_{1/2}$ at 0.93 V (vs. Ag+/Ag; ΔE_p= 85 mV). This electrochemical feature of both **1a** and **1b** in acetonitrile supported a facile formation of high-valent Fe^{V} species. The redox peak corresponding to a Fe^{III}/Fe^{IV} couple observed for **1a** ($E_{1/2}$ at 0.41 V) is almost 350 mV lower in comparison with the Fe-TAML complex **Fe-B***.[14] This indicates that presence of the-Me group increases the donor ability of the amide nitrogens in the 6-membered ring of the macrocyclic complex.

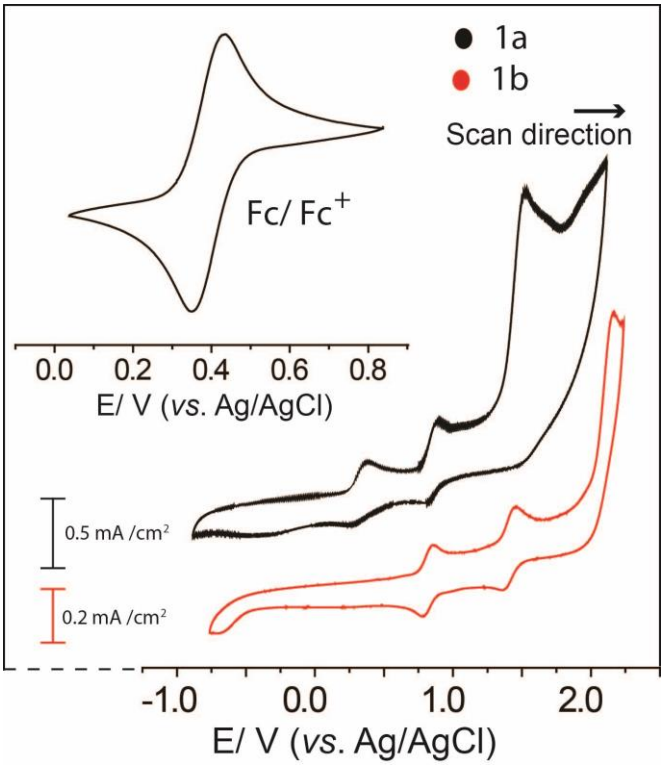

Figure 2.3: Cyclic voltammogram of **1a** (black) and **1b** (red) in acetonitrile (1 mM).

2.3.3 *Chemical properties*

2.3.3.1 *Stability of biuret-modified Fe-TAML at neutral to basic medium*

It is well known that most synthetic iron complexes (especially containing neutral nitrogen donating ligands) are unstable in aqueous basic medium (pH > 8) and hydrolyze to form iron oxide/hydroxide nanoparticles.[33,34] However, at basic pH Fe-TAMLs are extremely stable and more reactive towards degradation of various pollutants. To evaluate if this was also true for biuret modified Fe-TAML, the hydrolytic stability of the

biuret-modified Fe-TAML was measured at neutral to basic medium. UV-vis spectral scans were monitored for **1a** (71 µM in 10 mM phosphate buffer) at 356 nm. No change in the UV-vis spectral feature (Figure 2.4) was observed over a period of one day which indicates that the Fe^{III} species was intact over the experimental time period without formation of any iron oxide NPs.

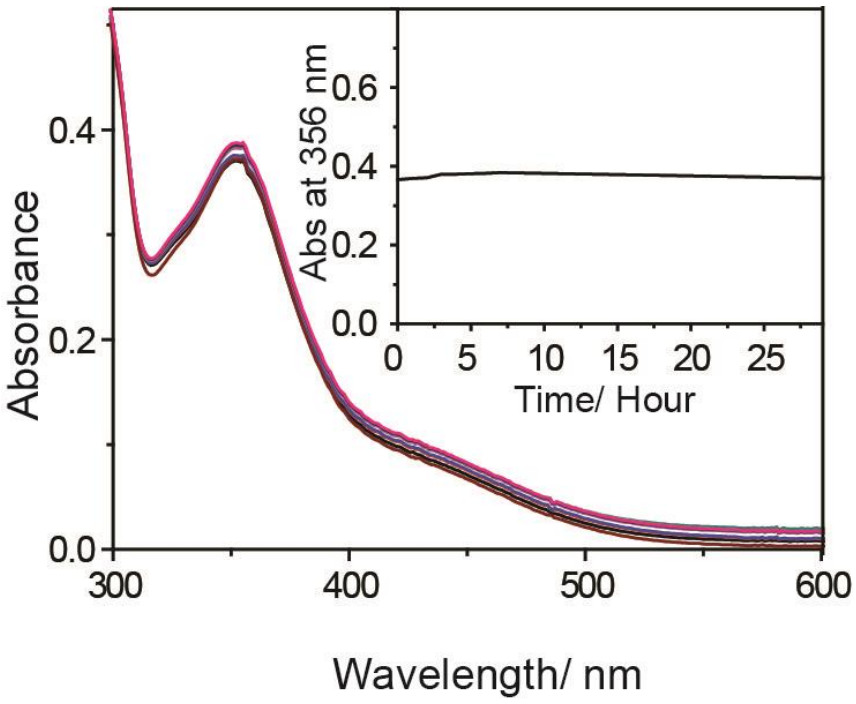

Figure 2.4: UV-vis spectral scan of 71 µM **1a** in 10 mM phosphate buffer at pH 9, Inset: absorbance change at 356 nm as a function of time.

2.3.3.2 *Stability of biuret-modified Fe-TAML in acidic medium*

In contrast to its high stability in basic medium, biuret-modified Fe-TAML undergoes acid induced demetallation at pH < 3 but with remarkably slower rates in comparison to the Fe-TAML (**Fe-B***).[19,20,29] A generally accepted mechanism for acid induced demetallation for Fe-TAMLs is outlined in Scheme 2.2 where the amido-nitrogens coordinated to the iron gets protonated at acidic pH there by weakening the bond between them. Finally the Fe-N bond is heterolytically cleaved leading to the free ligand and Fe^{III} ion. The kinetics for the demetallation of **1a** was studied at different pH using $HClO_4$ to quantitatively probe its stability in comparison to **Fe-B***. Same procedure

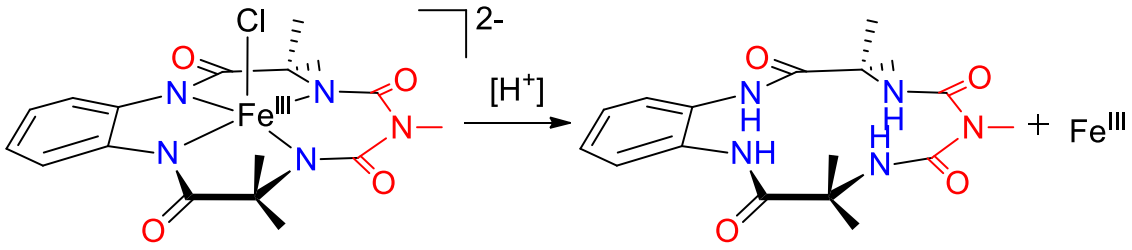

Scheme 2.2: Brønsted acid induced demetallation of biuret-modified Fe-TAML.

was also followed for **1b** and a rate equation was derived considering all the possible proton dependent equillibria and demetallation steps as shown in Scheme 2.3 below. The rate equation was simplified to the form $k_d = k_1^*[H^+] + k_2^*[H^+]^2 + k_3^*[H^+]^3$ where k_d is the first order rate constant in respect of demetallation and the terms k_1^*, k_2^* and k_3^* correspond to the first, second and third order proton dependencies respectively. Initial rate approach (up to 100 sec) was used to calculate the first order rate constants for demetallation at different pH (Table 2.2).

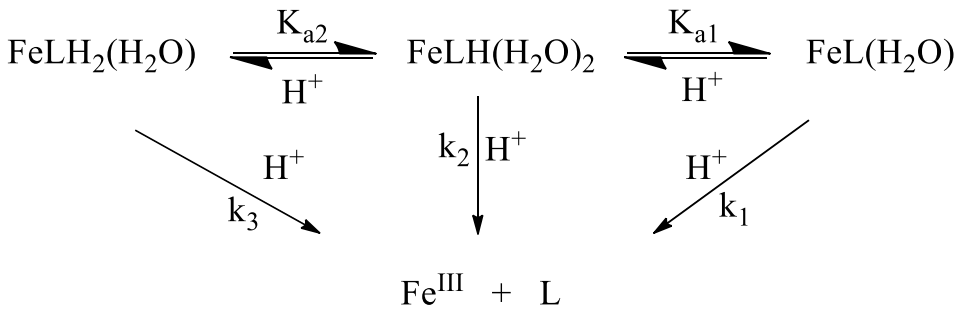

Scheme 2.3: Proposed mechanism of acid induced demetallation.

According to the Scheme 2.3, the rate law can be of the form,

$$k_d = \frac{k_1 K_{a1} K_{a2}[H^+] + k_2 K_{a2}[H^+]^2 + k_3[H^+]^3}{K_{a1}K_{a2} + K_{a2}[H^+] + [H^+]^2}$$

$$= k_1^*[H^+] + k_2^*[H^+]^2 + k_3^*[H^+]^3 \qquad (1)$$

k_d vs. $[H^+]$ plot (Figure 2.5) results were best fitted by using: $k_d = k_1^*[H^+] + k_3^*[H^+]^3$ as has been described before.[19,20] Adding the second order $k_2^*[H^+]^2$ term did not improve the fit.

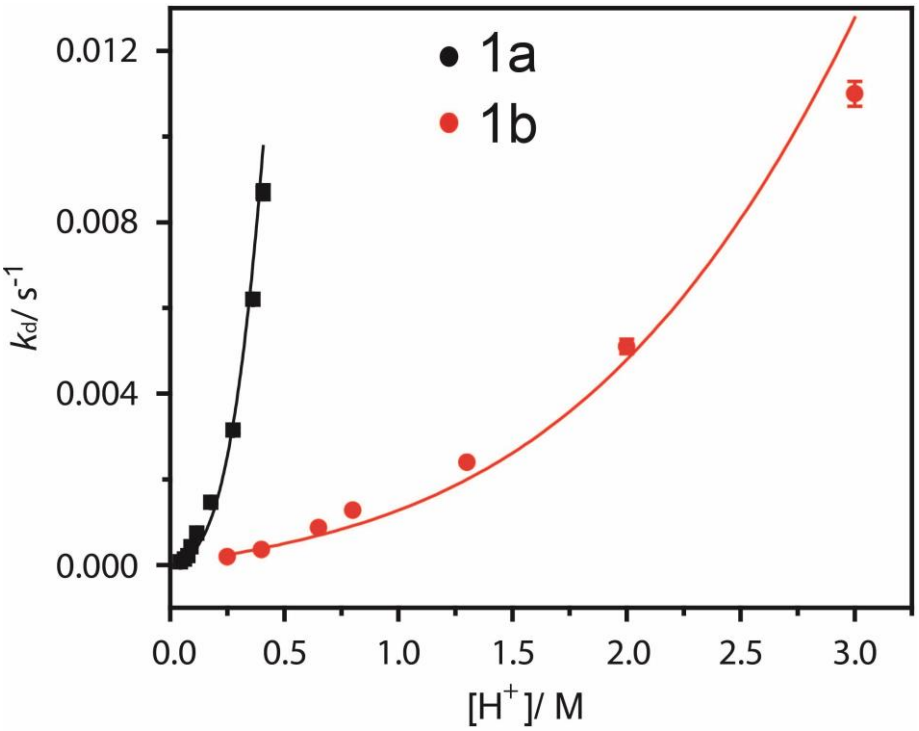

Figure 2.5: Kinetics of acid induced demetallation of **1a** and **1b** (173 µM each) at 25 °C in 0.1 M KPF_6 showing k_d vs. acid concentration.

Table 2.2: Kinetic parameters of acid catalyzed demetallation of **1a** and **1b**.

Catalyst	k_1^* $[M^{-1}s^{-1}]$	k_3^* $[M^{-3}s^{-1}]$	$t_{1/2}$ [pH 1]/sec
1a	$(1.78 \pm 0.05) \times 10^{-3}$	$(1.34 \pm 0.04) \times 10^{-1}$	2222
1b	$(0.90 \pm 0.09) \times 10^{-3}$	$(3.72 \pm 0.10) \times 10^{-4}$	7632
Fe-B*[20]	2200 ± 700	$(6.7 \pm 0.2) \times 10^{5}$	0.001

A nicely fitted nonlinear curve was obtained when all the k_d were plotted against $[H^+]$ from where the values of k_1^*, k_2^* and k_3^* can be easily calculated. Kinetic fitting of Equation 1 for catalyst **1a** and **1b** indicates that at lower acid concentration the first order (k_1^*) proton dependency dominates. However at higher acid concentrations the third

order (k_3*) parameter dominates and the contribution of k_2* values are very negligible to the overall dissociation (Figure 2.5). It was determined that replacement of the –CMe_2 group in **Fe-B*** by –NMe to afford **1a** provided a stabilization of 10^3 and 10^6 folds against acid induced demetallation in mildly and strongly acidic solutions, respectively (Table 2.2).[19,20,29] Installation of an electron withdrawing nitro group at the head aromatic ring (**1b**) further improved acid stabilization (10^9 in terms of k_3*). Most probably the lone pair on the non-coordinated nitrogen in the biuret tail plays the crucial role of altering electron density at the directly bonded nitrogens and stabilizes a proton to more extent than TAML. Further introduction of the nitro group at the head aromatic ring makes the amido-nitrogens directly bonded to iron electron deficient and resists a proton attack there by increasing overall hydrolytic stability. This is well reflected by comparing the half-lives at pH 1 of **Fe-B*** (0.001 sec) with **1a** (2222) and **1b** (7632 sec) (Table 2.2).

Fe-TAML such as **Fe-B*** is also known to degrade in the presence of phosphate buffer[19] and hence the stability of **1a** and **1b** was tested in the presence of phosphate buffer at various ionic strengths. Figure 2.6 shows the UV-vis spectra of **1a** in the presence of 0.1 M (pH 5) and 0.5 M (pH 7) phosphate buffer over a time period of 5 hrs. It was found that only 10% of the complex degraded during this time period. The $t_{1/2}$, calculated to be approximately 18 hrs, showed biuret-modified Fe-TAML to be remarkably stable at high ionic strength and low pH.[29]

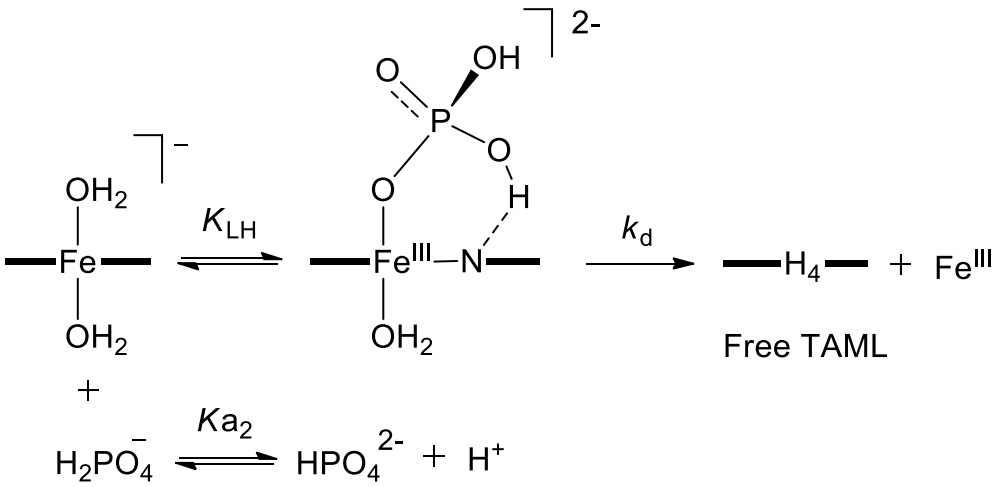

Scheme 2.4: Proposed mechanism of phosphate buffer mediated demetallation of Fe-TAMLs.[19]

The proposed mechanism of phosphate induced demetallation of **Fe-B*** involves pre-coordination of the O-$PO(OH)_2$ into the Fe(III) center followed by the intramolecular attack of the H^+ onto the amide N- donors and subsequent dissociation into free ligand and iron ion (Scheme 2.4).[19] The same argument that was discussed in the section of acid induced demeatallation can also be applied for the phosphate buffer mediated demetallation.

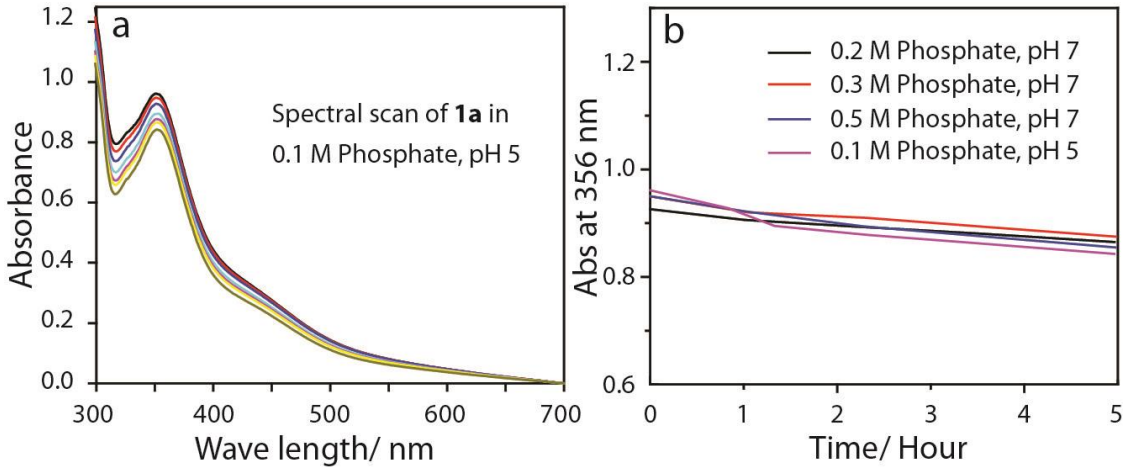

Figure 2.6: a) UV-vis spectral scan of a solution containing **1a** (0.173 mM) in 100 mM phosphate buffer at pH 5 over a period of five hours; b) Time trace of spectral scan of **1a** in different ionic strengths of phosphate buffer and at pH 5 and 7.[29]

2.3.4 *Biuret-modified Fe-TAML as peroxidase mimic*

2.3.4.1 *Biuret-modified Fe-TAML based oxidants produced in presence of H_2O_2*

To understand the reactive intermediates generated during oxidation reactions, equimolar amounts of H_2O_2 was added to **1a** in 10 mM phosphate buffer pH 7 and the reaction was probed by UV-vis spectroscopy. The UV-vis spectrum showed absorbance maxima at 417 nm, 530 nm, 626 nm and a broad peak ranging from 850 to 1100 nm (Figure 2.7; red spectrum). This spectral pattern is very similar to the μ-Oxo-Fe^{IV} dimer as previously reported by Collins[16] and us (this is extensively discussed in chapter III). Upon increasing the pH to 12 by slow addition of NaOH a change in the spectral features was observed in which the peak at 850-1100 nm completely disappeared. The spectrum of the new species formed (Figure 2.7; blue spectrum) resembled a mononuclear Fe^{IV}(O)

species that has been reported for the Fe-TAML counterpart **Fe-B***.[16] The existence of the μ-Oxo-Fe^{IV} dimer pH ~7 can be correlated to first protonation of the mononuclear $Fe^{IV}(O)$ species to form the corresponding $Fe^{IV}(OH)$ followed by removal of one water molecule leading to the formation of μ-Oxo-Fe^{IV} dimer as depicted in the Equation 2. Therefore, in the presence of H_2O_2 the biuret-modified Fe-TAML under goes formation of a high valent $Fe^{IV}(O)$ or μ-Oxo-Fe^{IV} dimer which could be the active species during the oxidation reaction.

$$Fe^{III} + H_2O_2 \longrightarrow \underset{\text{pH 12}}{Fe^{IV}(O)} \xrightarrow{H^+} \underset{\text{pH 7}}{Fe^{IV}(OH)} \underset{-H_2O}{\rightleftharpoons} Fe^{IV}\text{-}(O)\text{-}Fe^{IV} \quad (2)$$

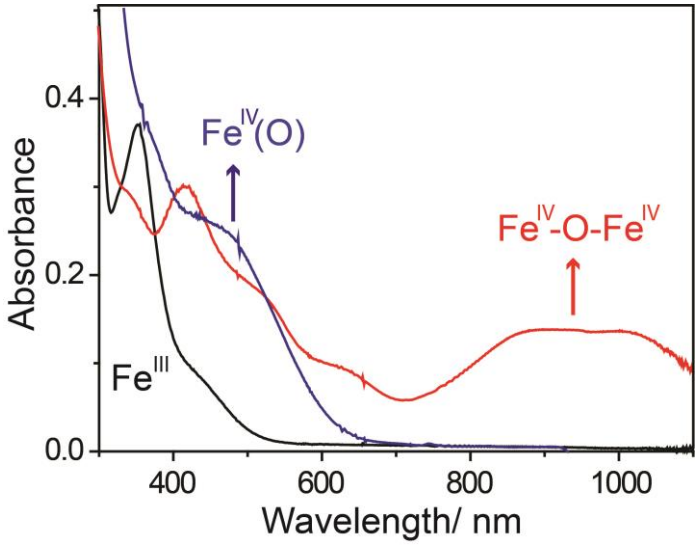

Figure 2.7: Formation of μ-Oxo-Fe^{IV} dimer at pH 7 and mononuclear $Fe^{IV}(O)$ at pH 12 from biuret-modified Fe-TAML (**1a**) and one equivalent of H_2O_2 in 10 mM phosphate buffer.

2.3.4.2 *Environmentally important dye degradations*

The use and discharge of common synthetic dyes in the textile industries have been enormously increased owing to the current worldwide growth in fiber consumption. The unused dyes in the industrial effluents being discharged into water body, present significant environmental problems. Most of the textile dyes are chemically stable and resistant to aerobic degradation by sunlight, water, soap, bleach, and perspiration (Figure

2.8).[35a] Azo dyes that incorporate the –N=N– moiety account for up to 70% of all textile dyestuffs produced.[35a] Hence the degradation of organic dyes has attracted much attention in the scientific community for devising new technologies for wastewater decolorization. Chemical methods those have been used in this context include photodegradation by TiO_2,[35b] Fenton systems,[35c] and soluble transition metal based molecular catalysts in combination with various oxidizing agents.[35d] Several research groups have studied the catalyzed decolorization of dyes by H_2O_2.[35e] Tosik and Wiktorowski have reported on the decolorization by ozone and H_2O_2 with Fenton reagent.[35f] The reactions are slow at lower temperatures and require higher catalyst and H_2O_2 doses. T. J. Collin's approach of using H_2O_2 activators (Fe-TAMLs) has found enormous attention in the oxidative degradation of azo dyes.[2,6,14-16] For the present study we have chosen the common dyes orange II and safranin O (Figure 2.8) as the substrate for examining the peroxidase activity of our designed biuret-modified Fe-TAMLs.

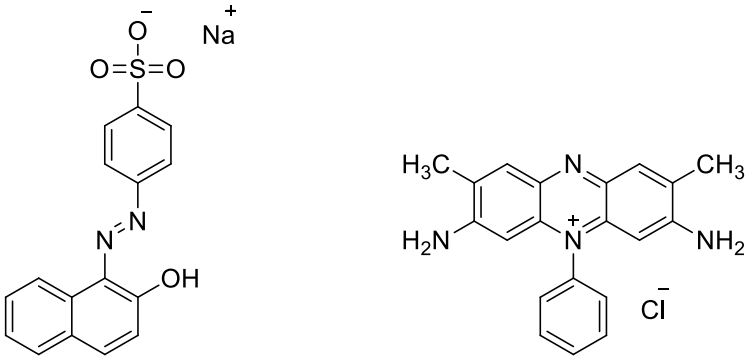

Figure 2.8: Molecular structures of the dyes used in this work.

2.3.4.3 *Catalytic bleaching of orange II dye*

Among others, orange II ([4-[(2-hydroxynaphthyl)azo]-benzene sulphonic acid], Na^+ salt) is a commonly used azo dye in textile industries and the unused dye after the dyeing is discharged as effluents. Orange II was chosen as a substrate to study the effectiveness of complex **1a** as a functional model of peroxidase since peroxidase enzymes are also known to efficiently bleach orange II.[14] Oxidation of orange II with H_2O_2 is very slow. However, the rate increases significantly in presence of catalytic

amounts of an activator like **1a**, **1b** and **Fe-B***. At pH 11, submicromolar concentrations of **1a** (2×10^{-7} M) was found to be very efficient in the activation of H_2O_2 for the complete bleaching of the dye orange II in 3 min at a catalyst to substrate ratio of 1:200 (Figure 2.9). The mechanism of orange II degradation involves first activation of H_2O_2 by catalyst to form a high valent reactive intermediate species which in turn oxidizes the substrate very fast as shown in Equation 3. The bleaching reactions are extremely fast and the pseudo first order rate constant k_{obs} was calculated to be 0.021 ± 0.001 s^{-1}.[29]

$$[\text{Fe-TAML}] + H_2O_2 \underset{k_{-I}}{\overset{k_I}{\rightleftharpoons}} [\text{Fe-TAML}]_{Ox} \xrightarrow[k_{II}]{\text{Substrate}} \text{Product} \qquad (3)$$

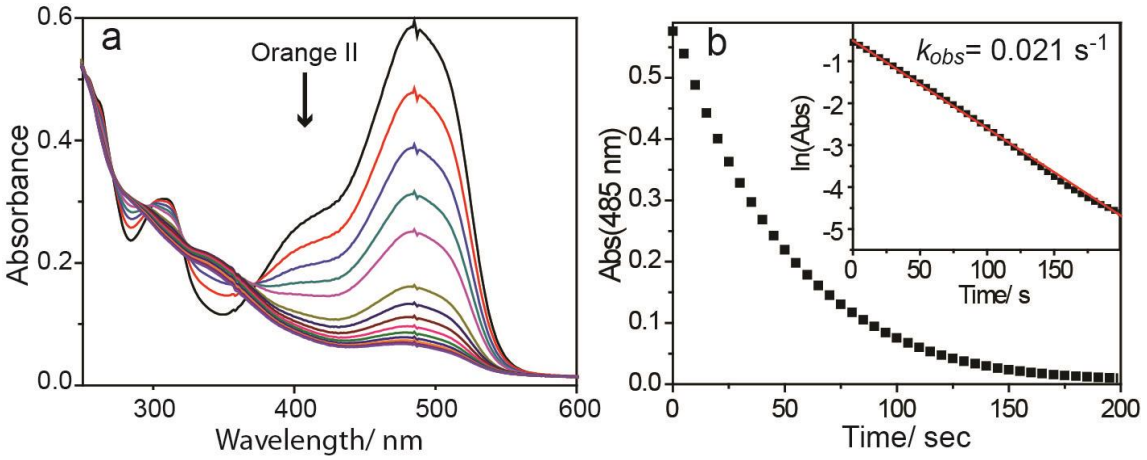

Figure 2.9: a) Spectral scan of a typical orange II (4×10^{-5} M) dye degradation using biuret-modified Fe-TAML (**1a**; 2×10^{-7} M) and H_2O_2 (1.5×10^{-3} M) in 10 mM phosphate buffer pH 11 at 25 °C; b) Time traces of the spectral scan of orange II oxidation.

Considering all the rate constants in equation (3), the following equation of the rate law for orange II dye degradation was derived (Equation 4 below). Initial rate approach (up to 100 sec) was applied to analyze kinetic data for peroxidase activity as biuret-modified Fe-TAML catalyzed oxidation of orange II in presence of H_2O_2 follows Michaelis-menten type kinetics. The initial rate law (Equation 4) was derived considering the steady state of [biuret-modified Fe^{III}-TAML]$_{oxidized}$ species using mass balance equation $[Fe^{III}]_{Total}$ = {[biuret-modified Fe^{III}-TAML] + [biuret-modified Fe^{III}-TAML]$_{oxidized}$}. At pH 11 the inverse initial rate has linear dependence on inverse

concentrations of the both reagents which suggests k_{-I} is negligible (Figure A27; Appendix I: up to 2×10^{-5} M for orange II and 1×10^{-3} for H_2O_2 at [**1b**] = 1×10^{-7} M). The initial rates as a function of $[H_2O_2]$ have been measured at different concentrations of orange II covering at least a ten-fold concentration range. All the data obtained were fitted to equation (4) (Appendix I; Figure A14 to A24 and Table A1 to A12) to obtain a non-linear curve from which the values of k_I and k_{II} are determined (Table 2.3). The data suggest a six fold faster H_2O_2 activation rate (k_I) and a twenty fold faster substrate oxidation rate (k_{II}) at pH 7 for **1b** in comparison to **1a**.

$$\frac{d[Sub]}{dt} = \frac{k_I[H_2O_2]k_{II}[Sub][Fe^{III}]_{Total}}{k_{-I} + k_I[H_2O_2] + k_{II}[Sub]} \qquad (4)$$

Table 2.3: Rate constants k_I and k_{II} ($M^{-1}s^{-1}$) for **1a** and **1b** catalyzed bleaching of orange II by $[H_2O_2]$ at 25 °C in 0.01 M phosphate buffer at different pH

Catalyst	pH	k_I $[M^{-1}s^{-1}]/10^4$	k_{II} $[M^{-1}s^{-1}]/10^5$
1a	7.0	0.02 ± 0.00	0.20 ± 0.01
	9.4	0.28 ± 0.02	1.12 ± 0.10
	11.0	3.40 ± 0.20	1.60 ± 0.10
1b	7.0	0.12 ± 0.01	4.10 ± 0.50
	9.4	0.24 ± 0.06	4.20 ± 0.40
	11.0	2.40 ± 0.20	4.90 ± 0.50
Fe-B* [2]	11.0[a]	0.35	0.15

[a] **Fe-B*** shows maximum activity at pH 11.0 [2]

A significant pH dependency of k_I both in case of **1a** and **1b** was observed as has been reported for related Fe-TAML complexes.[2] For example **1a** showed approximately 100 fold higher reactivity (in terms of k_I) and **1b** almost 20 fold when the pH was increased from 7 to 11. This feature can be attributed to the facile deprotonation of H_2O_2 coordinated to iron to form the corresponding $Fe^{III}(OOH)$ intermediate species. The $Fe^{III}(OOH)$ species thus formed may either undergo cleavage of the O-O bond in a heterolytic or homolytic fashion to generate the corresponding high valent $Fe^{V}(O)$ or

$Fe^{IV}(O)$ species that are expected to be the real oxidant. However, modest change in reactivity was observed in terms of the second step i.e. substrate oxidation (k_{II}) upon pH change from 7 to 11. Comparison of reactivity in terms of k_I between **1a** and **1b** suggest that the latter is almost 10 times more reactive than the former at pH 7. This observation can be corroborated to the electron deficient nature of **1b** (because of the head NO_2 group) that allows easy deprotonation of H_2O_2 immediately after binding to the iron active centre to form the high valent iron oxo species. Hence based our observation and comparison with reported values, **1b** is the most powerful H_2O_2 activator as well as better oxidation catalyst among **1a**, **1b** and **Fe-B***.

The bleaching of azo dyes by several other peroxidase mimics such as Fe/Mn complexes of water soluble synthetic porphyrins and phthalocyanins have been studied. Most of these systems employ a very high catalyst to substrate ratio (typically 1:10) and the bleaching remains incomplete for several dyes.[36-41] The very low turnover numbers for these synthetic porphyrin mimics is due to the auto oxidation and degradation of the metalloprophyrins during the bleaching reaction. In contrast, **1a** has very high turnover numbers (>200) which is indicative of the robustness of the catalyst system. The oxidative robustness of **1a** is also implied in the exponential kinetic curve; that holds for at least 6 half-lives (inset; Figure 2.9b). Therefore, little or no degradation of the catalysts takes place during the course of the oxidation. This is expected since the C-H bonds of the –NMe group is situated very far away from the proposed Fe-oxo intermediate, thereby reducing the chances of ligand degradation by intramolecular C–H abstraction as has been proposed before for other Fe-TAML complexes.[12] Comparison of the catalytic activity of **1a** and **Fe-B*** for the bleaching of orange II at pH 7 and 9 shows that **1a** is much faster in oxidizing orange II (Figure A13; Appendix I). Hence the substitution of the $–CMe_2$ group in the malonyl fragment of **Fe-B*** with the –NMe group produces a new generation oxidation catalyst that constitutes a successful peroxidase mimic.

2.3.4.4 *Activity stability parameterization of biuret-modified Fe-TAML*

As discussed in chapter I, all the possible activation and deactivation pathways during substrate oxidation by **1a** and **1b** in presence of H_2O_2 are provided in Scheme 2.5. The activation parameters k_I and k_{II} and the medium induced deactivation contributions

are already discussed in the above sections. This section would solely consider the oxidative inactivation contributions k_i and k_{2i} which arises due to inter and intra-molecular self-oxidation. For determination of k_i, sub micro molar catalyst concentration was used to neglect the intermolecular self-oxidation. A relatively robust substrate than orange II was chosen so that the rate of catalyst oxidation was of the same order as substrate oxidation. The substrate considered for this study was the dye safranin O.

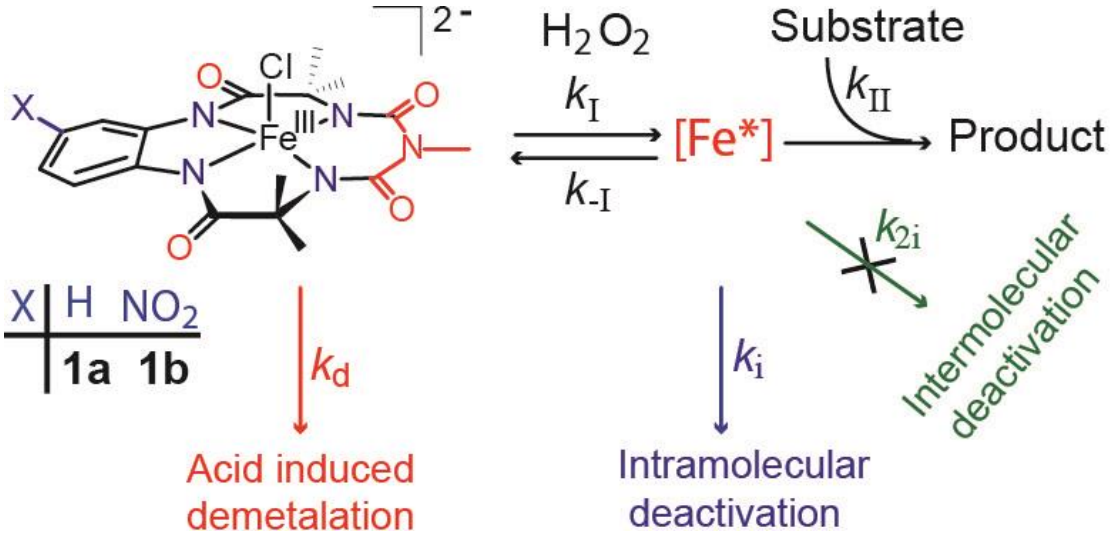

Scheme 2.5: Various activation and deactivation pathways of biuret-modified Fe-TAMLs in oxidizing conditions in presence of H_2O_2

2.3.4.5 *Kinetics of biuret-modified Fe-TAML catalyzed safranin O bleaching*

In contrast to orange II, safranin O is difficult to oxidize using H_2O_2 and catalyst. Under the reaction conditions ([H_2O_2] >>> [dye]) safranin O undergoes incomplete oxidation (Figure 2.10). The catalytic bleaching after 20,000 sec reaches a saturation level and resumes as soon as a new aliquot of catalyst was added. This suggests complete deactivation of the catalyst after end of first cycle. Hence safranin O oxidation is a perfect choice for finding the oxidative decay of the catalyst as has been shown by Collins *et. al*. before.[23]

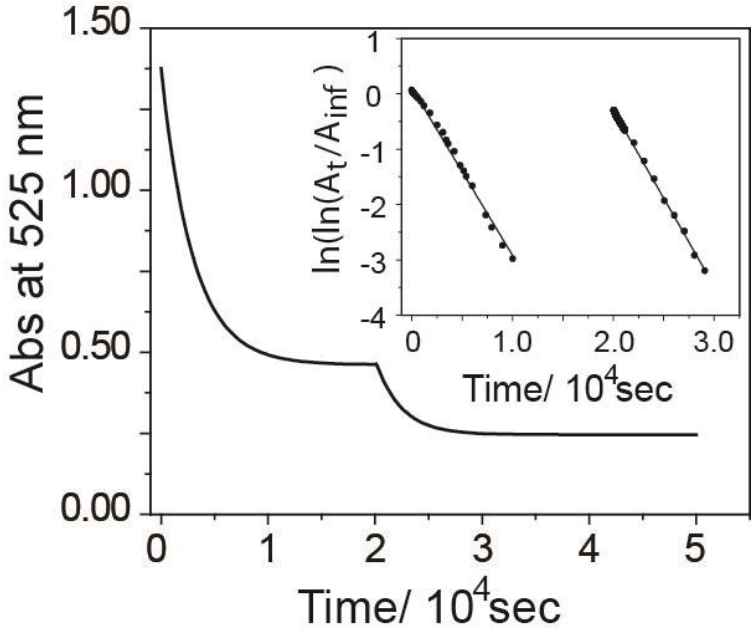

Figure 2.10: 1b catalyzed safranin O oxidation. Stepwise oxidation was followed to calculate the rate of intramolecular self-oxidation of the catalyst. Inset shows both the first and second cycle follows similar rates (very parallel).

2.3.4.6 *Intramolecular inactivation (k_i) measurement for safranin O bleaching at pH 11*

The intra-molecular oxidation of the ligand in case of Fe^{III}-TAMLs occurs by the high-valent Fe-oxo intermediate species via abstraction of the nearest hydrogen present in the malonoyl -CMe_2 group. This is only possible because the six membered ring in the tail part is in a boat conformation with the H of the –CMe_2 group proximally located to the Fe-oxo. In contrast the biuret bound iron six membered ring is completely planar and the –NMe is located far away from Fe-oxo moiety there by making intra-molecular hydrogen abstraction very difficult (discussed in chapter I). The monoexponential intra-molecular inactivation rate constant (k_i) measurement of the oxidized form of the catalyst was done by the method developed by Collins group.[23] The simplified differential rate law for dye bleaching is given by equation (5) where D_t and x are total concentrations of the dye and the bleached dye at time t respectively. Integrating the equation (5) under the boundary condition $x = x_\infty$ at $t = t_\infty$ results in equation (6). Equation (7) was derived by replacing the concentration terms by the absorbance terms which can be easily monitored by a spectrophotometer.

$$\frac{d(D_t - x)}{dt} = k_{II}(D_t - x)[Fe^{III}]_{Total}e^{-k_i t} \quad (5)$$

$$\ln\left[\ln\left(\frac{D_t - x}{D_t - x_\alpha}\right)\right] = \ln\left(\frac{k_{II}}{k_i}[Fe^{III}]_{Total}\right) - k_i t \quad (6)$$

$$\ln\left[\ln\left(\frac{A_t}{A_\infty}\right)\right] = \ln\left(\frac{k_{II}}{k_i}[Fe^{III}]_{Total}\right) - k_i t \quad (7)$$

From the slope of the double logarithm of the ratio A_t/A_∞ vs. time plot in equation (7) the values of k_i (Figure 2.10, Table 2.4) were obtained. The rate constant k_{II} can also be calculated from the intercept of the plot by putting the value of k_i. The k_i values given in Table 2.4 indicate 10 fold stabilization against self oxidation for biuret-modified TAML **1b** [k_i = (3.1 ± 0.2) s^{-1}] in comparison to **Fe-B*** [(34 ± 3) s^{-1}]. Though the k_{II} for **1a** and **1b** are lower than **Fe-B***; lower k_i values allow them to remain for longer time period in the reaction mixture that is reflected by lager OD change per each aliquot of catalyst added (Figure 2.10) for oxidation of safranin O. For **Fe-B*** four cycles of catalyst addition is required for an OD change of 0.8. In contrast, one cycle of **1b** is sufficient for an the same OD change.[23] The kinetics for safranin O oxidation by **1a** is given in Figure A26, Table A13: Appendix I.

Table 2.4: Rate constants k_i (s^{-1}) and k_{II} ($M^{-1}s^{-1}$) of **1a** and **1b** in comparison with **Fe-B*** in terms of safranin O bleaching by H_2O_2 at pH 11.0 and 25 ^oC.

Catalyst	$10^4 k_i$ s^{-1}	$t_{1/2}$ min^{-1}	10^{-3} k_{II} $[M^{-1}s^{-1}]^a$	$10^{-3}k_{II}$ $[M^{-1}s^{-1}]^b$
1a	3.7 ± 0.1	31.2	2.0 ± 0.1	2.4 ± 0.1
1b	3.1 ± 0.2	37.3	5.6 ± 0.3	5.6 ± 0.1
Fe-B*[23]	34 ± 3.0	3.40	11 ± 1.0	12 ± 1.0

2.4 Conclusions

This chapter discusses the rationale design and synthesis of hydrolytically and oxidatively robust peroxidase mimics biuret-modified Fe-TAML. The precursor Fe^{III} complexes have been extensively characterized by conventional spectroscopy and X-ray

crystallography. Installing a substituted biuret moiety onto the ligand framework of TAML we have synthesized a new generation macrocyclic Fe(III) complex that exhibit both excellent reactivity and stability, especially at low pH and high ionic strength. The stability of **1a** increased 10^6 folds in strongly acidic media in comparison to **Fe-B***. Further, an electron withdrawing nitro group has been installed at the head aromatic ring to achieve huge (10^9 folds) improvement in hydrolytic stability. Rigorous kinetic study has been carried out in order to parameterize the stability and activity of the biuret-modified Fe-TAMLs as peroxidase mimics. The catalyst comprises of elements that are truly biocompatible which makes it a suitable candidate for environmental remediation. We also show that deprotonated Me-substituted biurets can be excellent ligands for the designing of functional peroxidase mimics. Synthesis of Fe(III) macrocyclic complexes with only alkyl or aryl substituted biuret donors can lead to new generation of peroxidase mimics. These catalysts can be used as a possible replacement for native peroxidase enzymes in environmental remediation and analytical biochemistry.

2.5 References

(1) Beach, E. S.; Duran, J. L.; Horwitz, C. P.; Collins, T. J. *Industrial & Engineering Chemistry Research* **2009**, *48*, 7072.

(2) Ellis, W. C.; Tran, C. T.; Denardo, M. A.; Fischer, A.; Ryabov, A. D.; Collins, T. J. *Journal of the American Chemical Society* **2009**, *131*, 18052.

(3) Collins, T. J.; Kostka, K. L.; Uffelman, E. S.; Weinberger, T. L. *Inorganic Chemistry* **1991**, *30*, 4204.

(4) Ellis, W. C.; Tran, C. T.; Roy, R.; Rusten, M.; Fischer, A.; Ryabov, A. D.; Blumberg, B.; Collins, T. J. *Journal of the American Chemical Society* **2010**, *132*, 9774.

(5) Kundu, S.; Chanda, A.; Espinosa-Marvan, L.; Khetan, S. K.; Collins, T. J. *Catalysis Science & Technology* **2012**, *2*, 1165.

(6) Chahbane, N.; Popescu, D.-L.; Mitchell, D. A.; Chanda, A.; Lenoir, D.; Ryabov, A. D.; Schramm, K.-W.; Collins, T. J. *Green Chemistry* **2007**, *9*, 49.

(7) Beach, E. S.; Malecky, R. T.; Gil, R. R.; Horwitz, C. P.; Collins, T. J. *Catalysis Science & Technology* **2011**, *1*, 437.

(8) Horwitz, C. P.; Fooksman, D. R.; Vuocolo, L. D.; Gordon-Wylie, S. W.; Cox, N. J.; Collins, T. J. *Journal of the American Chemical Society* **1998**, *120*, 4867.

(9) Collins, T. J.; Gordon-Wylie, S. Long-Lived Homogeneous Oxidation Catalysts. U.S. Patent5,847,120, December 8, **1998**.

(10) Popescu, D.-L.; Chanda, A.; Stadler, M. J.; Mondal, S.; Tehranchi, J.; Ryabov, A. D.; Collins, T. J. *Journal of the American Chemical Society* **2008**, *130*, 12260.

(11) Gupta, S. S.; Stadler, M.; Noser, C. A.; Ghosh, A.; Steinhoff, B.; Lenoir, D.; Horwitz, C. P.; Schramm, K.-W.; Collins, T. J. *Science* **2002**, *296*, 326.

(12) Collins, T. J. *Accounts of Chemical Research* **2002**, *35*, 782.

(13) Chanda, A.; Khetan, S. K.; Banerjee, D.; Ghosh, A.; Collins, T. J. *Journal of the American Chemical Society* **2006**, *128*, 12058.

(14) Ghosh, A.; Mitchell, D. A.; Chanda, A.; Ryabov, A. D.; Popescu, D. L.; Upham, E. C.; Collins, G. J.; Collins, T. J. *Journal of the American Chemical Society* **2008**, *130*, 15116.

(15) Ghosh, A.; Tiago de Oliveira, F.; Yano, T.; Nishioka, T.; Beach, E. S.; Kinoshita, I.; Münck, E.; Ryabov, A. D.; Horwitz, C. P.; Collins, T. J. *Journal of the American Chemical Society* **2005**, *127*, 2505.

(16) Chanda, A.; Shan, X.; Chakrabarti, M.; Ellis, W. C.; Popescu, D. L.; Tiago de Oliveira, F.; Wang, D.; Que, L.; Collins, T. J.; Münck, E.; Bominaar, E. L. *Inorganic Chemistry* **2008**, *47*, 3669.

(17) Demeter, E. L.; Hilburg, S. L.; Washburn, N. R.; Collins, T. J.; Kitchin, J. R. *Journal of the American Chemical Society* **2014**, *136*, 5603.

(18) Ellis, W. C.; McDaniel, N. D.; Bernhard, S.; Collins, T. J. *Journal of the American Chemical Society* **2010**, *132*, 10990.

(19) Polshin, V.; Popescu, D.-L.; Fischer, A.; Chanda, A.; Horner, D. C.; Beach, E. S.; Henry, J.; Qian, Y.-L.; Horwitz, C. P.; Lente, G.; Fabian, I.; Münck, E.; Bominaar, E. L.; Ryabov, A. D.; Collins, T. J. *Journal of the American Chemical Society* **2008**, *130*, 4497.

(20) Ghosh, A.; Ryabov, A. D.; Mayer, S. M.; Horner, D. C.; Prasuhn, D. E.; Sen Gupta, S.; Vuocolo, L.; Culver, C.; Hendrich, M. P.; Rickard, C. E. F.; Norman, R. E.;

Horwitz, C. P.; Collins, T. J. *Journal of the American Chemical Society* **2003**, *125*, 12378.

(21) Oliveira, F. T.; Chanda, A.; Banerjee, D.; Shan, X.; Mondal, S.; Que, L.; Bominaar, E. L.; Münck, E.; Collins, T. J. *Science* **2007**, *315*, 835.

(22) Kundu, S.; Thompson, J. V. K.; Ryabov, A. D.; Collins, T. J. *Journal of the American Chemical Society* **2011**, *133*, 18546.

(23) Chanda, A.; Ryabov, A. D.; Mondal, S.; Alexandrova, L.; Ghosh, A.; Hangun-Balkir, Y.; Horwitz, C. P.; Collins, T. J. *Chemistry – A European Journal* **2006**, *12*, 9336.

(24) Chavez, F. A.; Mascharak, P. K. *Accounts of Chemical Research* **2000**, *33*, 539.

(25) MacBeth, C. E.; Golombek, A. P.; Young, V. G.; Yang, C.; Kuczera, K.; Hendrich, M. P.; Borovik, A. S. *Science* **2000**, *289*, 938.

(26) Barbier, J. P.; El Biyyadh, A.; Kappenstein, C.; Mabiala, N. D.; Hugel, R. P. *Inorganic Chemistry* **1985**, *24*, 3615.

(27) Birker, P. J. M. W. L.; Bour, J. J.; Steggerda, J. J. *Inorganic Chemistry* **1973**, *12*, 1254.

(28) Thulstrup, P. W.; Larsen, E. *Dalton Transactions* **2006**, 1784.

(29) Panda, C.; Ghosh, M.; Panda, T.; Banerjee, R.; Sen Gupta, S. *Chemical Communications* **2011**, *47*, 8016.

(30) Ghosh, A.; Ramidi, P.; Pulla, S.; Sullivan, S.; Collom, S.; Gartia, Y.; Munshi, P.; Biris, A.; Noll, B.; Berry, B. *Catalysis Letters* **2010**, *137*, 1.

(31) Panda, C.; Debgupta, J.; Díaz, D. D.; Singh, K. K.; Gupta, S. S. and Dhar, B. B. *Journal of the American Chemical Society* **2014**, 136, 12273.

(32) George, P.; *Biochemical Journal* **1953**, 54, 267.

(33) Chen, G.; Chen, L.; Ng, S.-M.; Man, W.-L.; Lau, T. C. *Angewandte Chemie International Edition* **2013**, *52*, 1789.

(34) Hong, D.; Mandal, S.; Yamada, Y.; Lee, Y.-M.; Nam, W.; Llobet, A.; Fukuzumi, S. *Inorganic Chemistry* **2013**, *52*, 9522.

(35) a) Zollinger, H. Wiley, Weinheim, 3rd edn, **2003**; b) Lagrasta, C.; Bellobono; I. R. and Bonardi, M. *Journal of Photochemistry and Photobiology A: Chemistry* **1997**, 110, 201; Gouvea, C. A. K.; Wypych, F.; Moraes, S. G.; Duran, N.; Nagata, N. and

Peralta-Zamora, P. *Chemosphere* **1999**, 40, 433; Neppolian, B.; Sakthivel, S.; Arabindoo, B.; Palanichamy, M. and Murugesan, V. *Journal of Environmental Science and Health, Part A* **1999**, A34, 1829; Neppolian, B.; Choi, H. C.; Sakthivel, S.; Arabindoo, B. and Murugesan, V. *Chemosphere* **2002**, 46, 1173; c) Utset, B.; Garcia, J.; Casado, J.; Domenech, X. and Peral, J. *Chemosphere* **2000**, 41, 1187; d) Oakes, J.; Gratton, P. and Weil, I. *Journal of the Chemical Society, Dalton Transactions* **1997**, 3805; Oakes, J.; Welch, G. and Gratton, P. *Journal of the Chemical Society, Dalton Transactions* **1997**, 3811; Oakes, J. and Gratton, P. *Journal of the Chemical Society, Perkin Transactions* 2, **1998**, 2563; Oakes, J.; Gratton, P.; Clark, R. and Wilkes, I. *Journal of the Chemical Society, Perkin Transactions* 2, **1998**, 2569; Hodges, G. R.; Lindsay-Smith J. R. and Oakes, J. *Journal of the Chemical Society, Perkin Transactions* 2, **1998**, 617; e) Gould, D. M.; Griffith, W. P. and Spiro, M. *Journal of Molecular Catalysis A: Chemical* **2001**, 175, 289; Verma, P.; Baldrian, P. and Nerud, F. *Chemosphere* **2003**, 50, 975; f) Tosik, R. and Wiktorowski, S. *Ozone: Science & Engineering* **2001**, 23, 295.

(36) Johnstone, A. W.; Stocks, A.; Simpson, J.; A. *Chemical Communications* **1997**, 2277.

(37) Brausam, A.; Eigler, S.; Jux, N.; van Eldik, R. *Inorganic Chemistry* **2009**, *48*, 7667.

(38) Meunier, B.; Sorokin, A. *Accounts of Chemical Research* **1997**, *30*, 470.

(39) Nango, M.; Iwasaki, T.; Takeuchi, Y.; Kurono, Y.; Tokuda, J.; Oura, R. *Langmuir* **1998**, *14*, 3272.

(40) Rismayani, S.; Fukushima, M.; Ichikawa, H.; Tatsumi, K. *Journal of Hazardous Materials* **2004**, *114*, 175.

(41) Sorokin, A. B.; Kudrik, E. V. *Catalysis Today* **2011**, *159*, 37.

Chapter III

Homogeneous Chemical & Photochemical Water Oxidation Using Biuret-modified Fe-TAML

This chapter is adapted from the following publication.

(1) Panda, C.; Debgupta, J.; Díaz, D. D.; Singh, K. K.; Gupta, S. S. and Dhar, B. B.; *Journal of the American Chemical Society* **2014**, 136, 12273.

3.1 Introduction

For the past couple of decades, in a quest to develop sustainable energy conversion processes, many chemists around the globe have attempted water splitting using sunlight.[1-3] Water splitting into H_2 and O_2, a multi-proton coupled electron transfer (PCET) reaction that is energetically uphill, represents a major technological challenge.[4] Water splitting consists of two processes: water oxidation (WO) leading to oxygen evolution (OE) and proton reduction.[3] Water oxidation is a greater challenge, as the reaction consists of multi-electron transfers and some of them have a high redox potential. WO is of interest also from a biological perspective, because it is one of the crucial steps that occur in the oxygen-evolving complex of photosystem II (OEC-PSII) in green plants and algae, which are responsible for photosynthesis. The oxygen-evolving complex is composed of metal-oxo clusters of earth-abundant elements manganese[1] and calcium (Figure 3.1) that use sequential cascade reactions to catalyze the four-electron oxidation of water to evolve oxygen (O_2).[5,6]

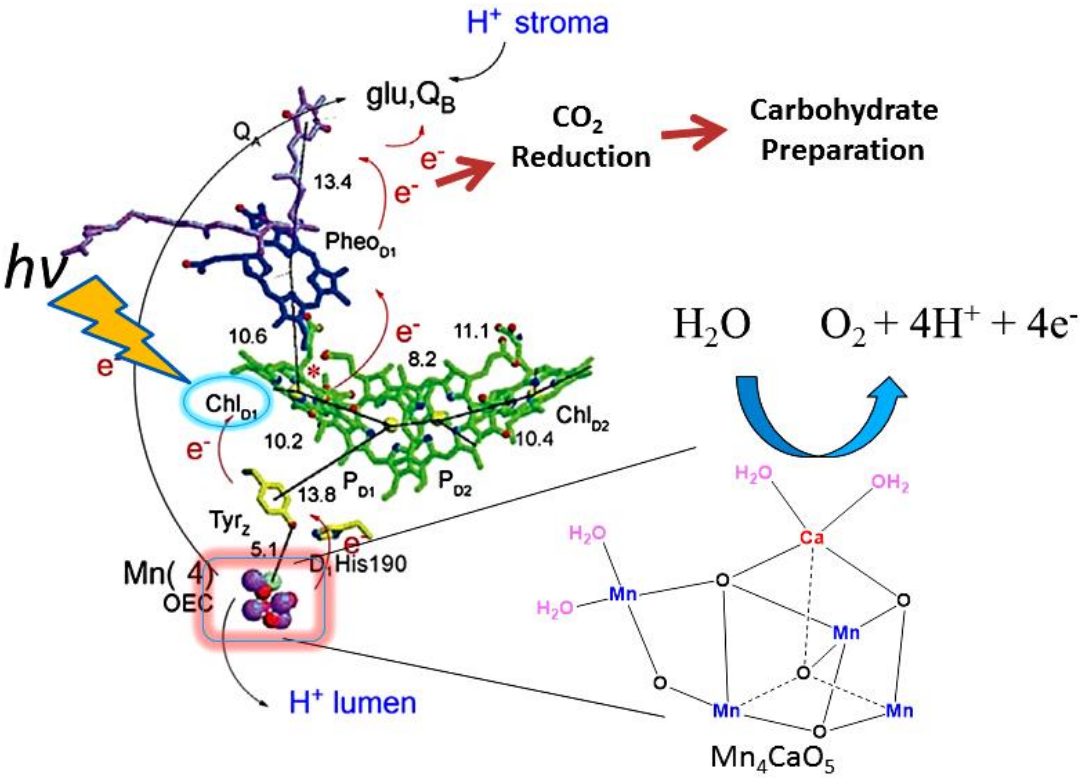

Figure 3.1: Natural O_2 evolution at Mn-OEC in photosystem II[8] (adapted with permission).

Seminal developments have taken place in the field of WO catalysis especially with regard to the discovery of a large body of molecular transition-metal complexes and active metal oxide NPs with relatively large turnover numbers (TONs ~10000).[7] Most of them involve metal complexes of noble metals (Ru[7,9-21], Ir[22-28]), polyoxometalates (POM)[10,29] and metal oxide NPs.[30-34] These homogeneous catalysts have been examined for both chemical oxidation (with a sacrificial oxidant like Ce^{IV}) as well as photochemical oxidation (in the presence of a photosensitizer and sacrificial oxidant like $Na_2S_2O_8$) to oxidize water. For ruthenium (Ru) catalyzed WO, high valent $Ru^{V}(O)$ complexes have been identified as the reactive intermediate responsible for WO.[19,35] However, it is extremely important to develop earth-abundant metal-based catalysts, such as iron (Fe) complexes for WO, since they are expected to be environmentally benign and cheap.[1,36,37] Chemical WO using iron complexes was first reported by Collins, Bernhard, and co-workers using fluorine-substituted Fe-TAML as a catalyst and Ce^{IV} as the oxidant.[38] Subsequently, Fillol and Costas *et al*. demonstrated that Fe complexes of tetradentate neutral organic ligands were able to catalyze WO at low pH with TON >350 and >1000 using Ce^{IV} and IO_4^- respectively.[39,40] They demonstrated that a high valent iron oxo species was involved in the formation of the O-O bond. Changes in the steric and electronic property of the liagnds have been made to tune the reactivity of iron complexes.[32,41,42] Meyer and co-workers have proposed the existence of a $Fe^{V}(O)$ species based on electrochemical kinetics (without any spectroscopic characterizations) in electro-catalytic WO that run with lower catalytic efficiency (TONs of 29 over 15 hours).[43] Another approach has been recently reported: that of photo-electrochemical WO, by anchoring molecular iron complexes to a solar responsive tungstate.[44] However, the ultimate goal is to develop first-row, transition metal-based systems that catalyze photochemical WO, as sunlight provides the largest renewable energy resource. For first-row transition metals, cobalt[36,45-47] and manganese[48-50] based molecular complexes, POMs and NPs have been shown to function as efficient catalysts for WO. In contrast, the use of Fe-complexes for photochemical WO is very limited. Very recently, Lau *et al*. have demonstrated light-driven WO catalyzed by a number of iron complexes and iron salts at pH 7-9 in borate buffer.[30] However, under the reaction conditions, the active species responsible for WO was not a high valent iron oxo complex but Fe_2O_3 NPs that

were formed upon decomposition of the iron complex. Hence, the use of simple iron salts like $Fe(ClO_4)_3$ showed similar catalytic activity, as they also form Fe_2O_3 NPs under reaction conditions. This represents a serious limitation for WO catalyst (WOC) design, since it does not allow researchers to understand fundamental design principles of metal ligand complexes that would make them highly active WOC. Further, understanding the reactive intermediate involved in WO is also critical to development of more efficient WOC. This would allow chemists to understand the electronic properties of the metal complex that can be used to design new WOC with improved activity.

As discussed in chapter II, our designed biuret-modified Fe-TAML represents a new member of the broad suite of catalysts Fe-TAML activators, which were invented by T. J. Collins in the mid-1990s.[51,52] This biuret-modified Fe-TAML showed improved stability (from pH 1-13) and reactivity towards azo dye degradation when mediated by H_2O_2 in comparison to the prototype Fe-TAMLs. We have also shown that this ligand framework stabilizes the reactive $Fe^V(O)$ in both CH_3CN[53] and CH_3CN-H_2O mixtures.[54a] Their high operational stability and ability to stabilize high valent iron oxo species prompted us to explore this biuret-modified Fe-TAML for chemical and photochemical WO. In this chapter, we report the chemical and photochemical WO by two biuret-modified Fe-TAML complexes with moderate TONs and yields. The molecularity of the complex remains intact during WO and no formation of iron oxide NP is observed.

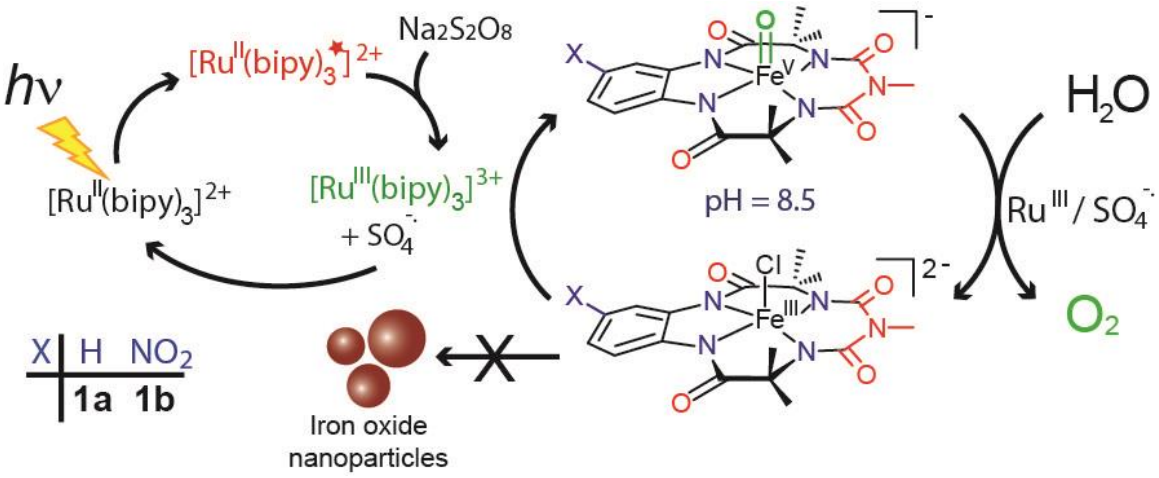

Scheme 3.1: Homogeneous photochemical water oxidation using biuret-modified Fe-TAML.[54b]

We also report for the first time, photochemical generation of a well-defined high valent $Fe^{V}(O)$ as one of the key intermediates and elucidate its role in WO (Scheme 3.1).[54b] Although similar studies showing photochemical formation of a high valent $Fe^{IV}(O)$ have been conducted by Fukuzumi, Nam[55], Costas[56] and co-workers, photochemical WO has not been explored in any of them. Identification of such $Fe^{V}(O)$ reactive intermediate helps us elucidate the exact mechanism of WO as well as provide insight for designing newer generation WOC based on earth-abundant elements.

3.2 Experimental section

3.2.1 *Physical Measurements*

All synthetic products were characterized by ^{1}H and ^{13}C NMR spectroscopy carried out on a Bruker (200 MHz) spectrometer at room temperature using the residual solvent signal as the internal standard. Chemical shifts (δ) are expressed in ppm and coupling constants (J) in Hertz. Infrared spectra were obtained on a Perkin-Elmer FT-IR spectrum GX instrument. UV-vis spectra were monitored using an Agilent 8453 diode array and a Perkin-Elmer-λ35 spectrophotometer using 1.00 cm quartz cell at a constant temperature of 25 ± 5 °C. High resolution mass spectrometry (HR-MS) was done in the negative ion mode of a Thermo Scientific Q-Exactive, using electron spray ionization source, Orbitrap as analyzer and connected with a C18 column (150 mm × 4.6 mm × 8 μm). Gas chromatography mass spectrometry (GC-MS) of the isotope labelled O_2 was recorded in an Agilent Series 7890B model chromatograph interfaced with an Agilent Series 5977A model mass spectrometer operating in electron impact ionization mode to collect the mass spectrometry data. The X-band EPR spectra were recorded in a Bruker EMX X-band spectrometer operating at a field modulation of 100 kHz, modulation amplitude of 5 G and microwave radiation power of 10 mW at 77 K.

The differential pressure measurements during water oxidation were recorded on a HTC make manometer with an operating range of 0.01−34.5 kPa and accuracy within 0.3%. The oxygen produced as a result of water oxidation was detected and quantified with a monitor gas line of nitrogen using an Agilent make GC with model no 7890A. Dissolved O_2 measurements in single turnover reactions were performed using a Clark type electrode (dissolved oxygen meter) from MicroSet (MS 0257), India working in the

range of 0 to 45 ppm with resolution of 0.01 ppm. Dynamic Light Scattering (DLS) analyses were run in Brookhaven 90 Plus instrument and Transmission Electron Microscopy (TEM) imaging was recorded in a FEI Tecnai TF-20 instrument.

Figure 3.2: Two port sensing approach for monitoring differential pressure increase in the reaction vial (left) with respect to the reference vial (right) by a manometer at 25 °C.

A typical photochemical WO set up has been shown in Figure 3.6 below. Custom made cooling apparatus with an array of six LEDs (λ_{max} = 440 nm, 3 W) used for photo oxidations: i) LEDs connected in series to a power supply. ii) Set up with a stainless steel jacket to maintain constant temperature of the vials. The distance between the LEDs and the reaction vials was adjusted to 0.9 ± 0.1 cm.[57] The apparatus allows also magnetic stirring of the mixtures. iii) Typical irradiation experiment in progress with two ports connected to the manometer.

3.2.1.1 *GC-MS analysis of head space gas sample using ^{18}O-enriched water*

A solution of 1.2 mL containing 7.4 µM **1a**, 0.83 mM $[Ru(bipy)_3]^{2+}$, 8.30 mM $S_2O_8^{2-}$ and 41% ^{18}O enriched water in 40 mM borate buffer pH 8.7 was completely

degassed with Helium for 20 min and then the photochemical reaction was initiated. The reaction was run for 10 min under vigorous stirring in order to homogenize the head space oxygen concentration. Then 10 µL of head space gas sample was injected into the GC-MS for analysis of all possible isotopes of evolved oxygen. Each reaction was repeated at least three times and the average relative abundance for each ion was taken (Figure 3.3, Table B1, Appendix II) for calculation of net oxygen evolved and % ratio of $^{32}O_2$: $^{34}O_2$: $^{36}O_2$.

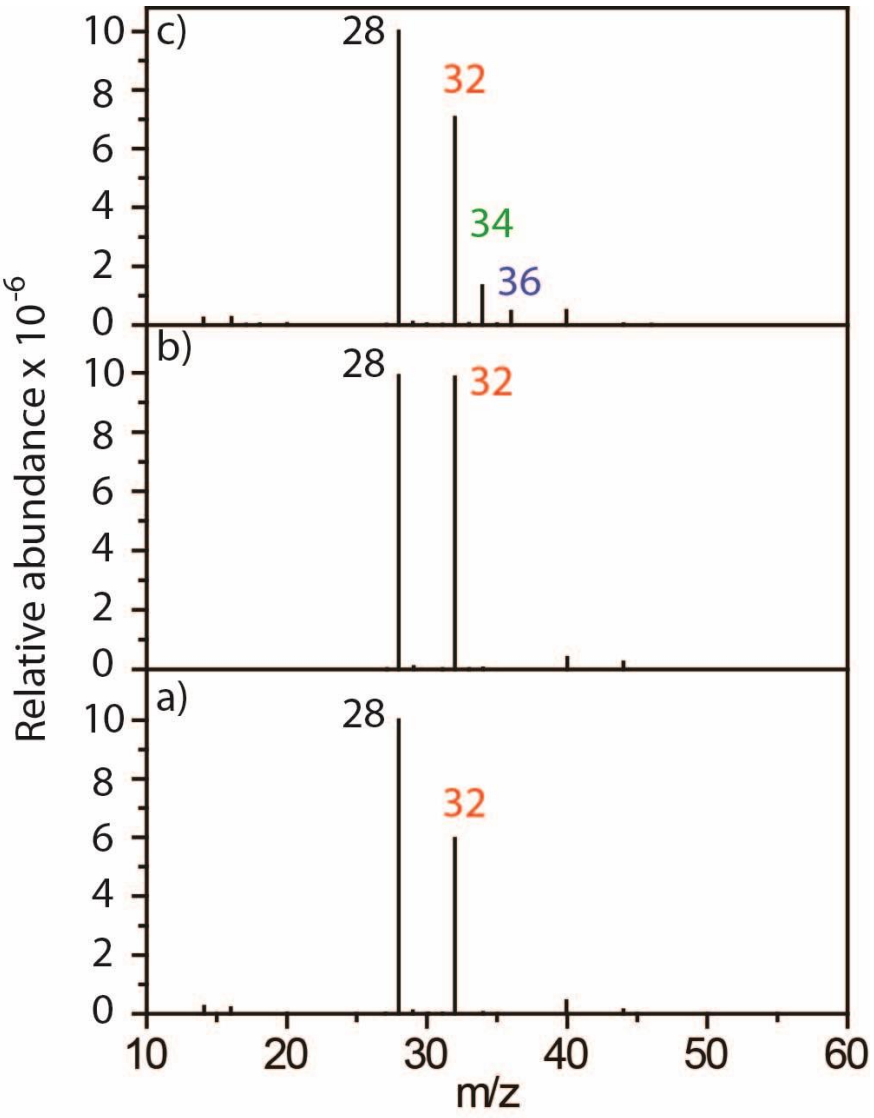

Figure 3.3: GC-MS spectra of evolved O_2 isotopic distribution pattern from a photochemical WO reaction; a) headspace sample for the photochemical reaction mixture (degassed with Helium) before irradiation for estimation of background O_2, b) head space sample after 10 min of photochemical reaction in 100% $H_2{}^{16}O$, and c) head space sample

after 10 min of photochemical reaction in 59% $H_2{}^{16}O$: 41% $H_2{}^{18}O$. The adventitious oxygen ($^{32}O_2$) was subtracted by using the background ratio of the $^{28}N_2$ and $^{32}O_2$ peaks ($^{28}N_2$: $^{32}O_2$ = 1.68). Conditions: 3 watt blue LED light source; 7.4 µM **1a**, 0.83 mM $[Ru(bpy)_3]^{2+}$, and 8.30 mM $Na_2S_2O_8$ in 40 mM borate buffer mixture at pH 8.7 at 30 °C; total reaction volume was 1 mL.

3.2.1.2 *Sample preparation for DLS and TEM studies*

Photochemical reaction mixture containing 7.4 µM **1a**, 0.83 mM $[Ru(bpy)_3]^{2+}$, and 8.30 mM $Na_2S_2O_8$ in 40 mM borate buffer at pH 8.7 at 30 °C was first filtered using a 0.22 µm filter paper from Millipore in dark. This sample was then divided into two parts where one sample was directly analyzed without irradiation (control) and the other was and irradiated continuously for 10 min and analyzed for any NP formation by DLS (Figure B1 and B2; Appendix II). Samples as were done for DLS were considered for TEM analyses too (Figure 3.4). Both the samples were diluted and 10 µL of the final stock solution was spotted on carbon coated 400 mesh copper grid, kept for drying in a desiccator for 20 hr and analyzed by transmission electron microscopy.

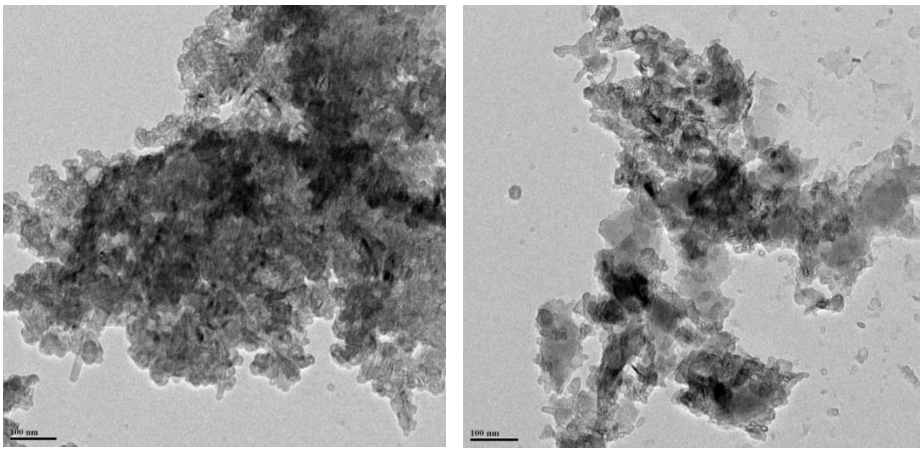

Figure 3.4: TEM images of a typical photochemical WO mixture before (left) and after (right) reaction. Reaction condition: 3 watt blue LED light source; 7.4 µM **1a**, 0.83 mM $[Ru(bpy)_3]^{2+}$, and 8.30 mM $Na_2S_2O_8$ in 40 mM borate buffer mixture (pH 8.7) at 30 °C. Samples were dropcasted upon a TEM grid, dried and then analyzed by TEM. The TEM images had shown no change in the sample before and after irradiation. The observed material in the TEM grid is probably a result of dried inorganic salts.

3.2.1.3 *Dissolved O_2 measurements in single turnover reactions using a Clark type electrode*

A Clark type electrode was used for recording the change in dissolved oxygen concentration during a single turn over reaction (Figure 3.5). The oxygen sensor was calibrated before each experiment following a two point calibration 0% (zero solution) and 100% (air). The membrane in the electrode which selectively allows O_2 to pass through was replaced for each new measurement in order to avoid any error associated with its functioning in a mixed solvent (50% CH_3CN-H_2O). The electrode with the reaction set up has been given in the Figure 3.5. For evaluation of $Fe^V(O)$ mediated O_2 formation, a solution containing **1a** (211 µM) in 50% CH_3CN-H_2O mixture (8 mL) was taken in a sealed vial containing a Clark type electrode. The solution of **1a** was thoroughly purged with N_2 such that the O_2 concentration was zero as was recorded by the Clark electrode. Subsequently 3.2 µL of 0.6 M NaOCl was added in to the solution containing **1a** to make the well-defined $Fe^V(O)$ (by UV-vis). Two separate experiments were performed to elucidate the role of $Fe^V(O)$ in WO (i) Well-defined $Fe^V(O)$ was left to for decay over a period of 10 min, and (ii) 4 equivalent of $[Ru(bipy)_3]^{3+}$ (an electron transfer oxidant that has been freeze-pump-thawed at least four times to exclude any dissolved O_2 in it before addition) was added immediately after formation of a $Fe^V(O)$. The change in dissolved O_2 was monitored in both these experiments.

Figure 3.5: Experimental set-up (left) for the determination of dissolved oxygen produced as a result of reaction of $[Ru(bipy)_3]^{3+}$ (4 eq; 0.84 mM) with a well-defined $Fe^V(O)$ (right).

The latter experiment showed approximately formation of 6.5 μM of O_2 while the former did not reveal any O_2 formation. Similarly control experiments that included $[Ru(bipy)_3]^{3+}$ addition into degassed solution of (i) **1a** (211 μM), (ii) the well characterized μ-Oxo-Fe^{IV}dimer (formed from **1a** and 0.55 equivalent of NaOCl), (iii) NaOCl (231 μM) and (iv) 50% CH_3CN-H_2O mixture were performed to determine if formation of O_2 took place.

3.2.2 *Materials*

Reagents for synthesis of the biuret-modified TAML were purchased from Sigma-Aldrich. CAN, tris (2,2′-bipyridyl) dichlororuthenium(II)hexahydrate 99.95% ($[Ru(bipy)_3]^{2+}$), sodium persulfate ($Na_2S_2O_8$) and 98% ^{18}O enriched water were also obtained from Sigma-Aldrich and used without further purification unless otherwise mentioned. Deionized water was used to make all the stock solutions for the kinetic and spectrophotometric runs.

3.2.3 *Water oxidation*

3.2.3.1 *Chemical*

A typical chemical WO was achieved by mixing a solution of **1a** or **1b** (100 μL of a 1.37 mM stock solution in water) with a solution of Ceric Ammonium Nitrate (CAN) (500 μL of a 365 mM stock solution in water) at pH 1 in a sealed vial under stirring at 25 °C. The total reaction volume was kept constant at 600 μL. For kinetic experiments, the catalyst concentration was varied from 0.23 to 0.06 mM. The kinetics of WO was studied by measuring the pressure generated as a result of oxygen evolution with a manometer (Figure 3.7). The differential head space pressure in the manometer was correlated to the amount of oxygen quantified by gas chromatography (GC). The manometer consisted of two sensing ports: one was connected to the reaction vial having both CAN and catalyst and the other one to a reference vial having only CAN solution. As the reaction progressed in the reaction vial, the pressure difference between the reaction and the reference vial increased, which was recorded by the manometer with respect to time. After a certain period of time, the pressure difference in the manometer reached saturation, and hence the oxygen evolution. The evolved oxygen was detected and

quantified by GC (Figure B11-13, Table B4; Appendix II). Each set of experiments was repeated at least three times to minimize the error associated with it.

3.2.3.2 *Photochemical*

In a typical catalytic photochemical WO reaction, 7.4 μM **1a** or **1b** together with 0.83 mM $[Ru(bipy)_3]^{2+}$ and 8.30 mM $Na_2S_2O_8$ in pH 8.7 borate buffer (40 mM) were added such that the total volume of the reaction mixture and head space volume were 4.83 mL and 3.42 mL respectively. The reaction was initiated by irradiating this mixture with the help of a 3 watt blue LED (λ_{max} = 440 nm) at 30 °C (Figure 3.6). Each reaction was run for five minutes and the detailed kinetics, identification and quantification (Figure B3-10, and Table B4; Appendix II) of the gaseous products were performed by the same procedure as was done in the case of chemical WO using CAN. Single turnover photochemical WO reactions were carried out at 30 °C in 50% CH_3CN-borate buffer (10 mM; pH 8.7) having 60 μM each of **1a** or **1b**, $[Ru(bipy)_3]^{2+}$ and $Na_2S_2O_8$.

Figure 3.6: Experimental setup for the photochemical WO. Extreme left picture: six blue LEDs in series connection as light source, a metallic water circulator having six holes to hold the reaction vials exactly over the lights; middle picture: blue light emission after switching on the LEDs; extreme right picture: the whole assembly while running photochemical WO under light irradiation and connected to a manometer for pressure measurements.

3.2.3.3 *Oxygen identification and quantification by GC*

After five minutes of catalytic photochemical WO, the excess pressure generated in the reaction vial was released by a Eudiometer[27] setup that displaces approximately 130

μL of water. Similar protocol was also followed for CAN mediated WO. 100 μL of headspace specimen gas was taken by a gas tight syringe from the reaction vial and injected in to the GC. The head space volume was calculated after one hour of reaction (assuming completion of reaction) by injecting extra water in to the sealed reaction vial which displaces same amount of water again by the Eudiometer. The total volume (volume displaced due to over pressure as a result of oxygen evolution + headspace volume) was multiplied by the GC quantified oxygen to get the total oxygen evolved in the reaction.[27] The GC was calibrated by using air as a standard (21% oxygen) in a Tedlar bag from Sigma-Aldrich, and this calibration curve was used to quantify the amount of oxygen that evolved from the reaction mixtures. The pressure difference in the manometer for this time period was correlated to the amount of oxygen quantified by GC. Similarly, the quantities of oxygen that evolved for different concentrations of catalyst were calculated and plotted against time.

3.3 Results and discussions

3.3.1 *Water oxidation using biuret-modified Fe-TAML*

The high stability of biuret-modified Fe-TAML at extreme pH values, ionic strength and their ability to stabilize high valent iron species in water encouraged us to study their efficacy in both chemical and photochemical WO. For chemical WO, Ce^{IV} was chosen as the sacrificial oxidant while in photochemical WO the photochemical sensitizer $[Ru(bipy)_3]Cl_2$ and sacrificial oxidant $Na_2S_2O_8$ were used.

3.3.2 *Water oxidation using CAN at pH 1*

CAN is known to be a very strong oxidant ($E_{1/2}$ of $Ce^{IV/III}$ is 1.61 V vs. SHE)[58] and is capable of oxidizing a variety of redox-active metal centers in acidic media. Since chemical oxidation by CAN operates at pH 1, it is imperative that the catalyst be stable at such low pH. It is well known that Fe-TAMLs are in general unstable at acidic pH because they undergo acid-catalyzed demetallation.[59,60] Substitution of $–CF_2$ to the prototypical $–CMe_2$ in the tail part of Fe-TAML has been shown to increase the acid stability several fold.[59,61] Hence, the WO catalysts reported by Collins and Bernarhd have focused on Fe-TAMLs that have a $–CF_2$ group in the tail position.[38] In the preceding

chapter, we have shown that the introduction of the –NMe in the tail position (biuret-modified Fe-TAML catalyst **1a**) significantly increases its acid stability ($t_{1/2}$ at pH 1 = 2222 sec^{-1}), however they are still susceptible to acid induced demetallation at low pH.[62] To improve the robustness of biuret-modified Fe-TAMLs under acidic media, an electron withdrawing $–NO_2$ group was introduced in the head aromatic ring (**1b**). Kinetic evaluation of the acid stability of **1b** revealed that the third order dependency (k_3*) was improved by 3 orders of magnitude in comparison to **1a**. This increased stability towards acid catalyzed demetallation of biuret-modified Fe-TAMLs encouraged us to study their efficacy towards WO using Ce^{IV}.

Addition of CAN (305 mM) to a solution of **1a** or **1b** (0.23 mM) at pH 1 leads to the formation of bubbles in the reaction mixture, which indicates the formation of a gaseous product, identified as dioxygen by GC-MS (Figure 3.3). Subsequently, a manometer was used to measure the pressure generated as a result of oxygen evolution to study the oxygen produced over the course of the reaction. The differential head space pressure in the manometer was correlated to the amount of oxygen evolved quantitatively by GC (Figure 3.7). The plot of initial rates of oxygen evolution for a time period of 50 sec as a function of catalyst concentration showed a linear dependency on the catalyst concentration (Figure 3.7b).

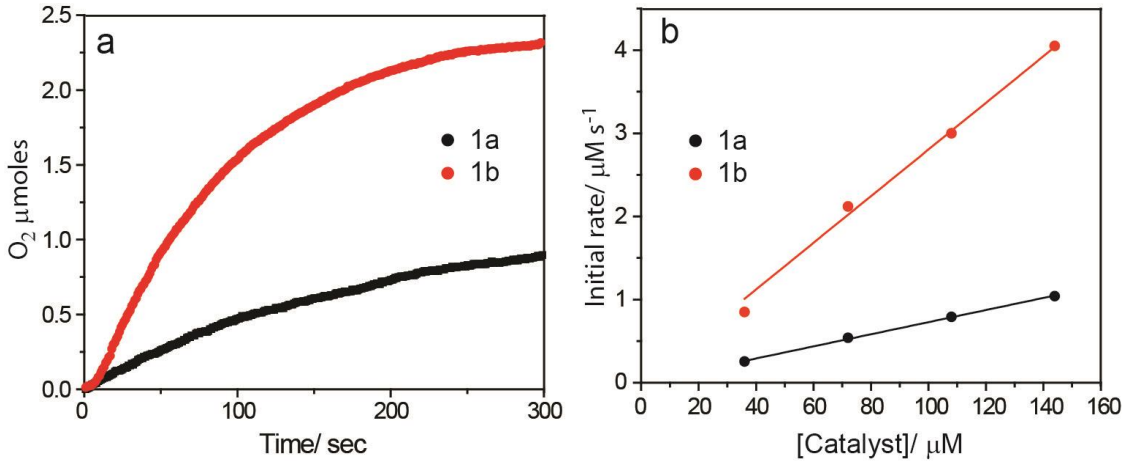

Figure 3.7: a) Kinetics of O_2 formation as a result of chemical WO by **1a** and **1b** in the presence of CAN. Conditions: 0.23 mM **1a** or **1b** and 304 mM CAN at pH 1 and 25 °C; total reaction volume 600 µL; b) Initial rate of O_2 evolution vs. concentration of **1a** and **1b**.

From this plot, the first order rate constant for WO using **1a** and **1b** was determined to be 0.007 and 0.03 sec^{-1} respectively. The TON over a period of 300 sec were calculated to be (10 ± 1) and (17 ± 1) for **1a** and **1b** respectively and TOF 0.03 and 0.06 sec^{-1} (Table B4; Appendix II). The TOF values reflect considerably slower reaction rates with respect to the fluorinated Fe-TAML (TOF = 1.30 sec^{-1}, TON = 16)[38], however the overall O_2 yield based on the TONs are very comparable. Also, careful analysis of the evolved gas by GC did not show formation of CO_2 which points to the robust nature of TAML ligand system in oxidizing environments.[51,63]

3.3.3 *Photochemical water oxidation using biuret-modified Fe-TAML*

3.3.3.1 *O_2 yield and turnover number (TON)*

In a typical catalytic photochemical WO, oxygen was generated by irradiating a mixture of 7.4 µM **1a** or **1b**, 0.83 mM $[Ru(bipy)_3]^{2+}$ and 8.30 mM $Na_2S_2O_8$ with the use of a 3 watt blue LED (λ_{max} = 440 nm) for ten minutes in pH 8.7 borate buffer (40 mM). The total amount of O_2 evolved was determined as has been described for chemical WO.

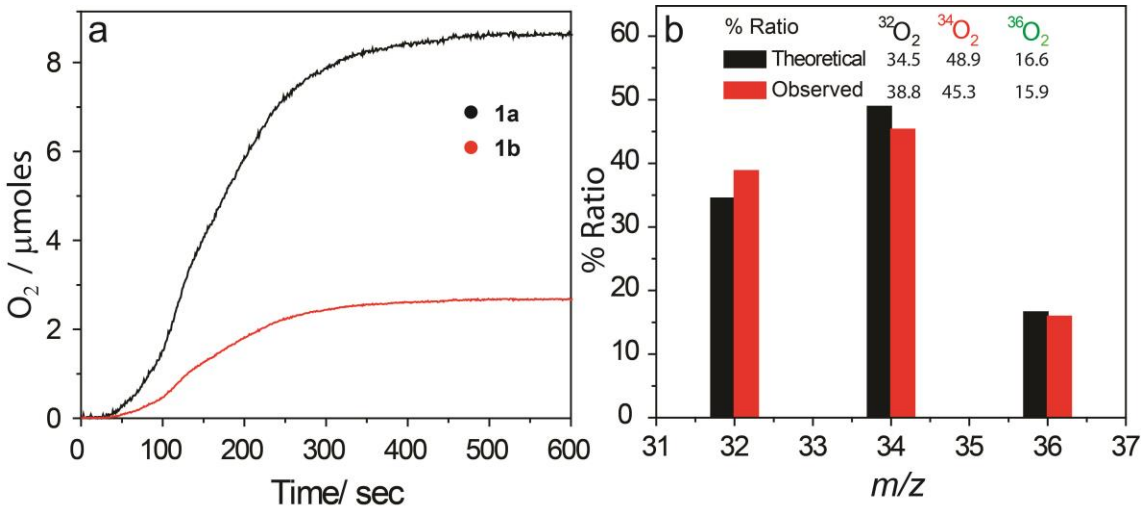

Figure 3.8: a) Plot of O_2 formation as a result of photochemical WO by **1a** (black curve) and **1b** (red curve); b) Comparison for the ratio of ^{32}O, ^{34}O and ^{36}O labelled molecular oxygen evolved (theoretical and observed) during photochemical WO oxidation using 41% $H_2{}^{18}O$ in $H_2{}^{16}O$; Conditions: 3 watt blue LED light source; 7.4 µM **1a** or **1b**, 0.83 mM $[Ru(bpy)_3]^{2+}$, and 8.30 mM $Na_2S_2O_8$ in 40 mM borate buffer pH 8.7 at 30 °C; total reaction volume 4.8 mL.

It was determined that for catalyst **1a** and **1b** the amount of O_2 generated was 7.87 and 2.07 μmoles respectively over a period of 300 sec (Figure 3.8a, Table B3; Appendix II). To prove that the oxygen evolved in the above reaction was indeed promoted by catalyst **1a** or **1b**, the following control experiments were performed. Photochemical WO reactions under standard conditions were performed in the absence of (i) photosensitizer, (ii) catalyst **1a** or **1b** and (iii) $Na_2S_2O_8$. The evolution of O_2 was not observed in any of these control experiments. This confirms that all the three components, i.e. catalyst **1a** or **1b**, photosensitizer and $Na_2S_2O_8$, are indeed involved in the catalytic WO process. To prove that the evolved dioxygen was only due to oxidation of water, and not from other sources such as $Na_2S_2O_8$ decomposition, photochemical WO reactions were performed using 41% ^{18}O enriched water under standard operating conditions, as described above.

Table 3.1: Chemical yields of O_2 evolution, turnover number (TON) and turnover frequency (TOF) for homogeneous photochemical WO by **1a**, **1b** and some of the reported first row transition metal complexes.

Catalyst	$[Na_2S_2O_8]$ (mM)	$[Ru(bipy)_3]^{2+}$ (mM)	$[O_2]$ yield (μmole)[a]	TON[b]	TOF (sec^{-1})[b]	Chemical yield[c]
1a (7.4 μM)	8.30	0.83	7.87	220 ± 10	0.670	44%
1b (7.4 μM)	8.30	0.83	2.07	60 ± 4	0.210	13%
[d]Mn-L[48] (84 μM)	20.0	-	0.40	4.20	~ 7.9×10^{-4}	~ 4%
Co-POM[45] (5 μM)	5.00	1.00	2.50	224	0.250	45%
Co-Slp[46] (50 μM)	5.00	1.00	8.20	17	0.002	-

[a]Total O_2 yield for a time period of 600 sec; [b]TON and TOF for 300 sec; [c]Overall chemical yield for a time period of 600 sec with respect to $S_2O_8^{2-}$ consumption; [d]L = 2,6-bis(4-carboxy-1*H*-benzimidazol-2-yl)-4-methylphenol.

The percentage isotopic ratio distribution of the evolved oxygen for $^{32}O_2$, $^{34}O_2$ and $^{36}O_2$ was 38.8: 45.3: 15.9 (Figure 3.8b), which nearly matches the theoretical ratio of 34.5: 48.9: 16.6 (Figure 3.3, Table B1; Appendix II). This confirmed that O-O bond formation occurred by the combination of two water molecules during WO process. **1a** was shown to have better overall efficiency (TON = 220 ± 10) and O_2 yield (~44%) than **1b** (TON = 60 ± 4, yield ~8.5%), (Table 3.1), which may be correlated to their differential reactivity towards an electron transfer oxidant (Figure 3.9). The chemical yields (= $[O_2]/2[S_2O_8^{2-}]$) were calculated with respect to the consumption of $Na_2S_2O_8$.[45] The evolution of O_2 during photochemical WO reaction using **1a** or **1b** displayed saturation at ~360 sec and the pH of the resultant solution dropped from 8.7 to 7.0. As 56% of $Na_2S_2O_8$ was still expected to be remaining in the reaction mixture at the end of 360 sec, the saturation observed for O_2 evolution was likely due to proton accumulation in the reaction mixture, which is well known for most PCET processes.[64] Therefore, we wanted to explore if increasing the pH back to 8.7 would restart the photochemical WO, and attempted to restart the **1a** catalyzed photochemical WO after 360 sec by increasing the pH of the mixture from 7.0 to 9.0.

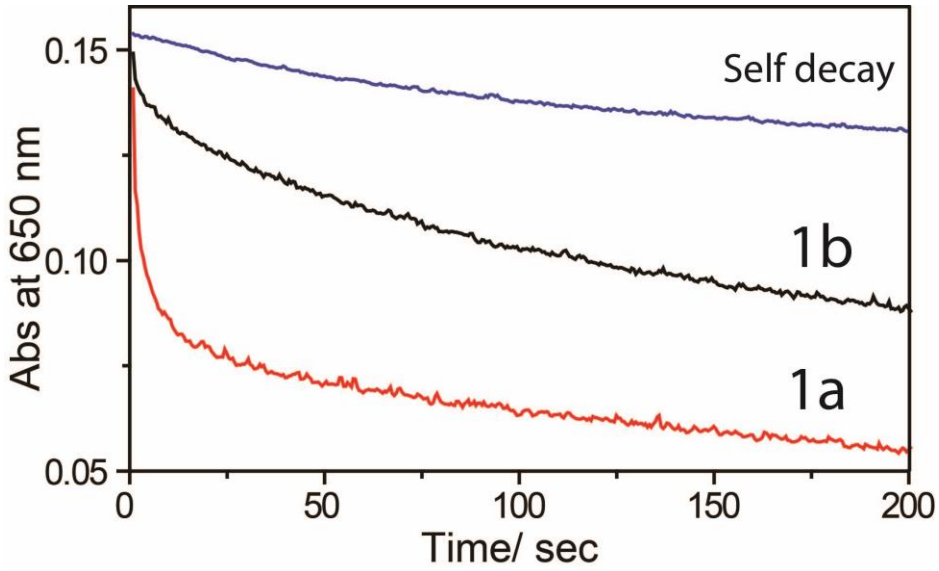

Figure 3.9: Decay profile of 350 µM $[Ru(bipy)_3]^{3+}$ by self (blue), **1b** (10 µM, black) and **1a** (10 µM, red). This plot suggests that the rate of electron transfer process in **1a** is much faster than**1b** which may one of the reasons why **1a** exhibit better overall efficiency in photochemical WO than **1b**.

Addition of 200 µL of 6 mM aqueous NaOH resulted in resumption of O_2 generation, albeit with lower reaction rates and O_2 formation (~ 20% of first set) (Figure 3.10). The lower efficiency is likely a result of the reduced amount of $Na_2S_2O_8$ that remained after completion of the first run (i.e. up to 360 sec). This experiment indicates that both the catalyst and $Na_2S_2O_8$ are still active even after saturation was observed.

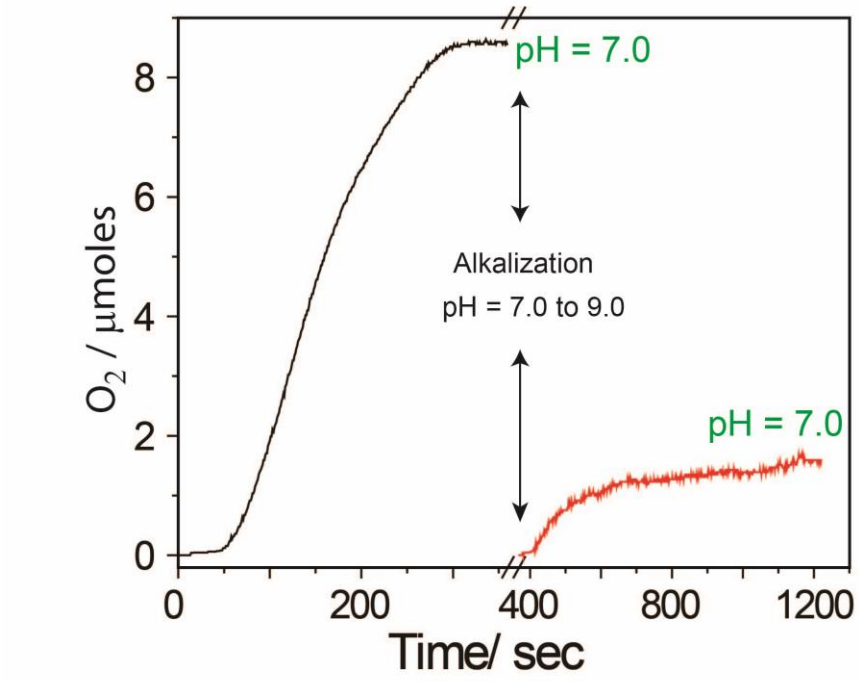

Figure 3.10: Reactivation of photochemical WO after observation of O_2 saturation (360 sec) by addition of aqueous NaOH solution (6 mM, 200 µL), Conditions: 3 watt blue LED light source; 7.4 µM **1a**, 0.83 mM $[Ru(bpy)_3]^{2+}$, and 8.30 mM $Na_2S_2O_8$ in 40mM borate buffer (pH 8.7) at 30 °C; total reaction volume was 3.6 mL.

3.3.3.2 *Biuret-modified Fe-TAML vs. Fe_2O_3 nanoparticle as active catalysts for WO*

In a recent paper, Lau *et al*. demonstrated Fe_2O_3 NPs to be the active catalyst for photochemical WO mediated by iron complexes at basic pH. Studies performed on a series of iron complexes show definitive evidence for ligand dissociation before or after oxidation of the iron complex to generate Fe_2O_3 NPs.[30] We therefore explored the operational stability of **1a** and **1b** in the presence and absence of blue visible light. It is very well established that unlike most other Fe-complexes[30,32] that catalyze WO, Fe-

TAMLs display remarkable stability in neutral to basic pH.[65,66] The UV-vis spectral scans of biuret-modified Fe-TAML (**1a**) solution in 40 mM borate buffer (pH 8.7) and 8.30 mM $Na_2S_2O_8$ showed no change in the spectrum over one hour (Figure 3.11a). To evaluate the photochemical stability of **1a**, a solution of 60 µM **1a** and 60 µM $Na_2S_2O_8$ in 40 mM borate buffer pH 8.7 was irradiated for sixteen minutes and the UV-vis spectrum was recorded. The difference in the absorbance value at the λ_{max} (356 nm/450 nm) before and after irradiation was less than 4%. This indicates that the complex is stable under the reaction conditions (Figure 3.11b).

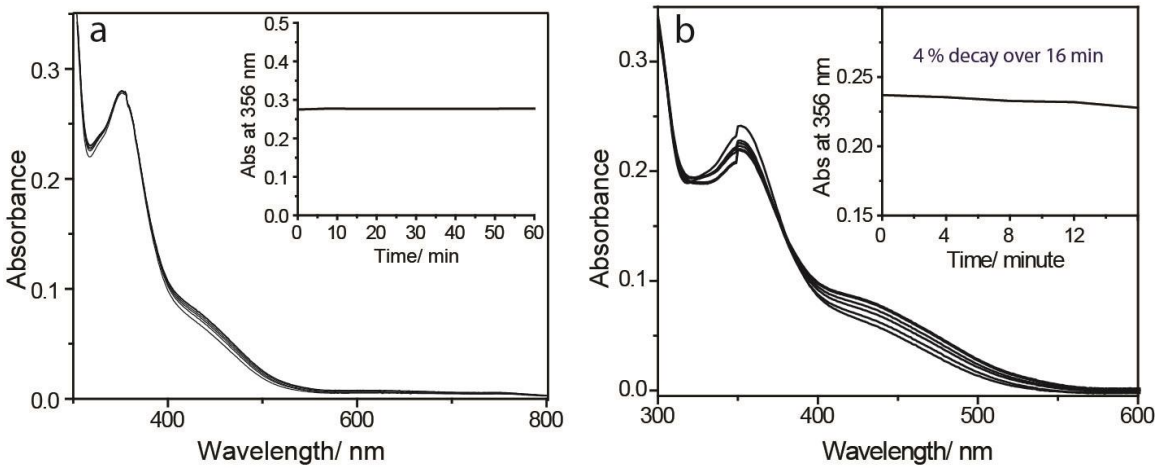

Figure 3.11: a) UV-vis spectral scan of 68 µM **1a** in 40 mM borate buffer pH 8.7 and 8.30 mM $S_2O_8^{2-}$ without irradiation, Inset: OD change at 356 nm as a function of time; b) UV-vis spectral scan of 60 µM **1a** in 40 mM borate buffer pH 8.7 and 8.30 mM $S_2O_8^{2-}$ under continuous irradiation at 440 nm for 16 min, Inset: OD change at 356 nm as a function of time.

To probe further, a photochemical WO reaction was initiated with **1a** and the reaction mixture was analyzed by HR-MS after completion of the reaction (10 minutes). HR-MS spectrum showed the characteristic peak at *m/*z = 413.08 for the anion of **1a**, indicating that the complex **1a** was still present after the completion of the reaction (Figure 3.12). In another experiment, O_2 evolution was monitored as a function of increasing concentrations of **1a**.

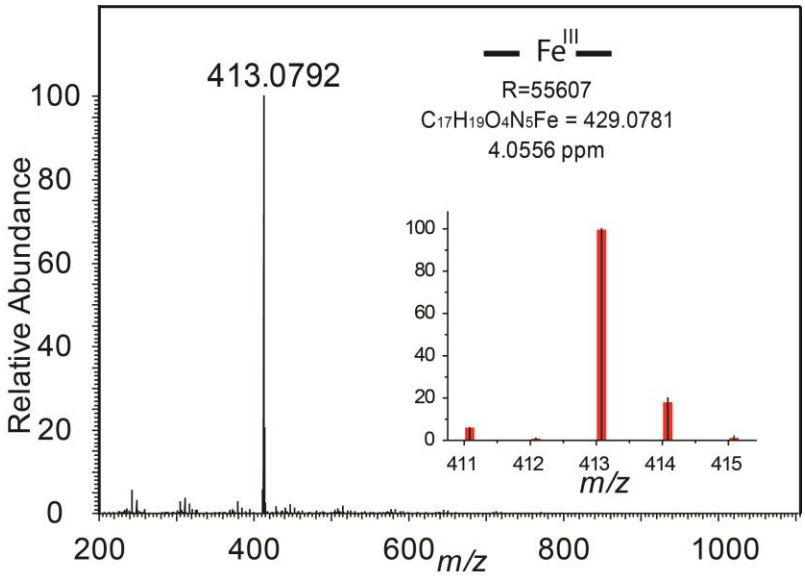

Figure 3.12: HR-MS of a reaction mixture after 10 min of catalytic photochemical WO using **1a** in 40 mM buffer. Conditions: 3 watt blue LED light source; 7.4 µM **1a**, 0.83 mM $[Ru(bpy)_3]^{2+}$, and 8.30 mM $Na_2S_2O_8$ in 40 mM borate buffer mixture at pH 8.7 at 30 °C; total reaction volume was 1 mL.

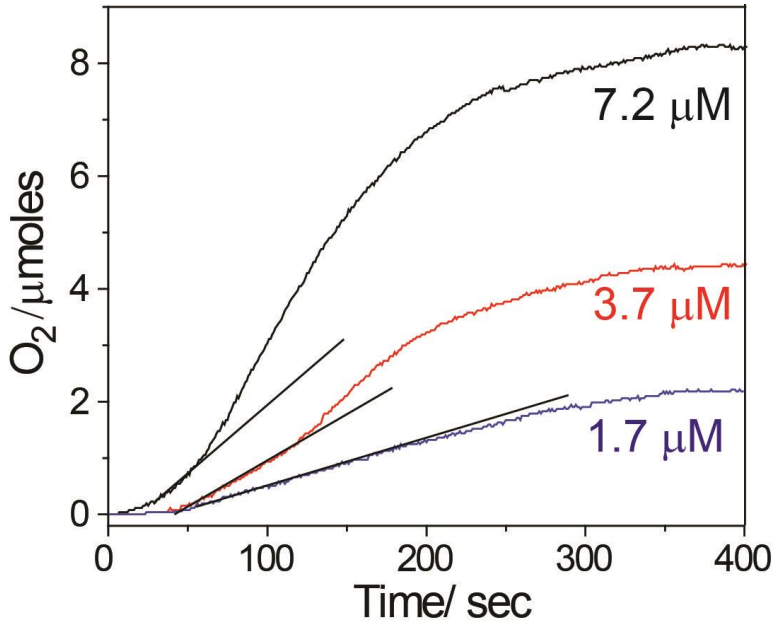

Figure 3.13: Kinetics of O_2 evolution showing increase of overall rate with increasing **1a** concentration; Conditions: 3 watt blue LED light source; **1a**, 0.83 mM $[Ru(bpy)_3]^{2+}$, and 8.30 mM $Na_2S_2O_8$ in 40 mM borate buffer (pH 8.7) at 30 °C; total reaction volume was 3.6 mL. The straight lines were drawn in correlation with initial rates there by neglecting the prior induction period.

The total amount of O_2 evolved, as well as the initial rates of O_2 production, increased with increase in amount of added **1a** (Figure 3.13 and 3.14). This is in contrast to water oxidation using Fe_2O_3 NPs, in which TONs decrease with increasing concentration of Fe_2O_3 NPs[30] (Figure 3.14). Finally, the reaction mixture was analyzed by both dynamic light scattering (DLS) (Figure B1 and B2; Appendix II) and transmission electron microscopy (TEM) (Figure 3.4). No evidence of iron oxide NPs was observed in both these studies. All of the above evidence indicates that the active intermediate was based on the biuret-modified Fe-TAML molecule rather than bare iron oxide NPs.

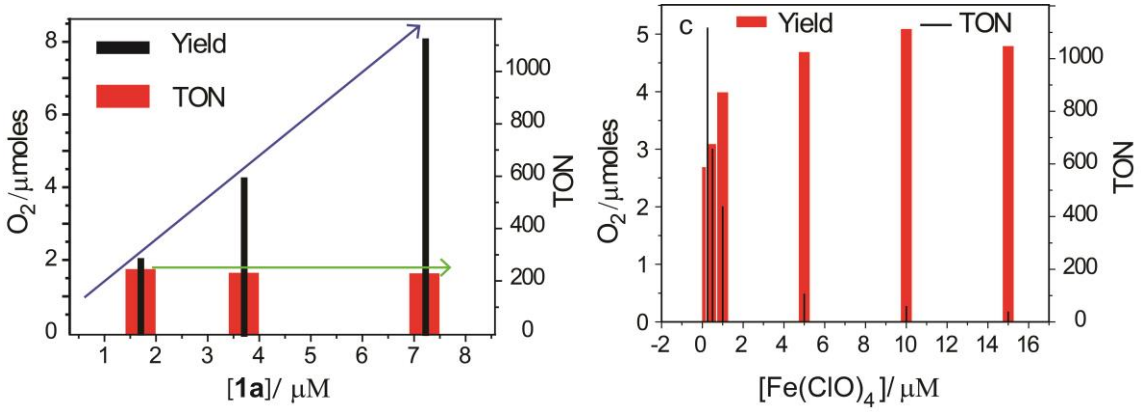

Figure 3.14: a) Plot of O_2 yield and TON vs. **1a** concentration in a photochemical WO reaction; Conditions: 3 watt blue LED light source; **1a**, 0.83 mM $[Ru(bpy)_3]^{2+}$, and 8.30 mM $Na_2S_2O_8$ in 40mM borate buffer (pH 8.7) at 30 °C; total reaction volume was 4.8 mL; b) Reported data showing plot of O_2 yield and TON vs. $[Fe(ClO_4)_3]$ concentration.[30]

Note: These data shows that in **1a** mediated photochemical WO, O_2 yield increases with **1a** concentration keeping TON constant, whereas in the case of $[Fe(ClO_4)_3]$ mediated photochemical WO, with increasing concentration of $[Fe(ClO_4)_3]$ O_2 yield remains thus reducing the TON. This may have arisen because of various particle size distribution of Fe_2O_3 NPs at higher and lower $[Fe(ClO_4)_3]$ concentrations leading to variation in number of catalytically active sites. Bigger the particle size lower would be the number of surface active centers. Whereas in **1a** mediated photochemical WO, **1a** remains in the molecular form and all of the iron sites are active. The TON remains constant with increasing **1a** concentration indicates zero or minimal catalyst deactivation during WO.

3.3.3.3 *Evidence of $Fe^{V}(O)$ species as intermediate in photochemical WO*

Although chemical WO by iron complexes have been shown to proceed through a $Fe^{IV}(O)$ intermediate,[38-40] very little is known about the oxidation states and nuclearity of reactive intermediates involved in photochemical WO by Fe complexes. We hypothesized that the active intermediate for WO in our case might also be a high valent iron oxo intermediate, as has been recently proposed for Fe-TAML catalysed chemical WO based on theoretical calculations.[67,68] Very recently, we have demonstrated that the $Fe^{V}(O)$ intermediate species can be formed with **1a** in CH_3CN-H_2O (v/v) mixture (10% to 90% H_2O).[54a] The stability of this $Fe^{V}(O)$ species decreases with increasing water content and is extremely short-lived in 95% water. This suggested that characterization of such a $Fe^{V}(O)$ intermediate would be very difficult in 100% H_2O. Additionally, under catalytic conditions used for photocatalytic WO reaction with **1a**, the fast reaction rates together with the presence of excess $[Ru(bipy)_3]^{2+}$ would make it extremely difficult to observe the formation of $Fe^{V}(O)$ using UV-vis spectroscopy.

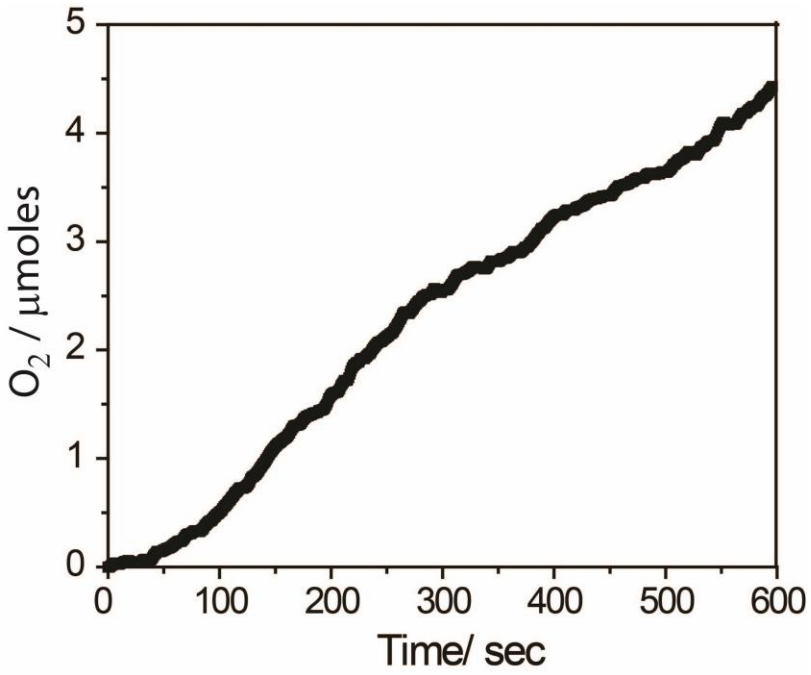

Figure 3.15: Kinetics of O_2 formation as a result of photochemical WO by **1a**, Conditions: 3 watt blue LED light source; 7.4 µM **1a**, 0.83 mM $[Ru(bpy)_3]^{2+}$, and 8.30 mM $Na_2S_2O_8$ in 50% CH_3CN-buffer mixture at pH 8.7 at 30 °C; total reaction volume was 4.8 mL.

Table 3.2: Comparative study of O_2 evolution in photochemical WO by **1a**, **1b** and $Fe(ClO_4)_3$

Catalyst (μM)	Medium	$[O_2]$ yield (μmole)[a]	TON[b]	TOF (sec^{-1})[b]	Chemical yield[c]
1a (7.4)	40 mM buffer	7.87	220 ±10	0.67 ± 0.03	44.0%
1b (7.4)	40 mM buffer	2.07	60 ± 4	0.21 ± 0.01	13.4%
[d]$Fe(ClO_4)_3$ (7.4)	40 mM buffer	4.27	120	0.40	23.9%
1a (7.4)	50% CH_3CN: buffer	4.58	128	0.20	25.6%

[a]Total O_2 yield for a time period of 300 sec; [b]TON and TOF for 300 sec; [c]Overall chemical yield for a time period of 600 sec with respect to $S_2O_8^{2-}$ consumption; [d]Photochemical WO by $Fe(ClO_4)_3$ under our operating conditions. Conditions: 3 watt blue LED light source; 7.4 μM **1a**, 0.83 mM $[Ru(bpy)_3]^{2+}$, and 8.30 mM $Na_2S_2O_8$ in 50% CH_3CN-buffer mixture at pH 8.7 at 30 °C; total reaction volume was 4.8 mL.

Hence, we attempted photochemical WO under single turnover conditions using one equivalent each of catalyst, $Na_2S_2O_8$ and $[Ru(bipy)_3]^{2+}$ in a 50% CH_3CN-buffer mixture. This was expected to reduce the reaction rates, and thus provide us an opportunity to identify and characterize reactive intermediates using spectroscopic techniques. Since such experiments would require the use of mixed solvents, we first carried out the photochemical WO in CH_3CN-buffer to ascertain if O_2 evolution occurred in presence of such mixed solvent. Photochemical WO in 50% CH_3CN-buffer using 7.4 μM **1a**, 0.83 mM $[Ru(bipy)_3]^{2+}$ and 8.30 mM $Na_2S_2O_8$ showed considerable amount of oxygen evolution with rates considerably slower than that in 100% buffer (Figure 3.15, Table 3.2). This is expected, because the reactivity of $Fe^{V}(O)$ is reduced as the CH_3CN content increases. The identification of high valent iron oxo intermediate was thus attempted in CH_3CN-buffer mixture solution using a variety of techniques including HR-MS, UV-vis and EPR. Photochemical WO was performed using equimolar amounts of **1a** or **1b**, $[Ru(bipy)_3]^{2+}$ and $Na_2S_2O_8$ (60 μM each) in 50% CH_3CN-buffer and the reaction mixture was analyzed using HR-MS. After five minutes of continuous irradiation, each

reaction was diluted twenty times and analysis of the spectrum obtained by HR-MS revealed two peaks: one for the unreacted precursor Fe^{III} complex (*m/z* = 413.08 for **1a** and 458.06 for **1b**) and the other for a $Fe^{V}(O)$ complex within the instrumental error limit (*m/z* = 429.07 for **1a** and 474.06 for **1b**) (Figure 3.16 and 3.17). Similarly in the presence of 15% $H_2{}^{18}O$, the corresponding $Fe^{V}(O^{18})$ was observed with *m/z* value of 431.08 for **1a** which again confirmed the presence of the $Fe^{V}(O)$ intermediate (Figure 3.18).

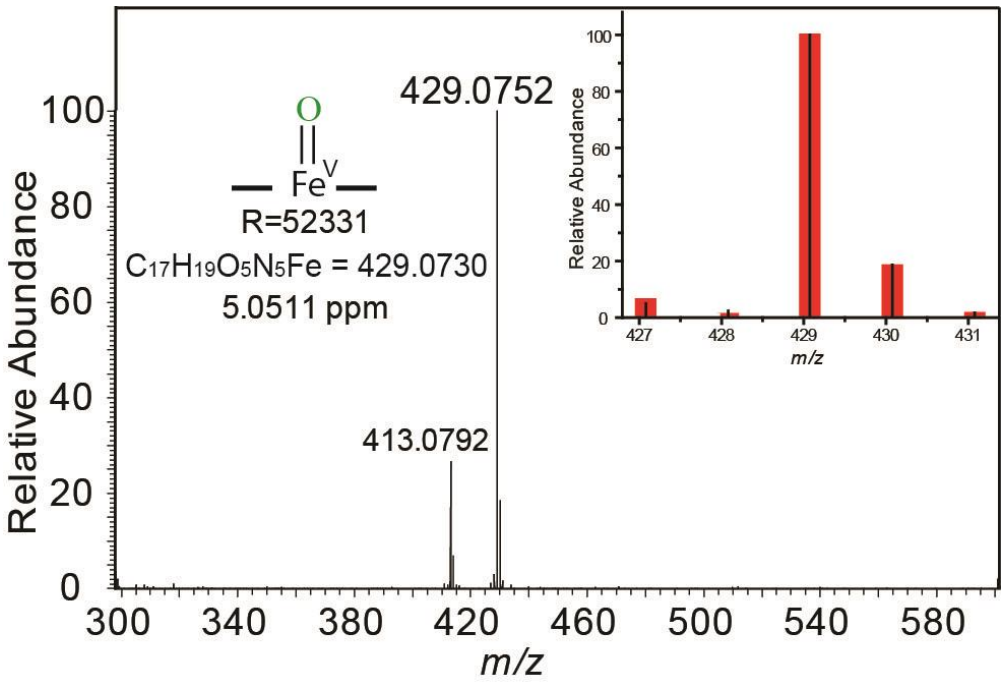

Figure 3.16: HR-MS spectra of $Fe^{V}(O)$ formed photochemically from **1a** (60 µM) in single turnover experiments using 60 µM each of $[Ru(bipy)_3]^{2+}$ and $S_2O_8{}^{2-}$ in 50% CH_3CN-buffer mixture, Inset shows comparison of simulated (red bars) and observed (black lines) isotopic distribution pattern for ion of interest.

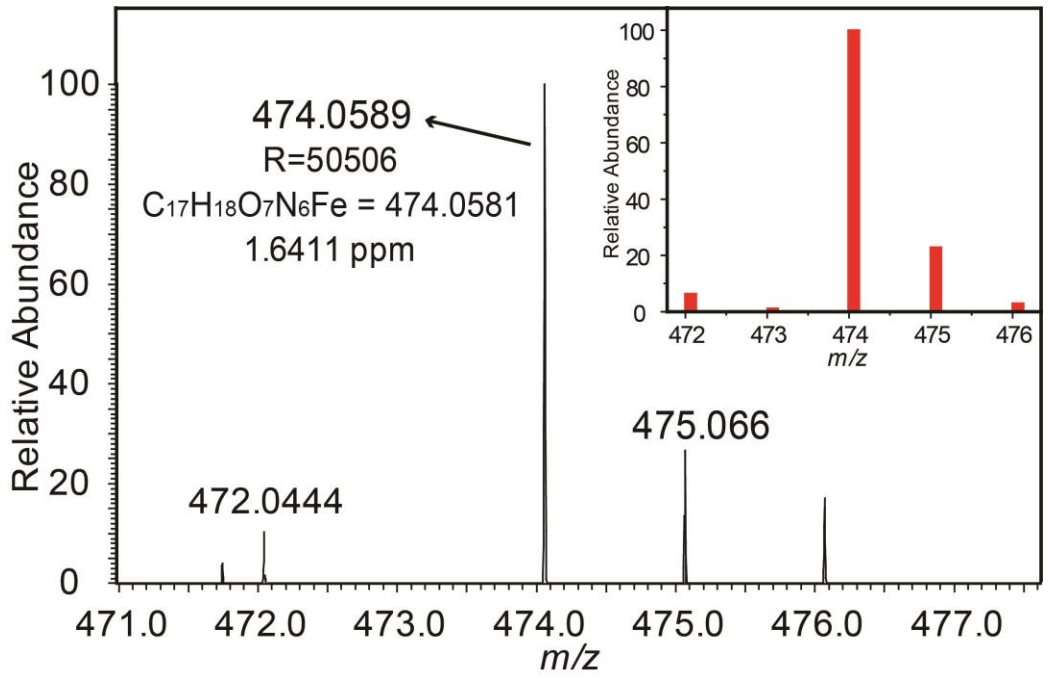

Figure 3.17: HR-MS spectrum of a catalytic photochemical WO reaction mixture having 60 µM each of **1b**, $[Ru(bipy)_3]^{2+}$ and $S_2O_8^{2-}$ in 50% CH_3CN-buffer mixture after 5 min of continuous irradiation. Inset shows the simulated isotopic distribution pattern for the corresponding $Fe^{V}(O)$ species.

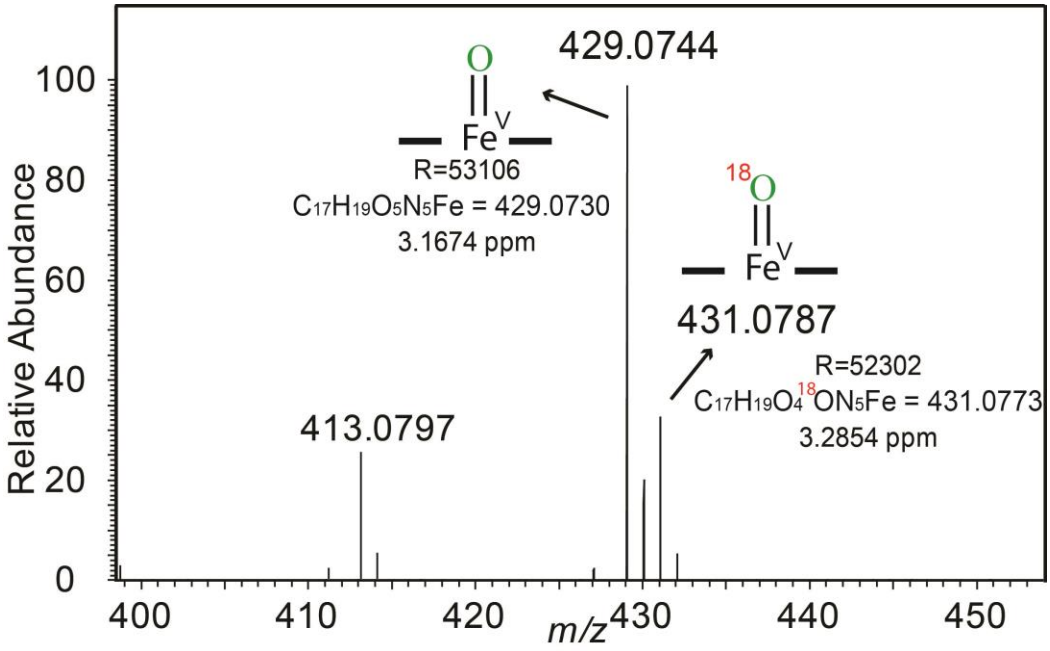

Figure 3.18: HR-MS spectrum of a photochemical WO reaction mixture having 60 µM each of **1a**, $[Ru(bipy)_3]^{2+}$ and $S_2O_8^{2-}$ in 50% CH_3CN-buffer after 5 min of continuous irradiation. The buffer contained $H_2{}^{18}O$: $H_2{}^{16}O$ in the ratio of 30:70.

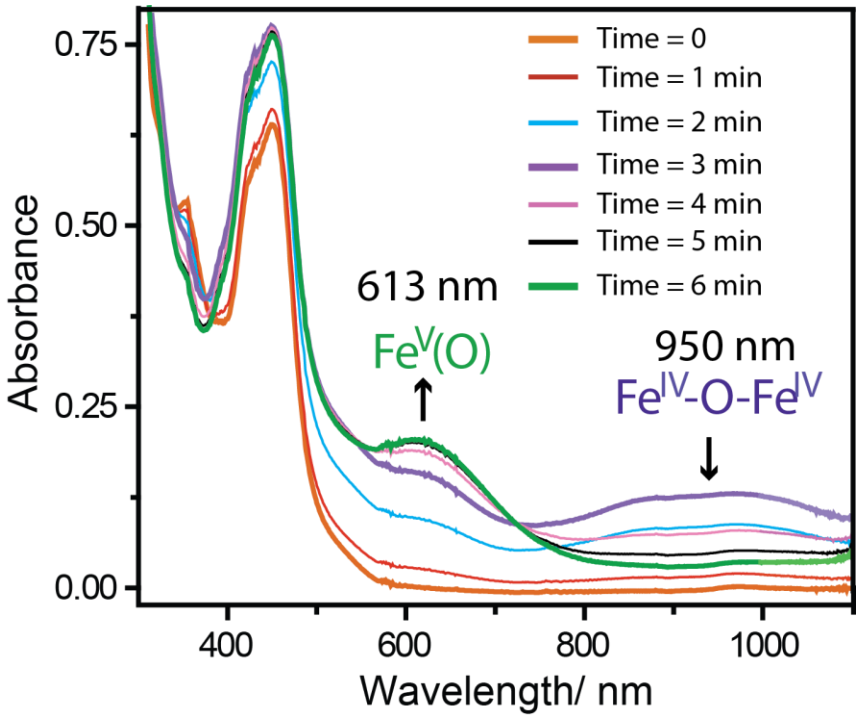

Figure 3.19: UV-vis spectral scan of a photochemical reaction mixture containing 60 µM each of **1a**, $[Ru(bipy)3]^{2+}$ and $S_2O_8^{2-}$ in 50% CH_3CN-buffer mixture. A broad peak from 800 to 1100 nm after 3 min of reaction (violet spectrum) represents a typical µ-Oxo-Fe^{IV}dimer and the peak 613 nm after 6 min (green spectrum) of reaction to a $Fe^{V}(O)$ species.

A series of UV-vis experiments were then performed to identify the high valent iron intermediates. An equimolar mixture of $[Ru(bipy)_3]^{2+}$, **1a** and $Na_2S_2O_8$ (60 µM each) was irradiated under dark conditions at 440 nm using the blue LED light source and the progress of the reaction was monitored by UV-vis (Figure 3.19). Appearance of a new broad peak centered at 950 nm (violet spectrum in Figure 3.19) was observed during the first three minutes, which then subsequently disappeared with concomitant appearance of another peak at 613 nm (green spectrum in Figure 3.19) over the next three minutes. The peaks centered at 950 nm and 613 nm match well with the µ-Oxo- Fe^{IV}dimer (violet spectrum in Figure 3.20) and the $Fe^{V}(O)$ (green spectrum in Figure 3.20) respectively, which have been independently synthesized using NaOCl and characterized by various techniques.[54a] The peak at 450 nm (which initially was due to the presence of $[Ru(bipy)_3]^{2+}$; λ_{max} = 450 nm) increased by 25% (Figure 3.19) over the course of the reaction (six minutes) can be attributed to the formation of µ-Oxo-Fe^{IV}dimer and $Fe^{V}(O)$.

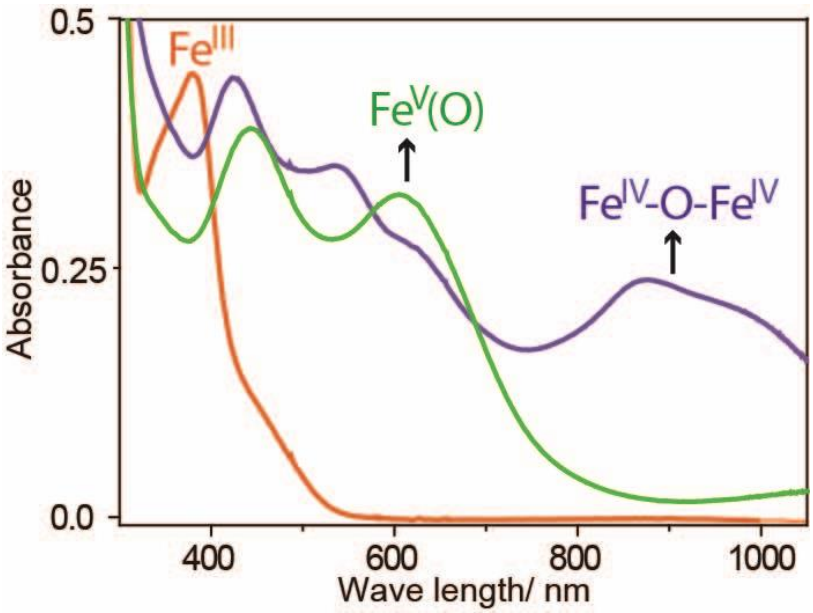

Figure 3.20: Quantitative formation of μ-Oxo-Fe^{IV}dimer (violet spectrum) followed by $Fe^{V}(O)$ (green spectrum) from biuret-modified Fe^{III}-TAML (orange spectrum, **1a**) using 1.1 eq NaOCl (stepwise addition of 0.55 eq twice) in 100% CH_3CN.[54a]

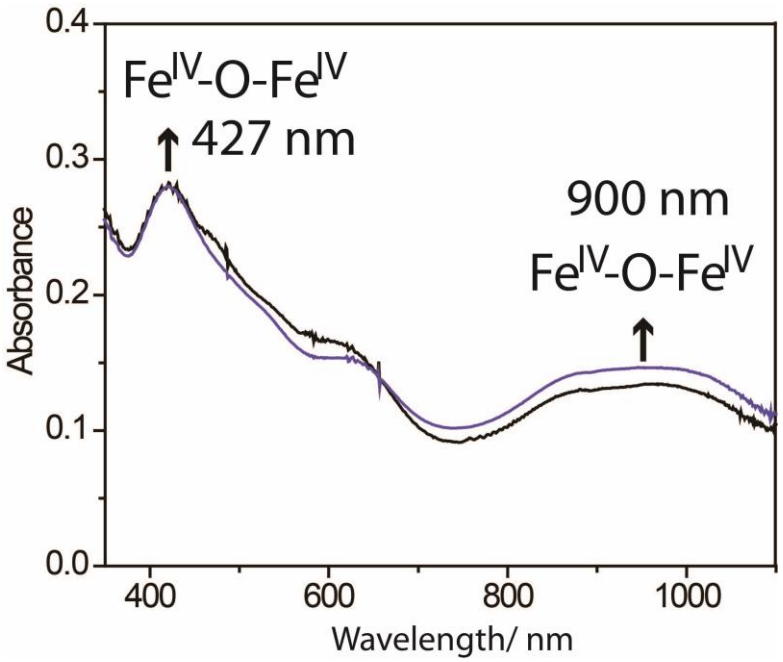

Figure 3.21: Spectra of µ-Oxo-Fe^{IV}dimer formed from **1a** using NaOCl (0.55 eq) in 50% CH_3CN: buffer mixture (violet spectrum), difference spectrum (black spectrum) obtained after subtraction of $[Ru(bipy)_3]^{2+}$ (Figure 3.22b) from the spectra generated during photochemical WO reaction mixture after 3 min (Figure 3.19).

Considering that 80% of unreacted $[Ru(bipy)_3]^{2+}$ was present in the reaction mixture at the end of three minutes, the difference UV-vis spectrum of the reaction mixture after three minutes (violet spectrum, Figure 3.19) and $[Ru(bipy)_3]^{2+}$ (48 µM i.e. 80% of starting $[Ru(bipy)_3]^{2+}$; Figure 3.22b exactly matches our previously reported diamagnetic µ-Oxo-Fe^{IV}dimer[53] (Figure 3.21). This indicated that irradiation of **1a** with $[Ru(bipy)_3]^{2+}$ and $Na_2S_2O_8$ led to the initial formation of the µ-Oxo-Fe^{IV}dimer. A similar difference spectrum (Figure 3.22c) from the reaction mixture after six minutes exactly matches with that of chemically synthesized $Fe^{V}(O)$ in 50% CH_3CN-buffer (Figure 3.22d). To prove further that the spectrum of the reaction mixture was truly due to presence of $Fe^{V}(O)$ and $[Ru(bipy)_3]^{2+}$, we took the UV-vis spectrum of a mixture of chemically synthesized $Fe^{V}(O)$ (Figure 3.22d) and $[Ru(bipy)_3]^{2+}$ (48 µM in 50% CH_3CN-buffer) (Figure 3. 22e). The resultant addition spectrum (Figure 3.22f) exactly matches with that of the photochemical reaction mixture observed after six minutes (green spectrum, Figure 3.22a).

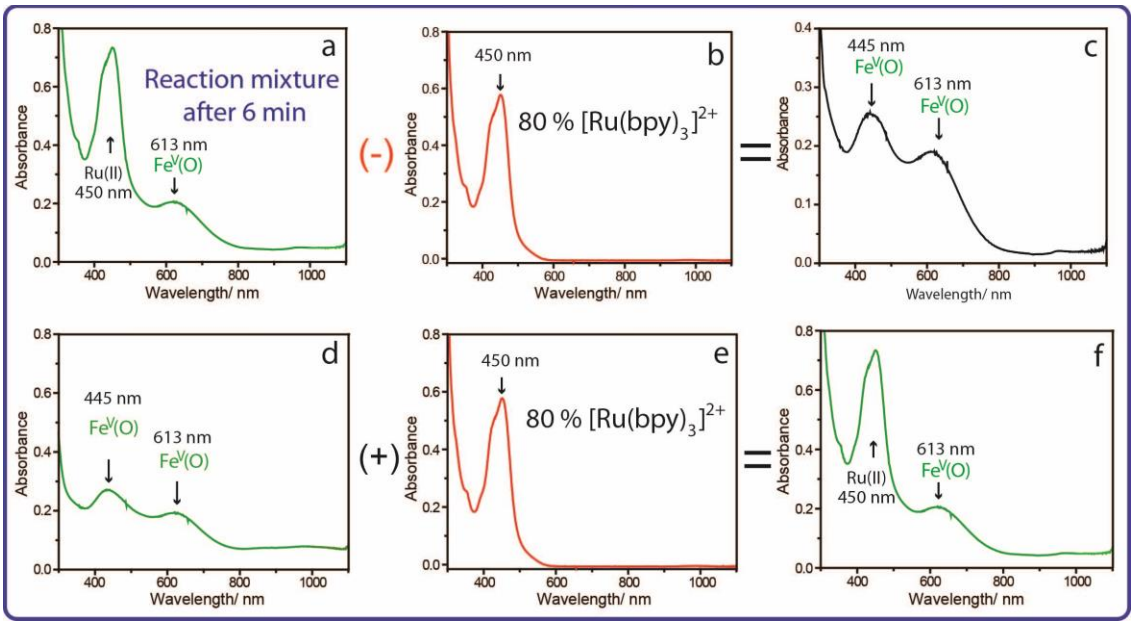

Figure 3.22: UV-vis spectrum of the a) photochemical reaction mixture after 6 min as mentioned in the "Figure 3.19"; b) $[Ru(bipy)_3]^{2+}$ around 80% (~ 48 µM) of the amount initially used in the reaction mixture; c) difference between 'a' and 'b'; d) well defined $Fe^{V}(O)$ formation from **1a** using 1.1 eq of NaOCl in 50% CH_3CN-buffer mixture; e) same as "b"; f) addition of 'd' and 'e' that exactly matches with that of "a".

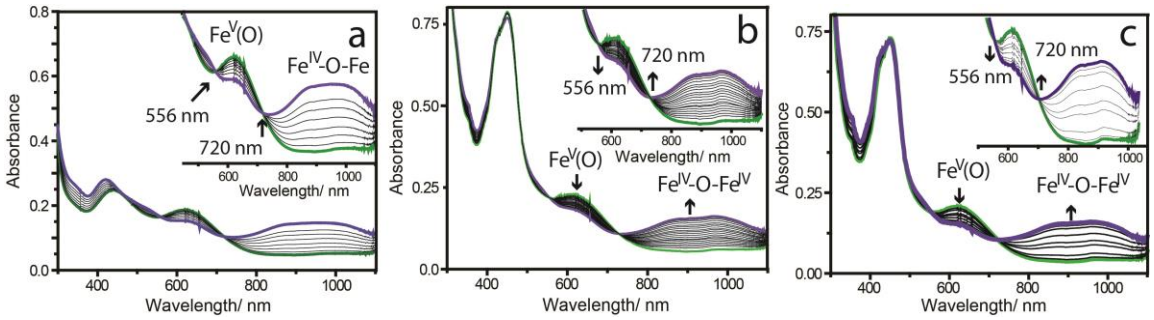

Figure 3.23: Spectral change showing decay of a $Fe^{V}(O)$ formed from **1a** (60 μM) using a) 66 μM NaOCl and b) 60 μM each of $Ru(bipy)_3]^{2+}$ and $S_2O_8^{2-}$ under irradiation; c) spectral change of a mixture having $Fe^{V}(O)$ (formed from **1a** and NaOCl) and $[Ru(bipy)_3]^{2+}$.

Note: All the three decay profiles follow very similar trend (maintain isosbestic points at 556 and 720 nm typical for a conversion of $Fe^{V}(O)$ to μ-Oxo-Fe^{IV} dimer).

This again confirmed that the high valent iron species present in the reaction mixture was truly the $Fe^{V}(O)$. Finally, the $Fe^{V}(O)$ that was generated photochemically slowly converted to μ-Oxo-Fe^{IV}dimer at room temperature with two clear isosbestic points at 556 and 720 nm; a feature that is characteristic of the spontaneous self-decay of chemically synthesized $Fe^{V}(O)$ complex of **1a** in CH_3CN[53] or CH_3CN-H_2O mixture (Figure 3.23). Based on these observations we propose the initial formation of μ-Oxo-Fe^{IV}dimer (λ_{max} = 950 nm) after three minutes of irradiation followed by slow conversion to the corresponding $Fe^{V}(O)$ complex.

We then proceeded to prove that the $Fe^{V}(O)$ intermediate can be regenerated after each cycle to demonstrate the catalytic nature of the reaction. This would also prove that the complex does not decompose under oxidative conditions produced by constant irradiation. First equimolar mixture of **1a**, $[Ru(bipy)_3]^{2+}$ and $Na_2S_2O_8$ (60 μM each) was irradiated for six minutes to generate $Fe^{V}(O)$ completely (monitored by UV-vis spectroscopy as described before). The irradiation was then stopped and the $Fe^{V}(O)$ was left to decay (decrease of peak at 613 nm) with concomitant formation of the μ-Oxo-Fe^{IV}dimer (peak at 950 nm). As soon as the μ-Oxo-Fe^{IV}dimer was completely formed, another equivalent of $Na_2S_2O_8$ was added to the reaction mixture and irradiated once

again to form $Fe^{V}(O)$. This procedure was followed up to four cycles to show that $Fe^{V}(O)$ gets regenerated at the end of each catalytic cycle (Figure 3.24).

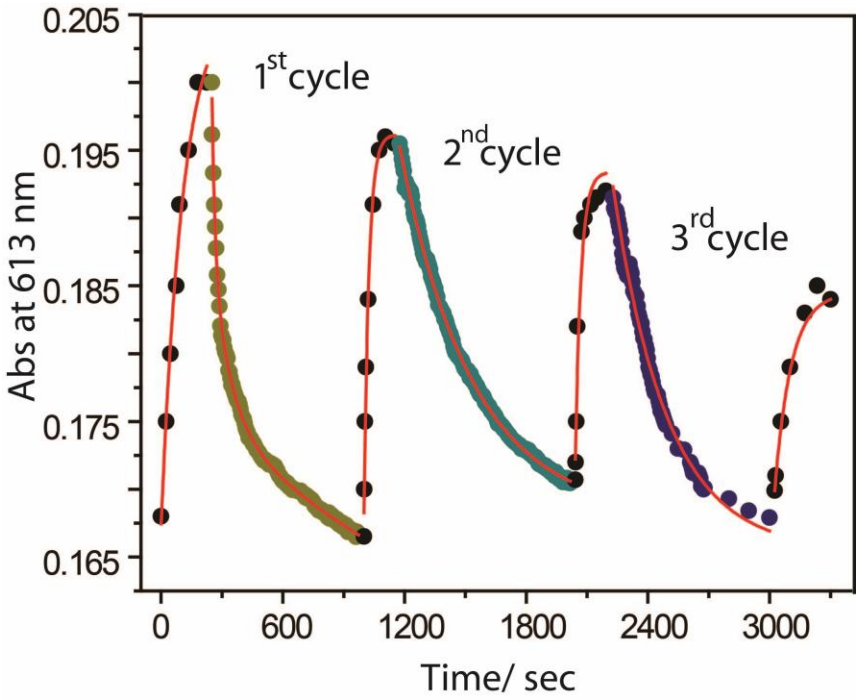

Figure 3.24: Photochemical regeneration of $Fe^{V}(O)$ after each catalytic cycle by addition of one eq of $S_2O_8^{2-}$ (60 µM) under irradiation to the mixture containing 60 µM each of **1a** and $[Ru(bipy)_3]^{2+}$. Reaction was followed up to four cycles.

Formation of the $Fe^{V}(O)$ intermediate species was further confirmed by X-band EPR measurements of the reaction mixture (Figure 3.25). A typical photochemical WO was initiated by addition of **1a** (0.7 mM) with one equivalent each of $[Ru(bipy)_3]^{2+}$ (0.7 mM) and $Na_2S_2O_8$ (0.7 mM) in a 50% CH_3CN-buffer mixture under continuous irradiation. After six minutes, the formation of a peak characteristic of $Fe^{V}(O)$ was observed by UV-vis. For EPR analysis at 90 K, the reaction mixture was quenched by freezing in liquid N_2 and absorption peaks at *g* values of 2.01, 1.98 and 1.76 were observed (Figure 3.25; red). They match very well to our previously reported $Fe^{V}(O)$ intermediate prepared by reaction of **1a** with *m*CPBA in CH_3CN.[53] An identical EPR spectrum was also observed by the reaction of 0.70 mM of **1a** and 0.77 mM NaOCl in 50% CH_3CN-buffer (Figure 3.25; green). Two additional peaks at g = 2.13 and 2.08 observed in the EPR spectrum of the reaction mixture probably correspond to some unidentified iron species. As the EPR spectrum of pure $[Ru(bipy)_3]^{3+}$ (also S = 1/2,

prepared chemically using reported procedure[69]), have *g* values 2.07, 2.03 and 1.99 (Figure 3.25; blue), the presence of this species in the photochemical reaction mixture is ruled out. Hence, EPR, UV-vis and HR-MS studies convincingly show the presence of $Fe^{V}(O)$ as an intermediate for WO.

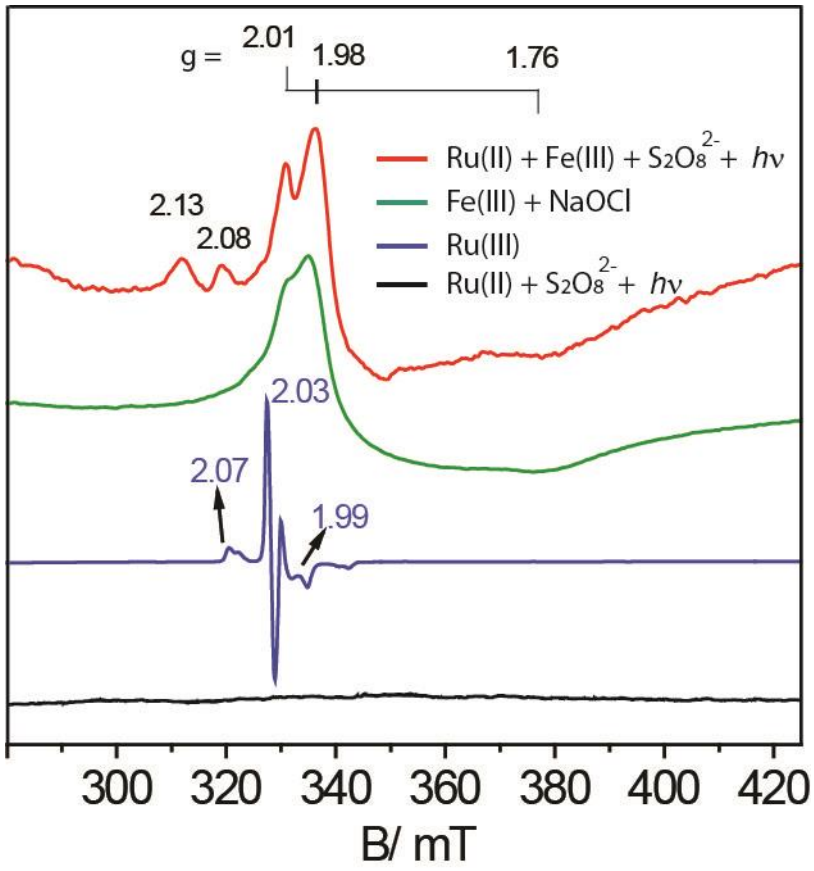

Figure 3.25: X-band EPR spectra (90 K) of photochemically (red, 0.7 mM each of **1a** ,$[Ru(bipy)_3]^{2+}$ and $S_2O_8^{2-}$ in 50% CH_3CN-buffer mixture irradiated for 5 min) and chemically (green; using 0.7 mM each of **1a** and NaOCl in 50% CH_3CN-buffer mixture) generated $Fe^{V}(O)$, the blue spectrum corresponds to the chemically synthesized $[Ru(bipy)_3]^{3+}$ (1mM) and black for a mixture having 0.7 mM each $[Ru(bipy)_3]^{2+}$ and $S_2O_8^{2-}$in 50% CH_3CN-buffer mixture after irradiation of 5 min.

We then proceeded to investigate the mechanism for the formation of $Fe^{V}(O)$ during the WO reaction. For other transition metal based systems such as ruthenium, it has been proposed that the $[Ru(bipy)_3]^{3+}$ (formed upon oxidation of the $[Ru(bipy)_3]^{2+}$ in the excited state by $Na_2S_2O_8$)[13] or the chemical oxidant cerium (IV)[35] oxidizes the

molecular WOC which in turn oxidizes water. We therefore wanted to explore if addition of preformed $[Ru(bipy)_3]^{3+}$ into a solution of **1a** in 50% CH_3CN-buffer would lead to formation of the $Fe^{V}(O)$. The UV-vis spectrum of a solution containing 60 µM **1a** and 242 mM $[Ru(bipy)_3]^{3+}$ in 50% CH_3CN-buffer at pH 8.7 (violet spectrum; Figure 3.26) showed a spectrum having a broad charge transfer band from 800 to 1100 nm that resembles the well characterized µ-Oxo-Fe^{IV}dimer, the species that is observed after the first three minutes of photochemical WO reaction (violet spectrum; Figure 3.19). The formation of the dimer is not in agreement with theoretical calculations that predict the formation of Fe^{IV}(OH) species from Fe^{III} aqua complex (**1a**) *via* PCET in the presence of an electron transfer oxidant.[67,68] However, when the same reaction was performed at pH ~3 (60 µM **1a**, 242 mM $[Ru(bipy)_3]^{3+}$, 0.5 mM H_2SO_4 in CH_3CN-H_2O), the UV-vis spectrum of the resultant species formed (red spectrum; Figure 3.26) did not match with µ-Oxo-Fe^{IV}dimer. The spectral features of this species resemble a mononuclear Fe^{IV} species of a related Fe-TAML that has recently been proposed by Nam *et al*.[70]

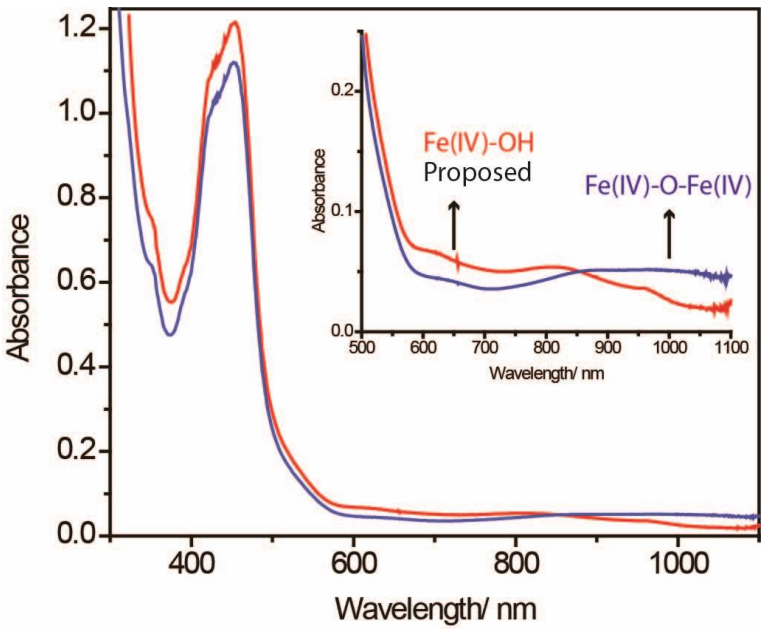

Figure 3.26: UV-vis spectrum of a reaction mixture containing 60 µM **1a** and 242 µM $[Ru(bipy)_3]^{3+}$ in 20 mM borate buffer (pH 8.7) showing characteristic features of the µ-Oxo-Fe^{IV}dimer (violet spectrum). When the same spectrum was obtained in acidic solution (dil H_2SO_4) a different spectrum (shown in red) was observed. We propose the red spectrum as the Fe^{IV}-OH species based on literature reports.

Further, addition of acid to the preformed µ-Oxo-Fe^{IV}dimer converted it into a species whose UV-vis spectral feature is similar to the species that was obtained at pH ~3 (Figure 3.27). We propose that a mononuclear Fe^{IV} species (likely to be Fe^{IV}-OH) and the µ-Oxo-Fe^{IV}dimer exist in a pH dependent equilibrium with the dimer being the predominant species at pH 8.7. During photochemical WO, Fe^{IV}-OH is first formed by PCET which is then immediately converted into the µ-Oxo-Fe^{IV}dimer in the reaction medium (pH 8.7).

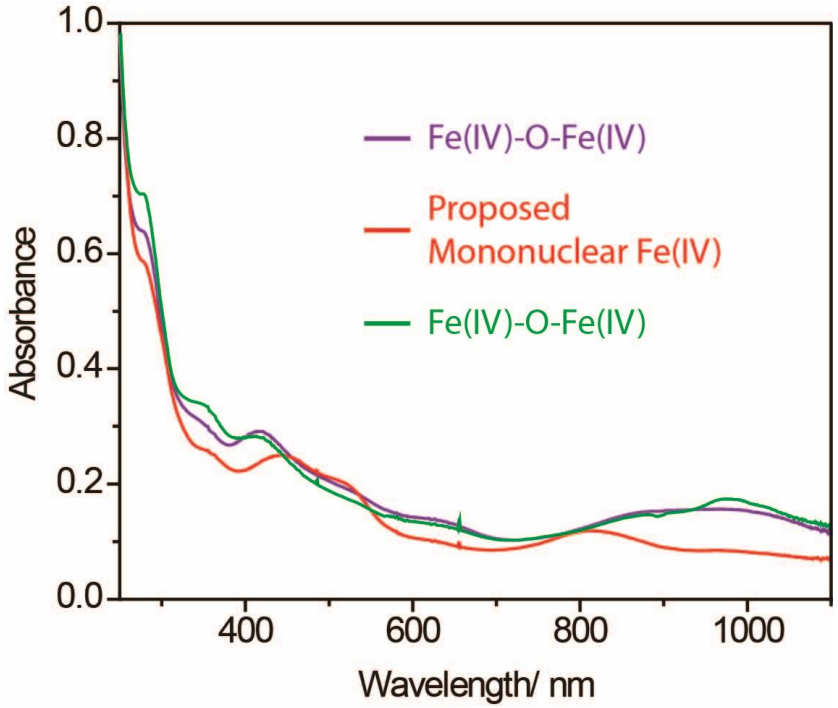

Figure 3.27: Spectral changes observed during acid mediated inter-conversion between dimeric and monomeric Fe^{IV} species. Violet spectrum: UV-vis spectrum of a reaction mixture containing **1a** (60 µM) and NaOCl (30 µM) in 10 mM borate buffer (pH 8.7) showing characteristic features of the µ-Oxo-Fe^{IV}dimer; Red spectrum: Spectrum obtained after addition of acid (20 µL of 50 mM H_2SO_4) to µ-Oxo-Fe^{IV}dimer (pH of reaction mixture ~3); Green spectrum: Spectrum obtained after addition of 20 µL of 1 M borate buffer to the Fe^{IV} species obtained at pH~3. The spectral features are typical of the µ-Oxo-Fe^{IV}dimer indicating that both the dimeric and monomeric species maintain a pH dependent equilibrium.

The mechanism for the formation of $Fe^{V}(O)$ from the µ-Oxo-Fe^{IV}dimer was then investigated. Addition of 4 equivalents $[Ru(bipy)_3]^{3+}$ to chemically generated µ-Oxo-Fe^{IV}dimer in 50% CH_3CN-buffer at pH 8.7 did not result in formation of $Fe^{V}(O)$ as was observed by UV-vis. In contrast, addition of one equivalent of $Na_2S_2O_8$ to the reaction mixture containing **1a** and four equivalents of $[Ru(bipy)_3]^{3+}$ followed by subsequent irradiation for three minutes resulted in a decrease in the µ-Oxo-Fe^{IV}dimer peak with concomitant increase in the $Fe^{V}(O)$ peak at 613 nm (Figure 3.28). It is therefore suggested that $[Ru(bipy)_3]^{3+}$ was not able to oxidize µ-Oxo-Fe^{IV}dimer to form $Fe^{V}(O)$. Electrochemical studies also support our observation.

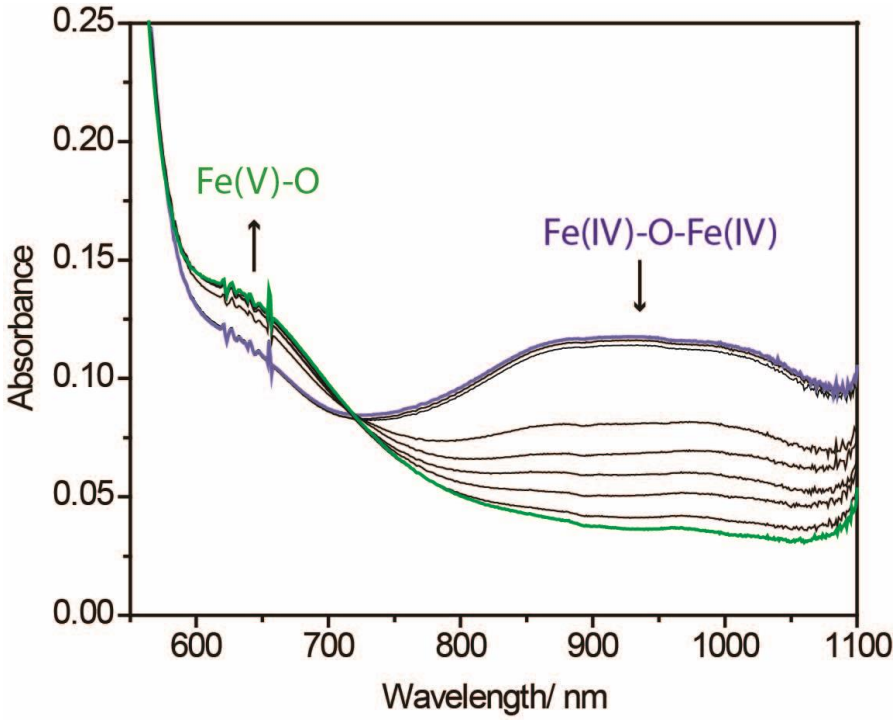

Figure 3.28: UV-vis spectra obtained immediately after addition of 242 µM $[Ru(bipy)_3]^{3+}$ to 60 µM **1a** to form the corresponding stable µ-Oxo-Fe^{IV}dimer (violet spectrum). This was followed by addition of $S_2O_8^{2-}$ and subsequently irradiated to form the $Fe^{V}(O)$ species (green spectrum; peak at 900 nm decreases with concomitant increase for the peak at 613 nm) through an isosbestic point at 720 nm.

The second redox peak of **1a** in CH_3CN (expected to be a $Fe^{IV/V}$ couple) has reduction potential close to the $[Ru(bipy)_3]^{II/III}$ couple (~1.05 V with respect to Ag/AgCl

reference electrode). Hence, addition of excess $[Ru(bipy)_3]^{3+}$ to **1a** does not lead to the formation of $Fe^{V}(O)$. However, we believe that in the presence of $Na_2S_2O_8$, the *in situ* generated sulphate radical ($SO_4^{\cdot-}$, $E_{1/2}$ = 2.1 V)[71] from the reaction of excited $[Ru(bipy)_3]^{2+}$ and one equivalent of $Na_2S_2O_8$ most likely oxidizes the μ-Oxo-Fe^{IV}dimer species leading to the formation of $Fe^{V}(O)$.

3.3.3.4 *Role of $Fe^{V}(O)$ in water oxidation*

Two different pathways may be considered to elucidate the role of $Fe^{V}(O)$ in water oxidation. First, it may be hypothesized that the $Fe^{V}(O)$ species is the real oxidant and is responsible for the generation of O_2. In an alternative scenario, $Fe^{V}(O)$ needs to be further oxidized in order to be a water oxidizing species leading to O_2 formation. In an attempt to investigate the role of $Fe^{V}(O)$, we prepared $Fe^{V}(O)$ chemically using **1a** (211 μM) and 1.1 equivalent NaOCl in 50% CH_3CN-buffer mixture with rigorous exclusion of O_2. This solution was left to decay over a period of ten minutes, and the change in the amount of dissolved O_2 in the reaction mixture was evaluated using a Clark-type electrode (Figure 3.5). In the reaction described above, no change in the amount of dissolved O_2 was detected during the course of the reaction (ten minutes). This indicates that $Fe^{V}(O)$ species was not the real oxidant for WO leading to O_2 formation. On the other hand, when the same experiment of $Fe^{V}(O)$ decay was carried out in the presence of four equivalents of $[Ru(bipy)_3]^{3+}$, 6.5 μM or 0.21 ppm of dissolved oxygen was detected within two minutes of the addition of $[Ru(bipy)_3]^{3+}$ (Figure 3.5). Control experiments that included the addition of $[Ru(bipy)_3]^{3+}$ to (i) **1a**, (ii) μ-Oxo-Fe^{IV}dimer and (iii) NaOCl (231 mM) in 50% CH_3CN-buffer separately did not show any change in dissolved O_2. We therefore conclude that $Fe^{V}(O)$ itself cannot oxidize water to generate O_2; to act as a WOC, it needs to be further oxidized. The steps that lead to the formation of O_2 from $Fe^{V}(O)$ based on our experimental observation are discussed below.

3.3.3.5 *Proposed mechanism of photochemical water oxidation*

Based on our experimental observations and recently reported theoretical calculations for Fe-TAML[67,68] catalyzed chemical WO, we propose the following catalytic cycle for photochemical WO (Figure 3.29). Irradiation of a mixture of Fe^{III} aqua

complex **1a**, $Na_2S_2O_8$ and $[Ru(bipy)_3]^{2+}$ at 440 nm leads to a stepwise formation of $Fe^{IV}(OH)$ first, followed by $Fe^{V}(O)$ *via* a two-step PCET processes.[64] However, the monoculear Fe(IV) species is not observed as it most likely gets converted into the μ-Oxo-Fe^{IV}dimer (the first intermediate observed experimentally) at the operating pH of 8.7. Formation of μ-Oxo-Fe^{IV}dimer might also arise from fast comproportionation between $Fe^{V}(O)$ and Fe^{III} as has been reported by us before.[53]

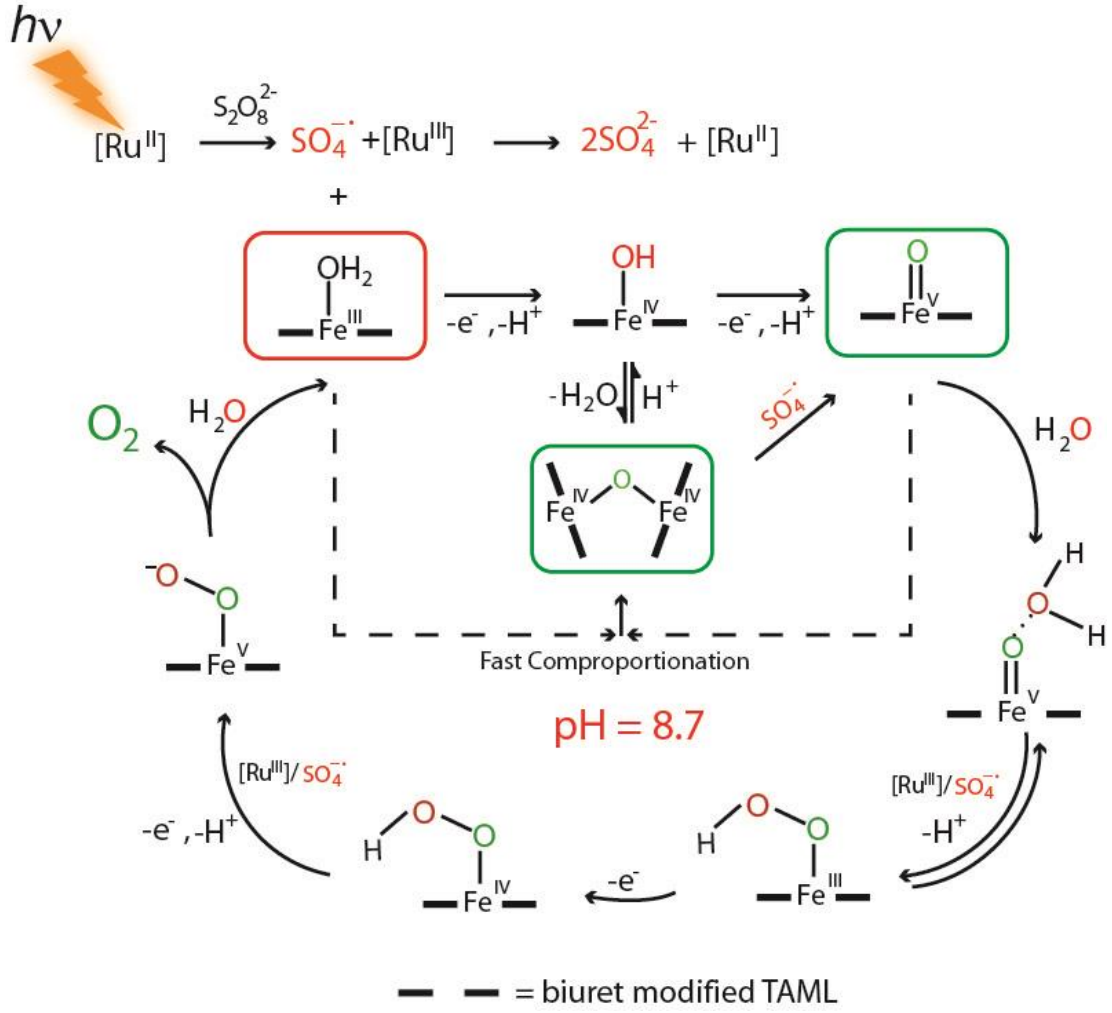

Figure 3.29: Proposed mechanism of catalytic photochemical WO by biuret-modified Fe-TAML (**1a**). Red box refers to the starting Fe^{III} complex; green boxes indicate intermediates that have been identified and characterized spectroscopically; unboxed intermediates were proposed based on our observations and supported by recently reported theoretical calculations.[67,68]

The $Fe^{V}(O)$ reactive intermediate may then undergo nucleophilic attack by a second water molecule followed by deprotonation and back electron transfer to form the monomeric Fe^{III}-hydroperoxo species. The reaction of $Fe^{V}(O)$ by a cluster of three adjacent water molecules to which proton transfer could occur has been shown to be feasible by DFT studies for a related Fe-complex.[66] The formation of monomeric Fe^{III}-hydroperoxo species has also been proposed by Fillol and Costas from a $Fe^{V}(O)(OH)$ species through a cyclic transition state involving one water molecule. The formation of such species with the oxo and hydroxo group positioned *cis* to each other is unlikely in our case. In our case, the $Fe^{V}(O)$ species is further oxidized (two equivalent) by the *in situ* generated oxidants like Ru^{III} and/or $SO_4^{-\cdot}$ to form a likely Fe^{V}-peroxo which then releases a molecule of oxygen to regenerate the starting aqua Fe^{III} complex (Figure 3.29). Recently reported theoretical calculations for chemical WO using a related Fe-TAML[67,68] support this proposed mechanism.

3.4 Conclusions

Biuret-modified Fe-TAML oxidation catalysts have been synthesized, fully characterized and shown to have high operational stability at extreme pH and under photochemical irradiation in water. The high operational stability and their ability to stabilize high valent iron oxo complexes allowed us to use them as successful catalysts in both chemical (acidic medium) and photo chemical (basic medium) WO. During photocatalytic WO, the molecular nature of the biuret-modified Fe-TAML remains intact unlike all other iron complexes that have been studied to date (which are known to decompose to iron oxide NPs). We have also demonstrated for the first time the generation of high valent $Fe^{V}(O)$ intermediate during photo chemical irradiation of biuret-modified Fe-TAML with $[Ru(bipy)_3]^{2+}$ and $Na_2S_2O_8$. The presence of $Fe^{V}(O)$ intermediate was supported *via* EPR, UV-vis and HR-MS studies. We propose that the possible nucleophilic attack of water onto $Fe^{V}(O)$ leads to the formation of a Fe^{III}-hydroperoxo complex, which is then further oxidized, leading to the release of O_2. Although the TONs and yield of O_2 are moderate compared to NP-based systems, this can be significantly improved by the modification of the ligand framework in Fe-TAMLs

to minimize the intra-molecular self-decay and by heterogenization onto solid support. Efforts in these directions are currently being pursued in our laboratory.

3.5 References

(1) Armstrong, F. A. *Philosophical Transactions of the Royal Society B: Biological Sciences* **2008**, *363*, 1263.

(2) Ciamician, G. *Science* **1912**, *36*, 385.

(3) McEvoy, J. P.; Brudvig, G. W. *Chemical Reviews* **2006**, *106*, 4455.

(4) Lewis, N. S.; Nocera, D. G. *Proceedings of the National Academy of Sciences* **2006**, *103*, 15729.

(5) Umena, Y.; Kawakami, K.; Shen, J.-R.; Kamiya, N. *Nature* **2011**, *473*, 55.

(6) Yano, J.; Kern, J.; Sauer, K.; Latimer, M. J.; Pushkar, Y.; Biesiadka, J.; Loll, B.; Saenger, W.; Messinger, J.; Zouni, A.; Yachandra, V. K. *Science* **2006**, *314*, 821.

(7) Duan, L.; Bozoglian, F.; Mandal, S.; Stewart, B.; Privalov, T.; Llobet, A.; Sun, L. *Nature Chemistry* **2012**, *4*, 418.

(8) Concepcion, J. J.; House, R. L.; Papanikolas, J. M.; Meyer, T. J. *Proceedings of the National Academy of Sciences* **2012**, *109*, 15560.

(9) Duan, L.; Araujo, C. M.; Ahlquist, M. S. G.; Sun, L. *Proceedings of the National Academy of Sciences* **2012**, *109*, 15584.

(10) Geletii, Y. V.; Huang, Z.; Hou, Y.; Musaev, D. G.; Lian, T.; Hill, C. L. *Journal of the American Chemical Society* **2009**, *131*, 7522.

(11) Jiang, Y.; Li, F.; Zhang, B.; Li, X.; Wang, X.; Huang, F.; Sun, L. *Angewandte Chemie International Edition* **2013**, *52*, 3398.

(12) Kärkäs, M. D.; Åkermark, T.; Chen, H.; Sun, J.; Åkermark, B. *Angewandte Chemie International Edition* **2013**, *52*, 4189.

(13) Kaveevivitchai, N.; Chitta, R.; Zong, R.; El Ojaimi, M.; Thummel, R. P. *Journal of the American Chemical Society* **2012**, *134*, 10721.

(14) Neudeck, S.; Maji, S.; López, I.; Meyer, S.; Meyer, F.; Llobet, A. *Journal of the American Chemical Society* **2013**, *136*, 24.

(15) Norris, M. R.; Concepcion, J. J.; Fang, Z.; Templeton, J. L.; Meyer, T. J. *Angewandte Chemie International Edition* **2013**, *52*, 13580.

(16) Romain, S.; Bozoglian, F.; Sala, X.; Llobet, A. *Journal of the American Chemical Society* **2009**, *131*, 2768.

(17) Sala, X.; Maji, S.; Bofill, R.; García-Antón, J.; Escriche, L.; Llobet, A. *Accounts of Chemical Research* **2013**, *47*, 504.

(18) Sala, X.; Romero, I.; Rodríguez, M.; Escriche, L.; Llobet, A. *Angewandte Chemie International Edition* **2009**, *48*, 2842.

(19) Tanaka, K.; Isobe, H.; Yamanaka, S.; Yamaguchi, K. *Proceedings of the National Academy of Sciences* **2012**, *109*, 15600.

(20) Tong, L.; Inge, A. K.; Duan, L.; Wang, L.; Zou, X.; Sun, L. *Inorganic Chemistry* **2013**, *52*, 2505.

(21) Wang, L.; Duan, L.; Stewart, B.; Pu, M.; Liu, J.; Privalov, T.; Sun, L. *Journal of the American Chemical Society* **2012**, *134*, 18868.

(22) Cline, E. D.; Adamson, S. E.; Bernhard, S. *Inorganic Chemistry* **2008**, *47*, 10378.

(23) Graeupner, J.; Hintermair, U.; Huang, D. L.; Thomsen, J. M.; Takase, M.; Campos, J.; Hashmi, S. M.; Elimelech, M.; Brudvig, G. W.; Crabtree, R. H. *Organometallics* **2013**, *32*, 5384.

(24) Grotjahn, D. B.; Brown, D. B.; Martin, J. K.; Marelius, D. C.; Abadjian, M.-C.; Tran, H. N.; Kalyuzhny, G.; Vecchio, K. S.; Specht, Z. G.; Cortes-Llamas, S. A.; Miranda-Soto, V.; van Niekerk, C.; Moore, C. E.; Rheingold, A. L. *Journal of the American Chemical Society* **2011**, *133*, 19024.

(25) Hull, J. F.; Balcells, D.; Blakemore, J. D.; Incarvito, C. D.; Eisenstein, O.; Brudvig, G. W.; Crabtree, R. H. *Journal of the American Chemical Society* **2009**, *131*, 8730.

(26) Lalrempuia, R.; McDaniel, N. D.; Müller-Bunz, H.; Bernhard, S.; Albrecht, M. *Angewandte Chemie International Edition* **2010**, *49*, 9765.

(27) McDaniel, N. D.; Coughlin, F. J.; Tinker, L. L.; Bernhard, S. *Journal of the American Chemical Society* **2007**, *130*, 210.

(28) Parent, A. R.; Brewster, T. P.; De Wolf, W.; Crabtree, R. H.; Brudvig, G. W. *Inorganic Chemistry* **2012**, *51*, 6147.

(29) Puntoriero, F.; La Ganga, G.; Sartorel, A.; Carraro, M.; Scorrano, G.; Bonchio, M.; Campagna, S. *Chemical Communications* **2010**, *46*, 4725.

(30) Chen, G.; Chen, L.; Ng, S.-M.; Man, W.-L.; Lau, T.-C. *Angewandte Chemie International Edition* **2013**, *52*, 1789.

(31) Gong, M.; Li, Y.; Wang, H.; Liang, Y.; Wu, J. Z.; Zhou, J.; Wang, J.; Regier, T.; Wei, F.; Dai, H. *Journal of the American Chemical Society* **2013**, *135*, 8452.

(32) Hong, D.; Mandal, S.; Yamada, Y.; Lee, Y.-M.; Nam, W.; Llobet, A.; Fukuzumi, S. *Inorganic Chemistry* **2013**, *52*, 9522.

(33) Hong, D.; Yamada, Y.; Nagatomi, T.; Takai, Y.; Fukuzumi, S. *Journal of the American Chemical Society* **2012**, *134*, 19572.

(34) Fu, S.; Liu, Y.; Ding, Y.; Du, X.; Song, F.; Xiang, R.; Ma, B. *Chemical Communications* **2014**, *50*, 2167.

(35) Moonshiram, D.; Alperovich, I.; Concepcion, J. J.; Meyer, T. J.; Pushkar, Y. *Proceedings of the National Academy of Sciences* **2013**, *110*, 3765.

(36) Kanan, M. W.; Nocera, D. G. *Science* **2008**, *321*, 1072.

(37) Singh, A.; Spiccia, L. *Coordination Chemistry Reviews* **2013**, *257*, 2607.

(38) Ellis, W. C.; McDaniel, N. D.; Bernhard, S.; Collins, T. J. *Journal of the American Chemical Society* **2010**, *132*, 10990.

(39) Codolà, Z.; Garcia-Bosch, I.; Acuña-Parés, F.; Prat, I.; Luis, J. M.; Costas, M.; Lloret-Fillol, J. *Chemistry – A European Journal* **2013**, *19*, 8042.

(40) Fillol, J. L.; Codolà, Z.; Garcia-Bosch, I.; Gómez, L.; Pla, J. J.; Costas, M. *Nature Chemistry* **2011**, *3*, 807.

(41) Zhang, B.; Li, F.; Yu, F.; Cui, H.; Zhou, X.; Li, H.; Wang, Y.; Sun, L. *Chemistry – An Asian Journal* **2014**, *9*, 1515.

(42) Hoffert, W. A.; Mock, M. T.; Appel, A. M.; Yang, J. Y. *European Journal of Inorganic Chemistry* **2013**, *2013*, 3846.

(43) Coggins, M. K.; Zhang, M.-T.; Vannucci, A. K.; Dares, C. J.; Meyer, T. J. *Journal of the American Chemical Society* **2014**, 136, 5531.

(44) Klepser, B. M.; Bartlett, B. M. *Journal of the American Chemical Society* **2014**, *136*, 1694.

(45) Huang, Z.; Luo, Z.; Geletii, Y. V.; Vickers, J. W.; Yin, Q.; Wu, D.; Hou, Y.; Ding, Y.; Song, J.; Musaev, D. G.; Hill, C. L.; Lian, T. *Journal of the American Chemical Society* **2011**, *133*, 2068.

(46) Pizzolato, E.; Natali, M.; Posocco, B.; Montellano Lopez, A.; Bazzan, I.; Di Valentin, M.; Galloni, P.; Conte, V.; Bonchio, M.; Scandola, F.; Sartorel, A. *Chemical Communications* **2013**, *49*, 9941.

(47) McAlpin, J. G.; Surendranath, Y.; Dincă, M.; Stich, T. A.; Stoian, S. A.; Casey, W. H.; Nocera, D. G.; Britt, R. D. *Journal of the American Chemical Society* **2010**, *132*, 6882.

(48) Karlsson, E. A.; Lee, B.-L.; Åkermark, T.; Johnston, E. V.; Kärkäs, M. D.; Sun, J.; Hansson, Ö.; Bäckvall, J.-E.; Åkermark, B. *Angewandte Chemie International Edition* **2011**, *50*, 11715.

(49) Limburg, J.; Vrettos, J. S.; Liable-Sands, L. M.; Rheingold, A. L.; Crabtree, R. H.; Brudvig, G. W. *Science* **1999**, *283*, 1524.

(50) Robinson, D. M.; Go, Y. B.; Mui, M.; Gardner, G.; Zhang, Z.; Mastrogiovanni, D.; Garfunkel, E.; Li, J.; Greenblatt, M.; Dismukes, G. C. *Journal of the American Chemical Society* **2013**, *135*, 3494.

(51) Collins, T. J. *Accounts of Chemical Research* **2002**, *35*, 782.

(52) Collins, T. J.; Gordon-Wylie, S. W.; Long-Lived Homogeneous Oxidation Catalysts. U.S. Patent5,847,120, December 8, **1998**.

(53) Ghosh, M.; Singh, K. K.; Panda, C.; Weitz, A.; Hendrich, M. P.; Collins, T. J.; Dhar, B. B.; Sen Gupta, S. *Journal of the American Chemical Society* **2014**, 136, 9524.

(54) a) Singh, K. K.; Tiwari. M.; Ghosh, M., Panda, C.; Hendrich, M.,Weitz,vA., Dhar, B.; Vanka, K.; Sen Gupta, S. (*submitted for publication*); b) Panda. C.; Debgupta. J.; Díaz. D. D.; Singh. K. K.; Gupta S. S. and Dhar. B. B.; *Journal of the American Chemical Society* **2014**, 136, 12273.

(55) Kotani, H.; Suenobu, T.; Lee, Y.-M.; Nam, W.; Fukuzumi, S. *Journal of the American Chemical Society* **2011**, *133*, 3249.

(56) Company, A.; Sabenya, G.; González-Béjar, M.; Gómez, L.; Clémancey, M.; Blondin, G.; Jasniewski, A. J.; Puri, M.; Browne, W. R.; Latour, J.-M.; Que, L.; Costas, M.; Pérez-Prieto, J.; Lloret-Fillol, J. *Journal of the American Chemical Society* **2014**, *136*, 4624.

(57) Bachl, J.; Hohenleutner, A.; Dhar, B. B.; Cativiela, C.; Maitra, U.; Konig, B.; Diaz, D. D. *Journal of Materials Chemistry A* **2013**, *1*, 4577.

(58) Wadsworth, E.; Duke, F. R.; Goetz, C. A. *Analytical Chemistry* **1957**, *29*, 1824.

(59) Ghosh, A.; Ryabov, A. D.; Mayer, S. M.; Horner, D. C.; Prasuhn, D. E.; Sen Gupta, S.; Vuocolo, L.; Culver, C.; Hendrich, M. P.; Rickard, C. E. F.; Norman, R. E.; Horwitz, C. P.; Collins, T. J. *Journal of the American Chemical Society* **2003**, *125*, 12378.

(60) Polshin, V.; Popescu, D.-L.; Fischer, A.; Chanda, A.; Horner, D. C.; Beach, E. S.; Henry, J.; Qian, Y.-L.; Horwitz, C. P.; Lente, G.; Fabian, I.; Münck, E.; Bominaar, E. L.; Ryabov, A. D.; Collins, T. J. *Journal of the American Chemical Society* **2008**, *130*, 4497.

(61) Ellis, W. C.; Tran, C. T.; Denardo, M. A.; Fischer, A.; Ryabov, A. D.; Collins, T. J. *Journal of the American Chemical Society* **2009**, *131*, 18052.

(62) Panda, C.; Ghosh, M.; Panda, T.; Banerjee, R.; Sen Gupta, S. *Chemical Communications* **2011**, *47*, 8016.

(63) Popescu, D.-L.; Chanda, A.; Stadler, M.; de Oliveira, F. T.; Ryabov, A. D.; Münck, E.; Bominaar, E. L.; Collins, T. J. *Coordination Chemistry Reviews* **2008**, *252*, 2050.

(64) Weinberg, D. R.; Gagliardi, C. J.; Hull, J. F.; Murphy, C. F.; Kent, C. A.; Westlake, B. C.; Paul, A.; Ess, D. H.; McCafferty, D. G.; Meyer, T. J. *Chemical Reviews* **2012**, *112*, 4016.

(65) Beach, E. S.; Duran, J. L.; Horwitz, C. P.; Collins, T. J. *Industrial & Engineering Chemistry Research* **2009**, *48*, 7072.

(66) Chanda, A.; Shan, X.; Chakrabarti, M.; Ellis, W. C.; Popescu, D. L.; Tiago de Oliveira, F.; Wang, D.; Que, L.; Collins, T. J.; Münck, E.; Bominaar, E. L. *Inorganic Chemistry* **2008**, *47*, 3669.

(67) Liao, R.-Z.; Li, X.-C.; Siegbahn, P. E. M. *European Journal of Inorganic Chemistry* **2014**, *2014*, 728.

(68) Ertem, M. Z.; Gagliardi, L.; Cramer, C. J. *Chemical Science* **2012**, *3*, 1293.

(69) Shafirovich, V. Y.; Khannanov, N. K.; Shilov, A. E. *Journal of Inorganic Biochemistry* **1981**, *15*, 113.

(70) Kwon, E.; Cho, K.-B.; Hong, S.; Nam, W. *Chemical Communications* **2014**, *50*, 5572.

(71) Kaledin, A. L.; Huang, Z.; Geletii, Y. V.; Lian, T.; Hill, C. L.; Musaev, D. G. *The Journal of Physical Chemistry A* **2009**, *114*, 73.

Chapter IV

Peroxide Activation by Biuret-modified Fe-TAML: Applications in Various Analyte Detection Through Signal Amplification

Chapter IV

Part A

In-gel Visual detection of Protein Bio-markers via Signal Amplification: A Potential Replacement of HRP in Western Blots

This chapter is adapted partly (synthesis of the clickable biuret-modified Fe-TAML) from the following publication.

(1) Malvi. B., Panda. C., Dhar. B. B. and Gupta. S. S., *Chemical Communications*, **2012**, *48*, 5289.

4A.1 Introduction

Detection of ultra-low amounts of various analytes is extremely important in many research areas such as diagnostic testing for disease or monitoring of environmental pollutants. For example, sensing of toxic metal ions, organic pollutants and explosives is critically important in assessing environmental pollution, food contamination and assuring security against terrorism.[1] Equally important is the ability to develop highly sensitive analytical techniques for detection of ultra-low concentration of proteins and other bio-markers for early diagnosis of lethal diseases.[1] Extensive research efforts in this field have led to various analytical techniques which have considerably lowered existing detection limits to molecular levels. For example, using various sophisticated microscopic techniques such as TEM,[2] SEM,[3] AFM,[4] surface plasmon resonance (SPR)[5] and surface enhanced Raman spectroscopy (SERS)[6] detection of single molecules have been achieved. However, the ultimate challenge in in this area remains the development of methodologies that permits \naked eye detection (visual; easy and inexpensive) of a particular analyte in a complex mixture, without the use of much sophisticated instrumentation.

In general, sensitivity of an analytical protocol is determined by the direct correlation between the analyte concentration and the strength of the output signal. For example, these assays can be broadly divided into two classes; i) direct assay and ii) assay via signal amplification (Figure 4A.1).[1] The former is based on the direct generation of output signal as soon as the analyte binds to a specific substrate and the sensitivity in this case is determined by the magnitude of binding constant (K) between them. However, in the latter case i.e. in assay via signal amplification, the analyte-substrate binding event generates a catalyst which converts a particular reactant into product which represents the output signal. Here, the sensitivity of the assay is determined by the number of catalytic cycles (TON) achieved by the catalyst formed as a result of analyte and substrate binding. As more than one product (i.e. more than one output signal) would be generated via signal amplification in comparison to the direct assay (only one output signal), the detection limits would be expected to be considerably lower. The importance of signal amplification assays is very nicely illustrated by the

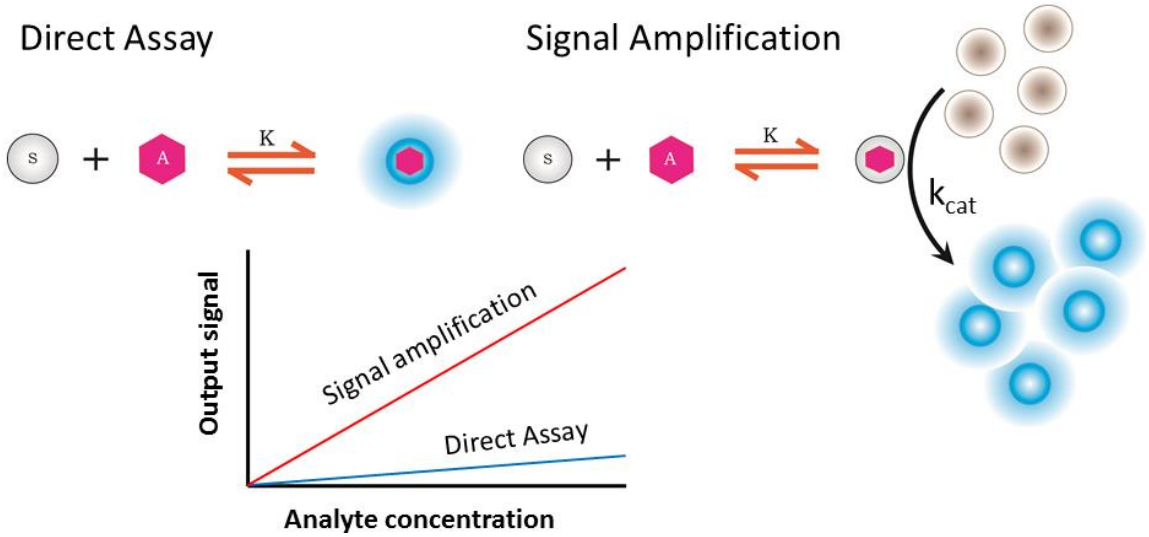

Figure 4A.1: Representation of direct and signal amplification assays in analyte detections.

development of various biological assays such as the enzyme-linked immunosorbent assay (ELISA)[7-9]and western blot[10,11]. In most of the biological assays such as in ELISA, a molecular recognition event of the analyte and a surface bound receptor co-immobilizes an enzyme,[10] which is used for the generation of an easy detectable signal. The enzyme that is routinely used for signal amplification in most of the biological assays is horseradish peroxidase (HRP) which in the presence of H_2O_2 converts a non-chemiluminiscent molecule into a chemiluminiscent molecule with several thousand turnovers, thus decreasing the detection limits by several folds.[12] The increased concentration of reporter molecules produced upon catalytic reaction by HRP renders detection of very low amounts of analyte using UV-vis and fluorescence spectroscopy feasible. Recently, several efforts have been made by researchers to design synthetic small molecular systems that mimic these enzymes[13,14] and function as signal amplification catalysts for analyte sensing. This chapter discusses the developement of a robust peroxidase mimicking small molecular catalyst (alkyne tailed biuret-modified Fe-TAML) and its role in H_2O_2 activation for detection of various analytes. The first part of this chapter includes visual detection of protein bio-markers. The second part of this chapter discusses the utilization of Fe-TAML immobilized inside mesoporous silica nanoparticle (Fe-MSN) for the naked eye detection of CN^- ion in tandem with the enzyme catalse through signal amplification.

4A.1.1 *Western blots*

In conventional biological assays like western blot,[10,11] biomolecules such as proteins and nucleic acids are first localized on a nitrocellulose membrane together with mixtures of other proteins and subsequently detected quantitatively. This requires at first gel electrophoresis of a particular cell lysate (mixture of protein biomarkers) through a sodium dodecyl sulfate poly acrylamide gel (SDS PAGE) so that proteins of different molecular weight get separated. Subsequently they are transferred from gel to a nitrocellulose/polyvinylidene difluoride (PVDF) membrane and then probed with antibody-HRP conjugates followed by incubation with H_2O_2 and a peroxidase substrate for development of an easy detectable signal. HRP is used as a catalyst for the oxidation of the substrate to generate a multitude of reporter molecules, which is correlated to the turn-over number of the enzyme. The conceptual novelty of Western Blot lies in the use of signal amplification: a single analyte molecule (protein of interest) recruits an enzyme that is able to produce many reporter molecules as the output signal. The increased concentration of reporter molecules renders detection using fluorescence and UV-vis

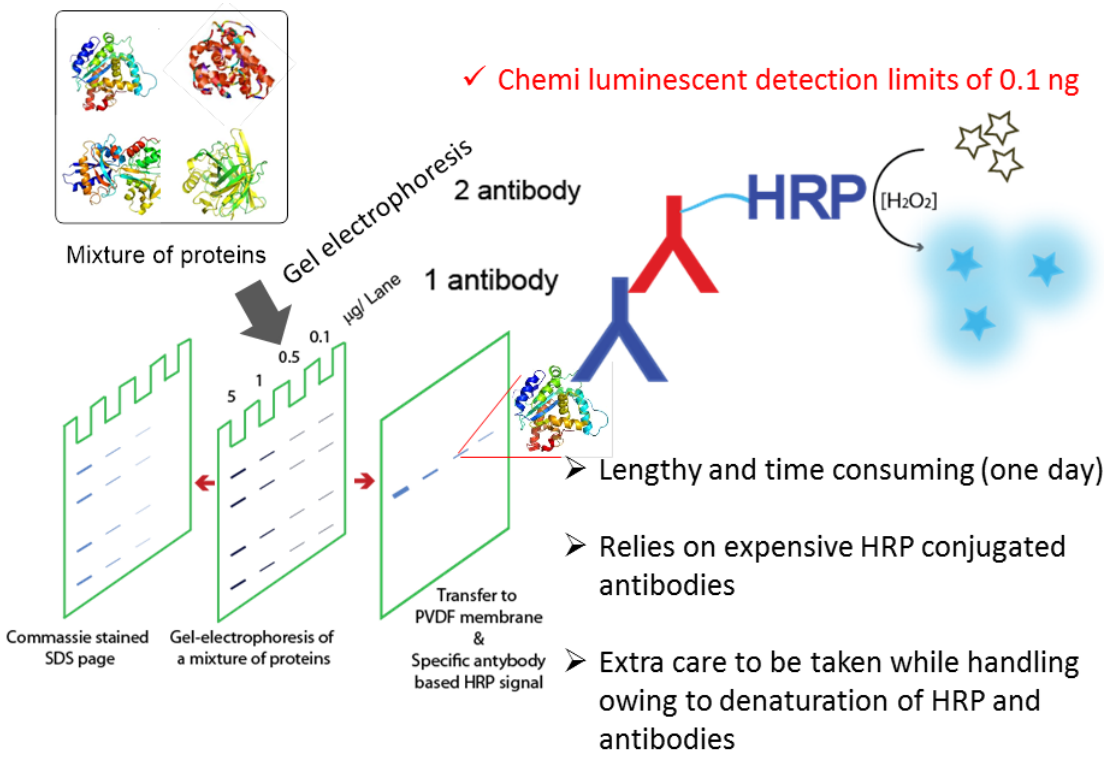

Figure 4A.2: Schematic representation of a typical western blot assay

spectroscopy feasible. Chemiluminiscent substrates that can be easily imaged are used as substrates for protein identification and quantification in the range of 1 to 0.1 ng. A schematic representation of all the steps in a typical western blot process is shown in Figure 4A.2. Although western blot assays are frequently used for ultra-low detection of proteins, there are several limitations that encourage the development of newer approaches that can potentially replace western blots. For example, the whole process of western blot is very time consuming (especially the transfer of protein from gel to PVDF membrane and several antibody incubation steps followed by many washing protocols), relies on usage of expensive antibody-HRP conjugates and requires special care during handling of the bio molecules (denature with slight change in operating conditions; temperature, medium etc.)

4A.1.2 *Activity based protein profiling*

Activity-based protein profiling (ABPP) has emerged as a key technology in the evolution of functional proteomics by providing quantitative read out for the activity of specific enzymes or proteins in complex proteomes (cell, tissue, and fluid samples).[15-25]. ABPP relies on the design of active-site directed covalent probes to investigate specific families of enzymes in complex proteomes. The fundamental building blocks of ABPP are small-molecule probes (chemical scaffolds including mechanism-based inhibitors, protein-reactive natural products, and general electrophiles) that covalently label the active site of a given enzyme or enzymes. These inhibitor probes which get covalently bound to the enzyme of interest are attached to a reporter tag to facilitate target characterization. Examples of reporter tags include fluorophores, biotin, and latent analytical handles such as alkynes or azides, which can be modified by click chemistry methods to visualize protein targets post-labeling by gel electrophoresis as has been shown by Cravatt *et al.* (Figure 4A.3). Typically fluorescent probes like rhodamine is used as the reporter tag and this limits the detection limit for the enzyme of interest. However, when the concentration of enzymes is very low, the rhodamine containing inhibitor probes are not fluorescent enough for detection.

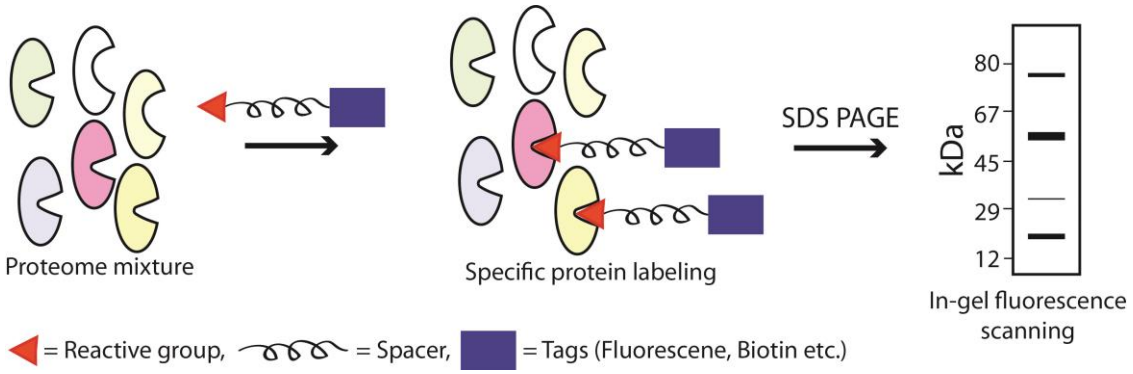

Figure 4A.3: Fluorescence based ABPP for in-gel protein detection

4A.1.3 *Hypothesis of this chapter*

We envisioned that if the ABPP probe can be chemically attached to a small molecule peroxidase mimic (e.g. our biuret-modified Fe-TAML reported in Chapter II) in place of the fluorescent tag; it would allow signal amplification by producing a large number of reporter signal molecules. This would allow in-gel colorimetric detection of proteins with lower detection limits than conventional ABPP. An illustrative example of the experiment is given below (Figure 4A.4). Let us assume that there is a mixture of 4 proteins with one being an enzyme of interest. The mixture of proteins is treated with an inhibitor probe that has an organoazide handle. This inhibitor probe will get covalently attached to our enzyme of interest. Now the whole protein mixture will be subject to click reaction with an alkyne-tagged Fe-TAML. Then the reaction mixture can be run on a polyacrylamide gel and after probing with a substrate 3,3',5,5'-tetramethylbenzidine (TMB) and H_2O_2, would generate a green colored species (oxidized TMB). A blue-green band will only be observed for the enzyme in which the Fe-TAML has been covalently attached (Figure 4A.4). Since Fe-TAML is a peroxidase mimic that catalyzes formation of several oxidized TMB, we believe that the detection limit of the enzyme of interest would be significantly lowered.

4A.2 Experimental section

4A.2.1 *Materials*

2-Nitro-1,4-phenylenediamine, 4-Pentynoic acid, 2-Aminoisobutyric acid, Phthalic anhydride, Hydrazine acetate, n-Butyl lithium, $FeCl_2$, 3 ,3′, 5, 5′-Tetramethylbenzidine

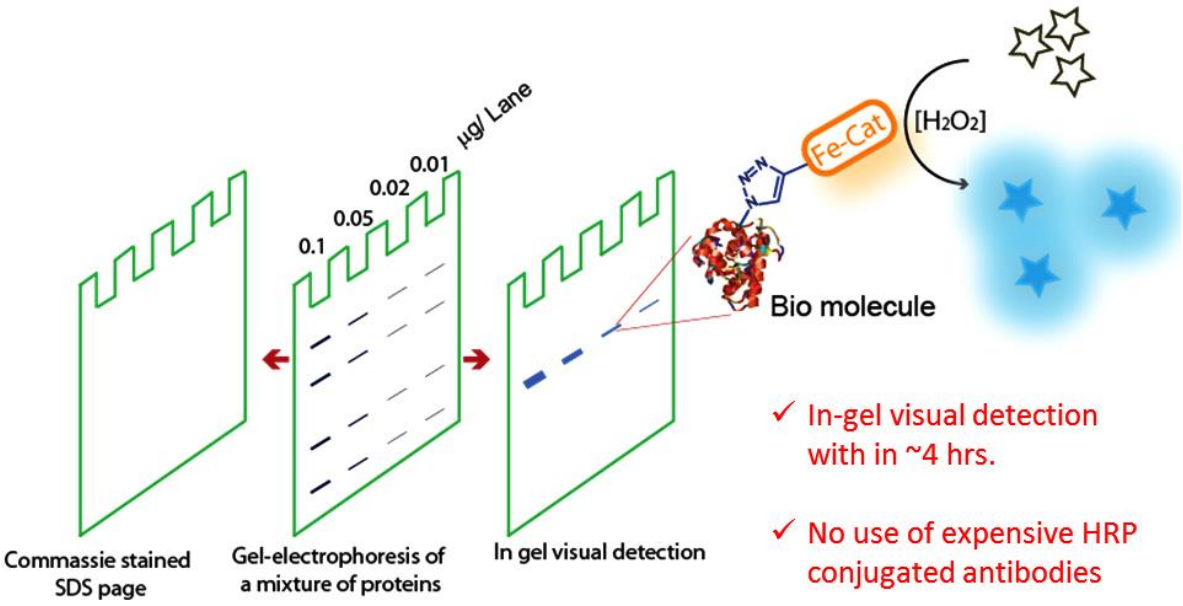

Figure 4A.4: In-gel visual detection assay in ABPP using biuret-modified Fe-TAML

(TMB), Acrylamide, N,N'-Methylenebisacrylamide, tris(hydroxymethyl)aminomethane (Tris), Sodiumdodecylsulphate (SDS), Ammonium persulphate (APS), N,N,N',N'-Tetramethylethylenediamine (TEMED), Protein bio-markers (6.5 to 67 KDa), Human serum albumin (HSA), Maleic anhydride, Alanine and N-hydroxy succinamide are obtained from Sigma-Aldrich and used without further purification. O-(2-Aminoethyl)-O′-(2-azidoethyl) hexaethylene glycol (compound **10**) was procured from polypure. Oxalyl chloride, Triethylamine, Zinc dust, Calcium chloride, $CuSO_4$, Sodium ascorbate, hydrogen peroxide, Thionyl chloride, Tetraethylammonium bromide and Amberlite-120 strong acid ion exchange resin were supplied by Merck-India. Solvents like Benzene, THF, Ethanol, DCM and Methanol were also purchased from Merck-India and purified before use following conventional procedure as reported elsewhere. Tris(3-hydroxypropyltriazolylmethyl) amine (THPTA) was prepared as reported procedure.[26]

4A.2.2 *Physical measurements*

All the synthetic products were characterized by ^{1}H and ^{13}C NMR spectra recorded on a Bruker (200 MHz) spectrometer & these data are reported in δ (ppm) vs. $(CH_3)_4Si$ with the deuterated solvent proton residuals as internal standards. UV-vis measurements were carried in Agilent-8453 spectrophotometer. Infrared spectra were obtained by

Perkin Elmer FT-IR spectrum GX instrument. High resolution mass spectrometry (HR-MS) was done either in the negative (for alkyne tailed catalyst) or positive ion mode (neutral organic compounds) of a Thermo Scientific Q-Exactive, using electron spray ionization source, Orbitrap as analyzer and connected with a C18 column (150m × 4.6mm × 8µm). The X-band electron paramagnetic resonance (EPR) spectrum was recorded in a Bruker EMX X-band spectrometer operating at a field modulation of 100 kHz, modulation amplitude of 5 G and microwave radiation power of 10 mW at 77 K. Gel electrophoresis were carried out using a mini dual vertical electrophoresis unit from Tarson with a power supply unit from Genie, Bangalore, India.

4A.2.3 *Synthesis of clickable biuret-modified Fe-TAML*[27a]

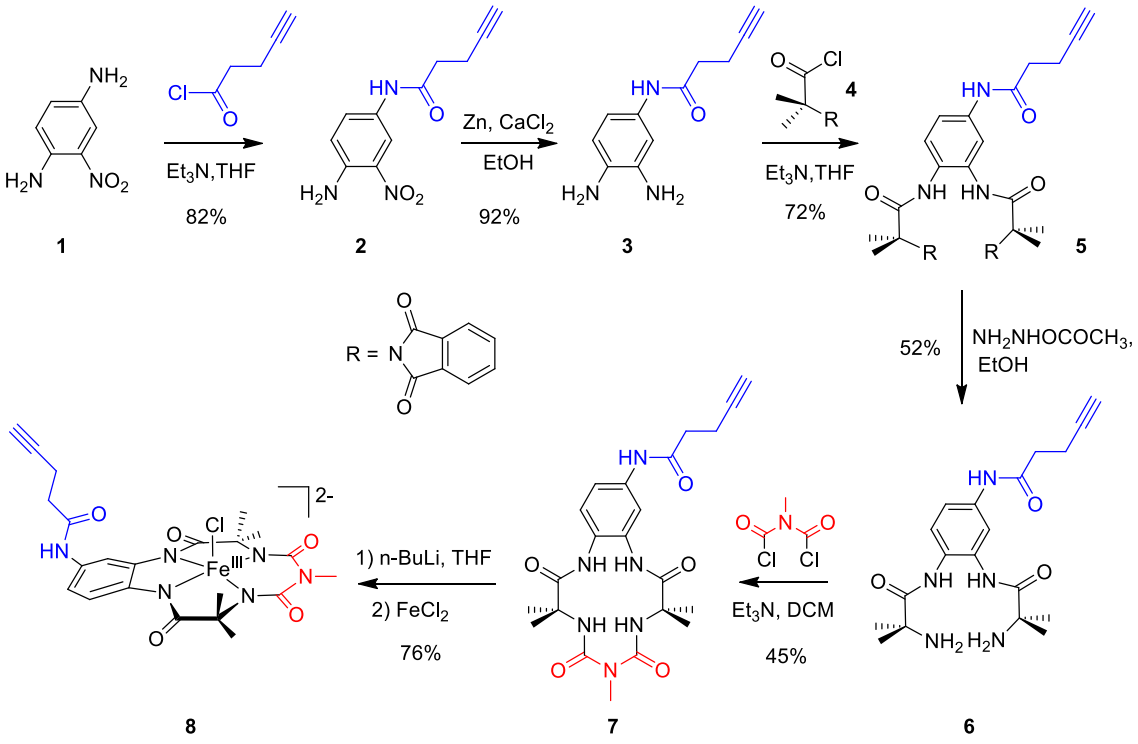

Scheme 4A.1: Synthesis of clickable biuret-modified Fe-TAML.

4A.2.3.1 *Synthesis of pent-4-ynoyl chloride*

To a solution of 4-pentynoic acid (1.50 g, 15.29 mmol) in dry benzene was added oxalyl chloride (6.56 mL, 76.45 mmol, 5 equivalent) and the reaction mixture was

refluxed for 2 to 3 hours with a $CaCl_2$ guard tube fitted to the reflux condenser. The excess oxalyl chloride was distilled of under reduced pressure. The remaining little oxalyl chloride was chased off with 5 mL of benzene twice. Subsequent reactions were performed considering a 100% yield. Success of the reaction was confirmed from shift of the infrared band of cabonyl 1699 cm^{-1} (4-pentynoic acid) to 1799 cm^{-1} (pent-4-ynoyl chloride).

4A.2.3.2 *Synthesis of N-(4-amino-3-nitrophenyl)pent-4-ynamide* **(2)**

To an ice cooled solution of **1** (2 g, 13.06 mmols) and dry triethylamine (2.0 mL, 14.37 mmol, 1.1 equivalent) in dry THF, a solution of pent-4-ynoyl chloride (1.67 g, 14.37 mmol, 1.1 equivalent) in dry THF was added dropwise over a period of 30 minutes. After completion of addition the ice was removed and the reaction was stirred at room temperature for a period of 12 hours. The reaction mixture was filtered to remove the triethylamine salt. Solvent was removed under reduced pressure to have **2** as the only product (TLC). **2** was then recrystlized from ethanol to yield 2.50g (82.08%). $C_{11}H_{11}N_3O_3$. IR (KBr, ν_{max}/cm^{-1}): 1654 (s, CO), 2119(s, C≡C), 3284 (s, NH), 3358(s, NH). ^{1}H NMR (200.13 MHz, CD_3OD): δ = 2.32(m, 1H), 2.58 (m, 4H), 6.95 (d, J = 9.10 Hz, 1H), 7.53 (dd, J_1 = 2.52 Hz, J_2 = 9.10 Hz, 1H), 8.35 (d, J = 2.66 Hz, 1H). ^{13}C NMR; (50.32 MHz, CD_3OD): δ = 15.54, 36.60, 70.39, 83.44, 117.46, 120.26, 128.57, 130.65, 131.50, 144.60, 172.29. ESI-MS: *m/z* 234.16($M\text{-}H^+$, 100%).

4A.2.3.3 *Synthesis of N-(3,4-diaminophenyl)pent-4-ynamide* **(3)**

2 (1.5 g, 6.43 mmol) was taken in 180 ml of 95% ethanol. To the reaction mixture, activated $CaCl_2$ powder (0.90 g, 8.10 mmol, 1.26 equivalent) and activated zinc dust (7.50 g, 114.74 mmol, 17.84 equivalent) were added. The reaction mixture was refluxed for two to three hours and he completion of reaction was followed by consumption of **2** by TLC (60% EtOAc in petrolium ether). As soon as the starting material was consumed the reaction mixture was cooled to room temperature and filtered. Ethanol was removed under reduced pressure, the solid residue was dissolved in water and the pH was adjusted to 11 by adding NaOH. Then the organic layer was extracted to 3 × 150 ml of EtOAc. Solvent evaporated to have pure **3** (1.20 g, yield 91.80%). Mol. formula: $C_{11}H_{13}N_3O$. IR

(KBr, ν_{max}/cm^{-1}): 1653 (s, CO), 2111 (s, C≡C), 3275 (s, NH). ^{1}H NMR (200.13 MHz, DMSO-d_6): δ = 2.44 (brs, 4H), 2.80 (m, 1H), 4.44 (brs, 4H), 6.42 (d, *J* = 8.39 Hz, 1H), 6.59 (dd, J_1 =2.18 Hz, J_2 = 8.21 Hz, 1H), 6.85 (d, *J* = 2.23 Hz, 1H), 9.42(s, 1H). ^{13}C NMR; (50.32 MHz, DMSO-d_6): δ = 14.52, 35.26, 71.62, 84.12, 107.07, 109.11, 114.50, 130.09, 131.13, 135.31, 168.28. ESI-MS: *m/z* 204.04($M-H^+$, 100%).

4A.2.3.4 *Synthesis of N, N' - (4 - (pent – 4 - ynamido) - 1, 2 - phenylene) bis(2 - (1, 3-dioxoisoindolin - 2 - yl) - 2 - methylpropanamide)* **(5)**

To an ice cooled solution of **3** (2 g, 9.84 mmol) and dry triethylamine (2.77 mL, 19.88 mmol, 2.02 equivalent) in dry THF, a solution of **4** (5.00g, 19.88 mmol, 2.02 equivalent) in dry THF was added dropwise over a period of 30 minutes. After completion of addition the ice was removed and the reaction mixture was stirred at room temperature for a period of 12 hours. The reaction mixture was filtered to remove the triethlamine salt. Solvent was removed under reduced pressure and the residue was dissolved in DCM and washed with 3 × 250 mL 1N HCl and 3 × 250 mL saturated $NaHCO_3$ respectively to remove the unreacted reactants. DCM was removed by rota evaporator and the solid was recrystalized from ethanol to have crystals of **5** (4.50g, yield 72.17%). Mol. formula: $C_{35}H_{31}N_5O_7$. IR (KBr, ν_{max}/cm^{-1}): 1661 (s, CO), 1668 (s, CO), 1710 (s, CO), 2119 (s, C≡C), 3420 (br, NH). ^{1}H NMR (200.13 MHz, DMSO-d_6): δ = 1.73 (s, 6H), 1.78 (s, 6H), 2.50 (m, 4H), 2.81 (m, 1H), 7.35 (d, *J* = 8.75, 1H), 7.50 (dd, J_1 = 2.28, J_2 = 8.85, 1H), 7.82 (m, 9H), 9.41 (s, 1H), 9.42 (s, 1H), 10.09 (s, 1H). ^{13}C NMR; (50.32 MHz, DMSO-d_6): δ = 14.23, 24.56(4C), 35.29, 61.20, 61.33, 71.67, 83.83, 114.49, 115.85, 123.06(4C), 124.87, 125.41, 131.20, 131.85(4C), 134.66(4C), 136.63, 168.51(4C), 169.48, 171.67, 171.82,. ESI-MS: *m/z* 634.18($M-H^+$, 100%).

4A.2.3.5 Synthesis of *N, N'-(4-(pent - 4- ynamido) - 1, 2 – phenylene) bis (2 – amino – 2 - methylpropanamide)* **(6)**

A mixture of **5** (2 g, 3.16 mmol, 1 equivalent) and hydrazine acetate (0.767 g, 8.52 mmol, 2.7 equivalent) were taken in 50 ml of ethanol and rufluxed for 8 hrs. After two to three hour, the reaction mixture became clear and then precipitation of pthalichydrazide starts following completion of reaction with additional 5 hrs. The reaction mixture was

cooled to room temperature and kept at -20 °C overnight. The reaction mixture was filtered through celite, followed by washing with cold ethanol. Ethanol was removed under reduced pressure, the solid residue was dissolved in water and the pH was adjusted to 11 by adding NaOH . Then the organic layer was extracted to 3 × 100 ml of DCM. The organic layer was dried and the solid obtained was recrystalized from solvent mixture of EtOAc and hexane to have pure **6** (yield 0.620 g, 52.60%). Mol. formula: $C_{19}H_{27}N_5O_3$. IR (KBr, ν_{max}/cm^{-1}): 1660 (s, CO), 1676 (s, CO), 2117 (s, C≡C), 3287 (s, NH). ^{1}H NMR (200.13 MHz, DMSO-d_6): δ = 1.32 (s, 12H), 2.50 (m, 4H), 2.82 (m, 1H), 4.69 (brs, 4H), 7.44 (m, 2H), 7.97 (m, 1H), 10.03 (s, 1H). ^{13}C NMR; (50.32 MHz, DMSO-d_6): δ = 14.31, 28.87(2C), 28.92(2C), 35.34, 55.07, 55.17, 71.73, 83.90, 114.53, 115.59, 125.02, 125.88, 131.85, 136.46, 169.45, 176.80, 177.09. ESI-MS: *m/z* 374.25($M-H^+$, 100%).

4A.2.3.6 Synthesis of *N-(3,3,6,9,9-pentamethyl-2,5,7,10-tetraoxo-2,3,4,5,6,7,8,9,10,11-decahydro-1H-benzo[i][1,3,5,8,11]pentaazacyclotridecin-13-yl)pent-4-ynamide* **(7)**

The experimental procedure followed was similar to the procedure described in our previous report.[14] Yield for 0.10 g (0.268 mmol) of **6** was 0.055 g (45%). The X-ray crystal structure for this alkyne tailed biuret-modified TAML was obatained and the details are provided in the appendix III. Mol. formula: $C_{22}H_{28}N_6O_5$. IR (KBr, ν_{max}/cm^{-1}): 1605 (s, CO), 1681 (s, CO), 1703 (s, CO), 2119 (s, C≡C), 3257 (s, NH), 3315 (s, NH). ^{1}H NMR (500.20 MHz, CD_3OD): δ = 1.64 (s, 6H), 1.65 (s, 6H), 2.30 (t, *J* = 2.67, 1H), 2.58 (m, 4H), 3.10 (s, 3H), 7.48 (dd, J_1 = 2.43, J_2 = 8.83, 1H), 7.57 (d, *J* = 8.84, 1H), 8.06 (d, *J* = 2.16, 1H). ^{13}C NMR; (125.78 MHz, CD_3OD): δ = 15.65, 26.21(2C), 26.43(2C), 31.95, 36.99, 60.79, 60.91, 70.48, 83.66, 117.66, 118.69, 127.30, 127.37, 132.85, 138.23, 158.59, 158.98, 172.44, 176.59, 176.97. ESI-MS: *m/z* 479.18($M-Na^+$, 100%).

4A.2.3.7 Synthesis of *alkyne tailed biuret-modified Fe-TAML* **(8)**

The experimental procedure followed was similar to the procedure described in our previous report with slight modification.[14] The only difference was the use of 6 equivalent of n-butyllithiun in place of 4.4 equivalents. Yield for 0.34 g (0.0745 mmol) of **7** was 0.046 g (76.53%). Mol. formula: $C_{38}H_{64}N_8O_5FeCl$. UV-vis: $\lambda_{max}(H_2O)$/nm; 356 ($\varepsilon/dm^3\ mol^{-1}\ cm^{-1}$, 5830), IR (KBr, ν_{max}/cm^{-1}): 1569 (s, CO), 1581 (s, CO), 1609 (s, CO),

3330 (s, NH). ESI-MS(negative ion mode): *m/z* 508.21(M-35, 100%). EPR, UV-vis and HR-MS spectra have been provided in appendix (Figure C 8 and C9; Appendix III).

4A.2.4 *Kinetics of TMB oxidation by biuret-modified Fe-TAML*

The kinetics of TMB oxidation was monitored at 650 nm (one of the absorption peaks of oxidized product of TMB) in the kinetic mode of the spectrophotometer (Agilent–8453 series) using 1 ml quartz cuvette of 1.00 cm path length thermostatted (25.0 ± 0.5 °C) cell housing. Initial rates approach was used for the initial 10 to 20% formation of the TMB oxidation product (at 650 nm) using the linear absorbance versus time plots and the extinction coefficients of 39000 $M^{-1}cm^{-1}$ which stands for oxidation product of TMB at 650 nm. Concentration of H_2O_2 was calculated by dividing the UV-vis absorbance at 230 nm by the characteristic molar extinction coefficient (ε = 72.8 dm^3 $M^{-1}cm^{-1}$).[27b] To investigate the kinetic parameters, H_2O_2 variations was done from 8.0 × 10^{-3} to 1.6 × 10^{-5} M while keeping the TMB concentration fixed at 2.5 × 10^{-4} M. For TMB variation, reverse procedure was followed ([H_2O_2] = 4.0 × 10^{-2} M; [TMB] = 1.0 × 10^{-3} – 5.0 × 10^{-4} M). In all kinetic runs, the catalyst concentration was kept constant at 1 × 10^{-8} M. Phosphate buffer pH of 7.4 was used for all the runs. The kinetic parameters were calculated according to the equation, $v = V_{max} \times [S]/(K_m + [S])$ where 'v' stands for initial rate or initial velocity, V_{max} is the maximal velocity, [S] is the concentration of the substrate and K_m is the Michaelis constant.

4A.2.5 *Synthesis of maleimide-azide linker* (11)

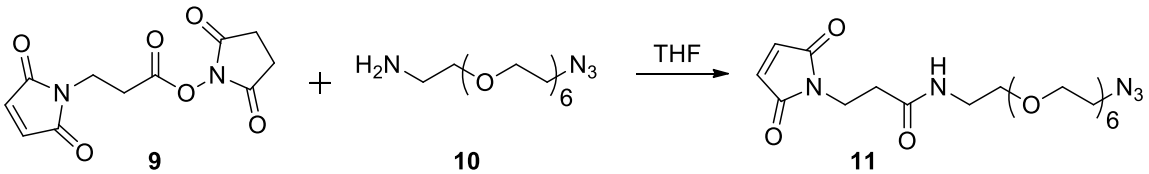

Scheme 4A.2: Synthesis of maleimide-azide linker (**11**)

The maleimide-NHS linker (**9**) was prepared by following a procedure reported before.[28] To a solution of maleimide-NHS ester (**9**; 6 mg; 22 mmole, 1 eq) in 0.75 mL of dry THF was added a solution of azido-peg-amine (**10**; 8.7 mg; 25 mmole, 1.1 eq) in 0.75

mL of dry THF. The reaction was monitored by TLC over time. The purification of the final compound (**11**) by conventional chromatographically was not possible because of its fast decomposition upon isolation. Hence as soon as **9** was consumed completely, the reaction mixture was taken out and kept at -20 °C for future use. Considering 100% completion of the reaction, the concentration of **11** was assumed to be 19 mM. HR-MS showed m/z values 282 and 305 m/z corresponding to the $M\text{-}H^+$ and $M\text{-}Na^+$ species in the positive ion mode of the instrument.

4A.2.6 *Azide labelling of the protein HSA*

To a 1 mL solution of 5 mg/mL (75 µM) HSA in 100 mM phosphate buffer pH 7.4 was added 750 µM of the linker maleimide-NHS-N_3 in DMSO and the resulting solution was shaken overnight at 6 °C. Subsequently, the reaction mixture was purified by dialysis against 100 mM phosphate buffer pH 7.4 over 24 hour there by changing the buffer after every four hour. The concentration of purified HSA-N_3 congugate was confirmed by Bradford assay (~5 mg/mL) and it was further used for conjugation reactions.

4A.2.7 *Click conjugation of biuret-modified Fe-TAML on to the HSA-N_3*

Stock solutions

$CuSO_4$: 20 mM (5 mg solid in 1 mL of water)

THPTA ligand: 50 mM (in water)

Sodium ascorbate: 100 mM (fresh solution was prepared just before use by adding 1 mL of water to 20 mg solid).

Aminoguanidine hydrochloride: 100 mM (11 mg of solid in 1 mL of water)

HSA-N_3: 5 mg/mL (~75 µM)

Alkyne tailed biuret-modified Fe-TAML: 20 mM

Buffer: 100 mM phosphate pH 7.4

Final concentrations

$CuSO_4$: 0.10 mM

THPTA ligand: 0.50 mM (ligand to copper ratio is 5:1)

Sodium ascorbate: 5 mM

Aminoguanidine: 5 mM

Alkyne tailed biuret-modified Fe-TAML: 400 µM, large excess used to achieve fast reaction kinetics

HSA-N_3: 1 mg/mL (15 µM)

Procedure for 0.2 mL reactions

The following click conjugation protocol was adopted from a previous report by Finn *et al*. with slight modifications.[26] In a 2 mL eppendorf tube, 40 µL of HSA-N_3 (5 mg/mL) was taken in 163 µL of 100 mM phosphate buffer pH 7.4. To this mixture was added 4 µL of alkyne tailed biuret-modified Fe-TAML, 3 µL of premixed solution of $CuSO_4$ and THPTA ligand (1 µL of $CuSO_4$ and 2 µL of THPTA ligand stock) and 10 µL of aminoguanidine. The reaction mixture was well mixed with the help of a vortex and degassed by bubbling with N_2 gas (to remove O_2) followed by addition of 10 µL of freshly prepared sodium ascorbate solution under positive flow of N_2. The reaction mixture was run for one hour and then loaded to the SDS page without further purification.

4A.2.8 *Gel electrophoresis and substrate development*

Upon completion of the click reaction (1 hr), the reaction mixture was diluted to a protein concentration of 4 µg/mL. Gel electrophoresis using SDS page was carried out by loading varying amounts of protein (40 ng to 5 ng). After completion of gel electrophoresis, the SDS page was taken out of the electrophoresis cassette and washed 4 to 5 times with deionized water. Subsequently a mixture of H_2O_2 (80 mM) and TMB (0.5 mM) in 40 mM phosphate buffer pH 7.4 was applied on the gel with gentle agitation for 5 minutes after which the presence of the protein band was confirmed by the appearance of a green colored band.

4A.3 Results and discussions

To ensure that the biuret-modified Fe-TAML can generate colored species by catalyzing oxidation of a colorless substrate (as HRP does in most biological assays), we studied the H_2O_2 mediated oxidation of the peroxidase substrate TMB. As a result of TMB oxidation a green colored species was generated which was utilised in various

analyte detection schemes. To prove that the green colored species (oxidized TMB charge transfer complex) generated in the oxidation reaction was indeed promoted by catalyst, control experiments performed without the use of H_2O_2 or catalyst did not produce the green colored species. To investigate the peroxidase like activity of biuret-modified Fe-TAML, the apparent steady-state kinetic parameters for the reaction was studied. The kinetic data were fitted perfectly to a typical Michaelis–Menten type curve and the K_m (Michaelis constant) and V_{max} (maximal reaction velocity) values determined from it (Table 4A.1). (Figure C10 and C11; Appendix III).

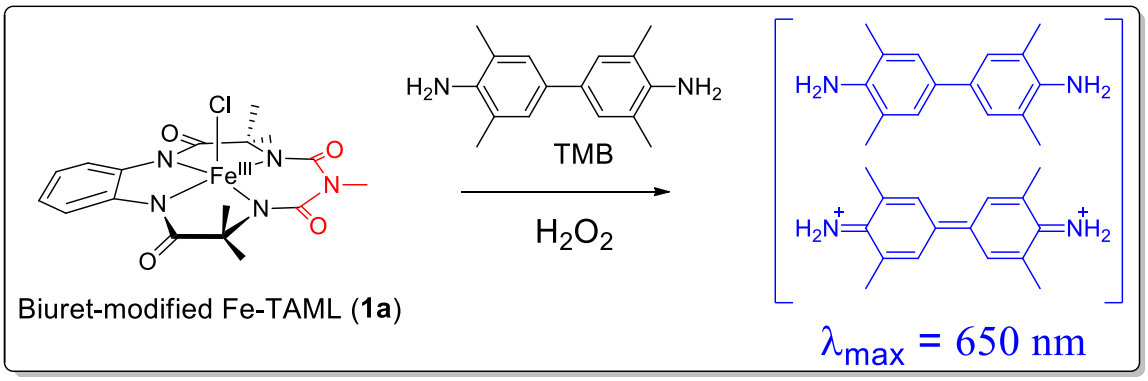

Scheme 4A.3: TMB oxidation using biuret-modified Fe-TAML in presence of H_2O_2

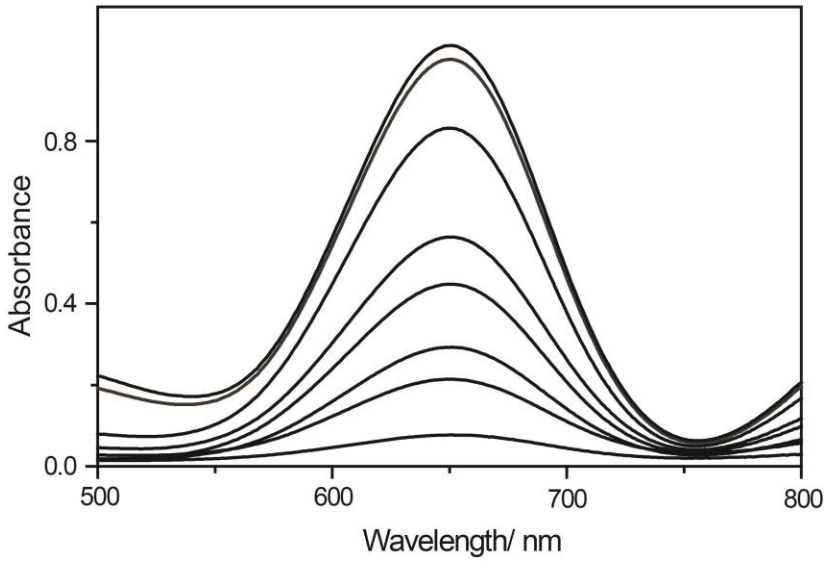

Figure 4A.5: Spectral scan of TMB oxidation in presence of biuret-modified Fe-TAML and H_2O_2.

The kinetic parameters especially the k_{cat} values suggest that the biuret-modified Fe-TAML to be less reactive than the native enzyme HRP by an order of two. However, owing to their exceptional robustness in ambient operating conditions (ionic strengths and pH 1 to 13) in comparison to HRP and other reported synthetic analogues, we wanted to explore their applications in the detection of analytes.

Table 4A.1: Michaelis–Menten parameters of TMB oxidation

Catalyst	Substrate	[Catalyst]/ M	K_m/ M	V_{max}/ Ms^{-1}	k_{cat} (s^{-1}) = V_{max}/[cat]
1a	TMB	10^{-8}	1.12×10^{-3}	9.79×10^{-8}	9.79
	H_2O_2	10^{-8}	1.74×10^{-4}	1.53×10^{-8}	1.53
HRP[29]	TMB	10^{-11}	4.34×10^{-4}	10.0×10^{-8}	4.00×10^{3}
	H_2O_2	10^{-11}	3.70×10^{-3}	8.71×10^{-8}	3.48×10^{3}

We then proceeded to develop a protocol for in-gel visual detection of protein biomarkers using biuret modified Fe-TAML with the aim to replace fluorescent tags and HRP in avidin blot based ABPPs. Our analytical methodology consists of the following consecutive steps: (i) azide incorporation in the desired protein to be detected by following a thiol-maleimide reaction where the surface thiol of HSA (cysteine 34 position) was reacted with a maleimide-N_3 linker; (ii) copper(I) catalysed cycloaddition

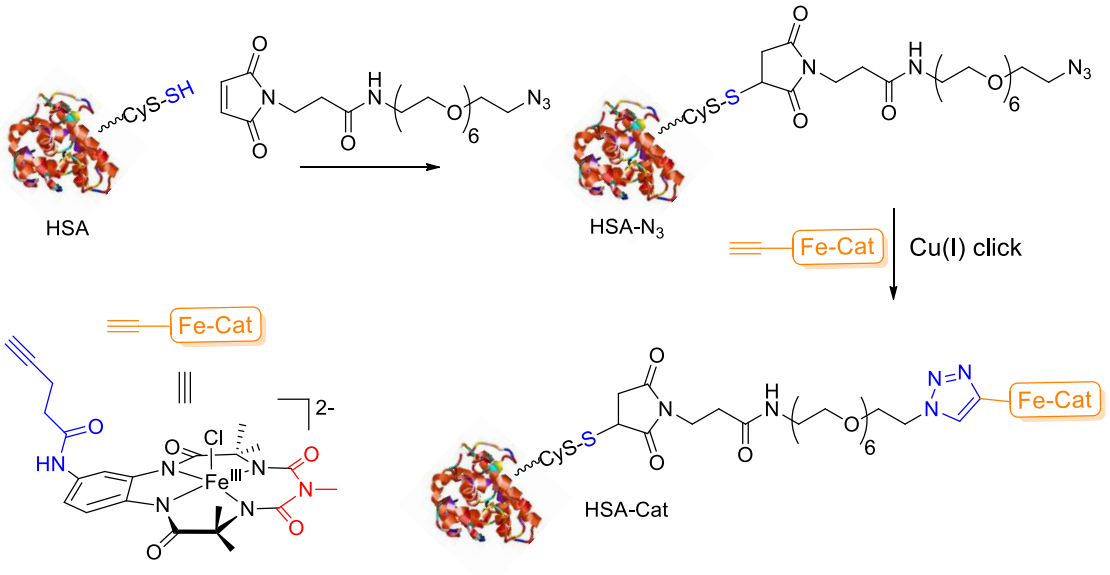

Scheme 4A.4: Synthesis of HSA-Fe-TAML conjugate.

reaction between azide and alkyne (CuAAC) to covalently attach the small molecule peroxidase mimic biuret modified Fe-TAML with the HSA-N_3 conjugate (Scheme 4A.4); (iii) conventional gel electrophoresis of this reaction mixture to localize the HSA-Fe-TAML conjugate (based on the molecular weight the HSA-Fe-TAML conjugate moves considerably slower than the unreacted small molecules) and, finally (iv) application of a mixture of H_2O_2 and a peroxidase substrate (TMB in our experiments) on the polyacyrlamide gel such that it generates a green colored band corresponding to the HSA-Fe-TAML conjugate.

When the above experiments were performed, a colored band was obtained in the gel (Figure 4A.6; right). This is attributed to the peroxidases activity of the biuret-modified Fe-TAML conjugated HSA towards oxidation of TMB to produce a green colored species as has been discussed above (Scheme 4A.3 and Figure 4A.5). To the best of our knowledge this represents a proof of concept where a synthetic functional model of peroxidase enzyme has been used for in-gel visual detection of protein biomarker. The same assay is not possible using the native enzyme HRP as it would denature during gel electrophoresis. Moreover, conjugation of HRP (molecular weight 45 KDa) would significantly alter its molecular weight and hence its mobility during gel electrophoresis. However, the conjugation of a small molecule HRP mimic (mol. wt ~500 Da; Fe-TAML) would not affect the mobility in gel electrophoresis in comparison to the native protein.

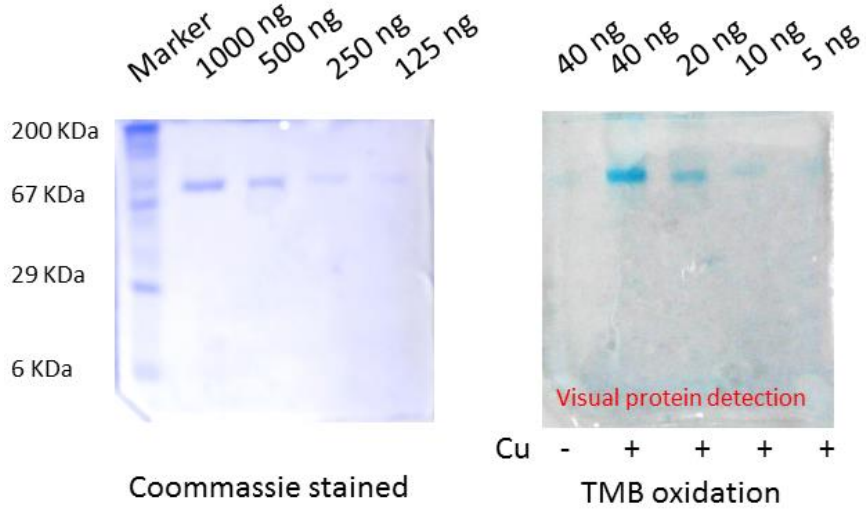

Figure 4A.6: Visualization of protein bands by coomassie staining (left) and TMB oxidation (right) of the SDS page with varying amounts of protein loaded in each well.

In this application therefore, the biuret-modified Fe-TAML synthetic HRP mimic outperforms the native enzyme. The limit of detection obtained in this approach is 20 ng/well with a considerable signal to noise ratio (Figure 4A.6). Coomassie staining which involves just physical adsorption of the coomassie blue indicator with proteins can be used to visualize protein of approximately 125 ng/well of the SDS page (left, Figure 4A.6). In our case, covalent labelling of proteins with peroxidase mimic biuret-modified Fe-TAML can be utilized to visualize approximately 20 ng/well of the page.

To probe that the appearance of the colored band was only as a result of the chemical conjugation of biuret modified Fe-TAML onto HSA-N_3 via "click reaction", we carried out several control reactions. The resulting reaction mixtures were analyzed by gel electrophoresis followed by subsequent treatment with TMB/H_2O_2. As a positive control in the gel, the reaction mixture from the click reaction between biuret modified Fe-TAML and HSA-N_3 that was carried out with all the three required components (Cu^{II}, THPTA and sodium ascorbate) was run (First lane, Figure 4A.7). In three subsequent control lanes, reaction mixtures which contained only two of the three required components were run. Hence lane 2, 3 and 4 (Figure 4A.7) in the gel contained reaction mixtures from the click reactions that was performed in the absence of THPTA, Cu^{II} and sodium ascorbate respectively.

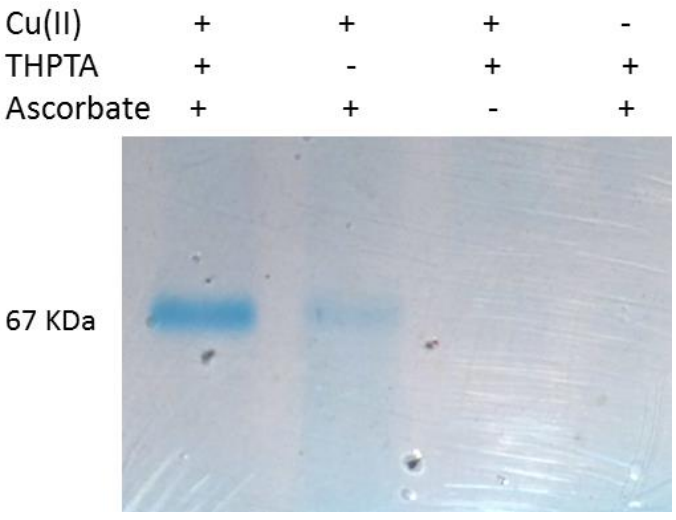

Figure 4A.7: Control experiments for click reagents. Lane 1: positive control, Lane 2: without THPTA, Lane 3: without sodium ascorbate and Lane 4: without copper.

Lane 3 and 4 showed no colored bands and this observation is on expected lines since absence of Cu(II) or ascorbate is known to completely inhibit the click reaction. Therefore, this experiment clearly shows that the bands observed in the gel are due to the formation of the triazole between the alkyne of biuret modified Fe-TAML and HSA-N_3. It also indicates that physical adsorption of Fe-TAML on the protein surface under the reaction conditions does not take place. In lane 2 (reaction carried out without THTPA) the intensity of the band was found to be much less than that in lane 1 indicating that the click reaction in the absence of THPTA is much less efficient.

Finally, the usefulness of this assay will depend on its ability to detect very small quantities of protein in a proteome mixture. Hence we were interested in carrying out model studies to determine if small quantities of HSA-N_3 can be determined by this assay. We therefore performed click reaction with varying concentrations of HSA-N_3 (500 - 30 µg/mL) and alkyne tailed biuret-modified Fe-TAML. The reaction mixtures were then subjected to gel electrophoresis followed by addition of TMB/H_2O_2. The gel electrophoresis data (Figure 4A.8) shows that we were able to detect a reaction with concentration up to 30 µg/mL of HSA-N_3.

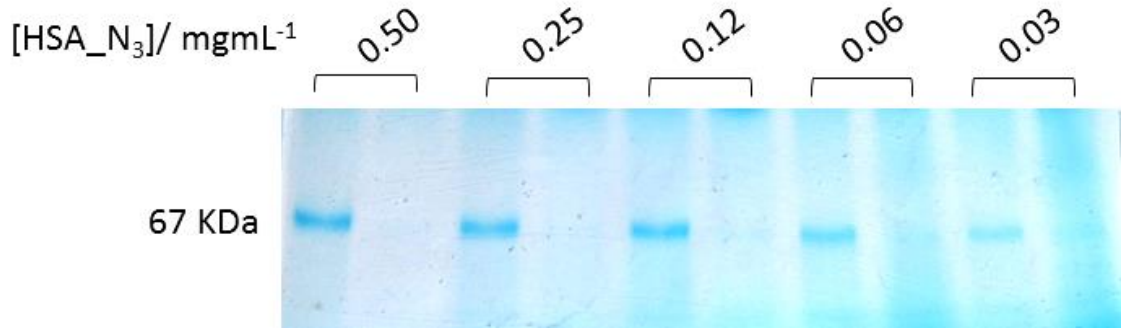

Figure 4A.8: Concentration optimization of click reaction at different HSA-N_3 concentrations. Lane 1, 3, 5, 7 and 9 correspond to typical click reaction mixtures at desired HSA-N_3 concentration and lane 2, 4, 6, 8 and 10 correspond to control reactions in the absence of sodium ascorbate with same HSA-N_3 concentration.

4A.4 Conclusions

In summary, biuret-modified Fe-TAML can be successfully used as a replacement for the native peroxidase HRP due to their high activity and operational stability under

extreme pH and high ionic strength. It can be used to replace fluorescent dyes for ABPP assays. The ability of biuret modified Fe-TAML to generate green color by addition of TMB/H_2O_2 allows for visual detection of proteins using this method we were able to detect HSA-N_3 up to 0.03 mg/mL. Further studies are now being carried out to evaluate real ABPP systems such as the serine protease to evaluate the efficacy of our method.

4A.5 References

(1) Scrimin. P. and Prins. L. J.; *Chemical Society Review*, **2011**, *40*, 4488–4505.

(2) Reimer. L. and Kohl. H, *Transmission Electron Microscopy; Physics of Image Formation, Springer, New York*, **2008**.

(3) Reimer. L., *Scanning Electron Microscopy: Physics of Image Formation and Microanalysis, Springer, New York*, **1998**.

(4) Giessibl. F. J., *Reviews of Modern Physics*, **2003**, *75*, 949.

(5) Raether. H., *Springer-Verlag, Berlin, Heidelberg*, **1988**.

(6) Nie. S. and Emory. S. R., *Science*, **1997**, *275*, 1102.

(7) Engvall. E. and Perlmann. P., *Immunochemistry*, **1971**, *8*, 871.

(8) Weemen. B. K. and Schuurs. A. H. W. M., *FEBS Letters*, **1971**, *15*, 232.

(9) Avrameas. S. and Guilbert. B., *Comptes Rendus Hebdomadaires des Seances de l Academie des Sciences. D: Sciences Naturelles* **1971**, *273*, 2705.

(10) Towbin. H., Staehelin. T., Gordon. J., *Proceedings of the National Academy of Sciences USA* **1979**, *76* (9): 4350.

(11) Renart. J., Reiser. J., Stark. G. R., *Proceedings of the National Academy of Sciences USA* **1979**, *76* (7): 3116.

(12) Azevedo. A. M., Martins. V. n. C., Prazeres. D. M. F., VojinoviA. V., Cabral. J. M. S. and Fonseca. L. P., *Biotechnology Annual Review*, **2003**, *9*, 199.

(13) Collins. T. J., *Accounts of Chemical Research*, **2002**, *35*, 782.

(14) Panda. C., Ghosh. M., Panda. T., Banerjee. R. and Gupta. S. S., *Chemical Communications*, **2011**, *47*, 8016.

(15) Adam, G. C.; Cravatt, B. F.; Sorensen*, E. J. *Chemistry & Biology* **2001**, *8*, 81.

(16) Adam, G. C.; Sorensen, E. J.; Cravatt, B. F. *Nature Biotechnology* **2002**, *20*, 805.

(17) Leung, D.; Hardouin, C.; Boger, D. L.; Cravatt, B. F. *Nature Biotechnology* **2003**, *21*, 687.

(18) Speers, A. E.; Adam, G. C.; Cravatt, B. F. *Journal of the American Chemical Society* **2003**, *125*, 4686.

(19) Speers, A. E.; Cravatt, B. F. *Chemistry & Biology* **2004**, *11*, 535.

(20) Evans, M. J.; Cravatt, B. F. *Chemical Reviews* **2006**, *106*, 3279.

(21) Cravatt, B. F.; Wright, A. T.; Kozarich, J. W. *Annual Review of Biochemistry* **2008**, *77*, 383.

(22) Weerapana, E.; Simon, G. M.; Cravatt, B. F. *Nature Chemical Biology* **2008**, *4*, 405.

(23) Nomura, D. K.; Dix, M. M.; Cravatt, B. F. *Nature Reviews Cancer* **2010**, *10*, 630.

(24) Wilke, K. E.; Francis, S.; Carlson, E. E. *Journal of the American Chemical Society* **2012**, *134*, 9150.

(25) Zuhl, A. M.; Mohr, J. T.; Bachovchin, D. A.; Niessen, S.; Hsu, K.-L.; Berlin, J. M.; Dochnahl, M.; López-Alberca, M. P.; Fu, G. C.; Cravatt, B. F. *Journal of the American Chemical Society* **2012**, *134*, 5068.

(26) Hong. V., Presolski. S. I., Ma. C. and Finn. M. G., A*ngewandte Chemie International Edition*, **2009**, *48*, 9879.

(27) (a) Malvi. B., Panda. C., Dhar. B. B. and Gupta. S. S., *Chemical Communications*, **2012**, *48*, 5289; (b) George, P.; *Biochemical Journal* **1953**, 54, 267.

(28) Song. H. Y., Ngai. M. H., Song. Z. Y., MacAry. P. A., Hobley. J. and Lear. M. J., *Organic and Biomolecular Chemistry*, **2009**, *7*, 3400.

(29) Gao. L. Z., Zhuang. J., Nie. L., Zhang. J. B., Zhang. Y., Gu. N., Wang. T. H., Feng. J., Yang. D. L., Perrett. S. and Yan. X., *Nature Nanotechnology*, **2007**, *2*, 577.

Chapter IV

Part B

Visual Cyanide Sensing Through Signal Amplification

This chapter is adapted from the following publication.

(1) Panda, C.; Dhar, B. B.; Malvi, B.; Bhattacharjee, Y.; Gupta, S. S. *Chemical Communications* **2013**, *49*, 2216..

4B.1 Introduction

Cyanide ion (CN^-) is extremely toxic to humans and animals as it is a very potent inhibitor for heme containing enzymes.[1,2] In spite of its very high toxicity, CN^- is used widely for the industrial synthesis of nylon, plastics and in metallurgy. Even micro molar CN^- contamination from industrial effluents is dangerous for the mammalian world and aquatic life. Hence it is very important to have improved analytical detection techniques to quantify µM levels of CN^-. Most of the methods developed involve the interaction of CN^- with a receptor molecule which results in a direct signal transduction by either turning "on" or "off" the optical property of the switch.[3-16] The final read-outs of the signal include potentiometric,[17,18] spectrophotometric and fluorimetric techniques. Broadly, three different approaches have been employed to design optical sensors for CN^-.[14] The most popular design involves a binding site that is covalently linked to the signalling site such that CN^- interacts with the binding site and induces an optical output signal (change in color/fluorescence). The second strategy utilises a coordination complex (mostly based on copper) in which the copper is coordinated to a fluorescent

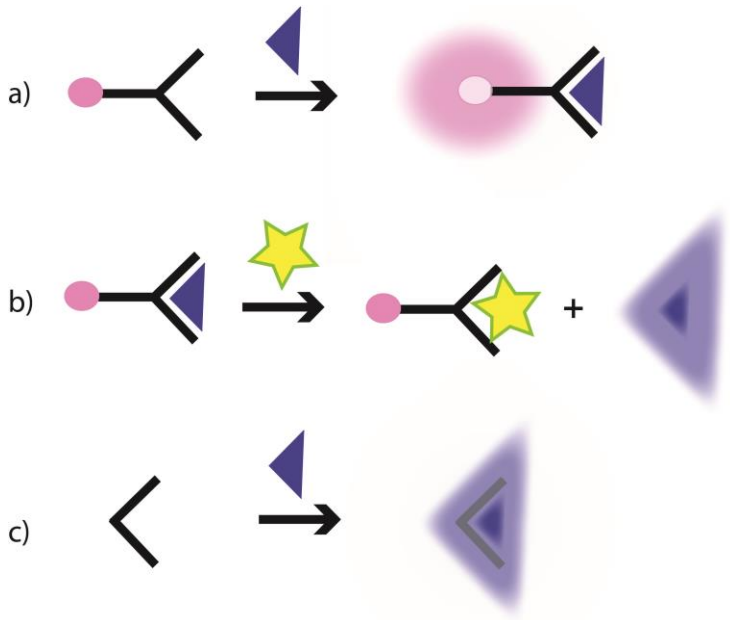

Figure 4B.1: Types of CN^- chemosensors: a) chemosensor bearing a signaling subunit as well as a binding site; b) displacement approach; c) chemodosimeter[14] (adapted with permission).

ligand. The presence of Cu(II) quenches the fluorescence and the complex remains in an off-state. Since CN^- has greater affinity to Cu(II) than that of the designed ligand, the formation of $Cu(CN)_2$ complex turns on the fluorescence upon addition of CN^-. The third method involves a chemodosimetric approach which involves an irreversible chemical reaction that takes place upon an addition of CN^-. Compared to other types of anion selective optical chemosensors,[19-24] CN^- selective optical chemosensors take advantage of two significant and characteristic properties of CN^-, its strong nucleophilicity and high binding affinity towards copper ions. Many of these methods are inadequate since they employ organic co-solvents and also suffer from considerable interference from other anions such as F^-, Cl^- and OAc^-.

However, unlike biological assays[25-27] signal amplification technique is poorly exercised in the chemical approach of analyte sensing. For example, supramolecular allosteric catalysis has been used as a very good signal amplification technique for sensing Cl^- ion at sub micro molar concentration.[28] Other interesting methods involve molecular wire approach,[29] catalytic Heck reaction,[30] and dendritic chain reactions[31] to amplify the signal for analyte detection. Recently gold nanoparticles have been used to improve biological assays by providing multivalency.[32] Most of these chemical assays use either purely organic solvents or a mixure of organic and aqueous solvents in contrast to biological assays which are completely performed in aqueous medium. This limits the scope of these chemical assays since most biologically relevant analytes are present in water. Hence development of synthetic systems that detect analytes in aqueous media with high selectivity and sensitivity is extrememely important from both biological and environmental perspective.

We have developed a method based on the consecutive catalytic reaction of the enzyme catalase and our HRP mimic Fe-MSNs. This allows visual detection of CN^- in aqueous media with the lowest detection limit of 0.9 μM without interference from other anions.[33] Recently we have developed biuret-modified Fe-TAML immobilized inside mesoporous silica nanoparticles (Fe-MSNs),[34] that are excellent functional mimics of the enzyme HRP. Fe-MSNs have several attributes that make them very attractive as replacement for HRP (i) Fe-MSNs exhibit excellent reactivity towards 3,3′,5,5′-Tetramethylbenzidine (TMB) in presence of H_2O_2 to generate a visually detectable green

oxidation product at neutral pH, (ii) they exhibit very high stability, especially at low pH, high ionic strength and in presence of anions like CN^- which is known to inhibit HRP, (iii) biuret-modified Fe-TAML catalysts are mostly grafted inside the MSN pores (2-3 nm) which limits their interaction with other enzymes during biological assays and (iv) the amount of immobilized catalyst and the distance between them can be controlled to achieve varying reactivity.[35,36] In this chapter we show that Fe-MSNs can be used as catalyst in tandem with the enzyme catalase for visual detection of the toxic CN^- in water via signal amplification. This protocol also demonstrates that the amount of reporter signal generated is approximately 8 folds that of the added CN^- ion.[33] Our analytical method consists of three consecutive reactions: (i) inhibition of the enzyme catalase by CN^-, (ii) disproportionation of H_2O_2 to water and oxygen by CN^- free catalase and (iii) activation of the residual H_2O_2 by Fe-MSNs to oxidize TMB to produce a green color which can be visually detected and quantified (Scheme 4B.1).

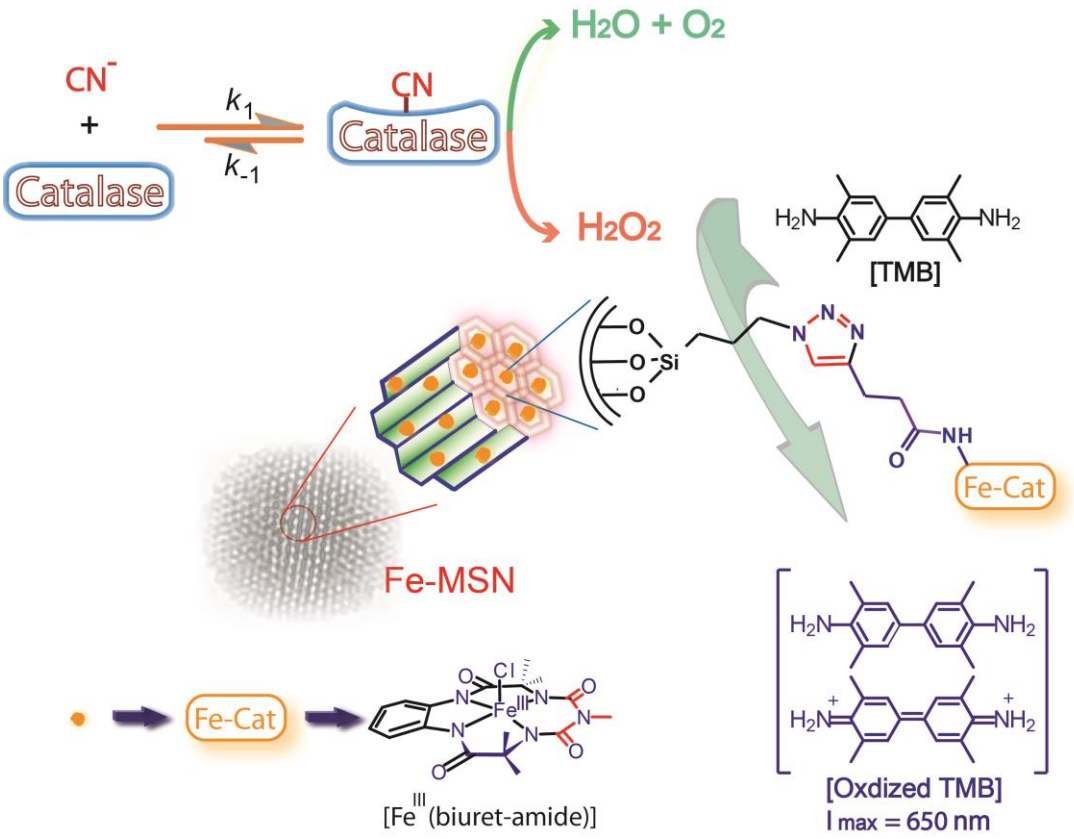

Scheme 4B.1: Visual CN^- detection assay using biuret-modified Fe-TAML immobilized mesoporous silica nanoparticles (Fe-MSN).[33]

It is very well known in literature that CN^- binds to the enzyme catalase very strongly and the binding constant is much higher than other common ions present in water.[1,2] We therefore envisaged that increasing the amount of CN^- to catalase would lead high residual H_2O_2 in the catalytic disproportionation of H_2O_2, which can then be converted to a colorimetric reporter molecule using our HRP mimic Fe-MSNs. In short, when no CN^- is added to catalase, the fast reaction rates of the enzyme would lead to complete disproportionation of H_2O_2. Therefore, addition of Fe-MSNs and TMB would not lead to any detectable colorimetric signal as Fe-MSNs are capable of oxidizing TMB only in the presence of H_2O_2. However, when CN^- would be added to catalase, its catalytic disproportionation reaction will be inhibited and that will lead to incomplete disproportionation of H_2O_2. The residual H_2O_2 can then be utilized by Fe-MSNs to oxidize TMB to generate a colorimetric signal which can be co-related to the amount of CN^- added.

4B.2 Experimental section

4B.2.1 *Materials*

Fe-MSN was synthesized by a procedure as reported earlier.[34] Catalase, Horseradish peroxidase (HRP), 3, 3′, 5, 5′-Tetramethylbenzidine (TMB) were obtained from sigma Aldrich and used without further purification. Potassium dihydrogen phosphate, hydrogen peroxide used was from Merck India and sodium cyanide from S. D Fine chemicals. De-ionized water was used for all the experiments.

4B.2.2 *Physical measurements*

All the UV-vis measurements were carried in Cary 300 spectrophotometer. For the calibration curve, absorbance maximum was measured at 650 nm for the green colored oxidized TMB. pH meter used was from Lab India and Inductively coupled plasma-optical emission spectroscopy (ICP-OES) from Spectro arcos.

4B.2.3 *Detection of CN^- in the linear range of 0 to 156 ppb*

Preparation of phosphate buffers

Stock solution of 1.0 M phosphate buffer of pH 7 was prepared using potassium dihydrogen phosphate. pH was adjusted by adding aqueous potassium hydroxide solution and persevered at 4 °C for further use.

Stock solutions

1) 50 mM sodium cyanide: 24.50 mg was dissolved in DI water (10 mL). This was further diluted to have the desired strength.

2) 0.1 mg/mL Catalase: 10 mg of solid was dissolved in 100 mL of 10 mM PB of pH 7 (~0.4 μM considering tetramer molecular weight ~250 KDa)

3) 0.8 M hydrogen peroxide: Desired volume of commercial hydrogen peroxide in DI water. Molar extinction coefficient of 72.8 $M^{-1}cm^{-1}$ at 230 nm was used to find the concentration of commercial stock.[37]

4) 50 mM solution of TMB: 12 mg of solid was dissolved in 1 mL of 0.1N aqueous hydrochloric acid. The reaction mixture was gently heated to warm, if necessary.

5) 1 mg/mL of Fe-MSN: 2 mg of solid Fe-MSN was dispersed well in DI water (2 mL) by sonication.

6) 50 mM solution of different anions: Desired amounts of salts were dissolved in 1 mL of DI water

***Procedure*:** In a 2.0 mL eppendorf tube, 410 μL of de-ionized water, 5 μL of phosphate buffer (1 M, pH 7), desired volume of 0.5 mM NaCN and 35 μL of 0.1 mg/mL catalase stock solutions were mixed and allowed to stand at room temperature with occasional shaking for 5 minutes. 5 μL of 0.8 M hydrogen peroxide solution was added to the mixture and allowed to stand for another 5 minutes with gentle shaking. Evolution of bubbles confirmed the disproportionation of hydrogen peroxide to water and oxygen. Then 5 μL of 50 mM TMB solution and 35 μL of 1 mg/mL Fe-MSN stock were added to it (Fe-MSN particles were dispersed by sonication each time before addition to the reaction mixture). DI water was used to adjust final volume of 500 μL in each case. The reaction mixture was mixed well by shaking for seven to eight minutes and then 400 μL of reaction mixture was diluted to 800 μL (hence OD was multiplied by 2 for the calculation of $[TMB]_{oxidized}$, Table 4B.1) by adding DI water and absorbance at 650 nm was taken at the 10^{th} minute of catalyst addition.

Final concentrations

1) [CN^-]: (0 to 12 μM or 0 to 312 ppb)

2) Catalase: ~0.028 μM

3) Hydrogen peroxide: 8 mM

4) TMB: 0.5 mM

5) Fe-MSN: 70 μg/mL (biuret-modified Fe-TAML = 3.5 μM, by ICP 0.05 mmoles of catalysts are present per gram of Fe-MSN).

Table 4B.1: CN^- detection in the linear range of 0 to 156 ppb

Sl. No.	Vol. of 0.5 mM CN^-/ μL	[CN^-]/ μM	[CN^-]/ ppb	Abs at 650 nm	*$[TMB]_{ox}$/ μM	[CN^-] : $[TMB]_{ox}$
1	0	0	0	0.077	3.95	-
2	0.75	0.9	23.4	0.253	12.97	1 : 14.41
3	1.50	1.8	46.8	0.357	18.31	1 : 10.17
4	2.50	3.0	78.0	0.547	28.05	1 : 9.35
5	3.50	4.2	109.2	0.696	35.70	1 : 8.50
6	5.0	6.0	156.0	1.040	53.33	1 : 8.88
7	7.50	9.0	234.0	1.263	64.77	1 : 7.19
8	10.0	12.0	312.0	1.310	67.18	1 : 5.59

*$[TMB]_{oxidized}$ = (2 × OD at 650 nm)/ 39000, $\varepsilon_{650\ nm}$ = 39000 $M^{-1}cm^{-1}$

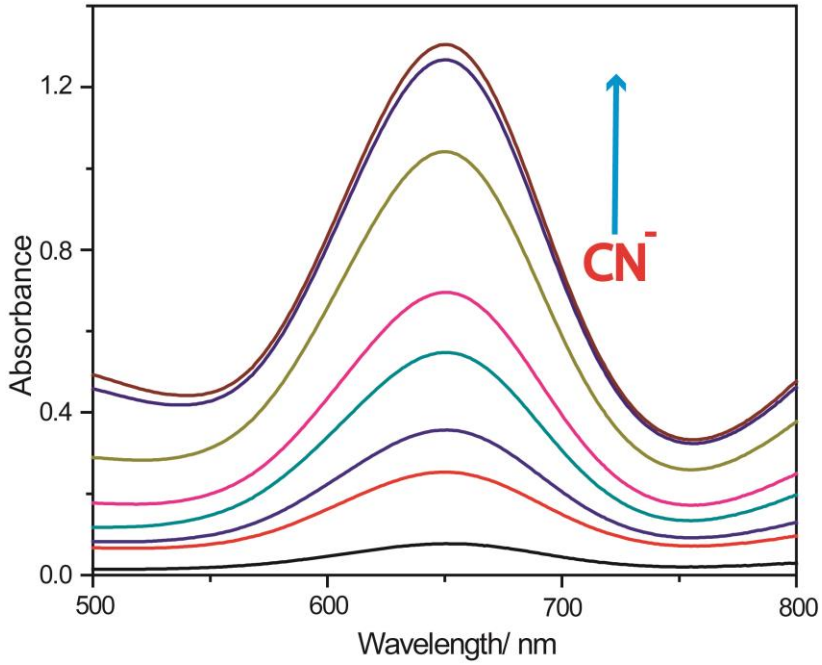

Figure 4B.2: Plot of absorbance of $[TMB]_{oxidized}$ vs. wavelength with the increase in CN^-.

4B.2.4 *Detection of CN^- in the linear range of 0 to 5.2 ppm*

The same above procedure was followed; only difference being addition of 10 µL of 1 mg/mL catalase in place of 35 µL of 0.1 mg/mL catalase and desired volume of 5 mM CN^- in place of 0.5 mM CN^-. DI water was used to compensate the volume difference.

Table 4B.2: CN^- detection in the linear range of 0 to 5.2 ppm

Sl. No.	Vol. of 5 mM CN^-/ µL	$[CN^-]$/ µM	$[CN^-]$/ ppm	Abs at 650 nm	*$[TMB]_{ox}$/ µM	$[CN^-]$: $[TMB]_{ox}$
1	0	0	0	0.070	3.60	-
2	5.0	50	1.3	0.310	15.70	1 : 0.31
3	10.0	100	2.6	0.593	30.05	1 : 0.30
4	12.5	125	3.25	0.789	40.41	1 : 0.32
5	15.0	150	3.9	0.938	48.10	1 : 0.32
6	20.0	200	5.2	1.140	58.37	1 : 0.29
7	25.0	250	6.5	1.220	62.74	1 : 0.25

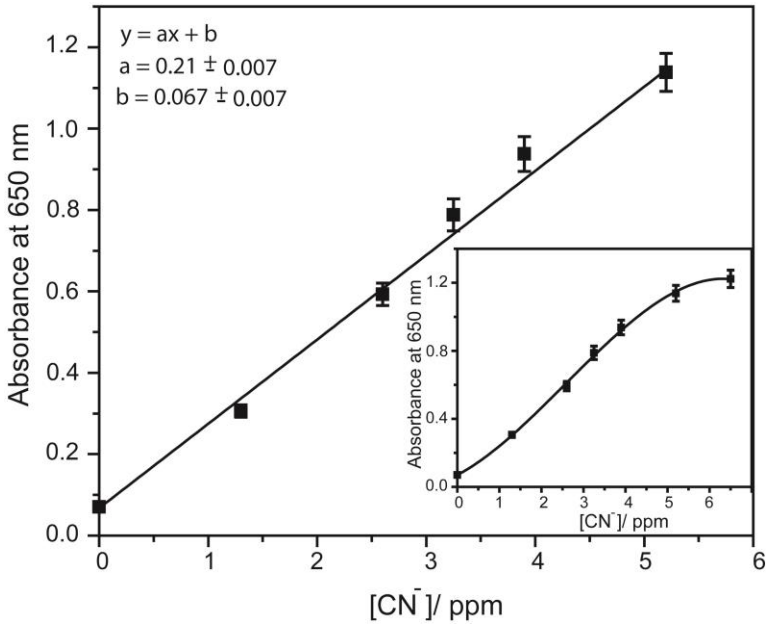

Figure 4B.3: Detection of CN^- in the linear range of 0 to 5.2 ppm.

4B.2.5 *Selectivity towards CN^- over other common anions*

The same above procedure was followed with addition 10 µL of 0.5 mM CN^- or 50 mM other anions.

Table 4B.3: Selectivity of the assay towards CN^-

Sl. No.	Anion	[Anion]/ µM	OD at 650 nm
1	No anion	-	0.069 ± 0.003
2	Cyanide	5	1.200 ± 0.060
3	Bromide	500	0.072 ± 0.004
4	Chloride		0.082 ± 0.004
5	Acetate		0.065 ± 0.003
6	Fluoride		0.075 ± 0.004
7	Bicarbonate		0.069 ± 0.003
8	Formate		0.071 ± 0.003
9	Iodide		0.070 ± 0.003
10	Nitrate		0.068 ± 0.003
11	Thiocyanate		0.065 ± 0.003

12	Sulphate		0.071 ± 0.003

4B.2.6 *HRP inhibition by CN^-*

To 900 µL of 2 mg/mL HRP (~45 µM) stock in 10 mM PB of pH 7 was added 100 µL of desired concentrations of CN^- stock. The final concentration of HRP was 40.5µM and that of sodium cyanide as mentioned in table 4B.4 below. The mixture was allowed to stand for 2 min and UV-vis absorbance spectra were taken (Figure 4B.4). The typical soret band was shifted from 403 nm to 420 nm with the increase of CN^- concentration. The OD change at 403 nm for each CN^- addition was measured (Table 4B.4, Figure 4B.4).

Table 4B.4: Spectral data of HRP soret band with the increase in $[CN^-]$

Sl. No.	$[CN^-]_{final}$/ µM	OD at 403 nm	ΔOD at 403 nm
1	0	0.814	0
2	0.5	0.811	0.003
3	2.5	0.761	0.053
4	5	0.705	0.109
5	9	0.649	0.164
6	12.5	0.632	0.182
7	25	0.617	0.197
8	50	0.579	0.234
9	200	0.559	0.255
10	500	0.549	0.265

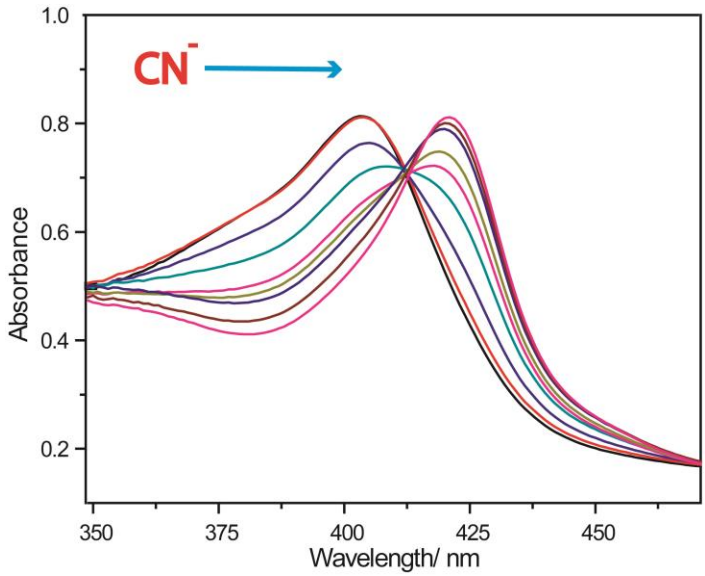

Figure 4B.4: UV-vis spectral change of HRP (soret band shift) with the addition of CN^-

4B.2.7 *Catalase inhibition by CN^-*

To 900 µL of 5 mg/mL catalase (~20 µM) stock in 10 mM PB, pH 7 was added 100 µL of desired concentrations of CN^- stock. The final concentration of catalase was 18 µM and that of sodium cyanide as mentioned in the table 4B.5 below. The mixture was allowed to stand for 2 min and UV-vis absorbance spectra were taken. The typical soret band was shifted from 405 nm to 425 nm with the increase of CN^- concentration. The OD change at 405 nm for each CN^- addition was measured (Table 4B.5, Figure 4B.5).

Table 4B.5: Catalase inhibition by CN^-

Sl. No.	$[CN^-]_{final}$/ µM	OD at 405 nm	ΔOD at 405 nm
1	0	0.969	0
2	5	0.951	0.017
3	25	0.893	0.075
4	50	0.860	0.109
5	150	0.822	0.147
6	250	0.815	0.154
7	500	0.807	0.162
8	2500	0.767	0.202

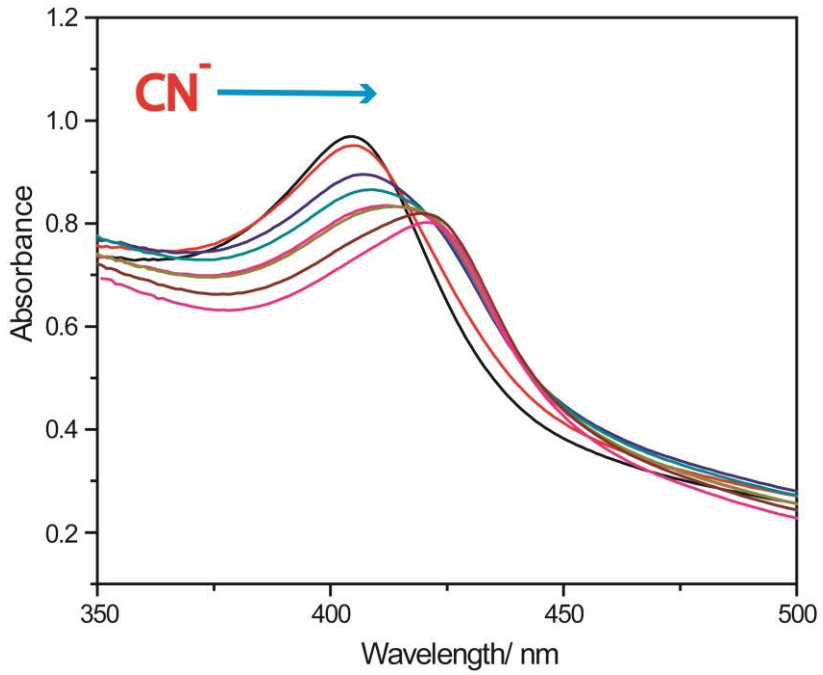

Figure 4B.5: UV-vis spectral change of catalase (soret band shift) with the addition of CN^-.

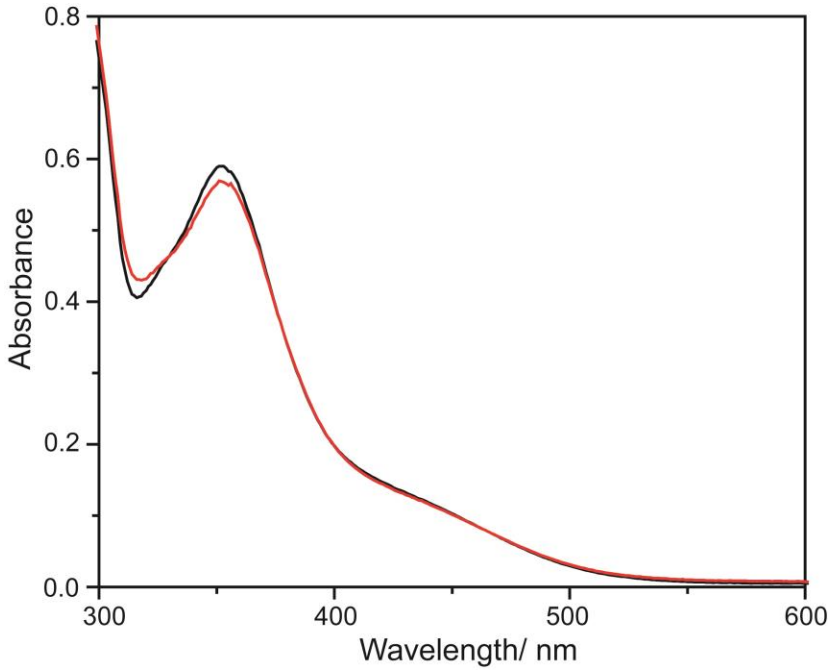

Figure 4B.6: UV-vis spectrum of 1.5×10^{-3} M biuret-modified Fe-TAML (**1a**) in presence (red) and absence (black) of CN^- in water.

4B.2.8 *Reactivity comparison of HRP and Fe-MSN in presence of CN^-*

To 960 µL of DI water, 10 µL of 1 M PB of pH 7 and 10 µL HRP (0.1 mg/ mL) or Fe-MSN (1 mg/ mL), desired volume of 50 mM CN^- solution was added and allowed to stand for 5 minutes. Then 10 µL each of TMB (50 mM) and H_2O_2 (0.8 M) were added, waited for one minute and then Uv-vis spectra were taken. The total volume of reaction mixture was adjusted to 1000 µL varying DI water.

Table 4B.6: Reactivity comparison of HRP and Fe-MSN in presence of CN^-

Sl. No.	Vol of 50 mM CN^-/ µL	$[CN^-]_{final}$/ mM	HRP		Fe-MSN	
			$OD_{650\ nm}$	% Reactivity	$OD_{650\ nm}$	% Reactivity
1	0	0	2.670	100	1.430	100
2	10	0.5	1.825	68	1.358	95
3	20	1.0	1.456	54	1.429	100
4	40	2.0	1.310	49	1.432	100
5	50	2.5	1.010	38	1.415	99
6	70	3.5	0.904	34	1.287	90
7	100	5.0	0.707	26	1.359	95
8	150	7.5	0.444	17	1.320	92
9	250	12.5	0.279	10	1.400	98

4B.2.9 *Oxidation of TMB by Fe-MSN in presence of CN^- and other anions*

To 960 µL of DI water 10 µL of 1 M PB of pH 7 and 10 µL of Fe-MSN (1 mg/ mL), 10 µL of 50 mM CN^- or other anions were added and allowed to stand for 5 minutes. Then 10 µL each of TMB (50 mM) and H_2O_2 (0.8 M) were added, mixed for one minute and UV-vis spectra were taken. The total volume of reaction mixture was adjusted to 1000 µL varying DI water.

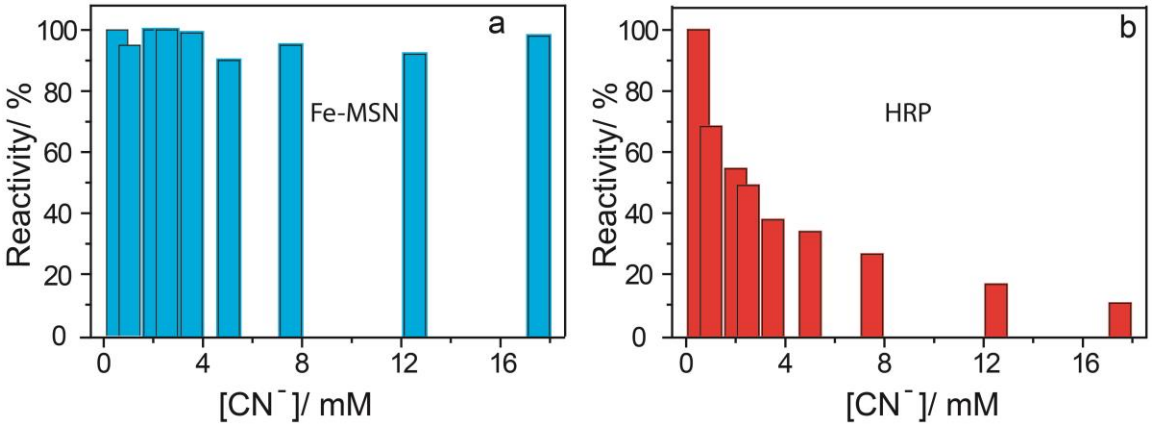

Figure 4B.7: Comparison of HRP (red bars) and Fe-MSN (blue bars) reactivity in presence of CN^-.

Table 4B.7: Reactivity comparison of Fe-MSN in presence of different anions

Sl. No.	Anion	$OD_{650\ nm}$	% Reactivity
1	No anion	1.143 ± 0.031	100
2	Acetate	1.180 ± 0.050	~ 100
3	Bromide	1.177 ± 0.052	
4	Chloride	1.142 ± 0.063	
5	Cyanide	1.189 ± 0.045	
6	Fluoride	1.139 ± 0.061	
7	Bicarbonate	1.133± 0.050	
8	Formate	1.090± 0.040	
9	Iodide	1.143 ± 0.057	
10	Nitrate	1.165 ± 0.051	
11	Thiocyanate	1.143 ± 0.052	
12	Sulphate	1.200 ± 0.052	

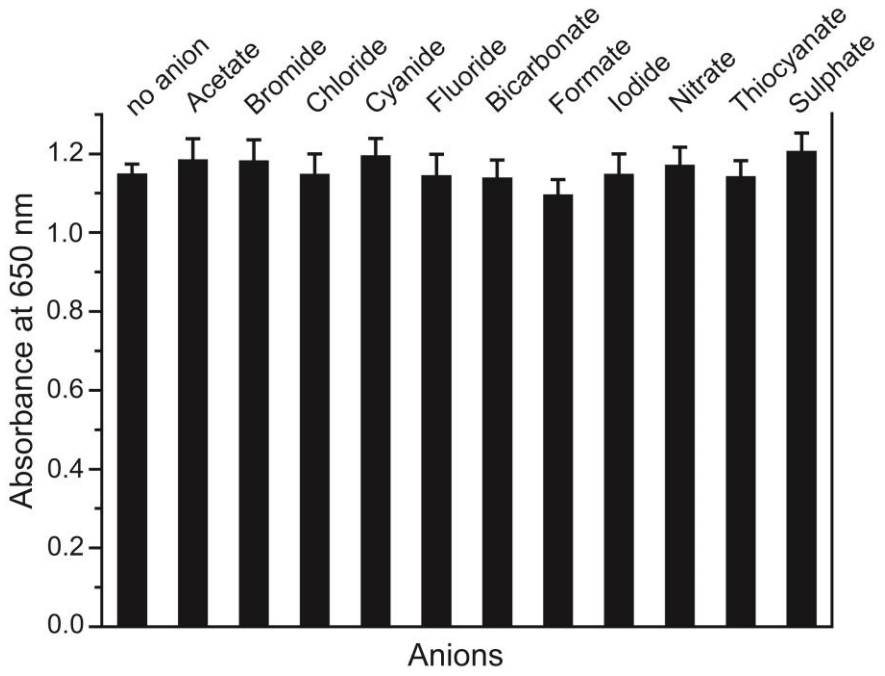

Figure 4B.8: Bar plot for TMB oxidation in presence of different anions

4B.2.10 *Spectrophotometric determination of half-lives of H_2O_2 in presence of CN^-*[38]

In a 2.0 mL eppendorf tube, 900 - 910 μL of DI water, 10 μL of phosphate buffer (1 M, pH 7), desired volume of 0.5 mM NaCN and 70 μL of 0.1 mg/mL catalase stock solutions were mixed and allowed to stand at room temperature with occasional shaking for 5 min. 10 μL of 0.8 M hydrogen peroxide solution was added to the mixture. Immediately mixing within 10 seconds the disproportionation is followed spectrophotometrically by tracking the rate of decrease of absorbance at 230 nm typical for hydrogen peroxide (ε = 72.8 $M^{-1}cm^{-1}$).[37] The duration of each kinetic run was chosen such that there was no effect from bubble formation. The decay curve was very smooth and fitted very nicely according to first order rate law. The $t_{1/2}$ of each set containing various amount of CN^- was calculated and the number of half-lives in 5 minutes was calculated from these values (H_2O_2 decomposition duration for the CN^- detection experiment). The UV-vis spectral kinetics data indicated number of half-life decrease with increasing CN^- concentration.

Table 4B.8: Half-life calculations for H_2O_2 in presence of CN^-

Sl. No.	Vol. of 0.5 mM CN^-/ µL	$[CN^-]_{final}$/ µM	k_{obs}/ s^{-1}	$t_{1/2}$/ s^{-1}	No. of half-lives in 5 min
1	0.0	0.00	0.023	30	10.0
2	0.5	0.25	0.019	36	8.33
3	1.0	0.50	0.016	43	7.00
4	2.5	1.25	0.015	47	6.40
5	5.0	2.50	0.013	52	5.77
6	10.0	5.00	0.011	62	4.84

4B.3 Results and discussions

To achieve this, the kinetics of H_2O_2 disproportionation by catalase in the presence and absence of CN^- was studied first to estimate the residual H_2O_2 in the reaction as a function of time. The catalytic disproportionation of H_2O_2 was measured spectrophotometrically by tracking the rate of decrease of absorbance at 230 nm that is typical for H_2O_2 (ε = 72.8 $M^{-1}cm^{-1}$).[37] The decay in the absorbance of H_2O_2 fitted very nicely according to the first order rate law. It was determined that the half-life of the reaction ($t_{1/2}$) was increased with increasing concentration of CN^- (Table 4B.8). From the $t_{1/2}$ values it was calculated that in a period of 5 min, the number of half-lives of the reaction would decrease from 10 to 5 upon addition of 0 to 10 µM of CN^- (Table 4B.8). To ascertain that the reactivity of catalase was unaffected by other ions, we performed control reactions where the disproportionation of H_2O_2 was carried out in presence of other ions like F^-, Cl^- and OAc^-. It was observed that the half-life of the disproportionation reaction remained unaltered in the presence of other ions. Hence, it was concluded that the inhibition of catalase under the assay conditions were specific for CN^- and this binding can be used to inhibit disprotortionation of H_2O_2 in amounts which is proportional to the added CN^-. Finally, Fe-MSNs catalyzed oxidation of TMB with H_2O_2 has to be used to generate a visual signal that is proportional to the amount of H_2O_2 present. This would then lead to a colored reporter molecule that is several times higher than the added CN^- leading to signal amplification of the analyte. However, it must be first ascertained that CN^- does not bind to Fe-MSNs and inhibits its activity; otherwise a

linear response for the presence of H_2O_2 will not be obtained. The titration of the complex biuret-modified Fe-TAML with CN^- shows virtually no change in its UV-vis spectra thereby indicating the CN^- did not bind to the Fe(III) complex (Figure 4B.6). Further, the reactivity of the Fe-MSNs towards oxidation of TMB in presence of H_2O_2 remained unchanged in the presence of CN^- as well as with a host of anions such as Cl^-, F^-, OAc^- among others (Table 4B.7, Figure 4B.8). Interestingly, when the same experiments were performed with the enzyme HRP, it was observed that CN^- did bind to HRP and the rates of TMB oxidation decreased up to 90% with increase in CN^- (Table 4B.4, Figure 4B.4 and 4B.7). Therefore, our HRP mimic Fe-MSNs would be much better suited for the estimation of CN^- by our methodology than the native enzyme HRP. We then proceeded to combine both these reactions to see if CN^- could be detected colorimetrically in a quantitative manner. For detection of CN^-, 28 nM of catalase was first incubated with varying amount of CN^- for five minutes and then H_2O_2 (0.8 mM) was added to it. After 5 min of incubation with H_2O_2, Fe-MSNs and TMB were added and the green color observed was recorded in UV-vis spectrophotometer after 10 min (Figure 4B.9, Left, *inset*).

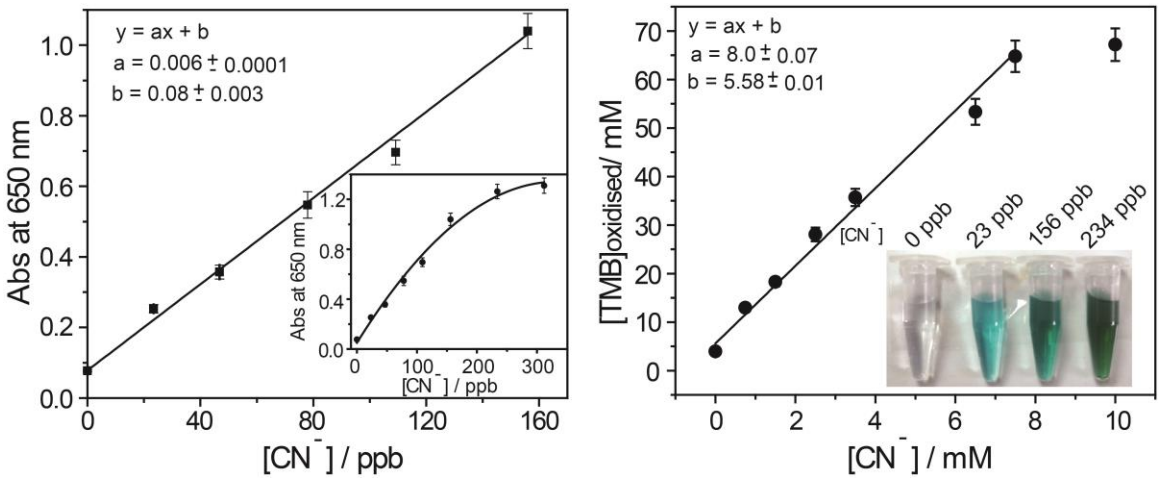

Figure 4B.9: Left: Linear calibration plot of CN^- vs. OD at 650 nm. Inset plot shows dependence of OD on CN^- concentration. Inset: photos for different concentration of CN^-; from left: 0 ppb, 23.4 ppb, 156 ppb and 234 ppb; **Right:** Concentration of CN^- incorporated vs. concentration of TMB oxidized. The slope indicates 8-fold signal amplification.

Control experiments when no CN^- was added remained colourless since nearly all the H_2O_2 was consumed by enzyme catalase in 5 min (10 half-lives by kinetic studies). Figure 4B.9 represents the increase in absorbance of the reporter TMB at 650 nm as a function of added CN^-. The plot shows that the OD increases with increasing CN^- and finally reaches a saturation level.

A linear dependence of absorbance versus CN^- concentration is obtained in the range of 0 to 156 ppb with the limit of detection (LOD) 23.4 ppb (0.9 µM). The allowed limit of CN^- (1.9 µM) in drinking water by world health organization falls in the linear range of detection illustrated in this method renders suitable for analysis of real-life sample. A plot of the concentration of oxidized TMB versus the concentration of added CN^- produces a straight line with a slope of approximately 8 (Figure 4B.9, Right). This indicates that on average the output signal was amplified 8-folds with respect to the CN^- ion present. We believe that this represents a first report of detection of CN^- anion in water by catalytic signal amplification.

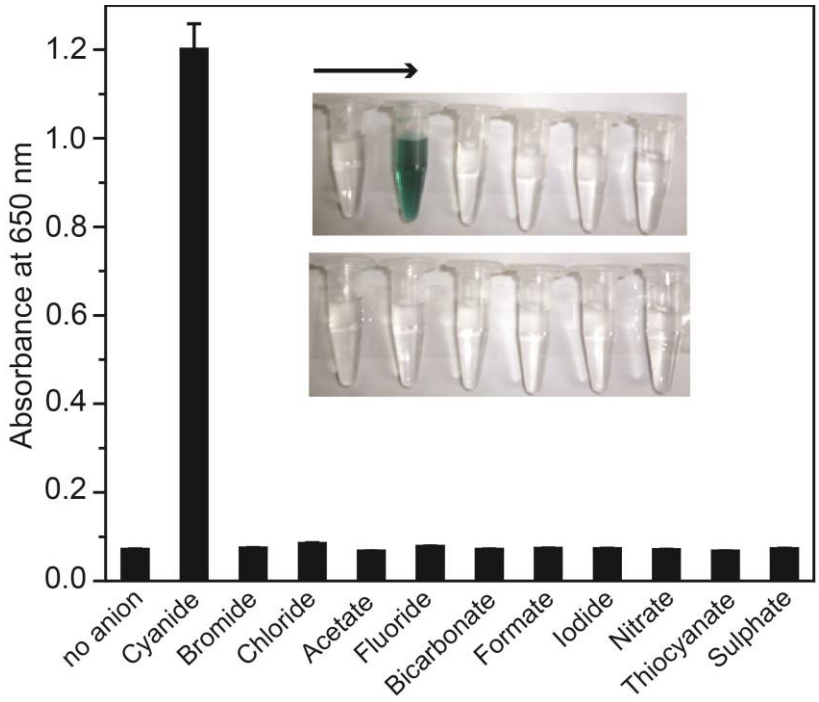

Figure 4B.10: Bar plot showing selectivity for 5 mM CN^- in comparison to 500 mM of other common anions. The inset shows corresponding photos in the same order of the bar plot.

This methodology has several attributes which makes it exciting. Since this analytical method is dependent on the cascade of reactions, changes in the concentration of catalase, H_2O_2 and Fe-MSNs would lead to different degree of output signals. For example, when 80 nM of catalase is used instead of 28 nM, the observed signal remained linear from 0 to 5.2 ppm although the LOD increases to 1.3 ppm (Table 4B.2, Figure 4B.3). Hence by simple varying kinetic parameters this method can be utilized to suitably detect CN^- over a broad range of concentration. However here signal amplification was not achieved because of limited solubility of TMB in water. Since catalase binds to CN^- very strongly, this method displayed very high selectivity towards CN^- ion over other common anions present in wastewater. Even the usage of hundred fold higher concentration of various anions (F^-, Cl^-, Br^-, I^-, SCN^-, $HCOO^-$, NO_3^-, OAc^-, SO_4^{2-} and HCO_3^-) did not elicit any response, as is indicated by plot and accompanying photographs (Figure 4B.10). Since all the experiments were done in DI water, we wanted to see if this method can be extended to regular tap water that is known to contain metal ions that may decompose H_2O_2. Therefore, known amounts of CN^- were spiked into tap water and quantification using the same calibration curve performed in DI water afforded accurate results (Figure 4B.9).

4B.4 Conclusions

In summary, the HRP mimic Fe-MSNs developed by us have been used in tandem with the enzyme catalase for the colorimetric detection of CN^- in aqueous media through signal amplification. This represents one of the very few examples in which catalytic signal amplification has been used for the detection of anions in water. Although the LOD was determined to be 0.9 μM, we believe it can be lowered several folds by using substrates which generate reporter molecules that either have very high extinction co-efficient or generate fluorescence upon oxidation. Also, improvement in the catalytic activity of biuret-modified Fe-TAML would also help to lower detection limits. Such efforts are underway in our laboratory.

4B.5 References

(1) Bidwai, A.; Witt, M.; Foshay, M.; Vitello, L. B.; Satterlee, J. D.; Erman, J. E. *Biochemistry* **2003**, *42*, 10764.

(2) Kremer, M. L. *The Journal of Physical Chemistry* **1981**, *85*, 835.

(3) Ding, Y.; Li, T.; Zhu, W.; Xie, Y. *Organic & Biomolecular Chemistry* **2012**, *10*, 4201.

(4) Divya, K. P.; Sreejith, S.; Balakrishna, B.; Jayamurthy, P.; Anees, P.; Ajayaghosh, A. *Chemical Communications* **2010**, *46*, 6069.

(5) Jiao, L.; Liu, M.; Zhang, M.; Yu, C.; Wang, Z.; Hao, E. *Chemistry Letters* **2011**, *40*, 623.

(6) Kim, H. J.; Ko, K. C.; Lee, J. H.; Lee, J. Y.; Kim, J. S. *Chemical Communications* **2011**, *47*, 2886.

(7) Kim, H. J.; Lee, H.; Lee, J. H.; Choi, D. H.; Jung, J. H.; Kim, J. S. *Chemical Communications* **2011**, *47*, 10918.

(8) Liu, Y.; Ai, K.; Cheng, X.; Huo, L.; Lu, L. *Advanced Functional Materials* **2010**, *20*, 951.

(9) Lou, X.; Zeng, Q.; Zhang, Y.; Wan, Z.; Qin, J.; Li, Z. *Journal of Materials Chemistry* **2012**, *22*, 5581.

(10) Ma, J.; Dasgupta, P. K. *Analytica Chimica Acta* **2010**, *673*, 117.

(11) Ma, J.; Dasgupta, P. K.; Zelder, F. H.; Boss, G. R. *Analytica Chimica Acta* **2012**, *736*, 78.

(12) Reddy G, U.; Das, P.; Saha, S.; Baidya, M.; Ghosh, S. K.; Das, A. *Chemical Communications* **2013**, *49*, 255.

(13) Tomasulo, M.; Sortino, S.; White, A. J. P.; Raymo, F. M. *The Journal of Organic Chemistry* **2005**, *71*, 744.

(14) Xu, Z.; Chen, X.; Kim, H. N.; Yoon, J. *Chemical Society Reviews* **2010**, *39*, 127.

(15) Yao, L.; Zhou, J.; Liu, J.; Feng, W.; Li, F. *Advanced Functional Materials* **2012**, *22*, 2667.

(16) Zelder, F. H. *Inorganic Chemistry* **2008**, *47*, 1264.

(17) Safavi, A.; Maleki, N.; Shahbaazi, H. R. *Analytica Chimica Acta* **2004**, *503*, 213.

(18) Shan, D.; Mousty, C.; Cosnier, S. *Analytical Chemistry* **2003**, *76*, 178.

(19) Gale, P. A. *Accounts of Chemical Research* **2006**, *39*, 465.

(20) Gunnlaugsson, T.; Glynn, M.; Tocci, G. M.; Kruger, P. E.; Pfeffer, F. M. *Coordination Chemistry Reviews* **2006**, *250*, 3094.

(21) Kim, S. K.; Lee, D. H.; Hong, J.-I.; Yoon, J. *Accounts of Chemical Research* **2008**, *42*, 23.

(22) Lee, H. N.; Xu, Z.; Kim, S. K.; Swamy, K. M. K.; Kim, Y.; Kim, S.-J.; Yoon, J. *Journal of the American Chemical Society* **2007**, *129*, 3828.

(23) Martínez-Máñez, R.; Sancenón, F. *Chemical Reviews* **2003**, *103*, 4419.

(24) Yoon, J.; Kim, S. K.; Singh, N. J.; Kim, K. S. *Chemical Society Reviews* **2006**, *35*, 355.

(25) Scrimin, P. and Prins, L. *Chemical Society Reviews* **2011**, 40, 4488; Zhu, L. and Anslyn, E. V.; *Angewandte Chemie International Edition* **2006**, 45, 1190.

(26) Graf, N.; Go¨ritz, M. and Kra¨mer, R.; *Angewandte Chemie International Edition* **2006**, 45, 4013.

(27) Saghatelian, A.; Guckian, K. M.; Thayer, D. A. and Ghadiri, M. R.; *Journal of the American Chemical Society* **2003**, 125, 344.

(28) Yoon, H. J. and Mirkin, C. A.; *Journal of the American Chemical Society* **2008**, 130, 11590.

(29) Swager, T. M.; *Accounts of Chemical Research* **1998**, 31, 201.

(30) Wu, Q. and Anslyn, E. V.; *Journal of the American Chemical Society* **2004**, 126, 14682.

(31) Karton-Lifshin, N. and Shabat, D.; *New Journal of Chemistry* **2012**, 36, 386; Xu, M.-H.; Lin, J.; Hu, Q.-S. and Pu, L.; *Journal of the American Chemical Society* **2002**, 124, 14239.

(32) Bonomi, R.; Cazzolaro, A.; Sansone, A.; Scrimin, P. and Prins, L. J.; *Angewandte Chemie International Edition* **2011**, 50, 2307; Lei, J. and Ju, H.; *Chemical Society Reviews* **2012**, 41, 2122; Liu, J. and Lu, Y.; *Journal of the American Chemical Society* **2003**, 125, 6642; Miranda, O. R.; Chen, H.-T.; You, C.-C.; Mortenson, D. E.; Yang,

X.-C.; Bunz, U. H. F. and Rotello, V. M.; *Journal of the American Chemical Society* **2010**, 132, 5285; Xie, X.; Xu, W. and Liu, X., *Accounts of Chemical Research* **2012**, 45, 1511.

(33) Panda, C.; Dhar, B. B.; Malvi, B.; Bhattacharjee, Y.; Gupta, S. S. *Chemical Communications* **2013**, *49*, 2216.

(34) Malvi, B.; Panda, C.; Dhar, B. B.; Gupta, S. S. *Chemical Communications* **2012**, *48*, 5289.

(35) Nakazawa, J.; Smith, B. J.; Stack, T. D. P. *Journal of the American Chemical Society* **2012**, *134*, 2750.

(36) Schlossbauer, A.; Schaffert, D.; Kecht, J.; Wagner, E.; Bein, T. *Journal of the American Chemical Society* **2008**, *130*, 12558.

(37) George, P.; *Biochemical journal* **1953**, 54, 267.

(38) Beers, R. F.; Sizer, I. W. *Journal of Biological Chemistry* **1952**, *195*, 133.

Chapter V

Conclusions and Future Directions

5.1 Summary and conclusions

This thesis describes the synthesis and characterization of a new generation of Fe-TAML complexes: the biuret-modified Fe-TAMLs. The activity of these complexes towards various substrate oxidation like organic dye degradation and water oxidation (both chemical and photochemical) were outlined in the initial chapters. Further these catalysts were covalently incorporated inside the pore channel of MSNs to prepare the hybrid Fe-MSNs that were used as bio-sensors in detection of the analyte CN^-. This chapter presents summary and conclusions of the work described in previous chapters and future directions based on this thesis.

Chapter I mainly provides an overview of the existing literature on bio-inspired oxidations. It describes the mechanism of action of several Fe-containing enzymes towards oxidation of organic substrates. Various strategies used to synthesize Fe complexes that functionally mimic the native enzymes are also reported. A brief introduction outlining the design principles to develop oxidative robust Fe based oxidation catalysts (minimizing hydrolytic and oxidative self-decompositions at ambient operating conditions) is also provided.

Chapter II highlights the evolution of the biuret-modified Fe-TAMLs as a new generation oxidation catalyst. The key modification was the replacement of the malonoyl fragment by a substituted biuret moiety. The detailed synthetic procedure and characterization of two different biuret-modified Fe-TAMLs with slightly different electronics around the iron active centre are discussed. The peroxidase activity of these complexes towards organic dye degradation in presence of H_2O_2 and activity-stability parameterization with comparison to the reported Fe-TAML counterparts which render them most successful peroxidase mimic till date.

Chapter III discusses the homogeneous chemical and photochemical water oxidation (WO) leading to molecular oxygen by biuret-modified Fe-TAMLs. Ce(IV) was used as a sacrificial oxidant in the case of chemical WO and a mixture of photosensitizer ($[Ru(bipy)_3]^{2+}$) and sacrificial oxidant, $Na_2S_2O_8$ was used in photochemical WO to

generate a high valent iron oxo intermediate which in turn oxidizes water. In the photochemical WO part, three first time important observations are discussed; i) a molecular iron complex can catalyse the photochemical WO in basic medium which is in contrast to all reported iron complexes, where they all undergo dissociation to F_2O_3 nanoparticle formation that actually acts as real WOC; ii) photochemical generation of a high valent $Fe^{V}(O)$ intermediate species and its spectroscopic identification and iii) $Fe^{V}(O)$ alone cannot oxidize water but further oxidation is required to evolve O_2. Based on reported theoretical calculations for Ce(IV) mediated chemical WO and our experimental observations, a proposed mechanism for photochemical WO is also provided which shows nucleophilic attack of a water molecule to the photochemically generated $Fe^{V}(O)$ to form the corresponding $Fe^{III}(OOH)$ which is further oxidised to release a molecule of O_2.

Chapter IV describes the use of biuret-modified Fe-TAML as a potential replacement of the HRP in various analyte detection methodologies. The concept relies on use of signal amplification as HRP does in most of the biological assays for detection of ultra-low concentrations biomarkers.

First part of this chapter provides the synthesis of a clickable tailed biuret-modified Fe-TAML and its usage to develop detection protocols for protein biomarker sensing. The conceptual novelty lies in the use of peroxide activating small molecular catalyst in place of the fluorescence tags in ABPP to allow signal amplification. The experimental observation suggests that up to 20 ng of a particular protein can be detected using this protocol.

The second part of this chapter discusses usage of mesoporous silica nanoparticles based hybrid material (Fe-MSN) as a functional mimic of the enzyme HRP towards at quantitative estimation of cyanide ion at physiological pH. This hybrid material contains the robust small molecule peroxidase mimic biuret-modified Fe-TAML that is covalently attached to azide containing MSN particles by Cu(I) catalyzed azide alkyne cycloaddition (CuAAC) reaction. The CN^- sensing protocol consists of three consecutive reactions: (i) inhibition of the enzyme catalase by CN^-, (ii) disproportionation of H_2O_2 to water and oxygen by cyanide free catalase and (iii) activation of the residual H_2O_2 by Fe-MSNs to

oxidize TMB to produce a green color which can be visually detected, quantified and correlated to the amount of CN^- used. It was observed that detection of CN^- was linear in the range 0 to 156 ppb (0 to 8 µM) with a detection limit of 23 ppb (0.9 µM) which is almost half of the amount that is permissible in drinking water by world health organization which renders this methodology suitable for analysis of real-life sample too.

5.2 Future directions

Based on the results of **chapter III**, potential follow up application could be devising a photo-electrochemical water splitting set up where both water oxidation and reduction can be performed in one pot. Water oxidation and reduction half reactions have been explored separately because combining them would require addition of both the sacrificial oxidant[1] and reductant[2] (for oxidation and reduction of the photosensitizer respectively in the excited state) in the same reaction mixture. To avoid this, new design could be invoked which would involve covalent linkage between the photosensitizer and the WOC and a water oxidising electrode can be fabricated containing this conjugate. This would allow facile electron transfer from WOC through the photosensitizer upon application of a bias voltage. The electrons transferred to the anode now can be used for reduction of protons to produce H_2 by a water reduction catalyst (WRC). The designed photosensitizer would contain both phosphonate group and an azide group on the bipyridyl to selectively bind onto the TiO_2[3] and alkyne tailed biuret-modified Fe-TAML (click chemistry) respectively. Generally huge excess of photosensitizer (~100 eq) are being used for photochemical WO to overcome the kinetic barrier. However this strategy of covalent linkage between the WOC and the sensitizer would probably minimize the concentration of latter. This will also eliminate the use of sacrificial oxidant and reductant. In conclusion an overall water splitting system that uses visible light to convert water to hydrogen and oxygen assisted by a small applied voltage is possible.

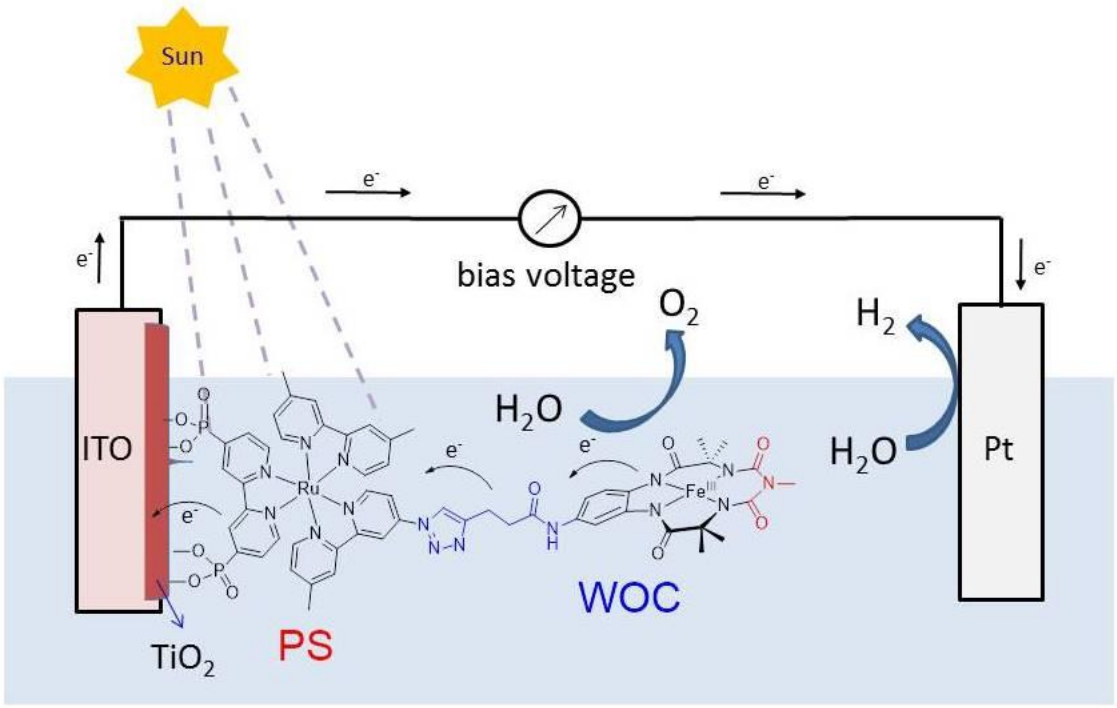

Figure 5.1: Schematic presentation of a photo-electro chemical water splitting shell

5.3 References

(1) Kaveevivitchai, N.; Chitta, R.; Zong, R.; El Ojaimi, M.; Thummel, R. P. *Journal of the American Chemical Society* **2012**, *134*, 10721; Moonshiram, D.; Alperovich, I.; Concepcion, J. J.; Meyer, T. J.; Pushkar, Y. *Proceedings of the National Academy of Sciences* **2013**, *110*, 3765.

(2) Tong, L.; Zong, R. and Thummel, R. P.; *Journal of American Chemical Society* **2014**, 136, 4881.

(3) Coggins, M. K.; Mendez, M. A.; Concepcion, J. J.; Periana, R. A. and Meyer, T. J.; *Journal of American Chemical Society* 2014, 136, 15845.

Appendix I

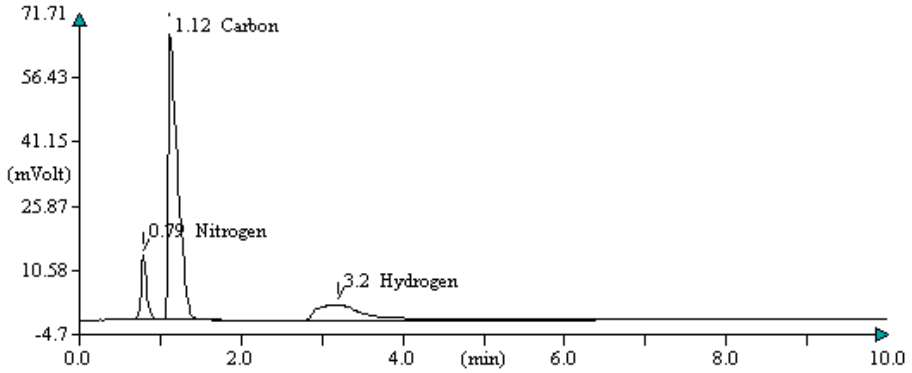

Peak Number (#)	Retention Time (min)	Area (.1*uV*sec)	Element %	Compone
1	0.792	758370	19.140	Nitroge
2	1.117	5334763	56.438	Carbon
3	3.200	1655041	6.312	Hydroge
		7748174	81.890	

Figure A1: Elemental (C, H and N) analysis of ligand **L2** (X = H).

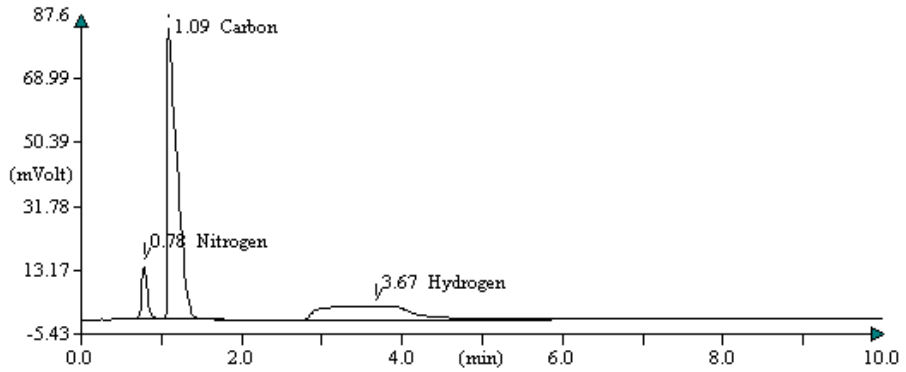

Peak Number (#)	Retention Time (min)	Area (.1*uV*sec)	Element %	Component
1	0.783	732786	13.688	Nitrogen
2	1.092	7259355	55.705	Carbon
3	3.667	3234449	8.137	Hydrogen
		11226590	77.529	

Figure A2: Elemental analysis of biuret-modified Fe-TAML (**1a**).

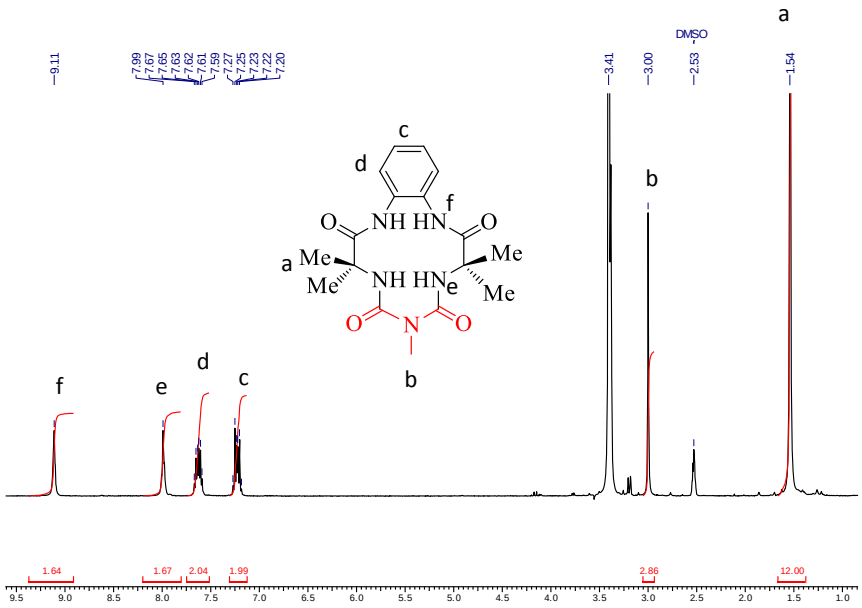

Figure A3: ^{1}H NMR spectrum of the ligand **L2** (X = H) in DMSO-d_6.

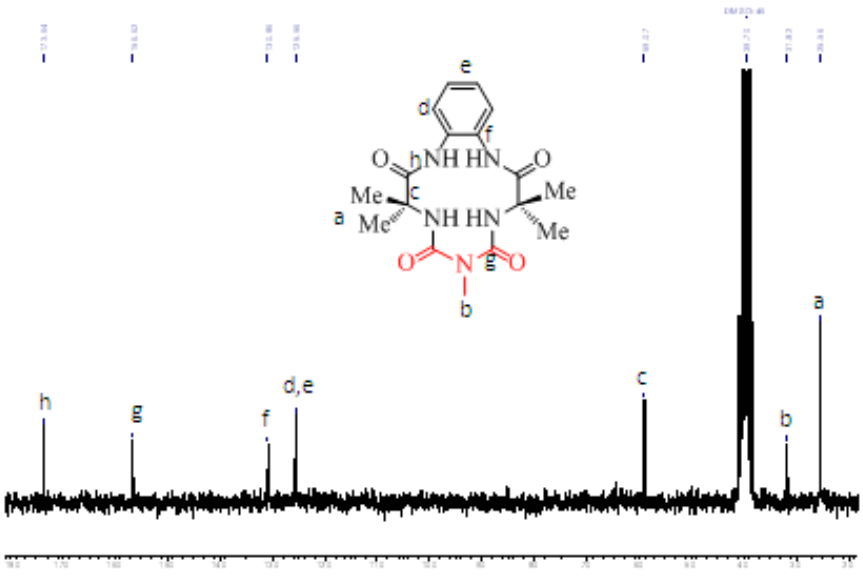

Figure A4: ^{13}C NMR spectrum of the ligand **L2** (X = H) in DMSO-d_6.

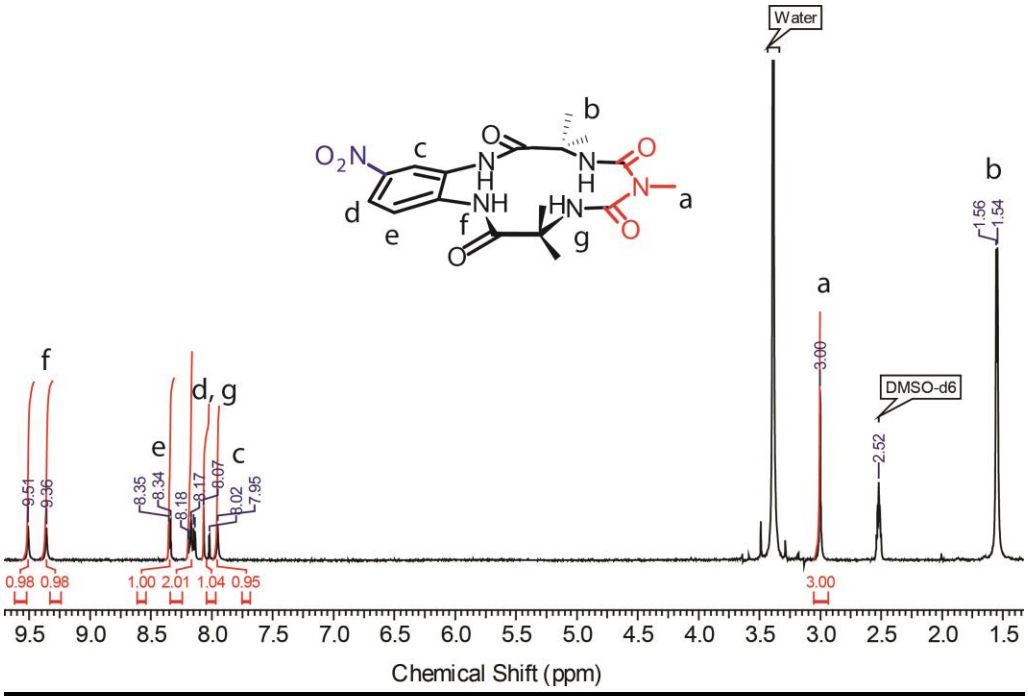

Figure A5: ^{1}H NMR spectrum of the ligand **L2** (X = NO_2) in DMSO-d_6.

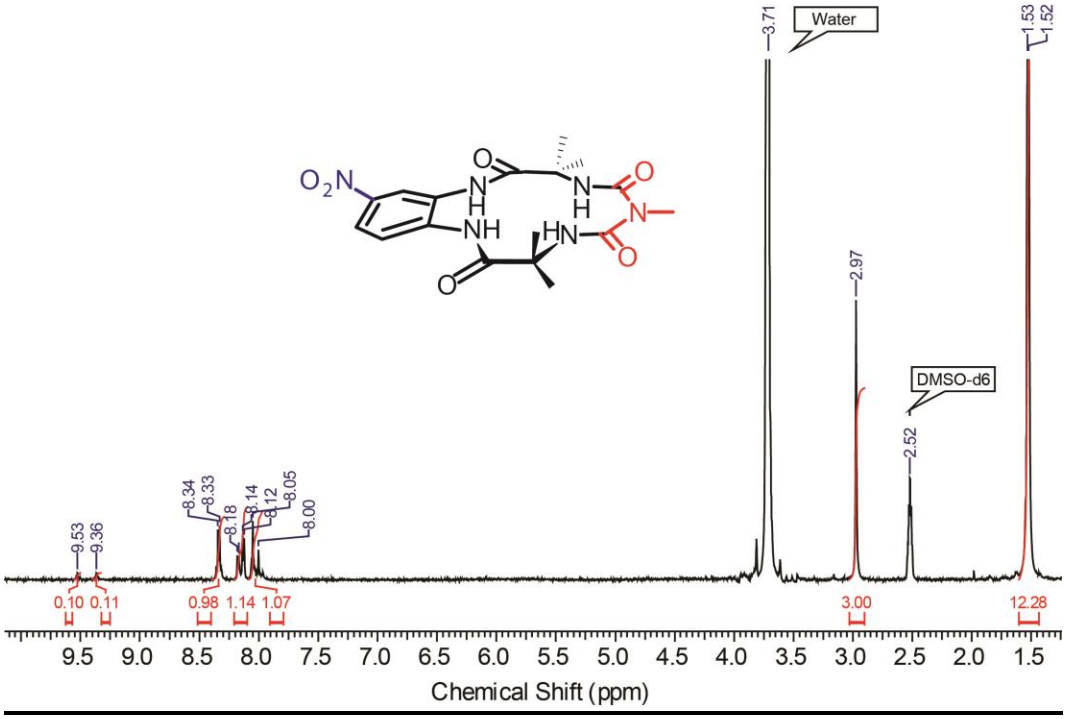

Figure A6: ^{1}H NMR spectrum of the ligand **L2** (X = NO_2) in DMSO-d_6 and D_2O. The amide protons are exchanged by deuterium in presence of D_2O.

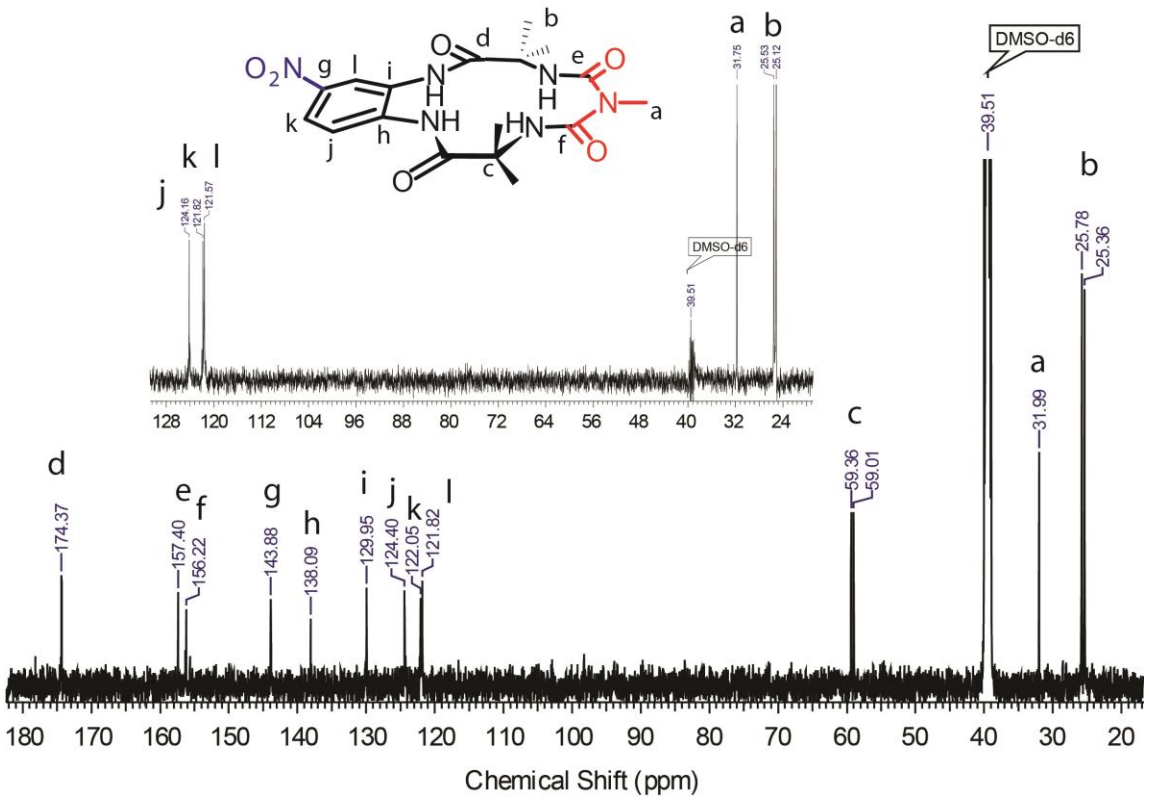

Figure A7: ^{13}C NMR spectrum of the ligand **L2** (X = NO_2) in DMSO-d_6, Inset: ^{13}C DEPT of the same ligand.

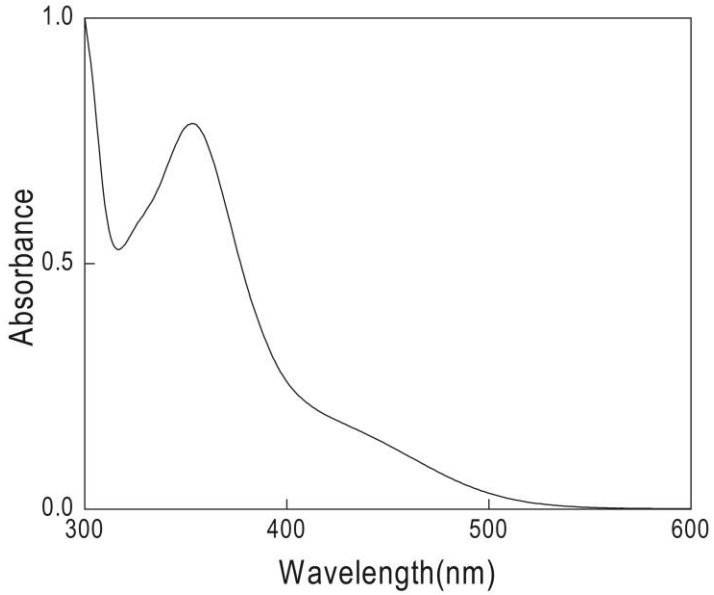

Figure A8: UV-vis spectrum of biuret-modified Fe-TAML (**1a**) in water (0.138 mM). $\varepsilon_{356\ nm}$ was determined to be 5160 $M^{-1}cm^{-1}$.

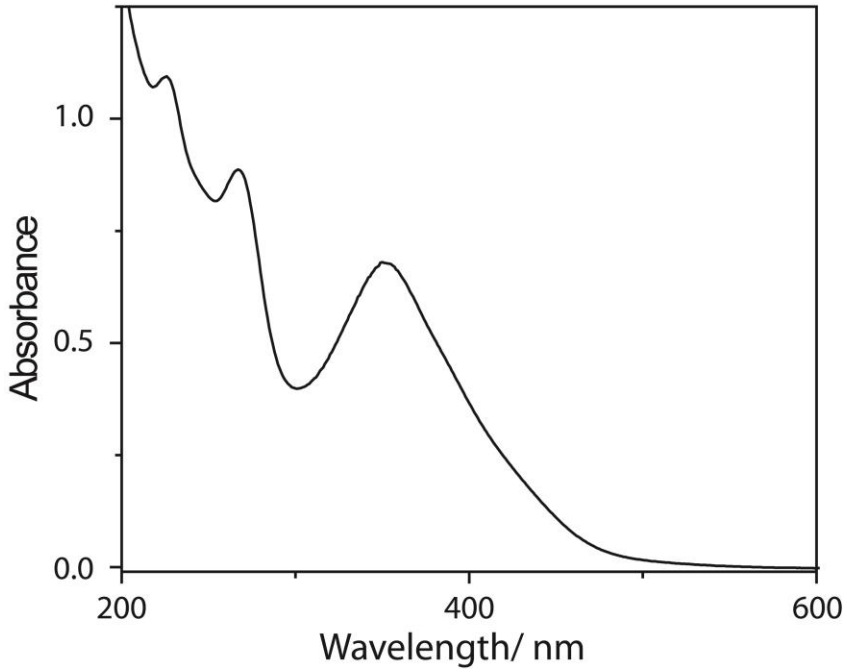

Figure A9: UV-vis spectrum of biuret-modified Fe-TAML (**1b**) in water (0.078 mM). $\varepsilon_{356\ nm}$ was determined to be 9020 $M^{-1}cm^{-1}$.

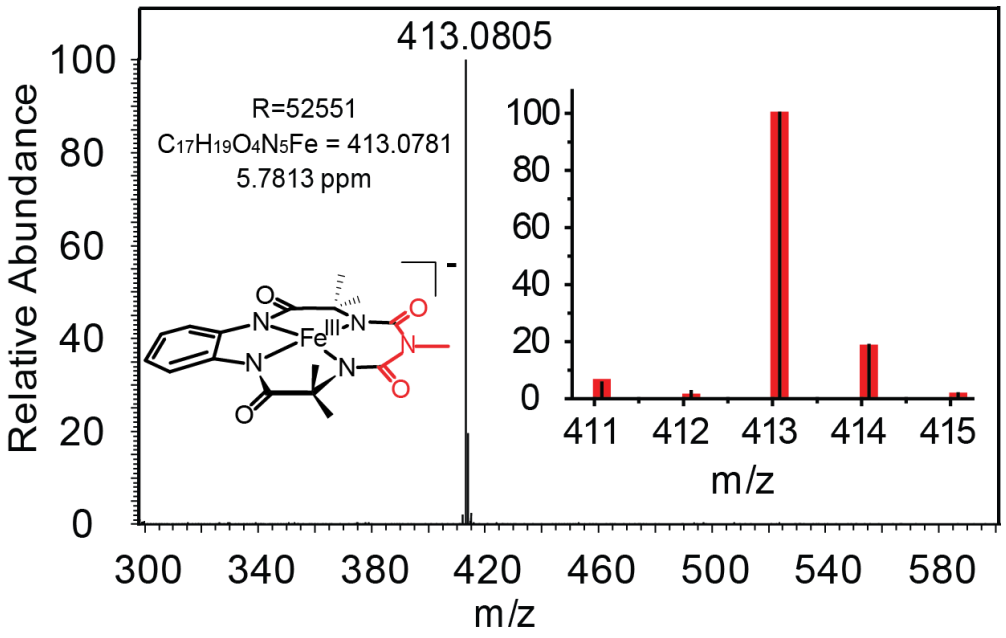

Figure A10: High resolution mass spectrum of **1a** in H_2O (*m/z* 413.08). Inset shows comparison of simulated (red bars) and observed (black lines) isotopic distribution pattern for ion of interest. The axial chloro ligand was not observed as this ligand is labile and gets dissociated under the conditions of the mass spectrometry experiment.

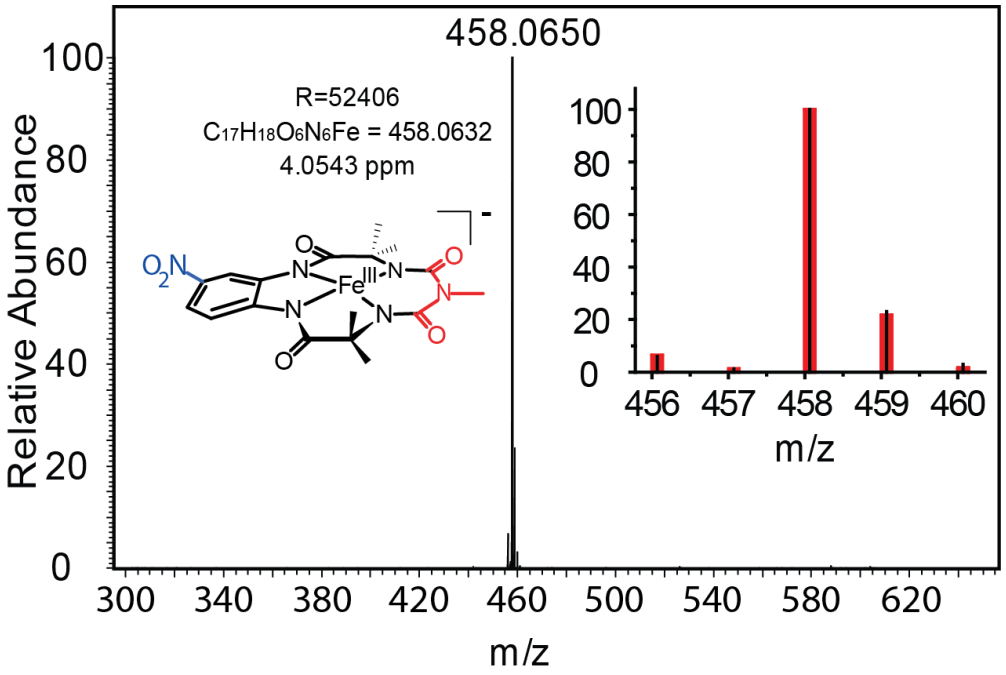

Figure A11: High resolution mass spectrum of **1b** in H_2O (*m/z* 458.0648). Inset shows comparison of simulated (red bars) and observed (black lines) isotopic distribution pattern for ion of interest. The axial chloro ligand was not observed as this ligand is labile and gets dissociated under the conditions of the mass spectrometry experiment.

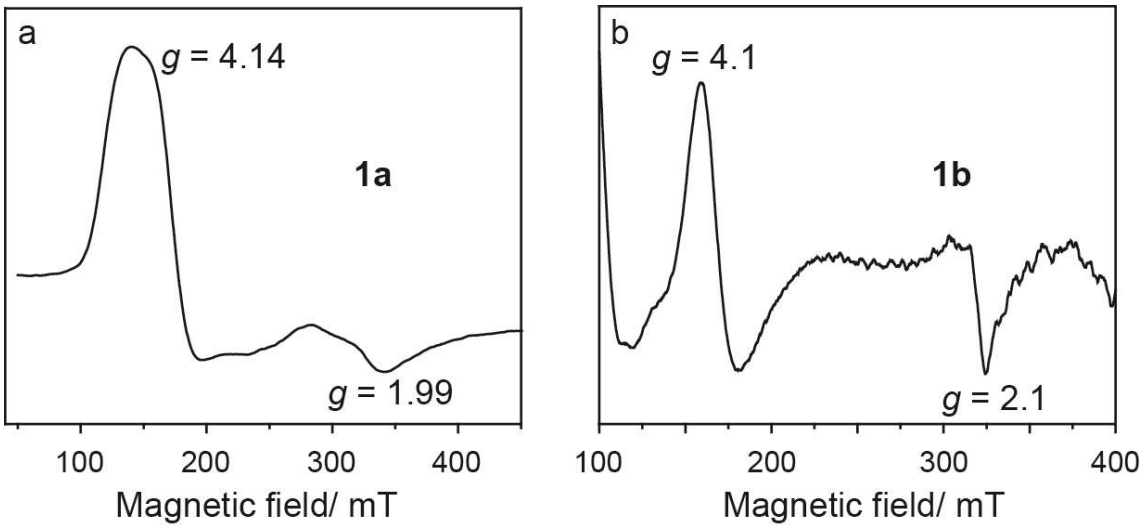

Figure A12: X-Band EPR spectrum of a) **1a** and b) **1b** in acetonitrile (2 mM) at 90 K.

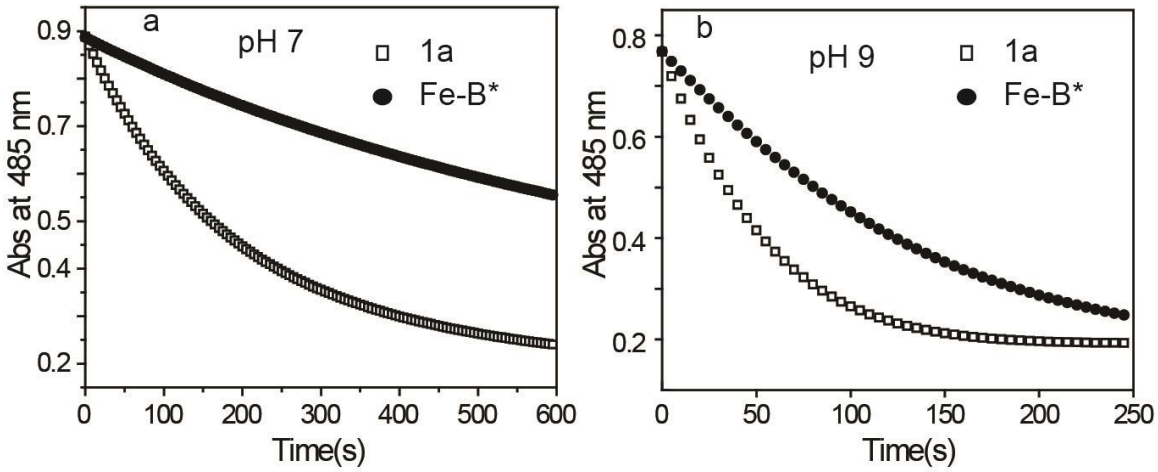

Figure A13: Comparative orange II bleaching by H_2O_2 at pH 7 (a) and 9 (b) for **1a** and **Fe-B***. [Catalyst] = 2×10^{-7} M, [H_2O_2] = 0.0015 M, [orange II] = 4×10^{-5} M; 0.01 M phosphate buffer at 25 °C.

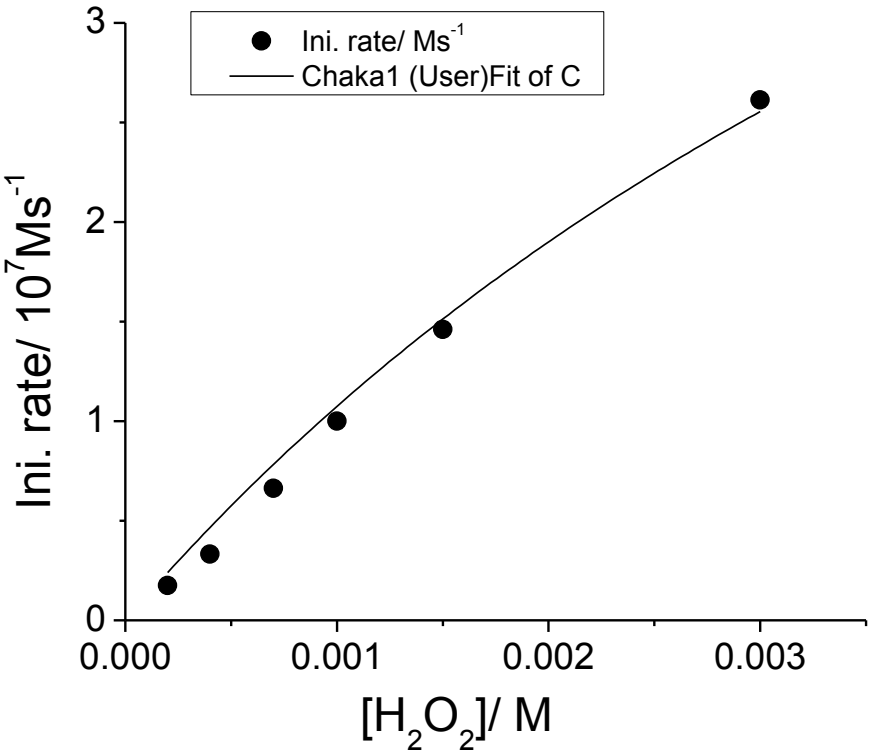

Figure A 14: Initial rate vs. $[H_2O_2]$ for orange II oxidation by **1b** at pH 7.

Table A1: Origin simulation for figure A 15

Model	Chaka1 (User)		
Equation	y = (A1*A2*C1*x*C2)/(A3+A1*x+A2*C2)		
Reduced Chi-Sqr	1.19524E-16		
Adj. R-Square	0.98525		
		Value	Standard Error
C	A1	1235.95	15.50
	A2	410787.32426	52577.87618
	A3	0	0
	C1	1E-7	0
	C2	2E-5	0

A1 = k_I, A2 = k_{II}, A3 = k_{-I}; in Equation (4), page 52.

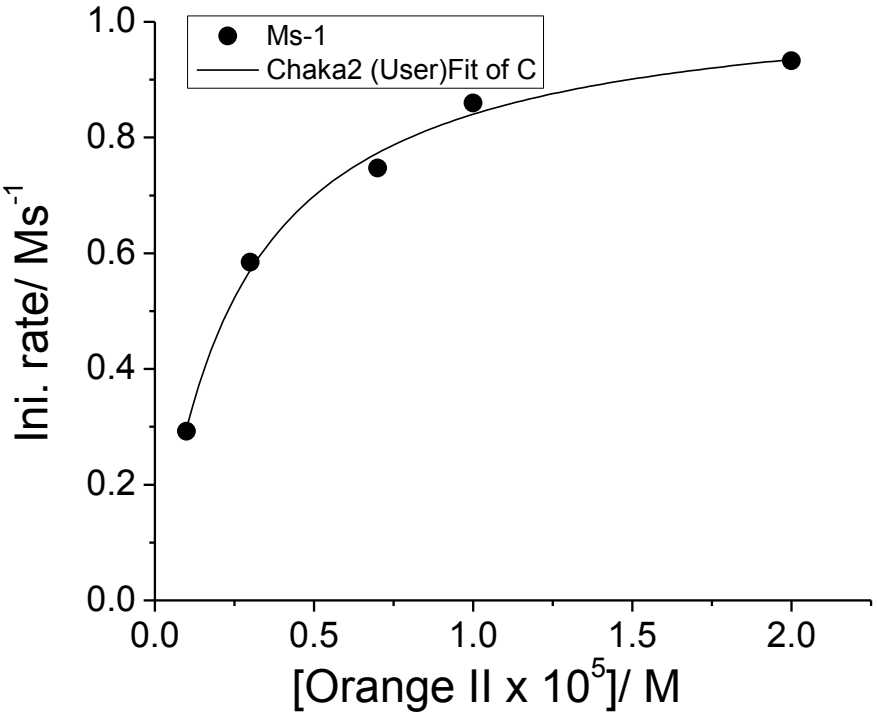

Figure A15: Initial rate vs. [orange II] for orange II oxidation by **1b** at pH 7.

Table A2: Origin simulation for figure A 16

Model	Chaka2 (User)		
Equation	y = (A1*A2*C1*x*C2)/(A3+A1*C2+A2*x)		
Reduced Chi-Sqr	4.23593E-18		
Adj. R-Square	0.99349		
		Value	Standard Error
D	A1	1504.97993	37.62763
	A2	415123.69385	29329.93772
	A3	0	0
	C1	1E-7	0
	C2	7E-4	0

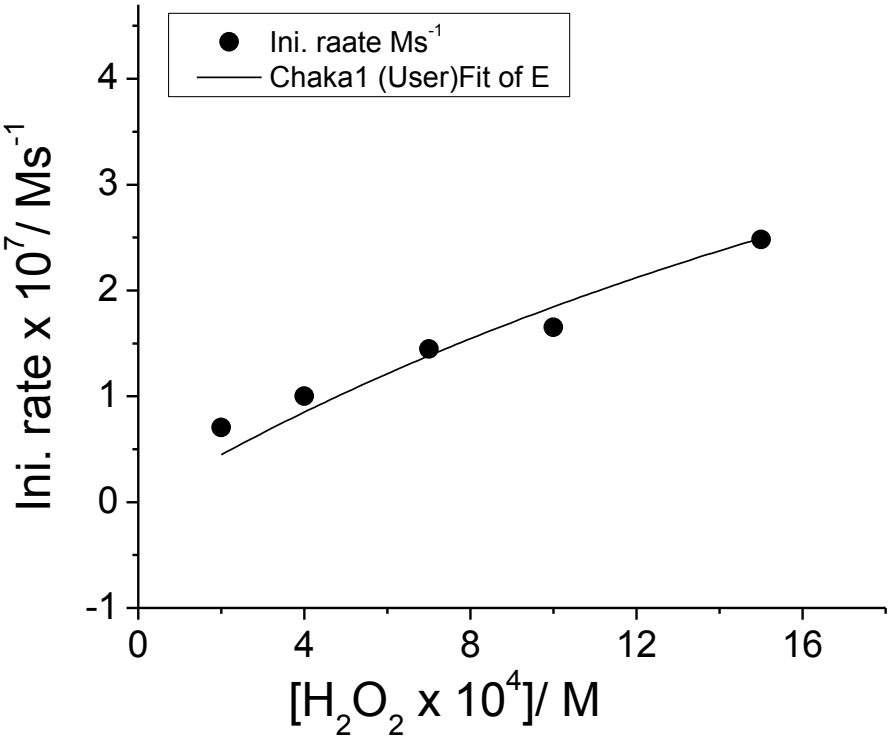

Figure A16: Initial rate vs. $[H_2O_2]$ for orange II oxidation by **1b** at pH 9.4.

Table A3: Origin simulation for figure A 17

Model	Chaka1 (User)		
Equation	y = (A1*A2*C1*x*C2)/(A3+A1*x+A2*C2)		
Reduced Chi-Sqr	3.24865E-16		
Adj. R-Square	0.93032		
		Value	Standard Error
E	A1	2364.77475	158.5191
	A2	420000	0
	A3	0	0
	C1	1E-7	0
	C2	2E-5	0

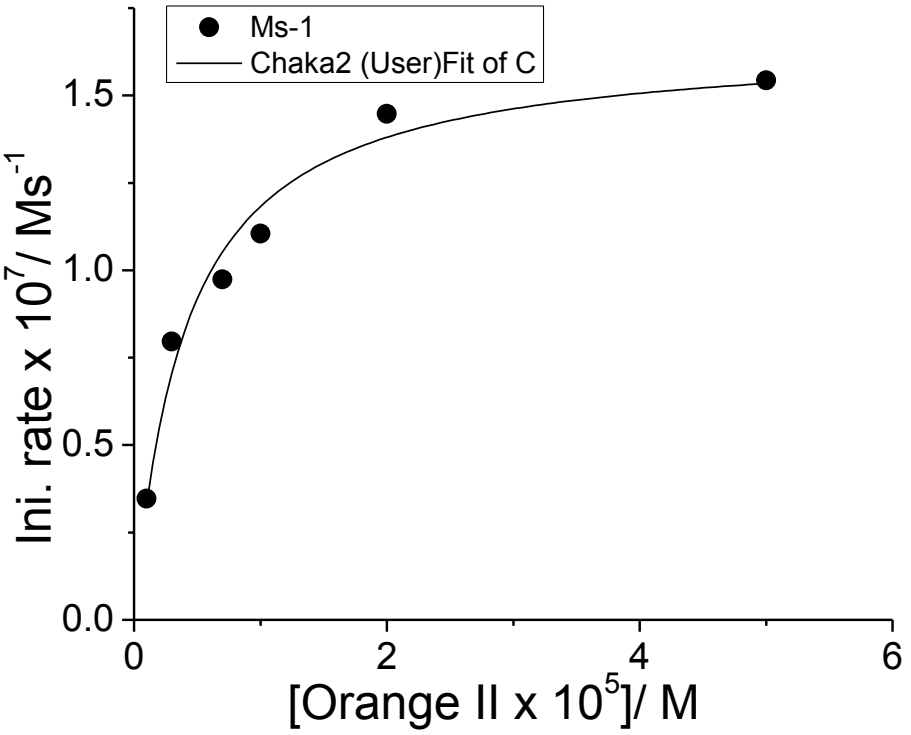

Figure A17: Initial rate vs. [orange II] for orange II oxidation by **1b** at pH 9.4.

Table A4: Origin simulation for figure A 18

Model	Chaka2 (User)		
Equation	y = (A1*A2*C1*x*C2)/(A3+A1*C2+A2*x)		
Reduced Chi-Sqr	6.2198E-17		
Adj. R-Square	0.96788		
		Value	Standard Error
C	A1	2368.29242	120.49048
	A2	412065.00005	59947.9821
	A3	0	0
	C1	1E-7	0
	C2	7E-4	0

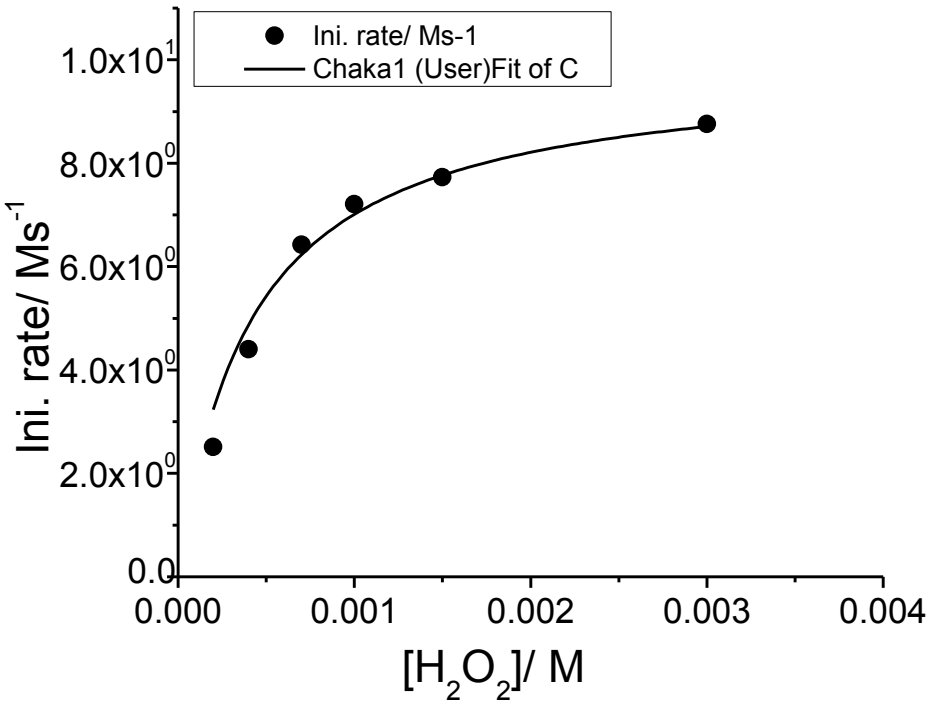

Figure A18: Initial rate vs. $[H_2O_2]$ for orange II oxidation by **1b** at pH 11.

Table A5: Origin simulation for figure A 19

Model	Chaka1 (User)		
Equation	y = (A1*A2*C1*x*C2)/(A3+A1*x+A2*C2)		
Reduced Chi-Sqr	1.65601E-15		
Adj. R-Square	0.96912		
		Value	Standard Error
C	A1	24000	1200.345
	A2	495244.42844	16897.76413
	A3	0	0
	C1	1E-7	0
	C2	2E-5	0

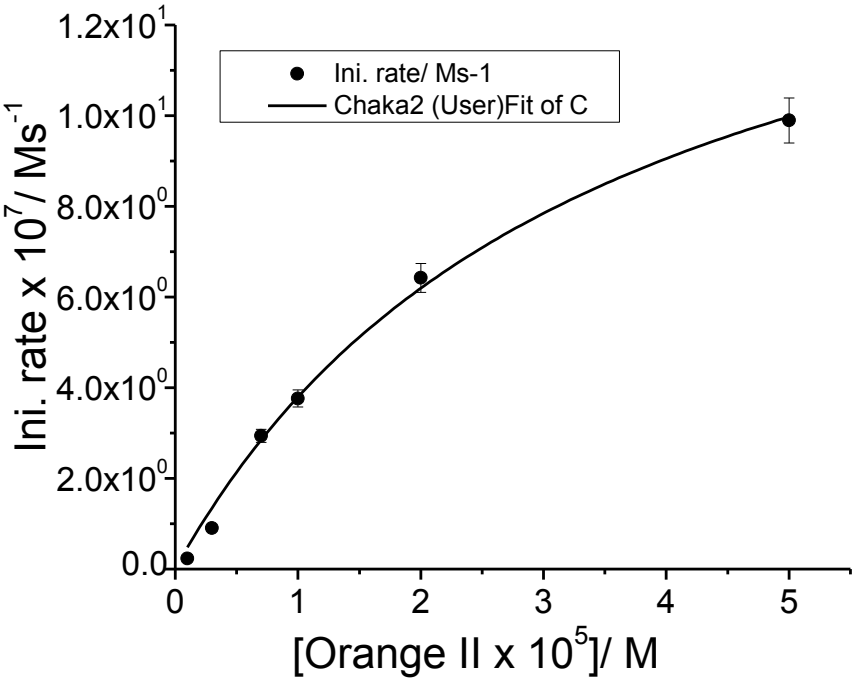

Figure A19: Initial rate vs. [orange II] for orange II oxidation by **1b** at pH 11.

Table A6: Origin simulation for figure A 20

Model	Chaka2 (User)		
Equation	y = (A1*A2*C1*x*C2)/(A3+A1*C2+A2*x)		
Reduced Chi-Sqr	8.21225E-16		
Adj. R-Square	0.99374		
		Value	Standard Error
C	A1	24029.77078	1915.68474
	A2	490230.4247	36263.70616
	A3	0	0
	C1	1E-7	0
	C2	7E-4	0

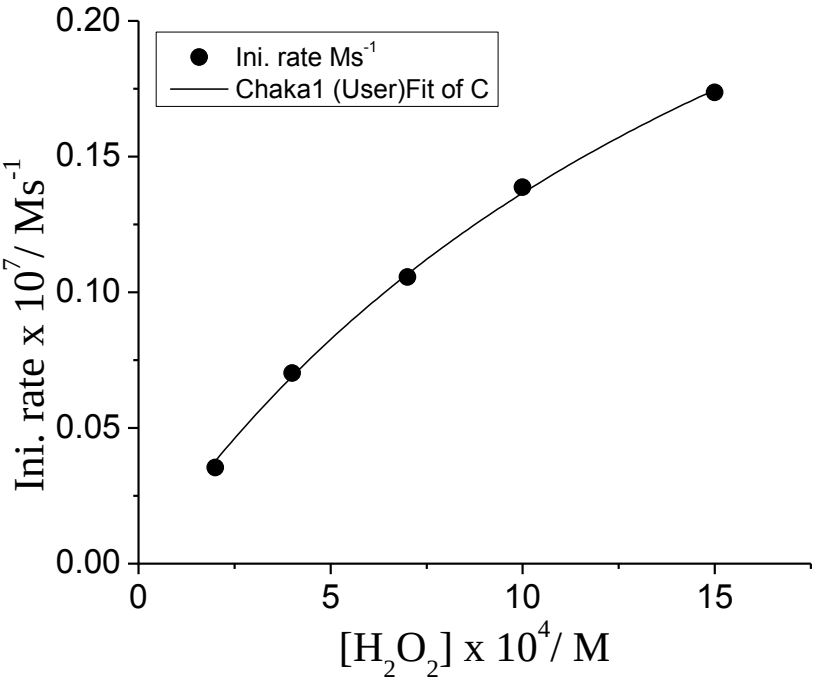

Figure A20: Initial rate vs. $[H_2O_2]$ for orange II oxidation by **1a** at pH 7.

Table A7: Origin simulation for figure A 21

Model	Chaka1 (User)		
Equation	y = (A1*A2*C1*x*C2)/(A3+A1*x+A2*C2)		
Reduced Chi-Sqr	3.53555E-20		
Adj. R-Square	0.99881		
		Value	Standard Error
C	A1	209	20
	A2	19701.39863	386.99761
	A3	0	0
	C1	1E-7	0
	C2	2E-5	0

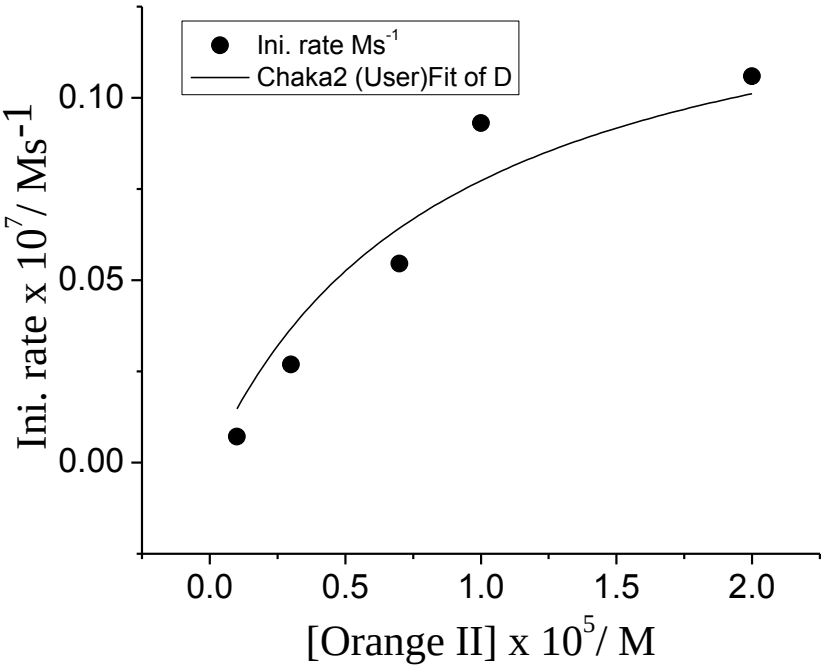

Figure A21: Initial rate vs. [orange II] for orange II oxidation by **1a** at pH 7.

Table A8: Origin simulation for figure A 22

Model	Chaka2 (User)		
Equation	y = (A1*A2*C1*x*C2)/(A3+A1*C2+A2*x)		
Reduced Chi-Sqr	1.30221E-18		
Adj. R-Square	0.9265		
		Value	Standard Error
D	A1	209	20
	A2	16376.9239	2781.30999
	A3	0	0
	C1	1E-7	0
	C2	7E-4	0

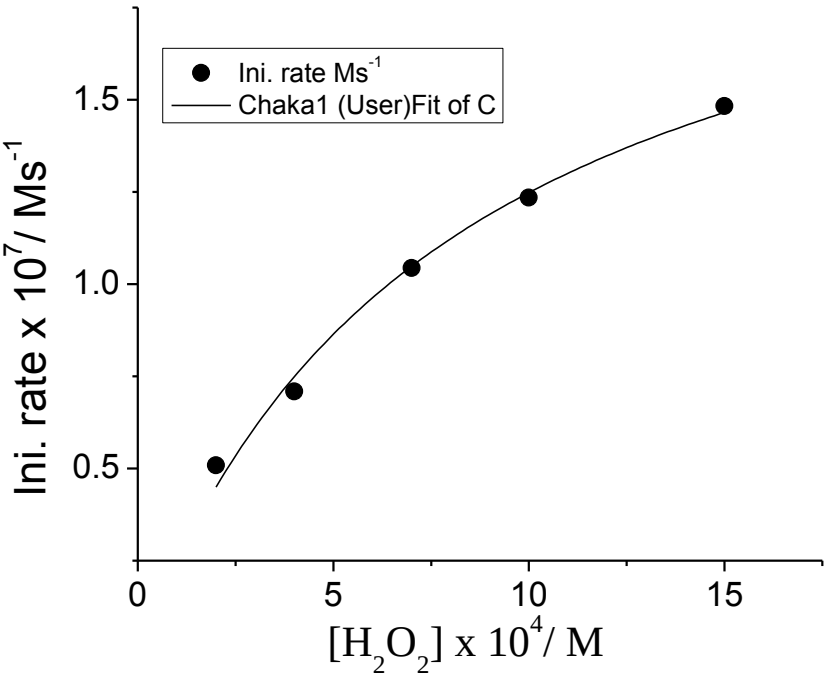

Figure A22: Initial rate vs. $[H_2O_2]$ for orange II oxidation by **1a** at pH 9.4.

Table A9: Origin simulation for figure A 23

Model	Chaka1 (User)		
Equation	y = (A1*A2*C1*x*C2)/(A3+A1*x+A2*C2)		
Reduced Chi-Sqr	1.41123E-17		
Adj. R-Square	0.99084		
		Value	Standard Error
C	A1	2805.6	35.602
	A2	112432.91998	3244.72502
	A3	0	0
	C1	1E-7	0
	C2	2E-5	0

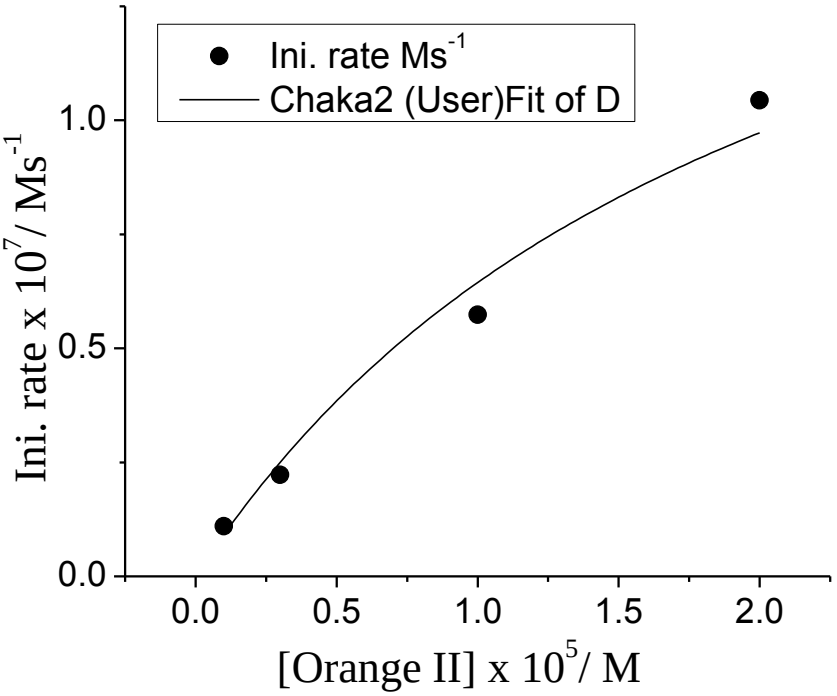

Figure A23: Initial rate vs. [orange II] for orange II oxidation by **1a** at pH 9.4.

Table A10: Origin simulation for figure A 24

Model	Chaka2 (User)		
Equation	y = (A1*A2*C1*x*C2)/(A3+A1*C2+A2*x)		
Reduced Chi-Sqr	3.69101E-17		
Adj. R-Square	0.97909		
		Value	Standard Error
D	A1	2833.656	34
	A2	95431.09014	8295.7761
	A3	0	0
	C1	1E-7	0
	C2	7E-4	0

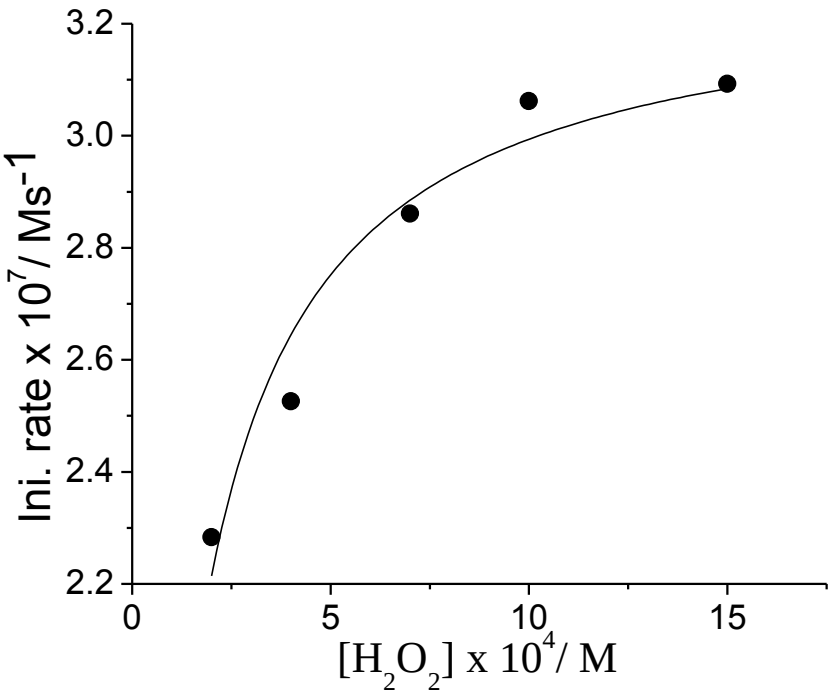

Figure A 24: Initial rate vs. $[H_2O_2]$ for orange II oxidation by **1a** at pH 11.

Table A11: Origin simulation for figure A 25

Model	Chaka1 (User)		
Equation	y = (A1*A2*C1*x*C2)/(A3+A1*x+A2*C2)		
Reduced Chi-Sqr	6.05355E-17		
Adj. R-Square	0.95096		
		Value	Standard Error
C	A1	34010	765
	A2	164136.24173	2370.90026
	A3	0	0
	C1	1E-7	0
	C2	2E-5	0

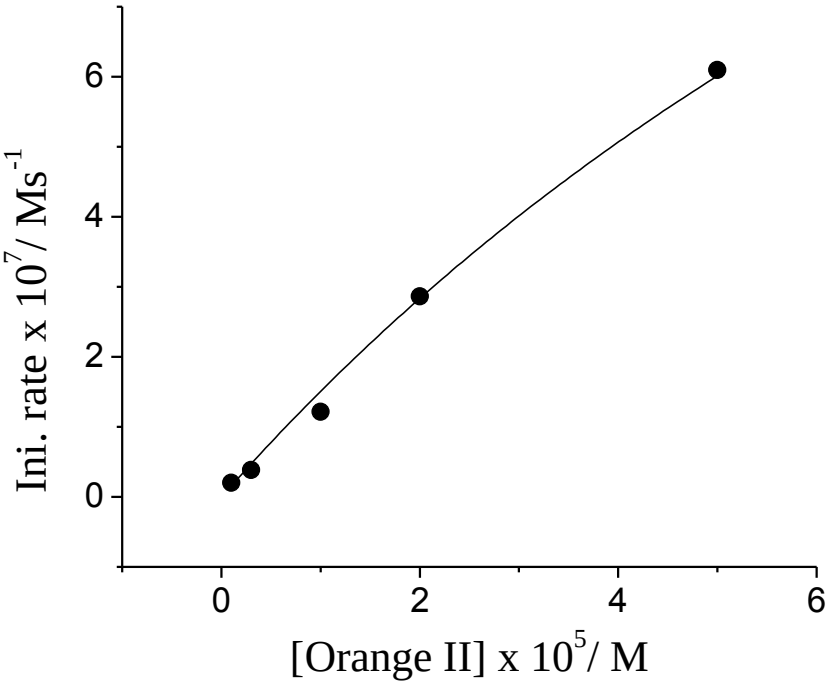

Figure A25: Initial rate vs. [orange II] for orange II oxidation by **1a** at pH 11.

Table A12: Origin simulation for figure A 26

Model	Chaka2 (User)		
Equation	y =(A1*A2*C1*x*C2)/(A3+A1*C2+A2*x)		
Reduced Chi-Sqr	2.53729E-16		
Adj. R-Square	0.99575		
		Value	Standard Error
D	A1	34010	656
	A2	160883.56409	4791.52705
	A3	0	0
	C1	1E-7	0
	C2	7E-4	0

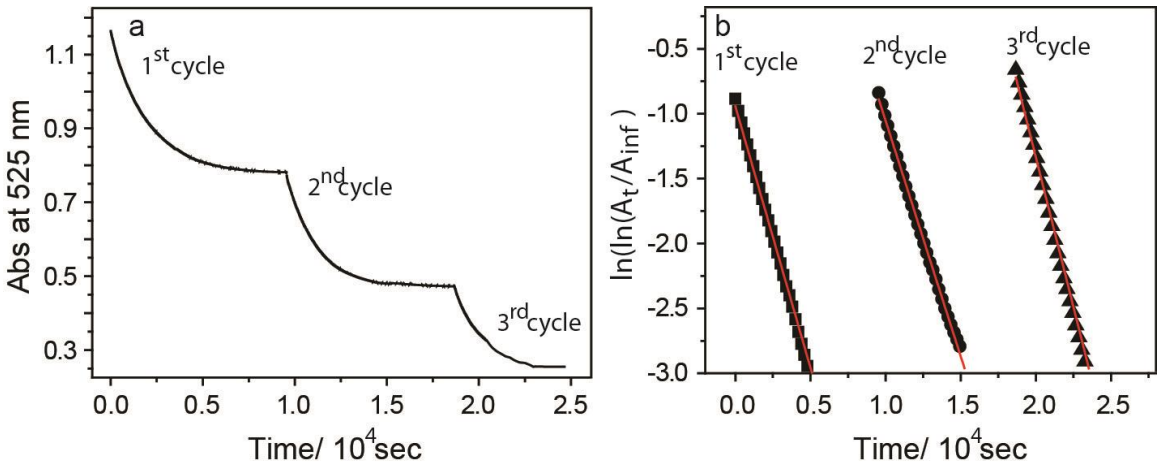

Figure A26: 1a catalyzed safranin O oxidation; a) Stepwise oxidation was followed to calculate the rate of intramolecular self-oxidation of the catalyst; b) All the three, first, second and third cycle follows similar rates (very parallel).

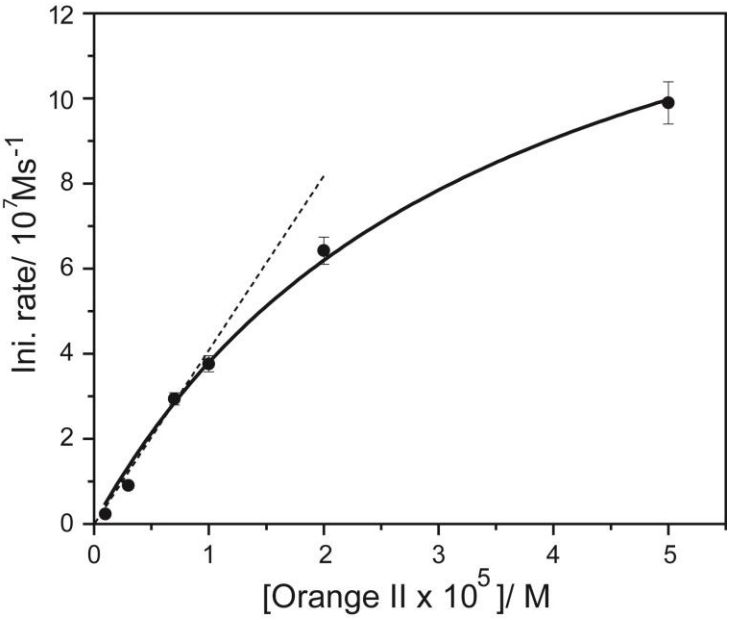

Figure A27: Initial rate/ Ms^{-1} was plotted as a function of [Orange II] at pH 11 in 0.01 M Phosphate Buffer, T = 25 °C. H_2O_2 and Fe^{III}-catalyst concentration were kept constant at 7×10^{-4} M and 01×10^{-7} M respectively. Solid line was data fitted according to the Equation 2. Fitting results $k_I = (2.4 \pm 0.2) \times 10^4$ $M^{-1}s^{-1}$, $k_{-I} \sim 0$ and $k_{II} = (4.9 \pm 0.5) \times 10^5$ $M^{-1}s^{-1}$. The dashed line passing through origin shows up to 1×10^{-5} M of Orange II,

initial rate increases linearly holding the condition $k_I[H_2O_2] > k_{II}$[Orange II] as well as $k_I[H_2O_2] > k_{-I}$ which gives $k_{II} = 4.5 \times 10^5\ M^{-1}s^{-1}$.

Table A13: Origin simulation for figure A 27

Equation	y = a + b*x		
Weight	No Weighting		
Residual Sum of Squares	18.44145	2.57515	36.70384
Adj. R-Square	0.99735	0.99856	0.99018
		Value	Standard Error
1st cycle	Intercept	-0.94273	0.00107
1st cycle	Slope	-4.02925E-4	2.3241E-7
2nd cycle	Intercept	2.57782	0.00231
2nd cycle	Slope	-3.63184E-4	1.86536E-7
3rd cycle	Intercept	7.88248	0.01294
3rd cycle	Slope	-4.6102E-4	5.96107E-7

Single crystal X-ray diffraction data collection, structure solution and refinement procedures

General Data Collection and Refinement Procedures

The complex, biuret-modified Fe-TAML (**1a**) crystallizes in tetragonal crystal system (space group, $P4_2$/mbc). The asymmetric unit of biuret-modified Fe-TAML (**1a**) contains one half biuret-modified Fe-TAML (**1a**) molecule (with mirror symmetry, no disorder), two one quarter Et_4N molecules and one half Et_4N. Biuret-modified Fe-TAML (**1a**) molecule occupies mirror symmetry where half biuret-modified Fe-TAML (**1a**) molecule is related to the other half by mirror. Single crystal data were collected on a Bruker SMART APEX three circle diffractometer equipped with a CCD area detector and operated at 1500 W power (50 kV, 30 mA) to generate Mo Kα radiation (λ=0.71073 Å). The incident X-ray beam was focused and monochromated using Bruker Excalibur Gobel mirror optics. Suitable crystal of **1a** reported in this chapter was mounted on nylon CryoLoops (Hampton Research) with Paraton-N (Hampton Research).

Initial scans of each specimen were performed to obtain preliminary unit cell parameters and to assess the mosaicity (breadth of spots between frames) of the crystal to select the required frame width for data collection. In every case frame widths of 0.5°

were judged to be appropriate and full hemispheres of data were collected using the *Bruker SMART*[1] software suite. Following data collection, reflections were sampled from all regions of the Ewald sphere to redetermine unit cell parameters for data integration and to check for rotational twinning using CELL_NOW[2]. In no data collection was evidence for crystal decay encountered. Following exhaustive review of the collected frames the resolution of the dataset was judged. Data were integrated using Bruker SAINT[3] software with a narrow frame algorithm and a 0.400 fractional lower limit of average intensity. Data were subsequently corrected for absorption by the program SADABS[4]. The space group determinations and tests for merohedral twinning were carried out using *XPREP*[6]. In all cases, the highest possible space group was chosen.

Crystal structure of biuret-modified Fe-TAML (**1a**) was solved by direct methods and refined using the *SHELXTL 97*[5] software suite. Atoms were located from iterative examination of difference F-maps following least squares refinements of the earlier models. Final model was refined anisotropically (if the number of data permitted) until full convergence was achieved. Hydrogen atoms were placed in calculated positions (C-H = 0.93 Å) and included as riding atoms with isotropic displacement parameters 1.2-1.5 times U_{eq} of the attached C atoms. Data were collected at 200(2) K. This lower temperature was considered to be optimal for obtaining the best data. Crystal structure of **1a** was examined using the *Adsym* subroutine of PLATON[5] to assure that no additional symmetry could be applied to the model. ORTEP diagram is displayed at the 50% probability level.

A colorless prismatic crystal (0.25 × 0.20 × 0.18 mm^3) of **1a** was placed in 0.7 mm diameter nylon CryoLoops (Hampton Research) with Paraton-N (Hampton Research). The loop was mounted on a SMART APEX three circle diffractometer. A total of 82276 reflections were collected of which 4743 were unique and 2863 of these were greater than 2σ(*I*). The range of θ was from 2.28 to 19.11º. All non-hydrogen atoms were refined anisotropically. **1a** contains half ligand molecule in the asymmetric unit. It should be noted that other supporting characterization data (*vide infra Synthesis*) are consistent with the crystal structure. Final full matrix least-squares refinement on F^2 converged to R_1 = 0.0551 and wR_2 = 0.1765(all data) with GOF = 0.905. Table A14 contains crystallographic data for **1a**.

Table A14: Crystal data and structure refinement for biuret-modified Fe-TAML (**1a**)

Empirical formula	C33 H39 Cl Fe N7 O4
Formula weight	689.17
Temperature	296(2) K
Wavelength	0.71073 Å
Crystal system	Tetragonal
Space group	*P42/mbc*
Unit cell dimensions	*a* = 22.169(17) Å α = 90° *b* = 22.169(17) Å β = 90° *c* = 14.93(2) Å γ = 90°
Volume	7338(13)
Z	8
Density (calculated)	1.247
Absorption coefficient	0.528
F(000)	2888
Crystal size	0.30 × 0.20 × 0.15 mm^3
Theta range for data collection	10.42– 18.13
Index ranges	-29<= h <= 29, -29<= k <= 29, -19<= l <= 19
Reflections collected	81929
Independent reflections	4711
Completeness to theta = 26.02°	98.7 %
Absorption correction	Semi-empirical from equivalents
Refinement method	Full-matrix least-squares on F^2
Data / restraints / parameters	4711 / 0 / 242
Goodness-of-fit on F^2	1.019
Final R indices [I>2sigma(I)]	R_1 = 0.0660, wR_2 = 0.1985

R indices (all data)	R_1 = 0.1108, wR_2 = 0.2182
Largest diff. peak and hole	1.662 and -0.490 e.Å^{-3}

Note: The carbon atoms of one the tetraethyl ammonium cation is disorder. So we could not locate or fixed so we refined the structure without adding any hydrogen atoms to it.

Comparison of the X-ray data with the Elemental analysis

The complex biuret-modified Fe-TAML (**1a**) crystallizes in tetragonal crystal system (space group, $P4_2$/mbc). The asymmetric unit of biuret-modified Fe-TAML (**1a**) contains one half Fe^{III}(biuret-amide)] molecule (with mirror symmetry, no disorder; 50% occupancy of Fe and Cl), and two one quarter (25% occupecy of nitrogen) and one half (50% occupecy of nitrogen) Et_4N molecules. Fe^{III}(biuret-amide)] molecule occupies a mirror symmetry where half biuret-modified Fe-TAML (**1a**) molecule is related to the other half by mirror. If we calculate the charge of the asymmetric unit considering Fe is in +3 oxidation stage.

Fe (50%) = (+)1.5

Two one quarter Et_4N molecules (25% occupecy of nitrogen)= (+)0.25+(+)0.25=(+)0.5

One half Et_4N molecules (50% occupecy of nitrogen)= (+)0.5

Total (+) charge of the asymmetric unit is (+)1.5+(+)0.5+(+)0.5= (+)2.5

Similarly for the (-) ve charge

Cl(50%) = (-)0.5

Two nitrogen (100%) from the (biuret-amide) moiety = (-)2.0

Total (+) charge of the asymmetric unit is (-)0.5+(-)2.0= (-)2.5

Hence we could conclude Fe in the biuret-modified Fe-TAML (**1a**) complex is indeed in +3 oxidation state. This is clearly indicative from the inspection of the CIF file (CCDC entry no. 812577). The sum formula for this revised cif is $C_{33}H_{59}Cl_1Fe_1N_7O_4$ and thus a molecular weight of M = 689.17 g/mol. We have not added the 20 hydrogen's of the disordered Et_4N molecule.

The charge on the Fe mentioned above is calculated based on the contents of the asymmetric unit or the content of the unit cell. In either case these have concluded that the oxidation state of the Fe here is +3.

The Elemental analysis data is as follows: Found: C, 55.71; H, 8.14; N, 13.688%. Calc. for $C_{33}H_{59}N_7ClFeO_4$: C, 55.85; H, 8.32; N, 13.820

The current elemental analysis matches exactly with the X-ray crystal structure. The sum formula for this revised cif is $C_{33}H_{39}Cl_1Fe_1N_7O_4$ and thus a molecular weight of M = 689.17 g/mol. We have not added the 20 hydrogen's of the disordered Et_4N molecule. The formula of the biuret-modified Fe-TAML (**1a**) hence derived from the crystal structure should be $C_{33}H_{59}Cl_1Fe_1N_7O_4$.

Table A15: Selected bond lengths

Atoms	Bond Lengths(A)
C1-N5	1.447(5)
C6-O2	1.245(4)
C6-N2	1.349(4)
C6-N5	1.416(3)
Cl-Fe1	2.3948(11)
Fe1-N2	1.879(2)
Fe1-N1	1.881(3)
Fe1-N5	3.149

Table A16: Selected bond angles

Atoms	Bond Angles(o)
O2-C6-N2	124.5(3)
O2-C6-N5	116.8(3)
N2-Fe1-N2	95.33(15)
N2-Fe1-N1	152.11(12)
N2-Fe1-N1	84.22(11)
N2-Fe1-N1	84.21(11)
N1-Fe1-N1	152.10(12)
N1-Fe1-N1	83.51(16)
N2-Fe1-Cl1	104.60(8)
N2-Fe1-Cl1	104.60(8)
N1-Fe1-Cl1	102.47(8)
N1-Fe1-Cl1	102.47(8)
C6-N2-C4	119.2(2)
C6-N2-Fe1	125.8(2)
C6-N5-C6	130.2(3)
C6-N5-C1	114.66(17)
C6-N5-C1	114.66(17)

Table A17: Crystal data and structure refinement for biuret-modified Fe-TAML (**1b**)

Empirical formula	C33 H58 Cl Fe N8 O6
Formula weight	753.35
Temperature/K	110.02(10)
Crystal system	tetragonal
Space group	$P4_2/mbc$
a/Å	22.2021(3)
b/Å	22.2021(3)
c/Å	15.0626(3)
α/°	90
β/°	90
γ/°	90
Volume/Å^3	7424.8(2)
Z	30
ρ_{calc}mg/mm^3	1.4044
m/mm^{-1}	0.536
F(000)	3237.3948
Crystal size/mm^3	N × N × N
Theta range for data collection	5.72 to 58.18°
Index ranges	$-29 \leq h \leq 12$, $-29 \leq k \leq 25$, $-20 \leq l \leq 17$
Reflections collected	23049
Independent reflections	4611[R(int) = 0.0329]
Data/restraints/parameters	4611/0/307
Goodness-of-fit on F^2	1.031395
Final R indexes [I>2σ (I)]	R_1 = 0.076847, wR_2 = N
Final R indexes [all data]	R_1 = 0.085036, wR_2 = 0.219815
Largest diff. peak/hole / e Å^{-3}	0.884127/-1.124195

Table A18: Bond Lengths for biuret-modified Fe-TAML (**1b**)

Atom	Atom	Length/Å	Atom	Atom	Length/Å
Fe1	Cl2	2.3725(13)	O24	C6	1.777(10)
Fe1	N6^1	1.870(3)	N4	C10	1.588(9)
Fe1	N6	1.870(3)	N4	C10^1	1.588(9)
Fe1	N10^1	1.882(3)	N4	C12^1	1.471(8)
Fe1	N10	1.882(3)	N4	C12	1.471(8)
N3	C7	1.419(3)	N4	C14^1	1.516(8)
N3	C7^1	1.419(3)	N4	C14	1.516(8)

N3	C9	1.464(6)	N4	C1c^{1}	1.605(8)
O4	C7	1.239(4)	N4	C1c	1.605(8)
N1	C8^{2}	1.532(5)	C2	C4	1.509(5)
N1	C8	1.532(5)	C1	C8	1.458(7)
N1	C8^{3}	1.532(5)	C1	C1b	1.381(12)
N1	C8^{4}	1.532(5)	C5	C5^{1}	1.423(12)
N1	C1b	1.539(11)	C5	C11	1.348(7)
N1	C1b^{2}	1.539(11)	C5	C18	1.557(11)
N1	C1b^{3}	1.539(11)	C11	C6	1.074(11)
N1	C1b^{4}	1.539(11)	C11	C3^{1}	1.613(11)
N6	C7	1.342(4)	C11	C18	0.682(9)
N6	C13	1.486(4)	C8	C1b	1.464(13)
N10	C23	1.349(7)	C8	C1b^{3}	1.792(12)
N10	C5	1.400(6)	C6	C3^{1}	1.136(9)
O11	N22^{1}	1.365(8)	C6	C18	1.405(11)
O11	N22	1.365(8)	C10	C10^{1}	1.373(17)
C13	C21	1.539(7)	C10	C12	1.887(12)
C13	C23	1.542(6)	C10	C16^{1}	1.343(10)
C13	C25	1.522(6)	C12	C19	1.525(15)
N2	C4^{5}	1.520(3)	C12	C1a	1.279(13)
N2	C4	1.520(3)	C12	C1c	1.191(12)
N2	C4^{6}	1.520(3)	C14	C14^{1}	1.045(14)
N2	C4^{7}	1.520(3)	C14	C15	1.301(10)
O19	C23	1.232(5)	C14	C1c^{1}	1.904(11)
N22	N22^{1}	1.778(14)	C17	C17^{7}	1.318(18)
N22	O24	1.219(9)	C19	C1a	0.871(14)
N22	C6	1.399(10)	C19	C1c	1.062(12)
N22	C3^{1}	1.580(7)	C1a	C1c	1.520(13)

Table A19: Selected Bond angles for biuret-modified Fe-TAML (**1b**)

Atom	**Atom**	**Atom**	**Angle/°**	**Atom**	**Atom**	**Atom**	**Angle/°**
N6^{1}	Fe1	Cl2	104.49(10)	C1c^{1}	N4	C12	112.1(5)
N6	Fe1	Cl2	104.49(10)	C1c^{1}	N4	C12^{1}	45.3(5)
N6	Fe1	N6^{1}	95.30(17)	C1c	N4	C12^{1}	112.1(5)
N10^{1}	Fe1	Cl2	102.68(11)	C1c^{1}	N4	C14^{1}	106.4(5)
N10	Fe1	Cl2	102.68(11)	C1c^{1}	N4	C14	75.2(4)
N10^{1}	Fe1	N6	152.00(15)	C1c	N4	C14	106.4(5)

N10[1]	Fe1	N6[1]	84.34(14)	C1c	N4	C14[1]	75.2(4)
N10	Fe1	N6	84.34(14)	C1c	N4	C1c[1]	102.6(6)
N10	Fe1	N6[1]	152.00(15)	C2	C4	N2	115.4(3)
N10	Fe1	N10[1]	83.2(2)	C1b	C1	C8	62.0(5)
C7[1]	N3	C7	131.0(4)	C5[1]	C5	N10	112.6(3)
C9	N3	C7	114.40(18)	C11	C5	N10	138.8(7)
C9	N3	C7[1]	114.40(18)	C18	C5	N10	113.1(5)
C8[2]	N1	C8	111.0(4)	C18	C5	C11	25.9(4)
C8[3]	N1	C8	108.69(19)	C6	C11	C5	161.2(11)
C8[3]	N1	C8[2]	108.7(2)	C3[1]	C11	C5	116.7(7)
C8[4]	N1	C8	108.7(2)	C3[1]	C11	C6	44.6(6)
C8[4]	N1	C8[2]	108.69(19)	C18	C11	C5	94.4(12)
C8[4]	N1	C8[3]	111.0(4)	C18	C11	C6	104.1(13)
C1b	N1	C8[3]	71.4(5)	C18	C11	C3[1]	148.6(12)
C1b	N1	C8[4]	164.1(5)	C1	C8	N1[3]	116.4(4)
C1b	N1	C8[2]	84.4(5)	C1b	C8	N1[3]	61.8(5)
C1b[2]	N1	C8	84.4(5)	C1b[4]	C8	N1[3]	54.5(4)
C1b[2]	N1	C8[2]	56.9(5)	C1b[4]	C8	C1	147.5(6)
C1b[2]	N1	C8[3]	164.1(5)	C1b	C8	C1	56.4(5)
C1b[2]	N1	C8[4]	71.4(5)	O24	C6	N22	43.1(4)
C1b	N1	C8	56.9(5)	C11	C6	N22	169.9(10)
C1b[3]	N1	C8	164.1(5)	C11	C6	O24	145.3(9)
C1b[3]	N1	C8[2]	71.4(5)	C3[1]	C6	N22	76.4(6)
C1b[3]	N1	C8[4]	84.4(5)	C3[1]	C6	O24	117.4(7)
C1b[3]	N1	C8[3]	56.9(5)	C3[1]	C6	C11	93.8(10)
C1b[4]	N1	C8	71.4(5)	C18	C6	N22	161.8(9)
C1b[4]	N1	C8[2]	164.1(5)	C18	C6	O24	119.2(7)
C1b[4]	N1	C8[4]	56.9(5)	C18	C6	C11	28.1(6)
C1b[4]	N1	C8[3]	84.4(5)	C18	C6	C3[1]	121.8(9)
C1b[2]	N1	C1b	110.8(9)	C10[1]	C10	N4[1]	64.4(3)
C1b[3]	N1	C1b	108.8(5)	C12	C10	N4[1]	49.2(4)
C1b[3]	N1	C1b[2]	108.8(4)	C16[1]	C10	N4[1]	120.0(6)
C1b[4]	N1	C1b[3]	110.8(9)	C16[1]	C10	C12	156.0(8)
C1b[4]	N1	C1b[2]	108.8(5)	C10	C12	N4[1]	54.8(4)
C1b[4]	N1	C1b	108.8(4)	C19	C12	N4[1]	113.0(7)
C7	N6	Fe1[1]	126.4(2)	C19	C12	C10	144.9(8)
C13	N6	Fe1[1]	114.3(2)	C1a	C12	N4[1]	147.8(9)
C13	N6	C7	118.2(3)	C1a	C12	C10	145.4(9)

O4	C7	N3	117.1(3)	C1a	C12	C19	34.8(6)
N6	C7	N3	118.1(3)	C1c	C12	N4^{1}	73.3(6)
N6	C7	O4	124.8(3)	C1c	C12	C10	104.9(7)
C23	N10	Fe1^{1}	116.7(3)	C1c	C12	C19	43.9(6)
C5	N10	Fe1^{1}	115.3(3)	C1c	C12	C1a	75.9(8)
C5	N10	C23	128.0(4)	N22	C3	N22^{1}	68.4(6)
N22	O11	N22^{1}	81.2(6)	C11^{1}	C3	N22	169.3(4)
C21	C13	N6	110.3(4)	C11^{1}	C3	N22^{1}	101.0(4)
C23	C13	N6	107.4(3)	C11	C3	N22	101.0(4)
C23	C13	C21	107.7(4)	C11	C3	N22^{1}	169.3(4)
C25	C13	N6	113.7(3)	C11	C3	C11^{1}	89.6(6)
C25	C13	C21	111.3(4)	C6^{1}	C3	N22	127.8(7)
C25	C13	C23	106.2(4)	C6^{1}	C3	N22^{1}	59.4(5)
C4^{5}	N2	C4	111.9(2)	C6	C3	N22	59.4(5)
C4^{6}	N2	C4	111.8(3)	C6	C3	N22^{1}	127.8(7)
C4^{6}	N2	C4^{5}	104.8(3)	C6^{1}	C3	C11^{1}	41.6(6)
C4^{7}	N2	C4	104.8(3)	C6^{1}	C3	C11	131.2(7)
C4^{7}	N2	C4^{5}	111.8(3)	C6	C3	C11^{1}	131.2(7)
C4^{7}	N2	C4^{6}	111.9(2)	C6	C3	C11	41.6(6)
N22^{1}	N22	O11^{1}	49.4(3)	C6	C3	C6^{1}	172.8(11)
O24	N22	O11^{1}	129.7(6)	C14^{1}	C14	N4	69.8(3)
C6	N22	O11^{1}	144.4(7)	C15	C14	N4	127.3(6)
C6	N22	O24	85.2(6)	C1c^{1}	C14	N4	54.5(4)
C3^{1}	N22	O11^{1}	102.8(5)	C1c^{1}	C14	C15	175.5(8)
C3^{1}	N22	O24	127.1(6)	C14^{1}	C15	C14	47.4(7)
C3^{1}	N22	C6	44.3(4)	C10	C16	C10^{1}	61.5(8)
C13	C23	N10	113.0(3)	C11	C18	C5	59.7(10)
O19	C23	N10	126.3(5)	C6	C18	C5	107.5(8)
O19	C23	C13	120.7(5)	C6	C18	C11	47.8(10)
C6	O24	N22	51.7(5)	C1a	C19	C12	57.0(11)
C10	N4	C10^{1}	51.2(6)	C1c	C19	C12	51.1(7)
C12^{1}	N4	C10	110.9(6)	C1c	C19	C1a	103.3(14)
C12^{1}	N4	C10^{1}	76.1(5)	C19	C1a	C12	88.2(12)
C12	N4	C10^{1}	110.9(6)	C1c	C1a	C12	49.5(6)
C12	N4	C10	76.1(5)	C1c	C1a	C19	42.8(9)
C12	N4	C12^{1}	87.5(8)	C1	C1b	N1	120.9(8)
C14	N4	C10	111.5(5)	C8^{3}	C1b	N1	54.1(4)
C14	N4	C10^{1}	93.9(5)	C8	C1b	N1	61.3(5)

C14[1]	N4	C10	93.9(5)	C8[3]	C1b	C1	150.3(9)
C14[1]	N4	C10[1]	111.5(5)	C8	C1b	C1	61.6(6)
C14	N4	C12[1]	113.5(5)	C12	C1c	N4[1]	61.4(5)
C14	N4	C12	151.1(5)	C14[1]	C1c	N4[1]	50.3(3)
C14[1]	N4	C12[1]	151.1(5)	C14[1]	C1c	C12	105.3(6)
C14[1]	N4	C12	113.5(5)	C19	C1c	N4[1]	138.2(9)
C14[1]	N4	C14	40.3(6)	C19	C1c	C12	85.0(10)
C1c[1]	N4	C10	151.5(5)	C19	C1c	C14[1]	169.7(10)
C1c[1]	N4	C10[1]	101.8(4)	C1a	C1c	N4[1]	115.5(7)
C1c	N4	C10	101.8(4)	C1a	C1c	C12	54.7(7)
C1c	N4	C10[1]	151.5(5)	C1a	C1c	C14[1]	155.4(7)
C1c	N4	C12	45.3(5)	C1a	C1c	C19	33.9(8)

References for Appendix I

1. Bruker (2005). *APEX2*. Version 5.053. Bruker AXS Inc., Madison,Wisconsin, USA.
2. G. M. Sheldrick, (2004). *CELL_NOW*. University of Göttingen, Germany. Steiner, Th. (1998). *Acta Crystallographica* **B54**, 456–463.
3. Bruker (2004). *SAINT-Plus* (Version 7.03). Bruker AXS Inc., Madison, Wisconsin, USA.
4. G. M. Sheldrick, (2002). *SADABS* (Version 2.03) and *TWINABS* (Version 1.02).University of Göttingen, Germany.
5. G. M. Sheldrick, (1997). *SHELXS '97* and *SHELXL '97*. University of Göttingen, Germany.

Appendix II

Brookhaven Instruments Corp.
90Plus Particle Sizing Software Ver. 3.94

Date: Jun 19, 2014
Time: 22:20:46
Batch: 0

Sample ID **before reaction (Combined)**
Operator ID **soumen**
Notes

Measurement Parameters:

Temperature	= 25.0 deg. C	Runs Completed	= 3
Liquid	= Water	Run Duration	= 00:01:00
Viscosity	= 0.890 cP	Total Elapsed Time	= 00:03:00
Ref.Index Fluid	= 1.330	Average Count Rate	= 1.1 kcps
Angle	= 90.00	Ref.Index Real	= 1.330
Wavelength	= 659.0 nm	Ref.Index Imag	= 0.000
Baseline	= Auto (Slope Analysis)	Dust Filter Setting	= 30.00

before reaction (Combined)

Effective Diameter: **0.0 nm**
Polydispersity: **0.000**
Baseline Index: **0.0/100.00%**
Elapsed Time: **00:03:00**

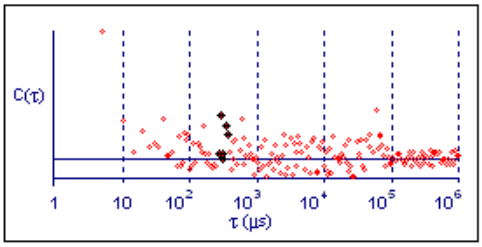

Correlation Function

Run	Eff. Diam. (nm)	Half Width (nm)	Polydispersity	Baseline Index
1	0.0	0.0	0.000	7.2/100.00%
2	0.2	0.1	0.088	0.0/100.00%
3	0.0	0.0	0.000	0.0/100.00%
Mean	0.1	0.0	0.029	2.4/100.00%
Std. Error	0.1	0.0	0.029	2.4/ 0.00
Combined	0.0	0.0	0.000	0.0/100.00%

Figure B1: DLS of a mixture containing **1a** (7.4 µM), $[Ru(bpy)_3]^{2+}$ (0.83 mM) and $Na_2S_2O_8$ (8.30 mM) in 40 mM borate buffer mixture that was filtered using 0.2 µm nylon filter paper before light irradiation and then analysed. Note: This is a control sample which was done before irradiation.

Brookhaven Instruments Corp.
90Plus Particle Sizing Software Ver. 3.94

Date: Jun 19, 2014
Time: 23:55:50
Batch: 0

Sample ID **10 min after photochemical rea (Combined)**
Operator ID **soumen**
Notes

Measurement Parameters:

Temperature	= 25.0 deg. C	Runs Completed	= 3
Liquid	= Water	Run Duration	= 00:01:00
Viscosity	= 0.890 cP	Total Elapsed Time	= 00:03:00
Ref.Index Fluid	= 1.330	Average Count Rate	= 1.1 kcps
Angle	= 90.00	Ref.Index Real	= 1.330
Wavelength	= 659.0 nm	Ref.Index Imag	= 0.000
Baseline	= Auto (Slope Analysis)	Dust Filter Setting	= 30.00

10 min after photochemical rea (Combined)

Effective Diameter: **0.0 nm**
Polydispersity: **0.000**
Baseline Index: **3.4/100.00%**
Elapsed Time: **00:03:00**

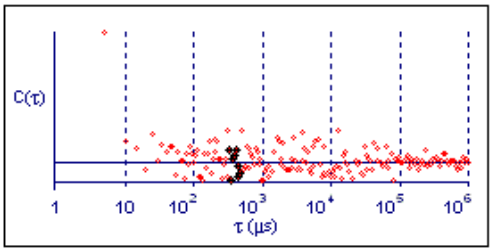

Correlation Function

Run	Eff. Diam. (nm)	Half Width (nm)	Polydispersity	Baseline Index
1	0.0	0.0	0.000	0.0/100.00%
2	0.0	0.0	0.000	0.0/100.00%
3	0.0	0.0	0.000	4.6/100.00%
Mean	0.0	0.0	0.000	1.5/100.00%
Std. Error	0.0	0.0	0.000	1.5/ 0.00
Combined	0.0	0.0	0.000	3.4/100.00%

Figure B2: DLS of a reaction mixture containing **1a** (7.4 µM), $[Ru(bpy)_3]^{2+}$ (0.83 mM) and $Na_2S_2O_8$ (8.30 mM) in 40 mM borate buffer mixture that was irradiated for 10 min.

Table B1: Details of photochemical WO showing calculations of isotopic distribution pattern of O_2 evolved in the absence and presence of $H_2{}^{18}O$

		Sample		
		[a]Background (before irradiation)	[b]100% $H_2{}^{16}O$	[c]59% $H_2{}^{16}O$: 41% $H_2{}^{18}O$
RELATIVE ABUNCE	$^{28}N_2$	999847	989816	999850
	$^{32}O_2$	594990	983856	705441
	$^{34}O_2$	2824	4285	131870
	$^{36}O_2$	-	-	45198
RATIO	$^{28}N_2$: $^{32}O_2$	**1.68 : 1.00**	1.01 : 1.00	1.42 : 1.00
	$^{28}N_2$: $^{34}O_2$	**354 : 1.00**	231 : 1.00	7.58 : 1.00
	$^{28}N_2$: $^{36}O_2$	-	-	22.1 : 1.00
Air Contributed $^{32}O_2$		-	589176	595149
Air Contributed $^{34}O_2$		-	2796	2824
Net $^{32}O_2$ abundance; %		-	394680	110292; 38.8%
Net $^{34}O_2$ abundance; %		-	1490	129046; 45.3%
Net $^{36}O_2$ abundance; %		-	-	45198; 15.9%

Headspace gas analysis of [a]typical photochemical WO mixture containing all the constituents (degassed with He for 20 min) before irradiation to determine background [b]after irradiation for 10 min; and [c] photochemical water oxidation mixture containing 41% $H_2{}^{18}O$ in $H_2{}^{16}O$ after irradiation for 10 min. The adventitious oxygen ($^{32}O_2$) can be subtracted by using the background ratio of the $^{28}N_2$ and $^{32}O_2$ peaks ($^{28}N_2$: $^{32}O_2$ = 1.68: 1.00) in the degassed control.

$$\text{Air contributed } 32O_2 = \frac{\text{Relative abundance of } 28_{N_2} \text{ in a particular WO reaction}}{\text{Ratio of } N_2 \text{ \& } 32O_2 \text{ in the degassed control}} \quad (2)$$

$$\text{Air contributed } 34O_2 = \frac{\text{Relative abundance of } 28_{N_2} \text{ in a particular WO reaction}}{\text{Ratio of } N_2 \text{ \& } 34O_2 \text{ in the degassed control}} \quad (3)$$

$$\text{Net } X_{O_2} \text{ abundance} = X_{O_2} \text{ Evolved in a particular WO reaction} - \text{Air contributed } X_{O_2} \quad (4)$$

Table B2: GC calibration using air as standard sample

Sample	Area for 100 µL injection	Average area	O_2 (considering 21% of air is O_2) (µmole)
Air1	493034	493564	0.9
Air2	493355		
Air3	494303		

Page 1 of 1

Area % Report

Air1

Data File: C:\Users\bharad\Desktop\23-11-13\air8.dat
Method: C:\EZChrom Elite\Enterprise\Projects\Default\Method\TCD Offline.met
Acquired: 11/23/2013 12:13:25 PM
Printed: 10/29/2014 2:20:01 PM

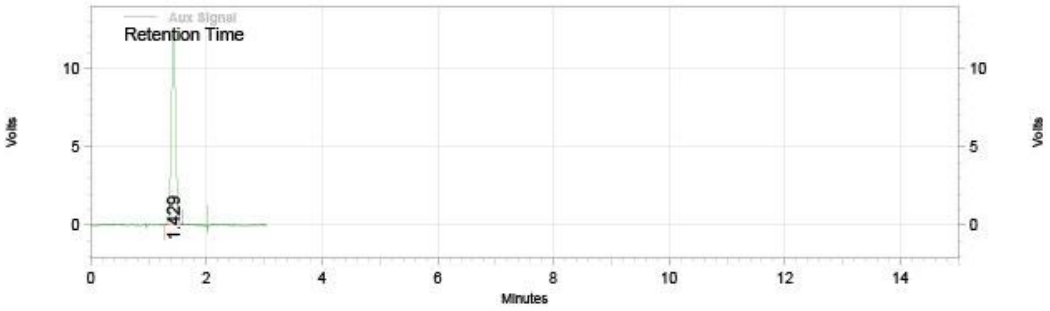

Aux Signal Results

Retention Time	Area	Area %	Height	Height %
1.429	493034	100.00	94987	100.00

Totals				
	493034	100.00	94987	100.00

Figure B3: GC of 100 µL air sample (Air1)

Page 1 of 1

Area % Report

Air2

Data File: C:\Users\bharad\Desktop\23-11-13\air10.dat
Method: C:\EZChrom Elite\Enterprise\Projects\Default\Method\TCD Offline.met
Acquired: 11/23/2013 12:39:00 PM
Printed: 10/29/2014 2:20:46 PM

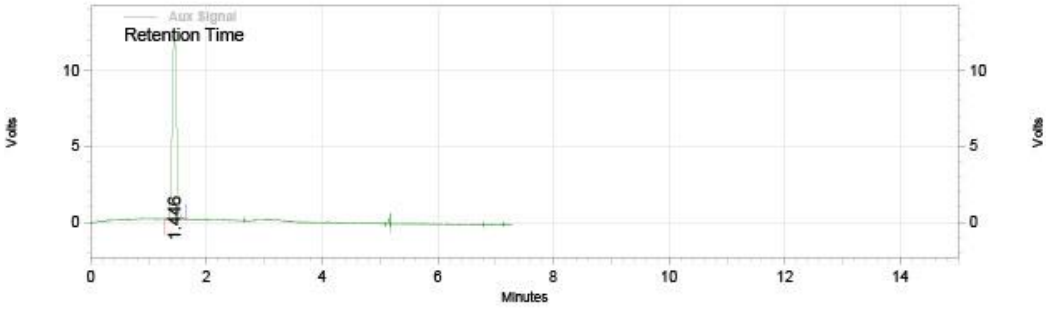

Aux Signal Results

Retention Time	Area	Area %	Height	Height %
1.446	493355	100.00	94859	100.00

Totals				
	493355	100.00	94859	100.00

Figure B4: GC of 100 µL air sample (Air2)

Air3

Page 1 of 1

Area % Report

Data File: C:\Users\bharad\Desktop\23-11-13\Air 11.dat
Method: C:\EZChrom Elite\Enterprise\Projects\Default\Method\TCD Offline.met
Acquired: 11/23/2013 1:18:22 PM
Printed: 10/29/2014 2:07:37 PM

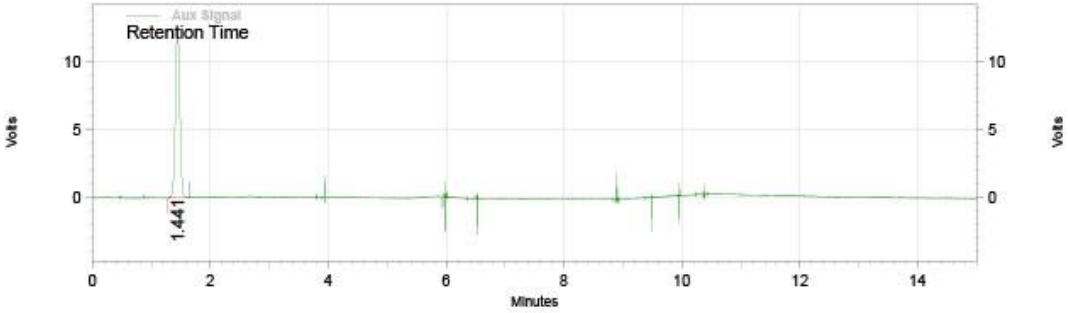

Aux Signal Results

Retention Time	Area	Area %	Height	Height %
1.441	494303	100.00	95292	100.00
Totals	494303	100.00	95292	100.00

Figure B5: GC of 100 µL air sample (Air3)

Area % Report $[Ru(bipy)_3]^{2+} + Na_2S_2O_8 + \mathbf{1a}$

Page 1 of 1

Data File: C:\Users\bharad\Desktop\23-11-13\set 1.dat
Method: C:\EZChrom Elite\Enterprise\Projects\Default\Method\TCD Offline.met
Acquired: 11/23/2013 8:08:02 AM
Printed: 10/29/2014 2:21:39 PM

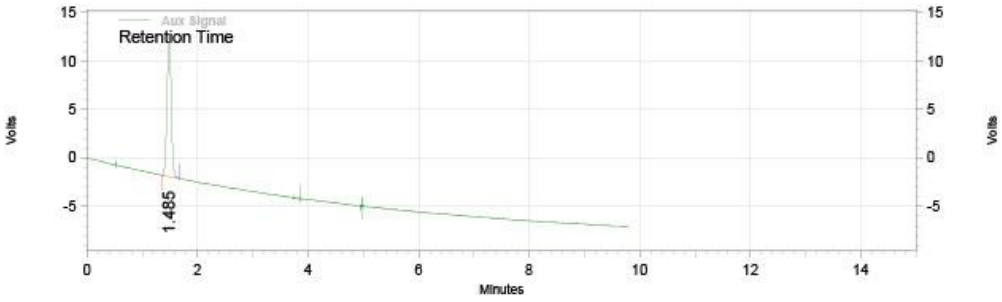

Aux Signal Results

Retention Time	Area	Area %	Height	Height %
1.485	600179	100.00	113251	100.00
Totals	600179	100.00	113251	100.00

Figure B6: Head space sample of a photochemical WO reaction by **1a**

$[Ru(bipy)_3]^{2+} + Na_2S_2O_8 + \mathbf{1b}$

Page 1 of 1

Area % Report

Data File: C:\Users\bharad\Desktop\23-11-13\set 9.dat
Method: C:\EZChrom Elite\Enterprise\Projects\Default\Method\TCD Offline.met
Acquired: 11/23/2013 10:12:53 AM
Printed: 10/29/2014 2:51:34 PM

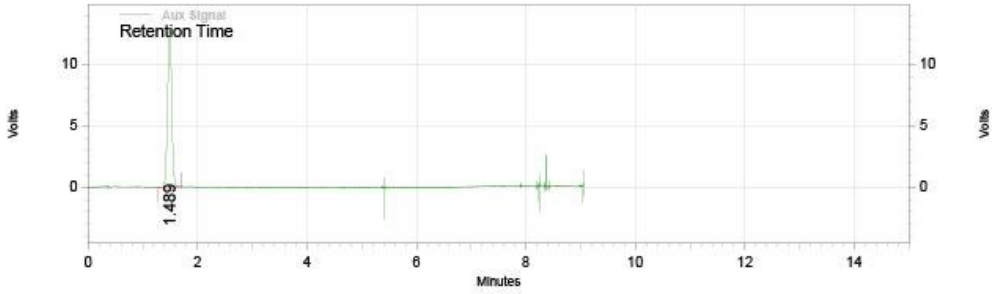

Aux Signal Results

Retention Time	Area	Area %	Height	Height %
1.489	521756	100.00	99482	100.00
Totals	521756	100.00	99482	100.00

Figure B7: Head space sample of a photochemical WO reaction by **1b**

$[Ru(bipy)_3]^{2+} + Na_2S_2O_8 + \mathbf{1b}$

Page 1 of 1

Area % Report

Data File: C:\Users\bharad\Desktop\23-11-13\set 10.dat
Method: C:\EZChrom Elite\Enterprise\Projects\Default\Method\TCD Offline.met
Acquired: 11/23/2013 10:23:35 AM
Printed: 10/29/2014 2:54:03 PM

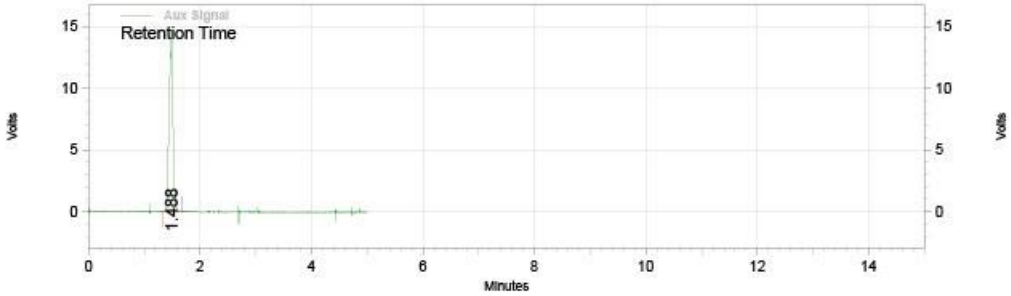

Aux Signal Results

Retention Time	Area	Area %	Height	Height %
1.488	523236	100.00	113613	100.00
Totals	523236	100.00	113613	100.00

Figure B8: Head space sample of a photochemical WO reaction by **1b**

Area % Report $[Ru(bipy)_3]^{2+} + Na_2S_2O_8 + Fe(ClO_4)_3$ Page 1 of 1

Data File: C:\Users\bharad\Desktop\23-11-13\set 6.dat
Method: C:\EZChrom Elite\Enterprise\Projects\Default\Method\TCD Offline.met
Acquired: 11/23/2013 9:37:17 AM
Printed: 10/29/2014 2:36:20 PM

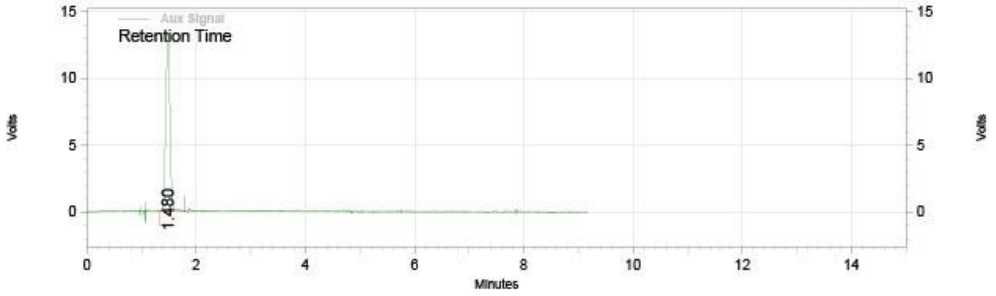

Aux Signal Results

Retention Time	Area	Area %	Height	Height %
1.480	546724	100.00	102932	100.00
Totals	546724	100.00	102932	100.00

Figure B9: Head space sample of a photochemical WO reaction by **$Fe(ClO_4)_3$**

Area % Report $[Ru(bipy)_3]^{2+} + Na_2S_2O_8 + Fe(ClO_4)_3$ Page 1 of 1

Data File: C:\Users\bharad\Desktop\23-11-13\set 7.dat
Method: C:\EZChrom Elite\Enterprise\Projects\Default\Method\TCD Offline.met
Acquired: 11/23/2013 9:47:50 AM
Printed: 10/29/2014 2:36:44 PM

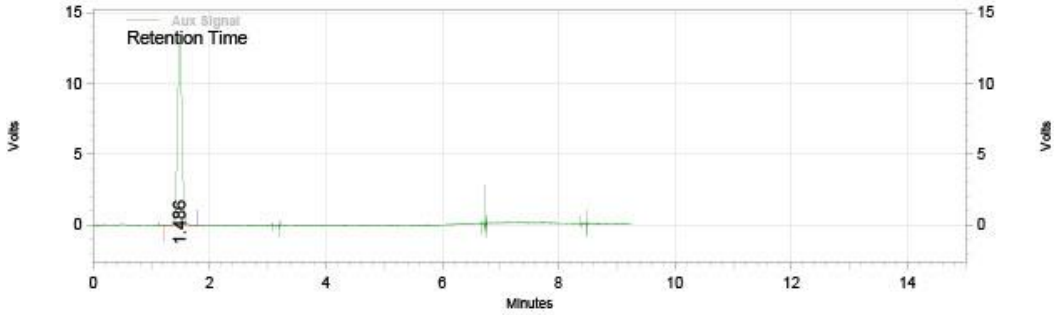

Aux Signal Results

Retention Time	Area	Area %	Height	Height %
1.486	549267	100.00	103852	100.00
Totals	549267	100.00	103852	100.00

Figure B10: Head space sample of a photochemical WO reaction by **$Fe(ClO_4)_3$**

Page 1 of 1

Area % Report

CAN

Data File: C:\Users\bharad\Desktop\16-01-2014\CAN Control 2.dat
Method: C:\EZChrom Elite\Enterprise\Projects\Default\Method\TCD Offline.met
Acquired: 1/16/2014 6:22:10 PM
Printed: 10/29/2014 2:03:37 PM

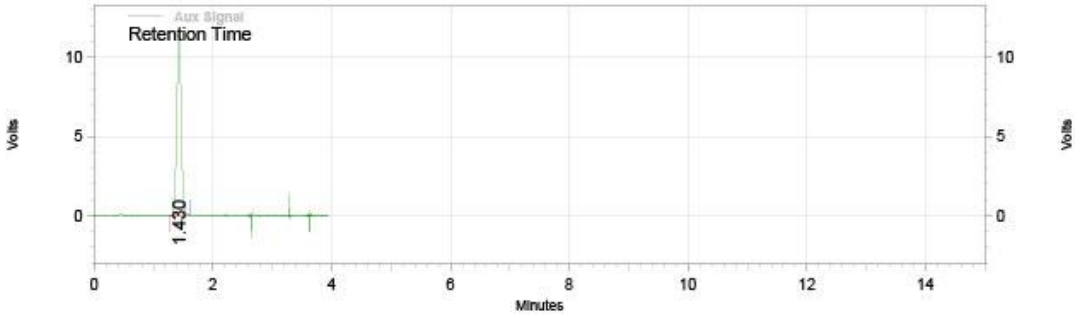

Aux Signal Results

Retention Time	Area	Area %	Height	Height %
1.430	467337	100.00	89690	100.00
Totals	467337	100.00	89690	100.00

Figure B11: Head space sample from a control chemical WO reaction

Page 1 of 1

Area % Report

CAN + **1a**

Data File: C:\Users\bharad\Desktop\16-01-2014\Normal cat 1.dat
Method: C:\EZChrom Elite\Enterprise\Projects\Default\Method\TCD Offline.met
Acquired: 1/16/2014 3:42:26 PM
Printed: 10/29/2014 2:05:40 PM

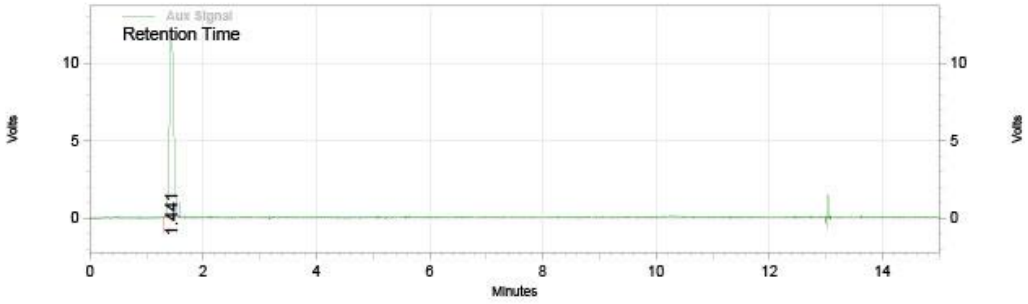

Aux Signal Results

Retention Time	Area	Area %	Height	Height %
1.441	485919	100.00	92883	100.00
Totals	485919	100.00	92883	100.00

Figure B12: Head space sample of a chemical WO reaction by **1a**

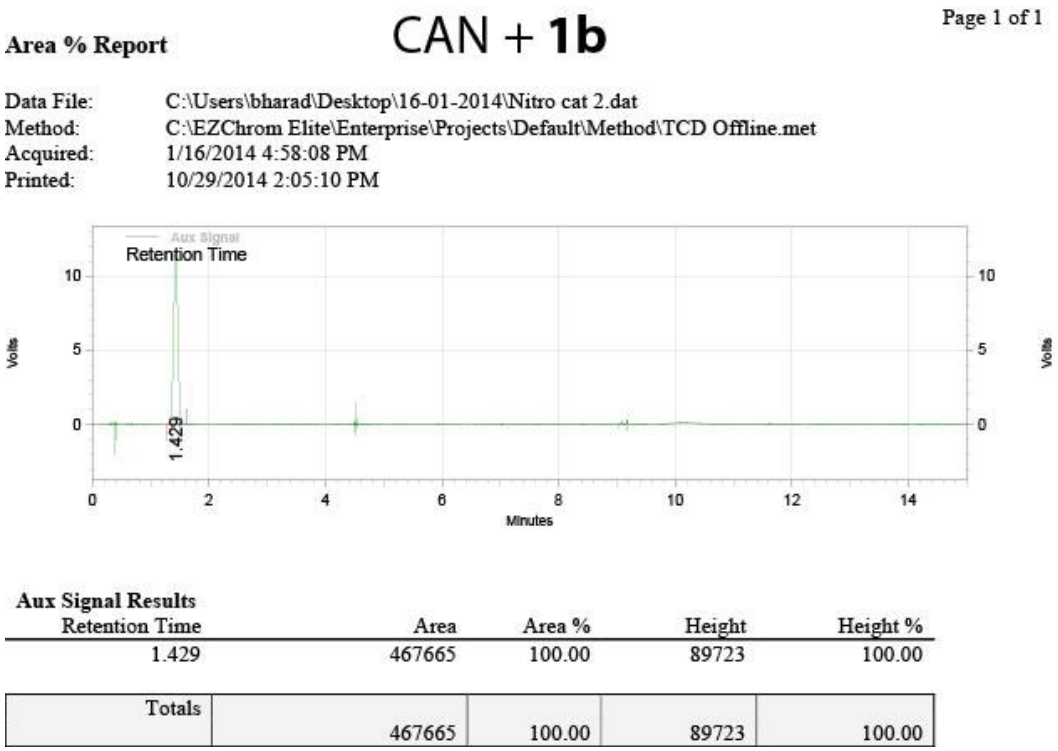

Figure B13: Head space sample of a chemical WO reaction by **1b**

Table B3: Total O_2 evolved in photochemical chemical water oxidation by **1a** and **1b**

Sample	Area for 100 µL injection (A1)	Vol. displaced (µL); V1	Head space Vol. (µL); V2	Total Vol. (µL); V3	Total area (A2) = (A1/100)*V3	O_2 evolved (µmole) = (0.9 µmole/493564 area for 100 µL of air)*A2	Average O_2 (µmoles)	O_2 yield = (O_2 evolved in control – O_2 evolved in sample)	TON = No of O_2 evolved (µmole)/No of Catalyst (µmole)
$[Ru(bipy)_3]^{2+}$ + $Na_2S_2O_8$	497255	0	3420	3420	17006121	31.01	30.70	-	
	486946	0	3420	3420	16653553.2	30.37			
$[Ru(bipy)_3]^{2+}$ + $Na_2S_2O_8$ +**1a**	600179	130	3420	3550	21306354.5	38.85	38.575	7.875	220
	589996	140	3420	3560	21003857.6	38.30			
$[Ru(bipy)_3]^{2+}$ + $Na_2S_2O_8$ +**1b**	521726	20	3420	3440	17947374.4	32.73	32.775	2.075	58
	523236	20	3420	3440	17999318.4	32.82			
$[Ru(bipy)_3]^{2+}$ + $Na_2S_2O_8$ +**$Fe(ClO_4)_3$**	546724	80	3420	3500	19135340	34.89	34.97	4.27	120
	549267	80	3420	3500	19224345	35.05			

Note 1: [Catalyst] = 7.4 µM, Total vol = 4.83 mL; No of catalyst = (7.4 × 4.83)/1000 µmole = 0.0357 µmole; 100 µL injection

Table B4: Total O_2 evolved in chemical water oxidation using CAN by **1a** and **1b**

Sample	Area for 100 µL injection (A1)	Vol. displaced (µL); V1	Head space Vol. (µL); V2	Total Vol. (µL); V3	Total area (A2) = (A1/100)*V3	O_2 (µmoles) = (0.9 µmole/493564 area for 100 µL of air)*A2	O_2 yield = (O_2 evolved in control – O_2 evolved in sample)	TON = O_2 (µmole)/Catalyst (µmole)
CAN	467337	0	4400	4400	20562828	37.50	-	
CAN+**1a**	485919	0	4400	4400	21380436	38.99	1.49	10
CAN+**1b**	467665	300	4400	4700	21980255	40.08	2.58	17

Appendix III

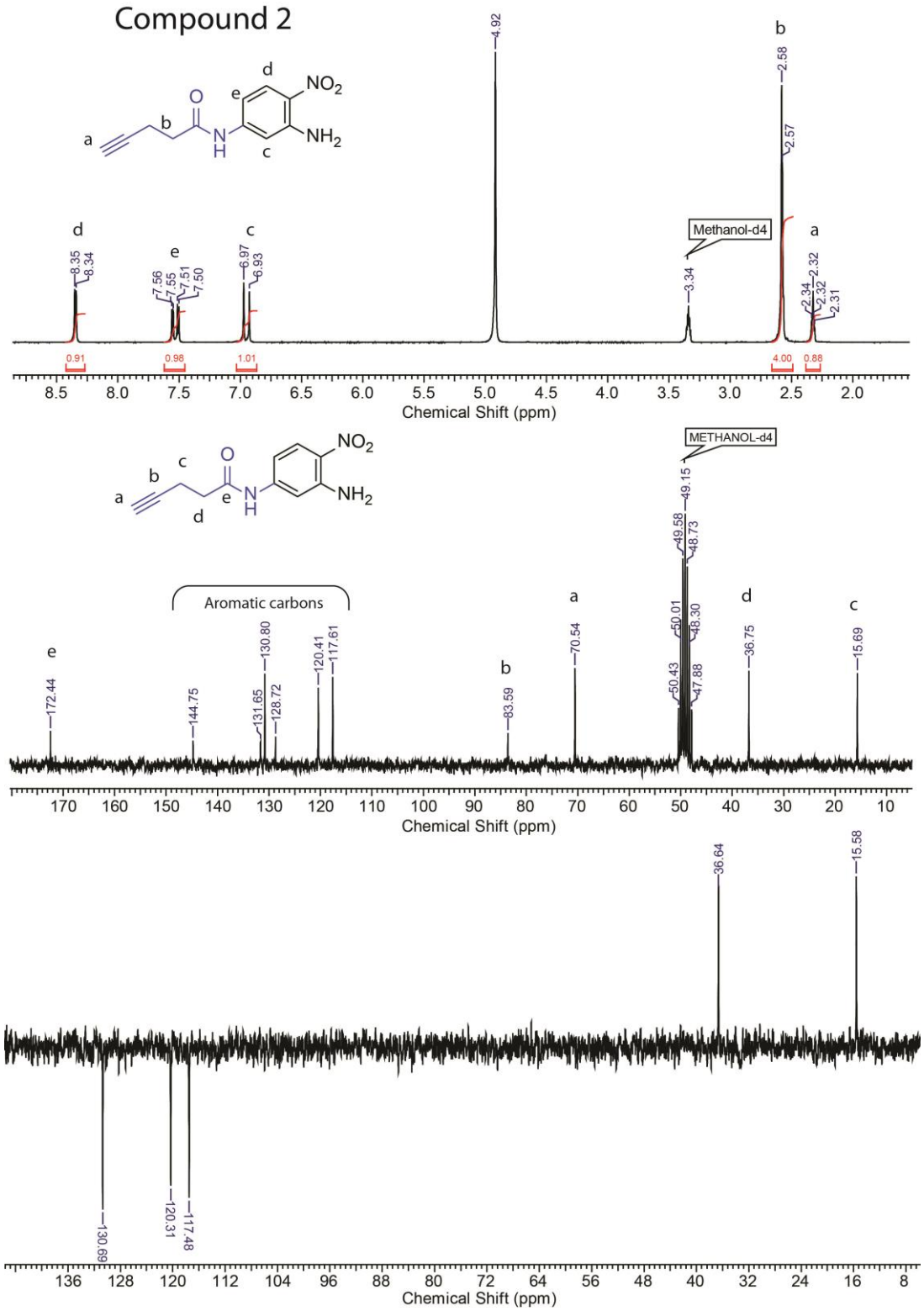

Figure C1: From top to bottom; 1H, 13C and DEPT NMR of compound **2** in methanol-d4.

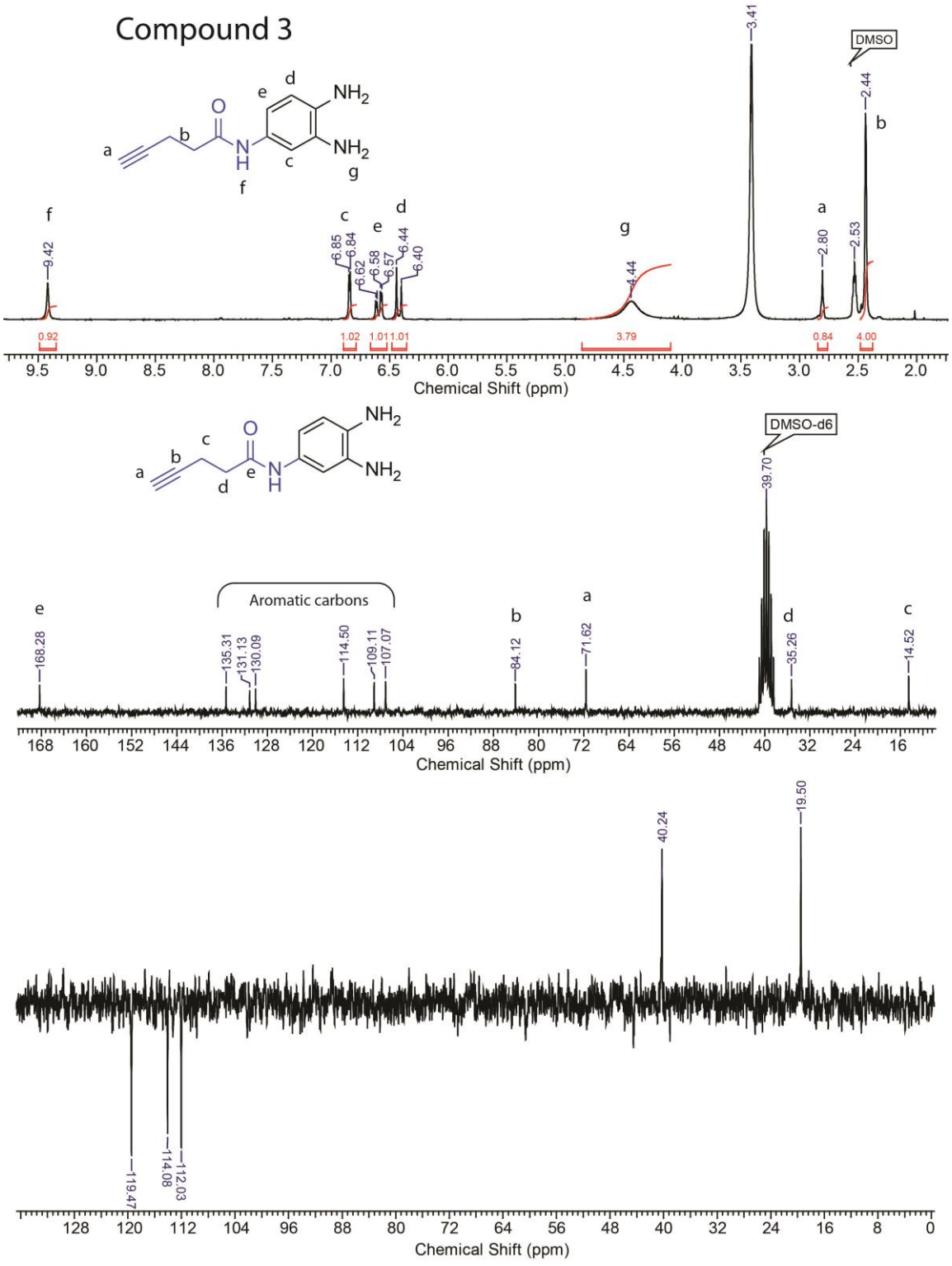

Figure C2: From top to bottom; 1H, 13C and DEPT NMR of compound **3** in DMSO-d6.

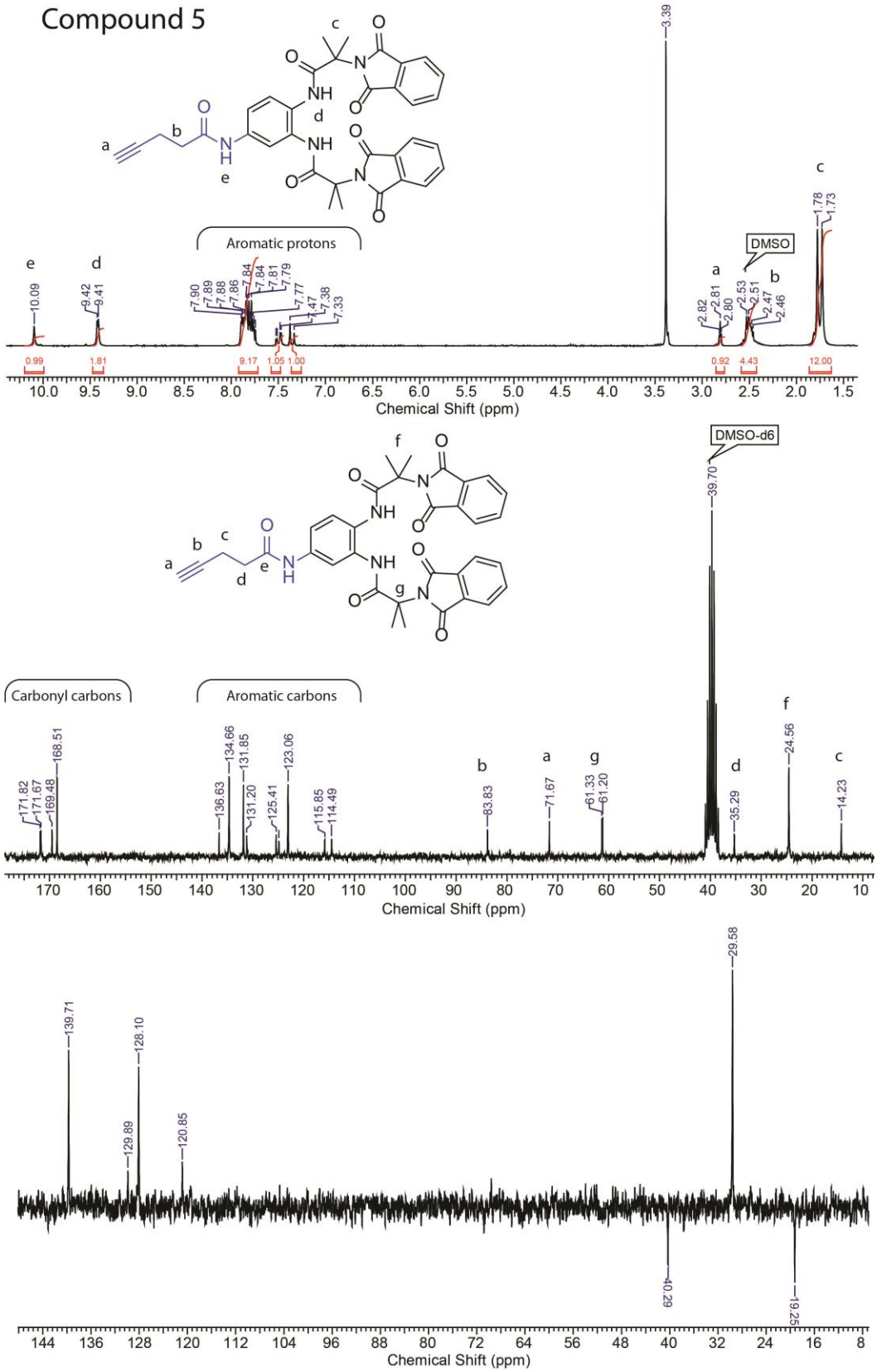

Figure C3: From top to bottom; 1H, 13C and DEPT NMR of compound **5** in DMSO-d6.

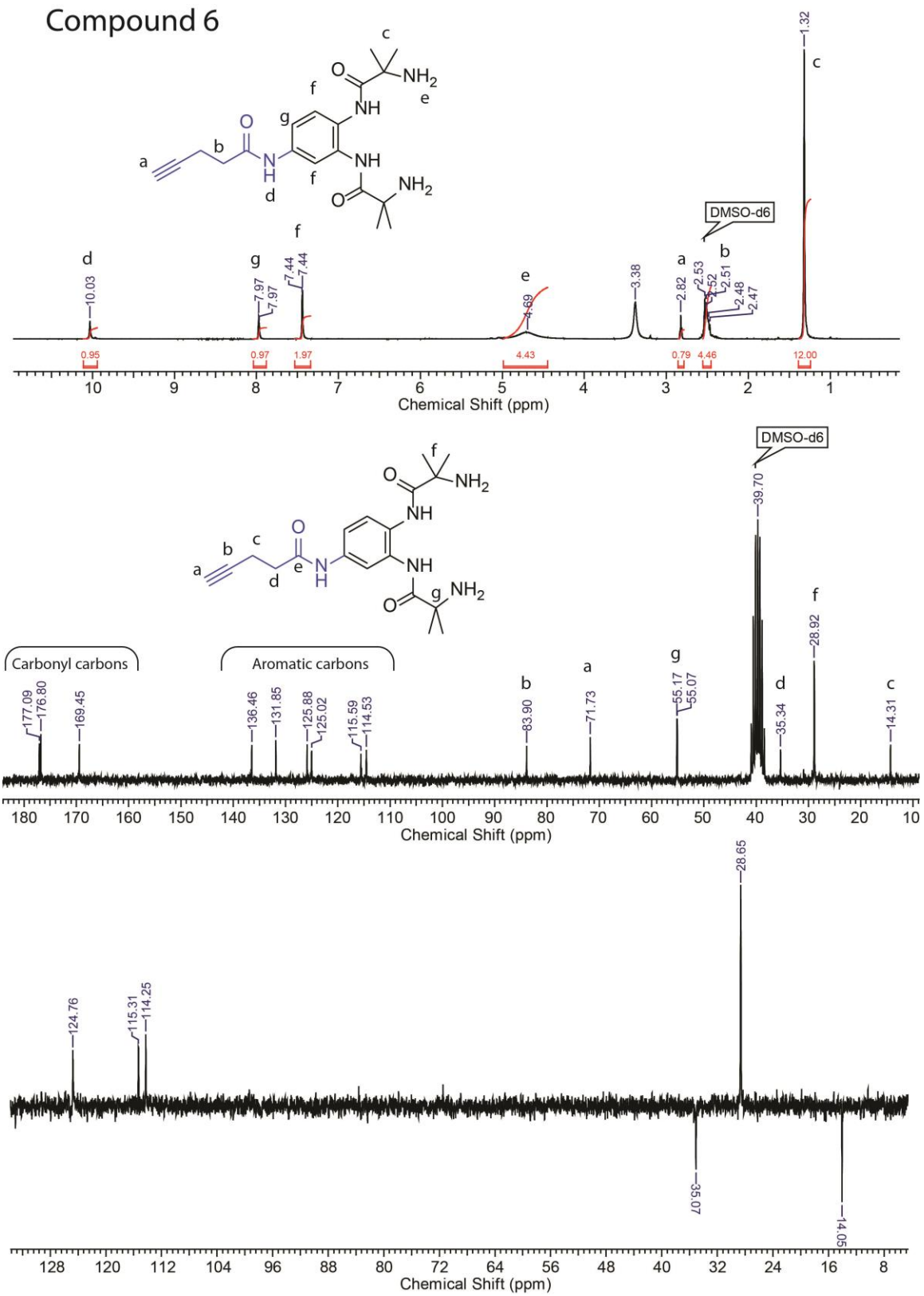

Figure C4: From top to bottom; 1H, 13C and DEPT NMR of compound **6** in DMSO-d6.

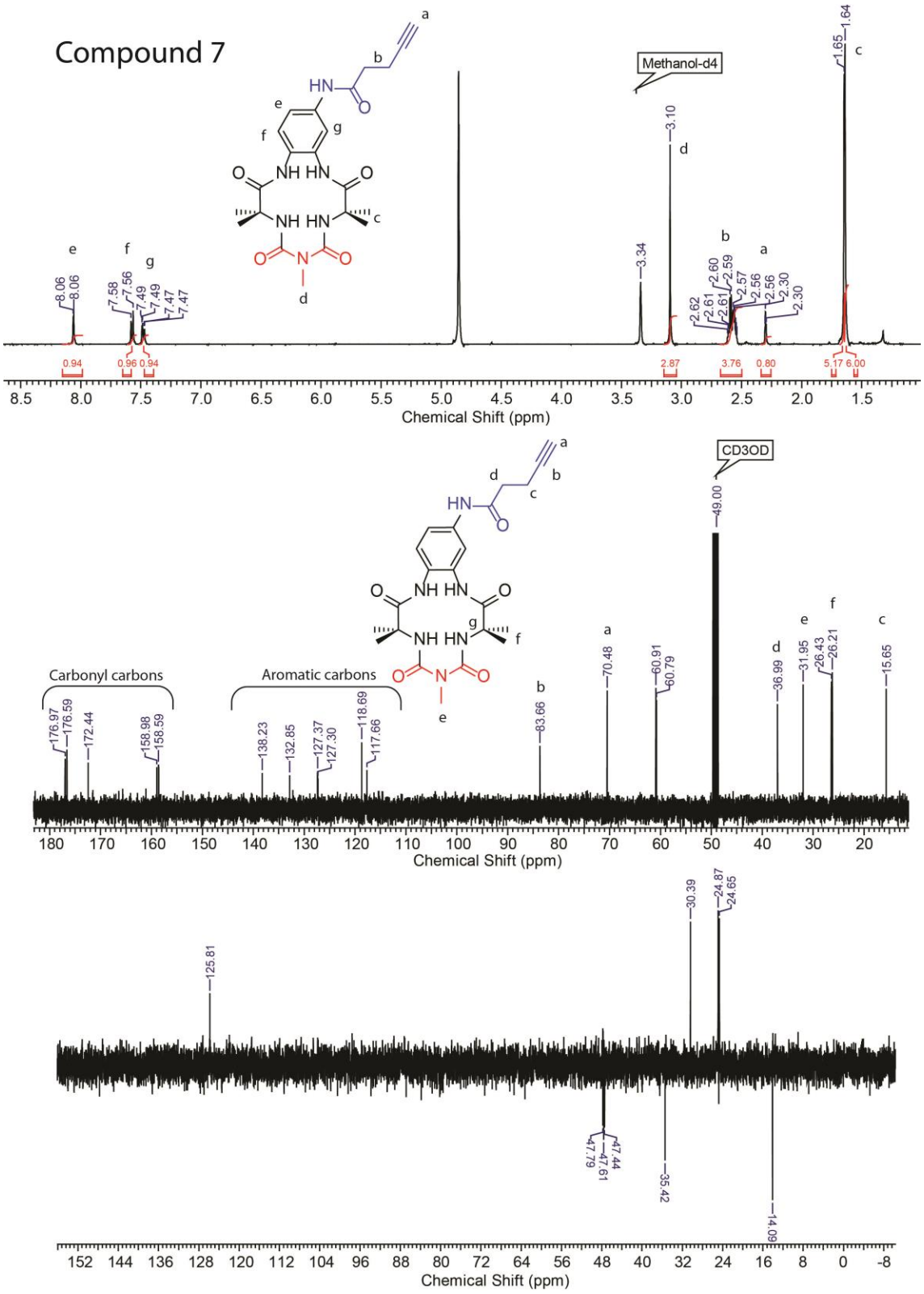

Figure C5: From top to bottom; 1H, 13C and DEPT NMR of compound **7** in methanol-d4.

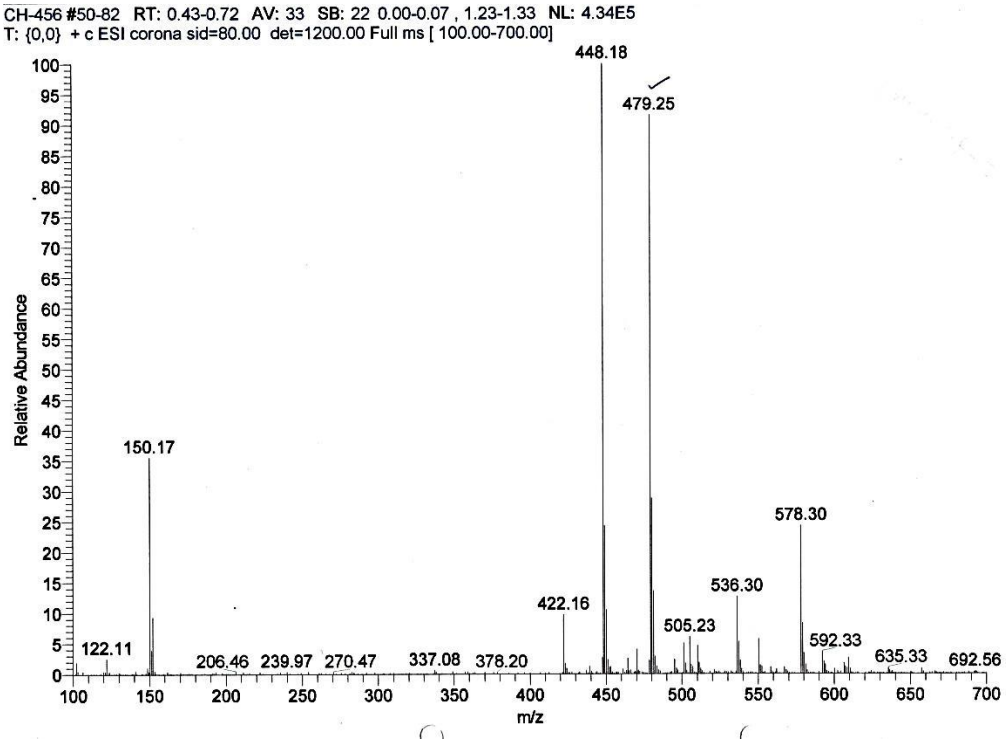

Figure C6: ESI-MS spectrum of the alkyne tailed biuret-modified TAML (m/z value at 479.25 corresponds to the sodiated molecular ion peak).

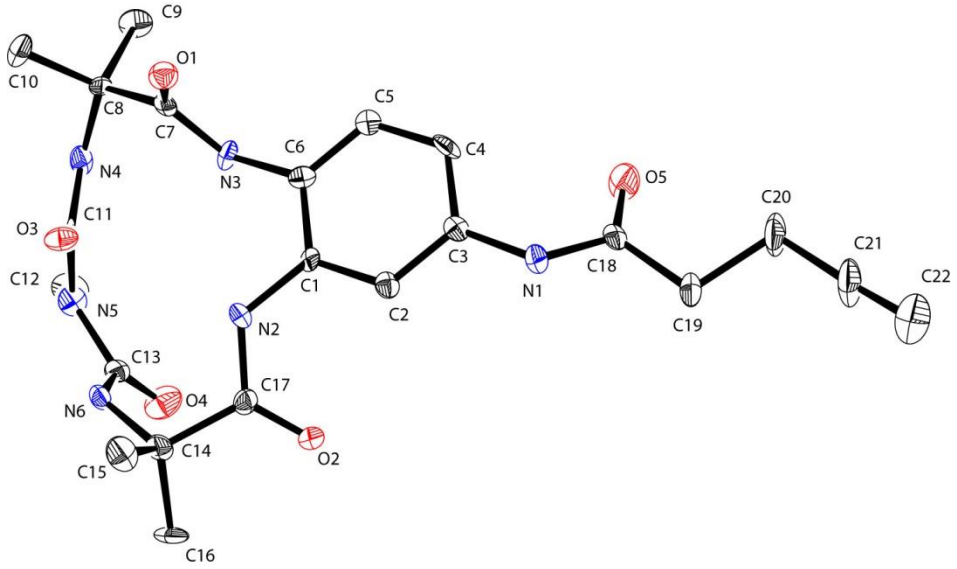

Figure C7: An ORTEP diagram of the alkyne tailed biuret-modified TAML (Compound **7**)

Table C1: Crystal data and structure refinement for Alkyne tailed biuret-modified TAML	
Identification code	Alkyne tailed biuret-modified TAML
Empirical formula	$C_{23}N_6O_4$
Formula weight	424.29
Temperature/K	566(2)
Crystal system	monoclinic
Space group	$P2_1/c$
a/Å	9.8498(16)
b/Å	19.932(3)
c/Å	11.9950(19)
α/°	90.00
β/°	100.528(3)
γ/°	90.00
Volume/Å^3	2315.3(6)
Z	4
ρ_{calc}mg/mm^3	1.217
m/mm^{-1}	0.088
F(000)	848
Crystal size/mm^3	? × ? × ?
Theta range for data collection	4.02 to 56.38°
Index ranges	$-12 \leq h \leq 12$, $-26 \leq k \leq 26$, $-15 \leq l \leq 15$
Reflections collected	25649
Independent reflections	5339[R(int) = 0.1427]
Data/restraints/parameters	5339/0/298
Goodness-of-fit on F^2	1.336
Final R indexes [I>2σ (I)]	R_1 = 0.2051, wR_2 = 0.4046
Final R indexes [all data]	R_1 = 0.2187, wR_2 = 0.4124
Largest diff. peak/hole / e Å^{-3}	0.870/-0.531

Table C2: Bond Lengths for H4MeN5-Alkyne.

Atom	**Atom**	**Length/Å**	**Atom**	**Atom**	**Length/Å**
C1	C2	1.390(9)	C11	O3	1.212(8)
C1	C6	1.415(9)	C12	N5	1.494(9)
C1	N2	1.419(8)	C13	N5	1.432(9)
C2	C3	1.399(9)	C13	N6	1.349(9)
C3	C4	1.396(10)	C13	O4	1.209(9)

C3	N1	1.427(9)	C14	C15	1.534(10)
C4	C5	1.397(10)	C14	C16	1.552(11)
C5	C6	1.370(10)	C14	C17	1.549(10)
C6	N3	1.450(9)	C14	N6	1.478(9)
C7	C8	1.545(10)	C17	N2	1.385(9)
C7	N3	1.379(9)	C17	O2	1.207(9)
C7	O1	1.209(9)	C18	C19	1.519(10)
C8	C9	1.561(10)	C18	N1	1.365(9)
C8	C10	1.553(10)	C18	O5	1.224(9)
C8	N4	1.482(10)	C19	C20	1.547(11)
C11	N4	1.364(9)	C20	C21	1.454(12)
C11	N5	1.408(9)	C21	C22	1.186(13)

Table C3: Bond Angles for H4MeN5-Alkyne.

Atom	**Atom**	**Atom**	**Angle/°**	**Atom**	**Atom**	**Atom**	**Angle/°**
C2	C1	C6	119.1(6)	O4	C13	N5	120.4(7)
C2	C1	N2	121.7(6)	O4	C13	N6	125.6(7)
C6	C1	N2	119.1(6)	C15	C14	C16	110.4(6)
C1	C2	C3	120.3(6)	C15	C14	C17	109.8(6)
C2	C3	N1	117.6(6)	C17	C14	C16	108.3(6)
C4	C3	C2	120.3(6)	N6	C14	C15	112.2(6)
C4	C3	N1	122.1(6)	N6	C14	C16	106.3(6)
C3	C4	C5	118.9(6)	N6	C14	C17	109.8(5)
C6	C5	C4	121.3(7)	N2	C17	C14	114.5(6)
C1	C6	N3	119.2(6)	O2	C17	C14	122.6(7)
C5	C6	C1	120.0(7)	O2	C17	N2	122.8(6)
C5	C6	N3	120.5(6)	N1	C18	C19	113.9(6)
N3	C7	C8	111.7(6)	O5	C18	C19	122.6(6)
O1	C7	C8	123.7(6)	O5	C18	N1	123.5(7)
O1	C7	N3	124.5(6)	C18	C19	C20	110.8(7)
C7	C8	C9	109.9(6)	C21	C20	C19	111.2(8)
C7	C8	C10	109.9(6)	C22	C21	C20	176.0(12)
C10	C8	C9	109.5(6)	C18	N1	C3	125.1(6)
N4	C8	C7	110.8(5)	C17	N2	C1	125.8(6)
N4	C8	C9	107.1(6)	C7	N3	C6	122.7(6)
N4	C8	C10	109.7(6)	C11	N4	C8	118.7(6)
N4	C11	N5	115.3(6)	C11	N5	C12	119.9(6)
O3	C11	N4	122.6(7)	C11	N5	C13	117.8(6)

O3	C11	N5	122.1(7)	C13	N5	C12	114.8(6)
N6	C13	N5	114.0(6)	C13	N6	C14	123.3(6)

Table C4: Torsion Angles for H4MeN5-Alkyne.

A	**B**	**C**	**D**	**Angle/°**
C1	C2	C3	C4	-2.0(10)
C1	C2	C3	N1	179.1(6)
C1	C6	N3	C7	-104.6(8)
C2	C1	C6	C5	0.9(10)
C2	C1	C6	N3	-173.3(6)
C2	C1	N2	C17	32.1(10)
C2	C3	C4	C5	0.3(11)
C2	C3	N1	C18	-145.2(7)
C3	C4	C5	C6	2.0(11)
C4	C3	N1	C18	35.9(10)
C4	C5	C6	C1	-2.7(11)
C4	C5	C6	N3	171.5(7)
C5	C6	N3	C7	81.2(9)
C6	C1	C2	C3	1.4(10)
C6	C1	N2	C17	-146.6(7)
C7	C8	N4	C11	-42.8(8)
C8	C7	N3	C6	-174.3(6)
C9	C8	N4	C11	-162.6(6)
C10	C8	N4	C11	78.7(8)
C14	C17	N2	C1	-176.2(6)
C15	C14	C17	N2	-167.2(6)
C15	C14	C17	O2	14.8(10)
C15	C14	N6	C13	68.5(8)
C16	C14	C17	N2	72.2(8)
C16	C14	C17	O2	-105.8(9)
C16	C14	N6	C13	-170.7(6)
C17	C14	N6	C13	-53.8(9)
C18	C19	C20	C21	-175.3(8)
C19	C18	N1	C3	170.8(6)
C19	C20	C21	C22	126(14)
N1	C3	C4	C5	179.1(7)
N1	C18	C19	C20	147.9(7)
N2	C1	C2	C3	-177.2(6)
N2	C1	C6	C5	179.6(6)

N2	C1	C6	N3	5.3(9)
N3	C7	C8	C9	75.1(7)
N3	C7	C8	C10	-164.4(6)
N3	C7	C8	N4	-43.0(7)
N4	C11	N5	C12	12.0(9)
N4	C11	N5	C13	-136.2(6)
N5	C11	N4	C8	165.1(6)
N5	C13	N6	C14	155.6(6)
N6	C13	N5	C11	-48.8(8)
N6	C13	N5	C12	161.5(6)
N6	C14	C17	N2	-43.4(8)
N6	C14	C17	O2	138.6(8)
O1	C7	C8	C9	-102.4(8)
O1	C7	C8	C10	18.1(9)
O1	C7	C8	N4	139.5(7)
O1	C7	N3	C6	3.2(10)
O2	C17	N2	C1	1.8(12)
O3	C11	N4	C8	-12.6(10)
O3	C11	N5	C12	-170.2(7)
O3	C11	N5	C13	41.6(9)
O4	C13	N5	C11	132.5(7)
O4	C13	N5	C12	-17.3(10)
O4	C13	N6	C14	-25.8(11)
O5	C18	C19	C20	-32.4(10)
O5	C18	N1	C3	-8.9(11)

.

[1] O. V. Dolomanov, L. J. Bourhis, R. J. Gildea, J. A. K. Howard and H. Puschmann, OLEX2: a complete structure solution, refinement and analysis program. J. Appl. Cryst. (2009). 42, 339-341.
[2] SHELXS-97 (Sheldrick, 1990)
[3] XL, G.M. Sheldrick, Acta Cryst. (2008). A64, 112-122

Crystal structure determination of [H4MeN5-Alkyne]

Crystal Data. $C_{23}N_6O_4$, M =424.29, monoclinic, a = 9.8498(16) Å, b = 19.932(3) Å, c = 11.9950(19) Å, β = 100.528(3)°, U = 2315.3(6) Å^3, T = 566(2), space group $P2_1/c$ (no. 14), Z = 4, μ(MoKα) = 0.088, 25649 reflections measured, 5339 unique (R_{int} = 0.1427) which were used in all calculations. The final $wR(F_2)$ was 0.4124 (all data).

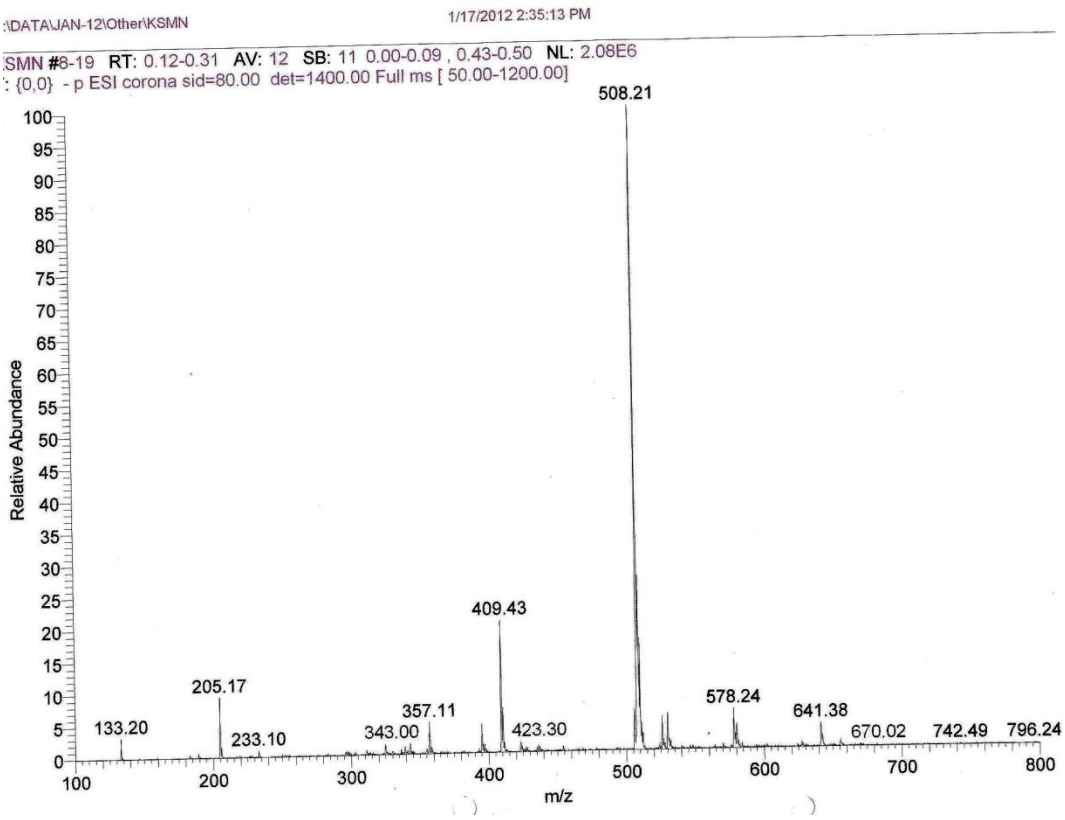

Figure C8: HR-MS spectrum of the alkyne tailed biuret-modified Fe-TAML (m/z value at 508.21 corresponds to the anionic Fe^{III} complex) in the negative mod of the instrument.

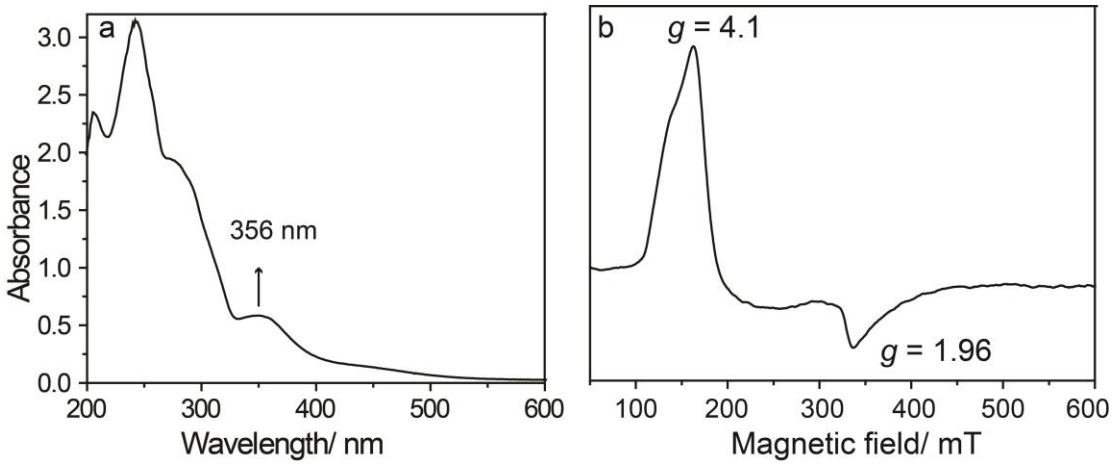

Figure C9: a) UV-vis spectrum of alkyne tailed biuret-modified Fe-TAML in water (0.1 mM); b) X-band EPR spectrum of same in acetonitrile at 90 K.

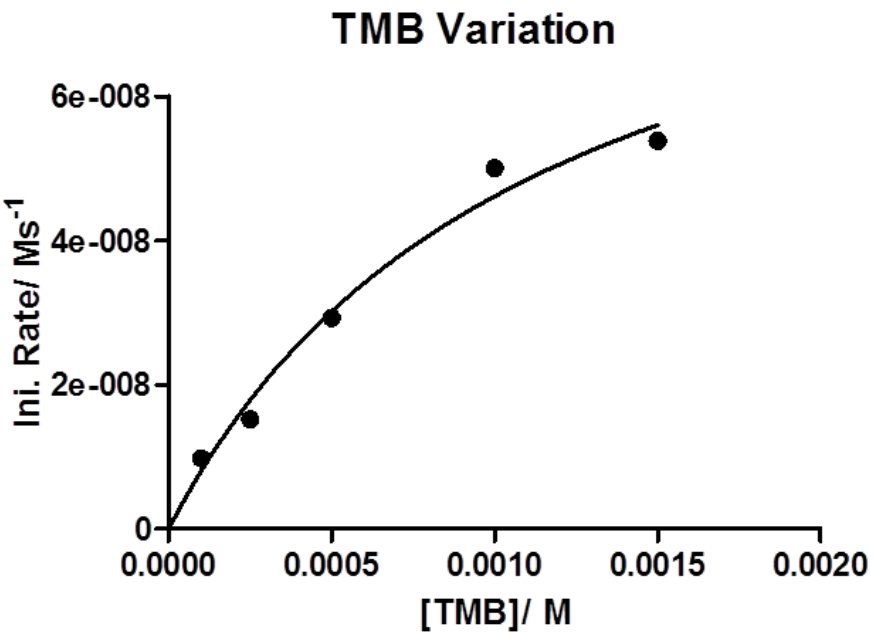

Figure C10: Kinetics of TMB oxidation; Initial rate vs. [TMB] at $[H_2O_2] = 4 \times 10^{-2}$ M and [Catalyst] = 10^{-8} M

Table C5: Michaelis-Menten fit parameters for TMB oxidation

Michaelis-Menten	
Best-fit values	
V_{max}	9.791e-008
K_m	0.001123
Std. Error	
V_{max}	1.746e-008
K_m	0.0003748
95% Confidence Intervals	
V_{max}	4.234e-008 to 1.535e-007
K_m	0.0 to 0.002315
Goodness of Fit	
Degrees of Freedom	3
R^2	0.9806
Absolute Sum of Squares	3.071e-017
Sy.x	3.199e-009
Constraints	
K_m	$K_m > 0.0$
Number of points Analyzed	5

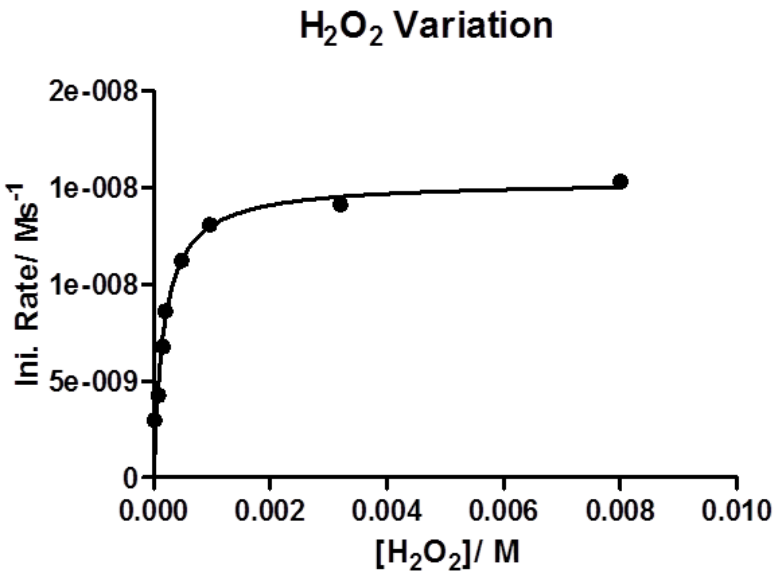

Figure C11: Kinetics of TMB oxidation; Initial rate vs. $[H_2O_2]$ at [TMB] = 2.5×10^{-4} M and [Catalyst] = 10^{-8} M

Table C6: Michaelis-Menten fit parameters for TMB oxidation

Michaelis-Menten	
Best-fit values	
V_{max}	1.532e-008
K_m	0.0001755
Std. Error	
V_{max}	5.824e-010
K_m	2.658e-005
95% Confidence Intervals	
V_{max}	1.389e-008 to 1.674e-008
Km	0.0001104 to 0.0002405
Goodness of Fit	
Degrees of Freedom	6
R^2	0.9735
Absolute Sum of Squares	3.952e-018
Sy.x	8.116e-010
Constraints	
K_m	$K_m > 0.0$
Number of points Analyzed	8

List of Publications

1. Homogeneous Photochemical Water Oxidation by Biuret Modified Fe-TAML: Evidence of Fe^{V}(O) Intermediate; **Chakadola Panda**, Joyashish Debgupta, David Díaz Díaz, Kundan K. Singh, Sayam Sen Gupta and Basab B. Dhar; *J. Am. Chem. Soc.*, **2014**, 136 (35), 12273–12282.
2. Fe-TAML Encapsulated inside Mesoporous Silica Nanoparticles as Peroxidase Mimic: Femtomolar Protein Detection; Sushma Kumari, Basab B. Dhar, **Chakadola Panda**, Abhishek Meena, and Sayam Sen Gupta; *ACS Appl. Mater. Interfaces*, 2014, 6 (16), 13866–13873.
3. Formation of a Room Temperature Stable Fe^{V}(O) Complex: Reactivity Toward Unactivated C-H Bonds; Munmun Ghosh, Kundan K. Singh, **Chakadola Panda**, Andrew Weitz, Michael P. Hendrich, Terrence J. Collins, Basab B. Dhar, and Sayam Sen Gupta; *J. Am. Chem. Soc.*, **2014**, 136 (27), 9524–9527.
4. Catalytic signal amplification using [Fe^{III}(biuret-amide)]-mesoporous silica nanoparticles: visual cyanide detection; **Chakadola Panda**, Basab B. Dhar, Bharmana Malvi, Yudhajit Bhattacharjeez and Sayam Sen Gupta; *Chem. Commun.*, **2013**, 49, 2216-2218.
5. One pot glucose detection by [Fe^{III}(biuret-amide)] immobilized on mesoporous silica nanoparticles: an efficient HRP mimic; Bharmana Malvi, **Chakadola Panda**, Basab B. Dhar and Sayam Sen Gupta; *Chem. Commun.*, **2012**, 48, 5289-5291.
6. Synthesis of functional hybrid silica scaffolds with controllable hierarchical porosity by dynamic templating; Anal Kr. Ganai, Sushma Kumari, Kamendra P. Sharma, **Chakadola Panda**, Guruswamy Kumaraswamy and Sayam Sen Gupta; *Chem. Commun.,* **2012,** 48, 5292-5294**.**
7. Fe(III) complex of biuret-amide based macrocyclic ligand as peroxidase enzyme mimic; **Chakadola Panda**, Munmun Ghosh, Tamas Panda, Rahul Banerjee and Sayam Sen Gupta; *Chem. Commun.*, **2011**, 47, 8016-8018.
8. In-gel Protein Bio-marker sensing Through Signal Amplification: A Potential Replacement of HRP in Western blots; **Chakadola Panda**, Sushma Kumari, Shyamalava Mazumdar and Sayam Sen Gupta. (*Manuscript under preparation*)

9. Tuning the Reactivity of $Fe^{V}(O)$ Towards C-H bonds at Room Temperature: Effect of Water; Kundan K. Singh, Mrityunjoy Tiwari, Munmun Ghosh, **Chakadola Panda**, Andrew Weitz, Michael P. Hendrich, Basab B. Dhar Kumar Vanka and Sayam Sen Gupta. (*Manuscript under preparation*)